Nuclear structure of ^{118}Sn studied through beta decay of ^{118}In and thermal neutron capture of ^{117}Sn(n, γ)

by

Kevin Alexander Ortner

B.Sc., Simon Fraser University, 2017

Thesis Submitted in Partial Fulfillment of the
Requirements for the Degree of
Doctor of Philosophy

in the
Department of Chemistry
Faculty of Science

SIMON FRASER UNIVERSITY
Summer 2023

Declaration of Committee

Name:	**Kevin Alexander Ortner**
Degree:	**Doctor of Philosophy**
Thesis title:	**Nuclear structure of ^{118}Sn studied through beta decay of ^{118}In and thermal neutron capture of ^{117}Sn(n, γ)**
Committee:	**Chair:** Neil Branda Professor, Chemistry

Corina Andreoiu
Supervisor
Professor, Chemistry

Zuo-Guang Ye
Committee Member
Professor, Chemistry

Adam Garnsworthy
Committee Member
Senior Scientist, TRIUMF

Peter Kunz
Examiner
Adjunct Professor, Chemistry

Alejandro Algora
External Examiner
Instituto de Física Corpuscular (CSIC-University of Valencia)

Abstract

The works presented here focus on the semi-magic, stable nucleus ^{118}Sn and the nuclear structure within. Two very different reactions were performed to populate excited states in ^{118}Sn: β-decay of ^{118}In and the thermal neutron capture, ^{117}Sn$(n,\gamma)^{118}$Sn.

In the β-decay experiment performed at TRIUMF, the 5^+ isomer of ^{118}In decayed to excited states in ^{118}Sn which subsequently decayed via γ-ray emission towards the ground state. The γ rays were detected with the GRIFFIN spectrometer and a total of 10^9 events were recorded in γ-γ coincidence. A total of 99 transitions from 23 levels were observed with one level and 49 transitions being newly observed. The focus of the analysis was on observing states with a collective proton two-particle two-hole, 2p-2h, excitation across the $Z = 50$ shell closure that gives rise to deformed states and shape coexistence. From the 2p-2h, 2_2^+ state, a known 284.5-keV transition was resolved from a triplet centred at 285.2 keV. A reduction in the intensity, compared to literature, was observed for this transition which led to a reduced $E2$ transition probability of 21(4) W.u. from the previous 39(7) W.u.—suggesting less collectivity.

The neutron capture experiment was performed at the Institut Laue-Langevin where the enriched ^{117}Sn target was bombarded with a high flux of thermal neutrons at the centre of the FIPPS array. Over 10^{10} γ-γ coincidence events were recorded. A total of 423 γ-ray transitions were placed to the level scheme of 96 states. From these, 357 transitions and 46 levels were newly observed. Primary γ-ray transitions from the capture state populated 33 potential $J = 2^+$ states in the 3–5 MeV region. A level density consisting of 2^+ states in this energy region is of interest for the study of the pygmy quadrupole resonances (PQR). The spins of these states were not firmly established and no conclusive evidence for the PQR was observed. However, the measured level energies could help constrain future calculations for these states.

Keywords: nuclear structure; beta decay; neutron capture; gamma ray spectroscopy; shape coexistence

Dedication

Knock, knock.
Who’s there?
For.
For who?
For Charlie, of course!

Acknowledgements

To get to the stage at which I am now thinking about all of the people I wish to thank is very surreal. It is humbling to think of how many people have helped me along the way. There are so many people!

Dr. Corina Andreoiu, you were there from the beginning when I was just an undergrad. I owe this degree to you and your encouraging words of wisdom ("chop-chop"). You were always available to talk about anything research related and always gave me time and a safe space to express personal struggles. I appreciate your level of care towards the person as much as the science which is conducted.

My committee, Dr. Adam Garnsworthy, and Dr. Zuo-Guang Ye, you both provided constructive feedback and remained positive throughout which helped keep me on track.

To everyone in our group, I appreciate the help and friendship you all provided. Drs. Pietro Spagnoletti and Kenneth Whitmore, you both helped immensely with my understanding of what it is that I was doing. At times, I really wasn't quite sure. Pietro, I know we talked more about food than science, but you actually helped me out with the science and not with where I want to go to eat. Drs. Fatima Garcia, David Cross, and Jenn Pore, you helped me when I was just starting out so that I didn't have a nervous breakdown within the first few weeks. Isiah Djianto, Kurtis Raymond, Frank Wu, you all helped keep the office a fun place to work, as well as providing me with plenty of feedback on my work along the way. Kurtis, you also helped greatly with the work you put into setting up the ILL coding which saved me many hours of work. Dom, Emily, Matt, Heinz, Melanie, Rebecca, Elliot, you also kept the office an inviting place and humoring me with responses to my many opinions and strange comments.

Tessa... I owe you the biggest thanks of all. Not for any help in this research—although I appreciate you trying to understand when I describe the science–but for helping me as a person. I have never met anyone as considerate as you, and I am lucky to have you in my corner when things get difficult. "You've made this day a special day, by just your being you. There's no person in the whole world like you, and I like you just the way you are.“ I love you just the way you are.

Table of Contents

List of Tables

List of Figures

Chapter 1

Introduction

With the greatest number of stable isotopes of any element, Sn ($Z = 50$) offers a testing ground for many theoretical models that aim to describe the strong nuclear force which binds the nucleus together. The chain extends from $^{100}_{50}\mathrm{Sn}_{50}$ to beyond $^{132}_{50}\mathrm{Sn}_{82}$, where the numbers, 50 and 82, are *magic numbers* corresponding to a shell closure—much like the closed valence shells of electrons that represent the noble gases. These magic numbers are not only observed, but are predicted by the nuclear shell model which is used to describe the arrangement of protons and neutrons within the nucleus. The closed shell of protons, $Z = 50$, gives rise to an increased stability, and by varying the number of valence neutrons from $N = 50$ to $N = 82$, observations on the evolution of nuclear structure can be made and compared to theory. This is especially true for the even-even Sn nuclei (even number of both protons and neutrons), which exhibit, relative to neighbouring odd-even, even-odd, and odd-odd nuclei, greater stability due to the pairing of like-nucleons [1]. This pairing results from a favourable spin coupling to $J = 0$ in the ground state which is described as being spherical for magic nuclei.

Generally, for even-even nuclei, the first excited state has a spin and parity of $J = 2^+$. For Sn, this state is the result of breaking a pair of valence neutrons as evidenced by the nearly unchanged energy of ≈ 1.2 MeV across the chain of isotopes [2,3], shown in Figure 1.1. This is a prime example of the seniority scheme which is a useful way to express the excited energy states based on the number of unpaired nucleons—in the case of the first excited state in even-even Sn, neutrons with seniority two, $\nu = 2$, would consist of breaking a pair of neutrons and coupling their orbital angular momentum to $J = 2^+$. Higher lying $\nu = 2$ states can also occur if the magnitude of the orbital angular momentum, j, allows for it. For non-magic nuclei in the Sn region, the energy of the first excited state, 2^+_1, is drastically reduced [2]. This is due to an increase in proton-neutron, p-n, interactions in the valence space which is attractive and lowers the energy associated with these configurations. States with a greater number of p-n interactions are often described as collective excitations rather than a simple breaking of a like-nucleon pair. It is also observed in the neutron midshell region of Sn that a 2-particle 2-hole (2p-2h) proton excitation across the $Z = 50$ shell closure occurs, increasing the number of p-n interactions and lowering of energy states that are associated with a deformed shape compared to the spherical ground state configuration. This is evident by the parabolic shape of the

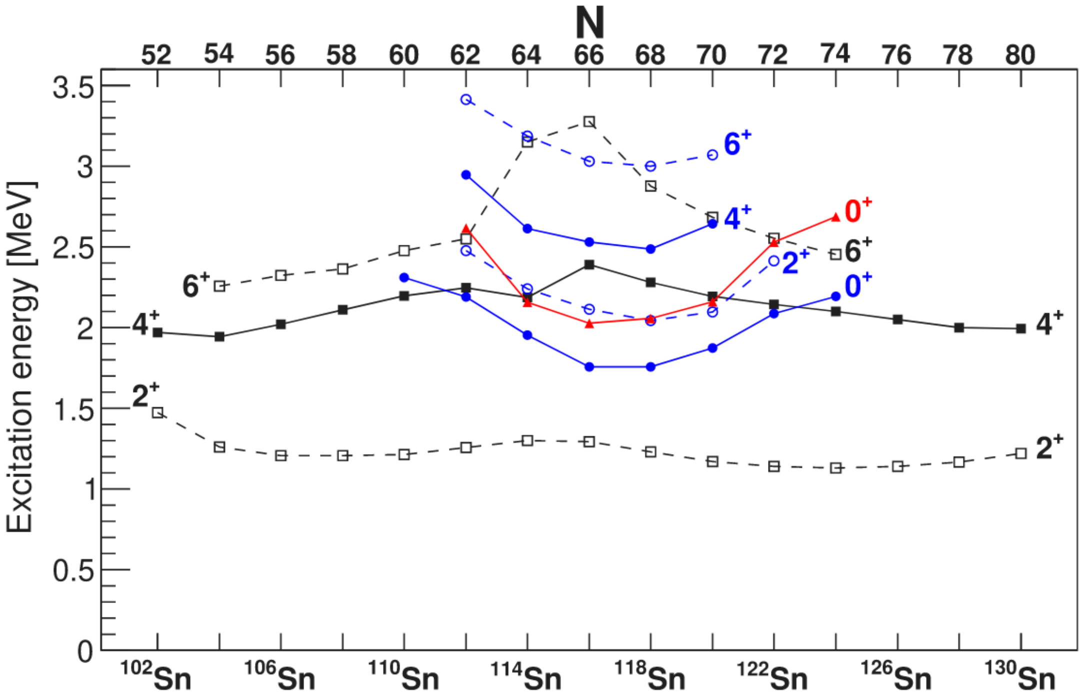

Figure 1.1: The lowest levels of the even-even Sn isotopes for the first instance of total spin, J. Of importance is the nearly constant energy of the first 2^+ state across the isotopic chain. This is evidence of the breaking of a neutron pair in the valence space with a closed shell of protons. Across the neutron midshell, it is also observed that states belonging to 0^+ 2-proton excitation across the shell closure (blue and red) decrease in energy to a minimum at $N = 66$. Reprinted with permission from Reference [4].

$0^+, 2^+, 4^+$ and 6^+ states shown in Figure 1.1. These collective particle-hole excitations across shell gaps intrude into the ground state configuration (spherical in the case of Sn) and result in competing shapes at similar energies. This description is known as *shape coexistence* and has been observed across much of the nuclear landscape—predominantly around proton magic numbers [4, 5].

The low-lying energy states that are attributed to shape coexistence in the even-even Sn nuclei have increased electric quadrupole strength since the quadrupole moment is a direct consequence of nuclear shape. As such, a signature of the 2p-2h states in Sn (and other nuclei that exhibit shape coexistence) is enhanced strength in the transition probabilities for electric quadrupole, or $B(E2)$ values. These values are one of the subjects of studies presented in the analysis of the β-decay of ^{118}In (see Section 4) to identify the states with the 2p-2h configuration in ^{118}Sn.

The collectivity of the 2p-2h states in Sn, being a closed shell nucleus, is rather weak relative to similar states in non-magic nuclei. However, recent studies have observed highly collective states in the stable even-even Sn isotopes which are attributed to a resonance mode with dipole or quadrupole character. It is not new to observe resonances in nuclei—one of the earliest nuclear structure discoveries is that of the Giant Dipole Resonance, GDR [6, 7] which is now an established concept exhibited in all but the lightest nuclei above the separation energies for the nucleons, and other multipolarities (eg. monopole and quadrupole) are also well known to occur at higher energies. The isovector GDR is described as an out-of-phase oscillation of the protons against the neutrons. However, weakly populated resonance states which occur below the neutron separation energies have recently been observed. The first to be observed was the Pygmy Dipole Resonance, PDR, which has increased dipole strength as a grouping of 1^- states in a resonance-like structure below the neutron separation energy on the low-energy tail of the GDR. The description often given (although debated [8]) is an excess-neutron skin oscillating against a saturated proton-neutron core in a dipole mode [9, 10]. This description has led to a proposed Pygmy Quadrupole Resonance, PQR, which, through observations and theoretical calculations, has been suggested in ^{112,114,124}Sn as a grouping of quadrupole states, 2^+, in the 3-5 MeV range, and having an increased decay probability directly to the ground state [11, 12]. The PQR is of interest to better understand the dynamics of the nuclear force and to see if these states are as prevalent throughout the nuclear landscape as shape coexistence is. As a second topic presented in these works, the observation of potential 2^+ states populated in the neutron capture reaction, ^{117}Sn$(n,\gamma)^{118}$Sn (see Section 5) with enhanced ground state feeding in^{118}Sn is of interest.

1.1 Nuclear Shell Model

The nuclear shell model is similar to what is understood of the quantum system of the atomic electrons which occupy available orbitals within a shell of increasing energy. Electrons cannot occupy the same energy state as the Pauli exclusion principle does not allow for fermions to occupy the same quantum state. Therefore, by increasing the number of electrons occupying orbitals, the number of higher energy states must also increase. Observations such as the atomic radius and ionization energies reveal electron shell structure where drastic changes in both quantities occur when the atomic number changes from one shell to the next, as shown in Figure 1.2.

The electron shell structure can be used to predict atomic properties based solely on the valence electrons while assuming an inert core of filled shells [1]. The theory can be used convincingly enough with the well-known external Coulomb potential that is generated by the central nucleus. A strong understanding of the potential, $V(r)$ allows one to solve the Schrödinger equation for the atomic shells and the subshells within them:

$$[-\frac{\hbar^2}{2m}\nabla^2 + V(r)]\psi(\vec{r}) = E\psi(\vec{r}). \tag{1.1}$$

Applying this theory to the nucleus is not as simple since the nuclear force potential is not well understood and is self generated—a nucleon moves independently in a field generated by all of the other nucleons [1]. That being said, observations of shell structure have been observed without the need for a theoretical description.

Evidence of nuclear shells has been shown by measuring the proton and neutron separation energies, shown in Figure 1.3. This yields a similar behaviour as that observed for the ionization

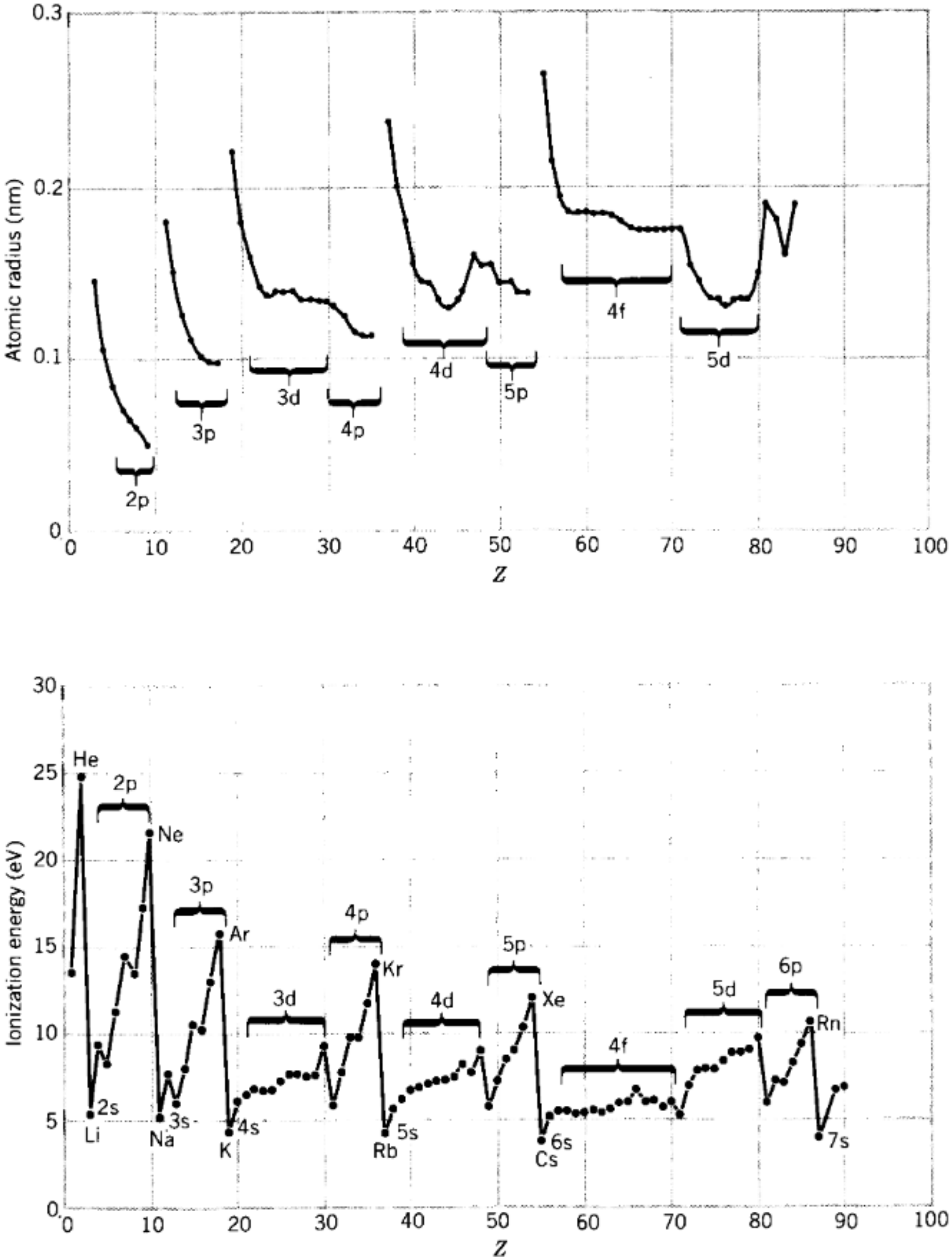

Figure 1.2: The atomic radius (top) and ionization energy (bottom), both with respect to proton number, Z, show large changes from one closed valence shell to the next, higher shell. These indicate shell structure in electron configuration. Reprinted with permission from Reference [1].

energies for atoms [1,13]. Furthermore, the excitation energy of the first excited 2^+ state for closed shell even-even nuclei (nuclei with an even number of protons and neutrons) is much greater than for neighbouring, non-magic nuclei, shown Figure 1.4, and the stability of closed shell nuclei is relatively greater to their immediate neighbours—both evident by the number of stable isotopes for closed proton shells as well as the ground-state lifetimes of closed shell nuclei [2,14].

The values at which closed shells are observed are 2, 8, 20, 28, 50, 82 and 126 for both protons and neutrons. Of course, $Z = 126$ is not an element that has been observed yet so it is unknown if 126 is a magic number for protons.

In order to reproduce these magic numbers, the potential must be determined. Simple potentials like the square well and the harmonic oscillator can be used to produce the first three magic numbers, 2, 8 and 20, but not the higher shell closures. These potentials are unrealistic as they are infinitely deep and, as previously shown, protons and neutrons can be separated with a finite amount of energy. A more accurate potential which represents the experimental data well, is the Woods-Saxon potential given by

$$V(r) = \frac{-V_0}{1+exp[(r-R)/a]} \tag{1.2}$$

where R is the mean nuclear radius, and a is the skin thickness [1]. This form of the potential is intermediate to the square well and harmonic oscillator and it removes the degeneracies associated with the harmonic oscillator in which the principle quantum number groups the allowed orbital angular momentum quantum numbers to the same energy. However, the Woods-Saxon potential still only reproduces the first three magic numbers.

Drawing from the atomic theory in which there is a fine structure of spectral lines due to a coupling of the electrons orbital motion, l, with its intrinsic spin, s, a consideration of spin-orbit coupling was applied to the nucleons [16]. While the effects of the spin-orbit force in atoms is very small, the splitting of nuclear orbitals is much more significant. The form of the spin-orbit potential is simply, $V_{so}(\vec{r})\vec{l}\cdot\vec{s}$, with

$$\vec{l}\cdot\vec{s} = \frac{1}{2}(\vec{j}^2 - \vec{l}^2 - \vec{s}^2). \tag{1.3}$$

Here, $\vec{j} = \vec{l} + \vec{s}$ and the expectation values are:

$$< j^2 > = j(j+1)\hbar^2 \tag{1.4}$$

$$< l^2 > = l(l+1)\hbar^2 \tag{1.5}$$

$$< s^2 > = s(s+1)\hbar^2 \tag{1.6}$$

The expectation value for Equation 1.3 can be determined as,

$$< \vec{l}\cdot\vec{s} > = \frac{1}{2}[j(j+1) - l(l+1) - s(s+1)]\hbar^2, \tag{1.7}$$

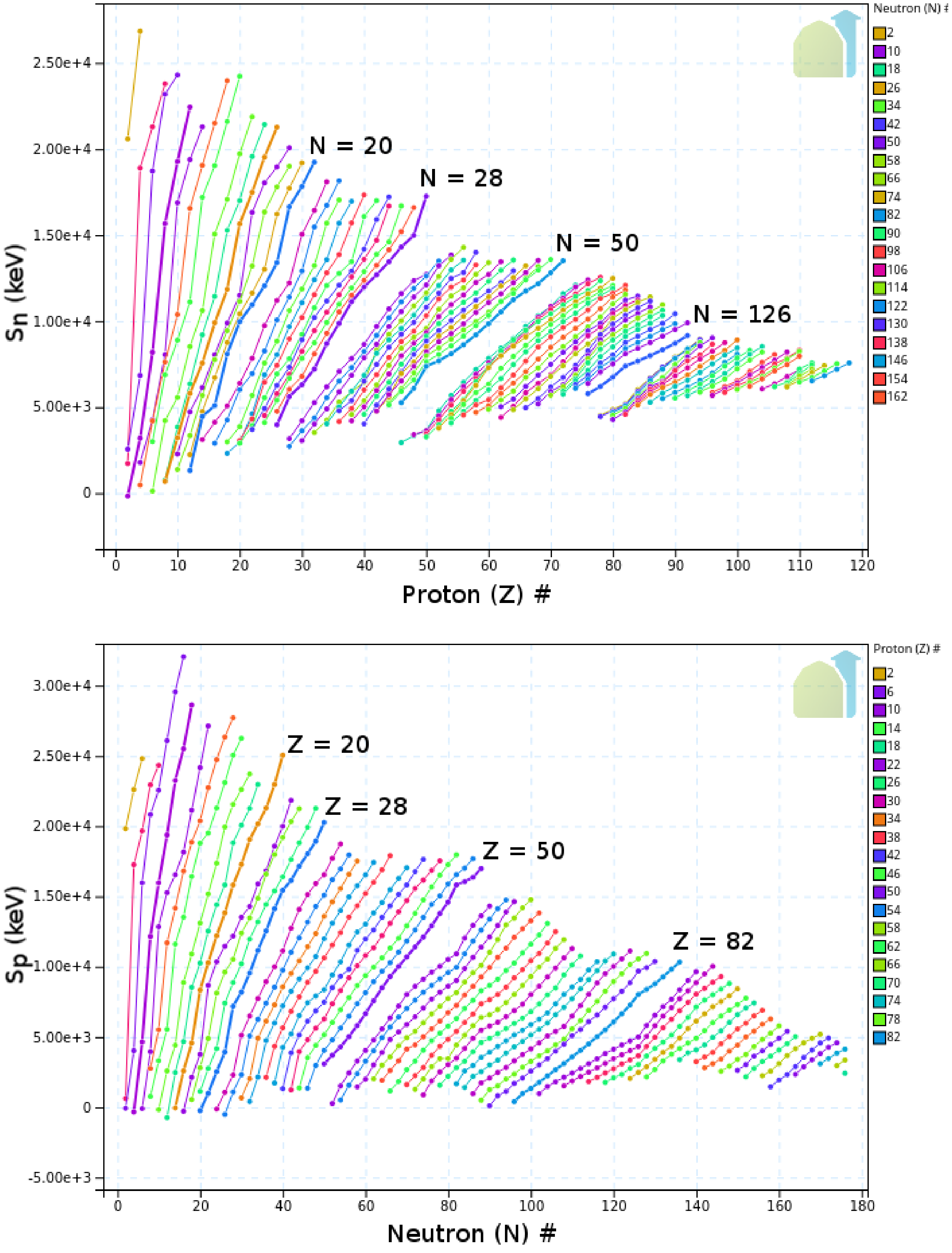

Figure 1.3: Neutron (top) and proton (bottom) separation energies (S_n and S_p, respectively) with respect to proton number, Z, and neutron number, N, respectively. These highlight a drastic decrease in separation energy when moving from a closed shell to the subsequent shell. Adapted from NuDat data [15].

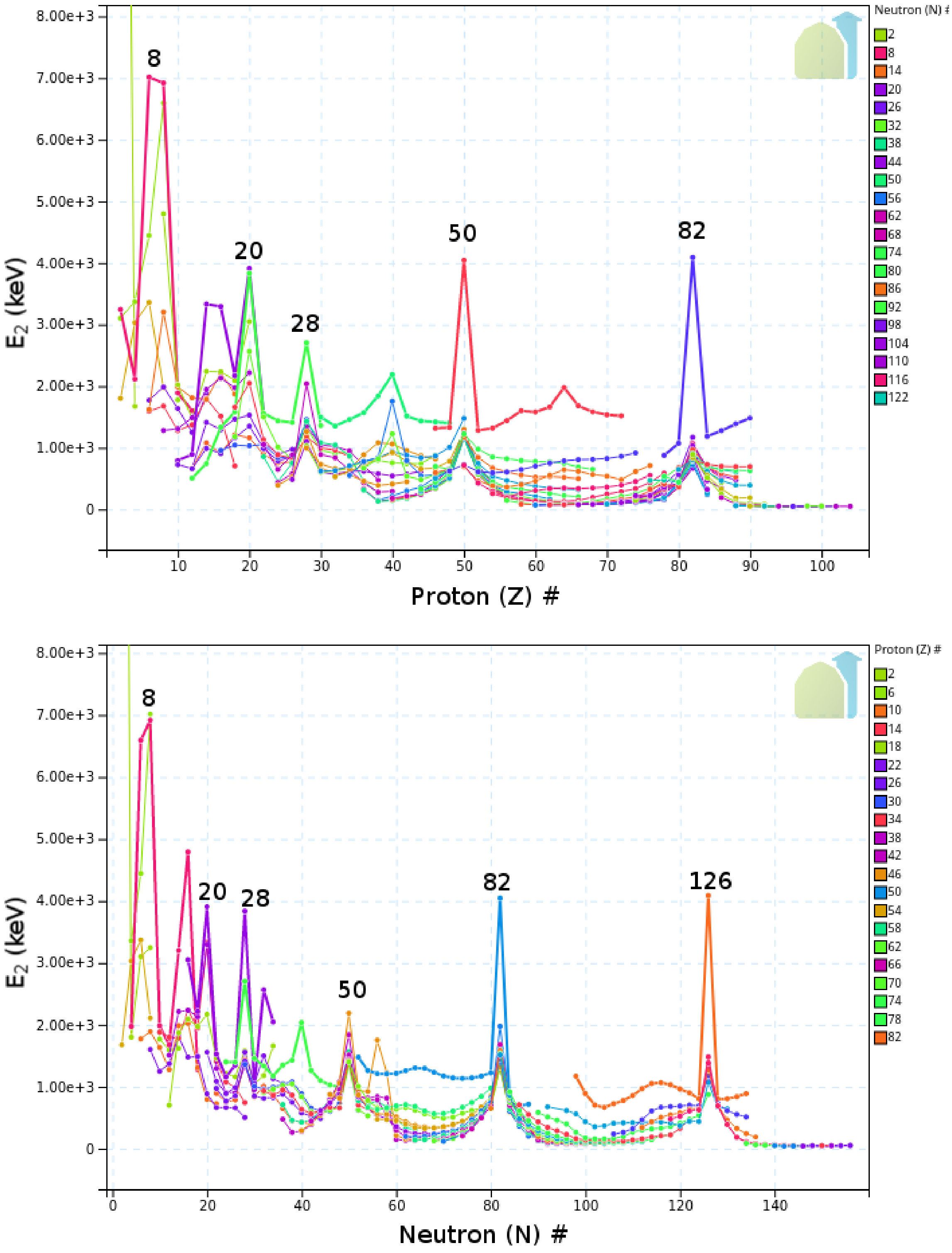

Figure 1.4: The first excited 2^+ state for even-even nuclei with respect to Z (top) and N (bottom). For closed shells, the energies of these states increase drastically. Adapted from NuDat data [15].

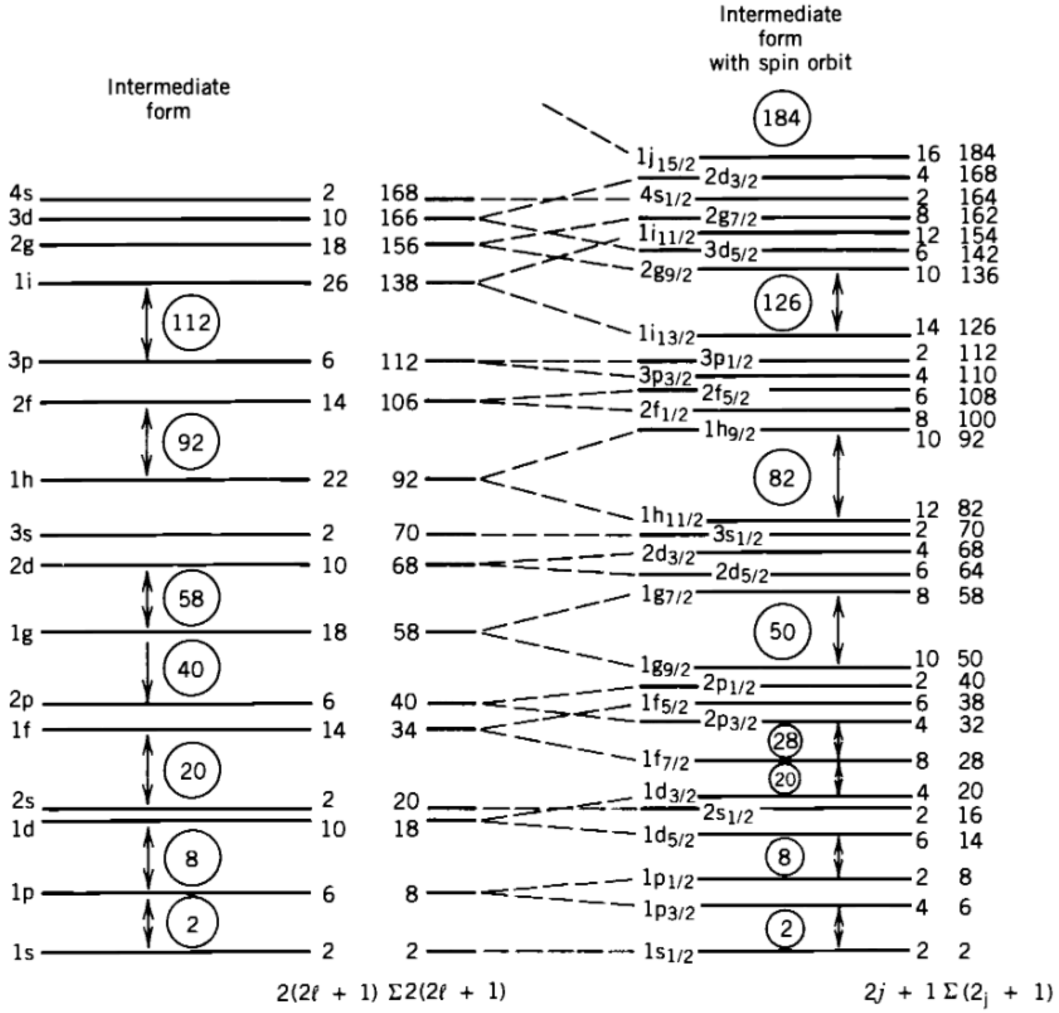

Figure 1.5: The energy levels of the Woods-Saxon potential without (left) and with (right) spin-orbit coupling. Reprinted with permission from Reference [1].

and with $j = l \pm \frac{1}{2}$, since the intrinsic spin is known to be $\pm\frac{1}{2}$, the difference in energy is

$$< l \cdot s >_{l+1/2} - < l \cdot s >_{l-1/2} = \frac{1}{2}(2l+1)\hbar^2. \tag{1.8}$$

This reveals there is an increase in energy splitting with increasing orbital angular momentum and with V_{so} taken to be negative, the higher j value $(l + 1/2)$ is pushed down and the the lower j value $(l - 1/2)$ is raised up in energy. This is indicated in the schematic of the nuclear shell structure, shown in Figure 1.5, which now accurately predicts the shell closures [1, 2]. In the intermediate Woods-Saxon potential, the shells are grouped with orbitals of the same parity given by $\pi = (-1)^l$. With spin-orbit coupling, the state that is lowered can intrude into a shell with opposite parity. These are called *intruder states* and can lead to pure states with little configuration mixing with the other states within the shell [2].

The nuclear shell model has been a fundamental model for the past 70 years. Yet, while many properties of nuclei can be explained using the shell model, especially an extreme model which considers only one valence nucleon and an inert core, the energy-level structure predicted with the shell model can be quite different than observed largely in part due to residual interactions between the many valence nucleons at play. This makes the shell model not really feasible for calculating or predicting structure in nuclei with many valence nucleons in the mid-shells when considering all but the lightest nuclei. However, it still remains the benchmark for other models which try to incorporate collective excitations in both microscopic and macroscopic views and states which are deformed.

1.2 β Decay

The radioactive decay process in which the mass number, A, remains the same but the atomic number, Z, changes is called β decay. This can occur in three forms: negative β decay (β^-), positive β decay (β^+), and electron capture (ε) [1, 17]. The underlying mechanism for β decay is governed by the weak interaction which, through the emission of a W boson, changes the flavour of a down quark within a neutron to an up quark causing it to transform into a proton (β^-), or an up quark within a proton to a down quark causing it to transform into a neutron (β^+ and ε). Furthermore, in the process, the β particle and its corresponding neutrino are leptons and are a result of the W boson decay. The lepton number is conserved in the process. The β-particles, while generated in the process for β^- and β^+, are simply electrons and positrons, respectively.

$${}^{A}_{Z}X_N \rightarrow {}^{A}_{Z+1}Y_{N-1} + e^- + \bar{\nu}_e \tag{1.9}$$

$${}^{A}_{Z}X_N \rightarrow {}^{A}_{Z-1}Y_{N+1} + e^+ + \nu_e \tag{1.10}$$

$${}^{A}_{Z}X_N + e^- \rightarrow {}^{A}_{Z-1}Y_{N+1}\bar{\nu}_e \tag{1.11}$$

In the three equations above, ${}^{A}_{Z}X_N$ represents the *parent* nucleus, and ${}^{A}_{X+1}Y_{N-1}$ and ${}^{A}_{X-1}Y_{N+1}$ are the *daughter* nuclei in their respective β-decay process. The energy available, Q, in each of these three processes is the difference between the initial and final nuclear masses, as shown in Equation 1.12 for the β^--decay.

$$Q_{\beta^-} = (M_P - M_D)c^2 \tag{1.12}$$

Here, the masses, M_P and M_D, are the neutral atomic masses for the parent and daughter, respectively. When $Q > 0$, the process is spontaneous and excited states in the daughter nucleus up to the Q-value can be populated. However, the Q-value alone does not indicate the rate at which the decay will happen. The decay probability, λ, which is the inverse of the mean lifetime, τ, can be quantum mechanically described using Fermi's Golden Rule [1]:

$$\lambda = \frac{2\pi}{\hbar}|V_{fi}|^2\rho(E_f). \tag{1.13}$$

The quantity V_{fi} is the transition matrix element given by,

$$V_{fi} = \int \psi_f^* V \psi_i dv, \tag{1.14}$$

where ψ represents the initial, i, and final, f, nuclear wave functions, which are considered to be stationary states of the potential, V. In Equation 1.13, $\rho(E_f)$ is the density of final states. This indicates that the greater number of final states available for a given transition, the more likely the given transition will occur. The density of final states for a given energy can also be expressed as dn/dE_f.

Considering that the final state wave function consists not only of the nuclear wave function, ψ_f, but also the wave functions of the electron and neutrino, ϕ_{e^-} and ϕ_{ν_e}, Equation 1.14 becomes,

$$V_{fi} = g \int [\psi_f^* \phi_{e^-}^* \phi_{\nu_e}^*] \hat{O} \psi_i dv. \tag{1.15}$$

The strength of the interaction, represented by the parameter g, characterizes the weak interaction. The wave functions for the electron and neutrino, with momenta p and q, respectively, have a free-particle form,

$$\phi_{e^-} \propto e^{i\vec{p}\cdot\vec{r}/\hbar} \tag{1.16}$$

$$\phi_{\nu_e} \propto e^{i\vec{q}\cdot\vec{r}/\hbar}, \tag{1.17}$$

which can both be approximated to $\cong 1$ and is known as the *allowed* approximation. This can be realized from an expansion with $pr \ll 1$ for the case of an electron with 1 MeV kinetic energy, as well as the assumption that the electron and neutrino are created at the origin, $r = 0$—providing no orbital angular momentum. Thus, only the density of states are dependant on the electron and neutrino energy:

$$dn_{e^-} = \frac{4\pi p^2 dp\, V}{h^3}, \tag{1.18}$$

and

$$dn_{\nu_e} = \frac{4\pi q^2\, dq\, V}{h^3}. \tag{1.19}$$

The number of final electron and neutrino states with momenta in the range of p to $p+dp$ and q to $q+dq$, respectively, is given by the previous Equations 1.18 and 1.19 [1]. In the allowed approximation, the partial decay rate for the electrons and neutrinos with the final energy $E_f = E_{e^-} + E_\nu$ is given by,

$$d\lambda = \frac{2\pi}{\hbar} g^2 |M_{fi}|^2 (4\pi)^2 \frac{p^2 dp\, q^2 dq}{h^6\, dE_f}, \tag{1.20}$$

which can be integrated over all values of the electron momentum, p, to determine the total decay rate:

$$\lambda = \frac{g^2|M_{fi}|^2}{2\pi^3\hbar^7c^3}\int_0^{p_{max}} F(Z',p)p^2(Q-T_{e^-})^2dp. \tag{1.21}$$

The quantity, M_{fi} is the nuclear matrix element that depends only on the nuclear wave functions. The terms $p^2(Q-T_{e^-})$ make up a statistical factor that comes from the number of final states for the reaction products, and $F(Z',p)$ is the Fermi function which takes into account the Coulomb field from the nucleus of the daughter with Z protons. The equation can be simplified with what is called the Fermi Integral,

$$f(Z',E_0) = \frac{1}{(m_ec)^3(m_ec^2)2}\int_0^{p_{max}} F(Z',p)p^2(E_0-E_{e^-})^2dp, \tag{1.22}$$

since the integral only depends on Z' and on the maximum total energy of the electron, E_0. This function has been tabulated for values of Z' and E_0 and can be used to obtain the comparative half-life using the relationship $\lambda = 0.693/t_{1/2}$:

$$ft_{1/2} = 0.693\frac{2\pi^3\hbar^7}{g^2m_e^5c^4|M_{fi}|^2}. \tag{1.23}$$

Using this equation, where $t_{1/2}$ is in seconds, β decay probabilities in different nuclei can be compared and the differences in measured values must be due to the differences in the nuclear matrix element, M_{fi}, and the wave functions within [1].

Since the half-lives of β-decaying nuclei can vary greatly (over 20 orders of magnitude from the extremely short lived to the long lived), it is conventional to report the comparative half-life as $\log ft$. This value is useful for distinguishing the type of β decay, as well as aiding in the spin assignment of a state in the daughter nucleus populated directly from the β decay of the parent nucleus.

1.2.1 Allowed Transitions

In the previous section, the allowed approximation assumed the factors which depended on the electron or neutrino energy was from the density of final states. This implies that neither emitted particle carry orbital angular momentum. However, like the nucleons, electrons and neutrinos are fermions with spin, $s = \frac{1}{2}$. The spins of the electron and neutrino can couple to $S = 0$ or $S = 1$, known as Fermi decay and Gamow-Teller decay, respectively.

In the allowed approximation, with no orbital angular momentum carried away, the Fermi β-decay has a change in nuclear spin, $\Delta J = |J_P - J_D| = 0$. In the Gamow-Teller β-decay, $\vec{J_P} = \vec{J_D} + 1$. To couple through a vector length of 1 in this type of β decay, $\Delta J = 0$ or 1. However, in the case of $J_P = J_D = 0$, only the Fermi decay is permitted.

Furthermore, the electron and neutrino not carrying any orbital angular momentum implicates the parities of the initial and final state be identical:

$$\pi_P = \pi_D \pi_l. \tag{1.24}$$

The parity associated with orbital angular momentum is given by

$$\pi_l = (-1)^l, \tag{1.25}$$

and for $l = 0$, $\Delta\pi = \pi_P - \pi_D = 0$.

It follows, then, that the selection rules for an allowed β decay transition are:

$$\Delta J = 0, 1 \qquad \Delta\pi = 0 \text{ or no}$$

1.2.2 Forbidden Transitions

The term *forbidden* is not as strict as it sounds. Forbidden truly means less probable than the allowed transitions and is effectively the second term in the expansion of Equations 1.16 and 1.17, which were assumed negligible in the allowed approximation.

For transitions which involve a change in the parity, $\Delta\pi =$ yes, it must be the case that $l = 1, 3, 5...$, so that $\pi_l = -1$ as indicated from Equation 1.25. However, with increasing orbital angular momentum, the probability decreases and only $l = 1$ is considered for what is called *first forbidden* decays. The same type of coupling between the intrinsic spins of the electron and neutrino apply, $S = 0$ for Fermi decay and $S = 1$ for Gamow-Teller decay, such that selection rules for the change in angular momentum can be made. The selection rules for first forbidden decays are:

$$\Delta J = 0, 1, 2 \qquad \Delta\pi = 1 \text{ or yes}$$

It follows that second-, third-, and fourth-forbidden transitions (higher degrees are available as well, but the probability of such decays are much weaker), can also occur with orbital angular momenta $l = 2, 3$ and 4, respectively. They also stem from the next terms in the expansion of Equations 1.16 and 1.17 as previously indicated. For the case that ΔJ is the maximum for any degree of forbiddeness, only the Gamow-Teller decay is possible and these are called unique.

A summary of the selection rules, as well as the corresponding $\log ft$ values for the type of β decay is presented in Table 1.1.

1.3 γ Decay

1.3.1 Energetics

In contrast to β decay, γ decay involves a re-ordering of nucleons within the same nucleus such that the number of protons and neutrons remains unchanged [13]:

$${}^{A}_{Z}X^{*}_{N} \xrightarrow{\gamma} {}^{A}_{Z}X_{N}. \tag{1.26}$$

Table 1.1: The selection rules of β decay transitions for the degree of forbiddenness and the corresponding $\log ft$ values [1, 13]. ΔJ corresponds to the change in angular momentum between the decaying parent nucleus and state populated in the nucleus. $\Delta\pi$ corresponds to if there is a change in parity between these two states.

Forbiddenness	ΔJ	$\Delta\pi$	$\log ft$
Superallowed	$0^+ \to 0^+$	no	2.9–3.7
Allowed	0, 1	no	4.4–6.0
First Forbidden	0, 1, 2	yes	6–10
Second Forbidden	1, 2, 3	no	10–13
Third Forbidden	2, 3, 4	yes	>15

The asterisk on the left indicates the nucleus is in an excited state and, through the emission of a γ ray, the nucleus loses energy to reach the ground state, shown on the right. The energy conservation is thus,

$$M_0^* c^2 = M_0 c^2 + E_\gamma + T_R, \tag{1.27}$$

where the mass energy of the excited nucleus, $M_0^* c^2$, is equal to the sum of the rest mass of the nucleus, $M_0 c^2$, the γ-ray energy, E_γ, and the recoil energy of the nucleus, T_R. The conservation law for momentum is simply,

$$0 = \vec{P}_R + \vec{P}_\gamma \tag{1.28}$$

Assuming the recoil is nonrelativistic, $T_R = p_R^2/2M_0$ and from Equation 1.28, $T_R = p_\gamma^2/2M_0 = E_\gamma^2/2M_0c^2$. Therefore, Equation 1.27 can be expressed as:

$$\Delta E = E_\gamma + \frac{E_\gamma^2}{2M_0c^2}. \tag{1.29}$$

The term on the left, ΔE, is the difference in the energy between the initial and final states. The recoil is considered negligible for typical γ-ray energies and nuclear masses. For example, a nucleus with mass number, $A = 100$, or mass, $M = 100 * 931.5$ MeV/c^2, the recoil is only 5 eV for a 1 MeV γ-ray photon. Generally, $\Delta E = E_\gamma$. However, the recoil energy is considered in the neutron capture experiment to follow where a 9.3 MeV γ ray is observed from ^{118}Sn. The recoil energy here is 0.39 keV which is greater than the systematic uncertainty of 0.3 keV.

1.3.2 Electromagnetic Transitions

The previous section on the energetics simplifies the γ-decay process to conservation laws without explaining the nature of the decay. Although the nucleons are bound by the strong nuclear force, the emission of γ rays is a result of electromagnetic properties of the nucleons. If the nucleus is regarded as a system of point nucleons with magnetic dipole moments, and of protons with a net charge, then a charge distribution which couples with an external field can cause an *electric* transition, and similarly, current loops from the proton orbital motion as well as the nucleons intrinsic *magnetism* can induce magnetic transitions [14]. These electromagnetic transitions are the dominant mode of decay for excited states below the nucleon separation energies and occur, generally speaking, at much faster rates than the previously discussed β decay. However, like β decay, the rates are dependent on the same form of the decay probability which is proportional to the square of the matrix element [1, 14]:

$$\lambda(\sigma L) = \frac{2(L+1)}{\varepsilon_0 \hbar L[(2L+1)!!]^2} \left(\frac{\omega}{c}\right)^{2L+1} [m_{fi}(\sigma L)]^2. \tag{1.30}$$

The terms to the left of the square of the matrix element comes from the understanding of electromagnetic theory and multipole expansion of the radiated power for multipole order 2^L, where $L =$ 1 for dipole, 2 for quadrupole, and so on. The term σ designates the type of radiation, where $\sigma = E$ for electric, and $\sigma = M$ for magnetic. The matrix element, like for β decay, is

$$m_{fi} = \int \psi_f^* \, m(\sigma L) \, \psi_i dv, \tag{1.31}$$

where the term $m(\sigma L)$ is the multipole operator for the type of electromagnetic transition.

Although the matrix element in Equation 1.30 needs to be evaluated before solving the decay probability further, a simplification can be made with the assumption that the transition is due to a single proton transitioning from an initial state to a final one [1, 18]. For electric transitions, EL, in which the radial parts of the wave functions are assumed to be constant in the nuclear volume, with radius, R, and zero outside, the transition probability for energy, E_γ, is

$$\lambda(EL) = \frac{8\pi(L+1)}{L[(2L+1)!!]} \frac{e^2}{4\pi\varepsilon_0 \hbar c} \left(\frac{E_\gamma}{\hbar c}\right)^{2L+1} \left(\frac{3}{L+3}\right)^2 cR^{2L} \tag{1.32}$$

and for magnetic transitions, ML,

$$\lambda(ML) = \frac{80\pi(L+1)}{L[(2L+1)!!]} \left(\frac{\hbar}{m_p c}\right)^2 \frac{e^2}{4\pi\varepsilon_0 \hbar c} \left(\frac{E_\gamma}{\hbar c}\right)^{2L+1} \left(\frac{3}{L+2}\right)^2 cR^{2L-2} \tag{1.33}$$

These simplified transition rates, known as Weisskopf estimates, may not describe the decay probability very well for all cases, but do offer a benchmark to compare the experimentally measured rates to. For the lowest multipole orders, and with $R = R_0 A^{1/3}$ the transition probability estimates are shown in Table 1.2. It is evident that for a single proton excitation, the lower multipolarities are much more probable, and for the same multipole order, L, electric radiation is more more probable than magnetic radiation.

1.3.3 Angular Momentum and Parity

The initial and final states in a given transition both have spin, J, and parity, π, associated with them. These are conserved quantities in γ decay and their coupling determines the angular momentum, L,

Table 1.2: Weisskopf estimates for single proton transitions of electric, EL, and magnetic, ML, transition types and of the first four multipolarities, $L = 1$ to 4. Values from Reference [1].

L	$\lambda(EL)$ [s^{-1}]	$\lambda(ML)$ [s^{-1}]
1	$1.0 \times 10^{14} A^{2/3} E_\gamma^3$	$5.6 \times 10^{13} E_\gamma^3$
2	$7.3 \times 10^{7} A^{4/3} E_\gamma^5$	$3.5 \times 10^{7} A^{2/3} E_\gamma^5$
3	$34 \times A^2 E_\gamma^7$	$16 A^{4/3} E_\gamma^7$
4	$1.1 \times 10^{-5} A^{8/3} E_\gamma^9$	$4.5 \times 10^{-6} A^2 E_\gamma^9$

that the emitted γ ray can carry away.

$$\vec{J_i} = \vec{J_f} + \vec{L} \tag{1.34}$$

$$|J_i - J_f| \leq L \leq J_i + J_f. \tag{1.35}$$

Given that it is possible to have several values of L for the same transition (e.g. $J_i = 4$ and $J_f = 2$ gives $L = 2, 3, 4, 5$ or 6), the radiation field would consist of a mixture of multipolarities. It was shown in Table 1.2, however, that the lowest multipole order is most probable. It is also noted that $L \neq 0$ in the case where $J_i = J_f$. This is due to the fact that photons have intrinsic angular momentum of $1\hbar$, $S = 1$, and so a monopole transition is not possible via a single γ-ray photon. The lowest multipole order in this instance is $L = 1$, corresponding to a dipole. Equation 1.35 is the selection rule for angular momentum and, with the decay probabilities, prove useful in predicting the multipolarity of the emitted radiation field.

Electric and magnetic fields of the same multipolarity have opposite parity [1]. The parity of the radiation field is dependent on L and is given by

$$\pi(EL) = (-1)^L \tag{1.36}$$

$$\pi(ML) = (-1)^{L+1}. \tag{1.37}$$

Therefore, for a transition between an initial and final state where there is a change in parity, L is odd for electric transitions and even for magnetic. If the parity does not change, the opposite is true where L is even for electric and odd for magnetic. These parity selection rules can be very useful in identifying the type of radiation, provided the parity of the initial and final states are known.

As an example of predicting the type of γ radiation that is emitted with these selection rules, consider a 1 MeV γ-ray transition from $J_i = 3$ to $J_f = 2$ in a $A = 118$ nucleus. This means $L = 1, 2, 3, 4$ or 5. If there is no change in parity, using Table 1.2, $\lambda(E2)/\lambda(M1) \approx 10^{-3}$ which means for every $E2$ transition, there are 1000 $M1$ transitions. Looking at the next multipole order, $M3$, the ratio, $\lambda(M3)/\lambda(M1) \approx 10^{-10}$, is even less probable. When there is a parity change, the lowest multipolarity is of the electric type with $\lambda(M2)/\lambda(E1) \approx 10^{-7}$. This highlights that an $E2$ transition can effectively compete with an $M1$ transition whereas the $M2$ transitions do not compete with the $E1$ transitions very strongly. Furthermore, this example highlights what is called the *mixing ratio*,

δ and is given by [14]

$$\delta^2 = \frac{\lambda(E(L+1))}{\lambda(ML)} \tag{1.38}$$

with λ being the decay probability defined by Equation 1.30. The mixing ratio can also be given as $\delta = m_{fi}(E2)/m_{fi}(M1)$ [1]. The mixing ratio can be measured using a technique called γ-γ angular correlations which will be discussed in Section 1.3.6.

1.3.4 $B(E2)$ Values

In the opening of the introduction, the concept of shape coexistence was discussed and described for the even-even Sn nuclei as a 2p-2h excitation across the closed $Z = 50$ shell. A quantitative measure of the electric quadrupole, E2, strength is the $B(E2)$ value,

$$B(E2 : J_i \to J_f) = \frac{\langle \psi_i || E2 || \psi_f \rangle^2}{2J_i + 1}, \tag{1.39}$$

which gives insight to nuclear deformation. This is the reduced transition probability for $E2$ transitions with the reduced matrix element, $\langle \psi_i || E2 || \psi_f \rangle$, that is related to the decay constant of Equation 1.30, and therefore contains the information about the lifetime and absolute branching ratios of the γ rays depopulating the state of interest. If the partial lifetime and branching ratio of a state are known, and if a mixing ratio for a transition which is not purely quadrupole is known, the $B(E2)$ value can be obtained [19].

$$B(E2) = \frac{816}{E_\gamma^5 \tau_p} e^2 \mathrm{fm}^4 \mathrm{MeV}^5 ps \tag{1.40}$$

Here the energy of the γ-ray energy, in MeV, is to the power of five, and the partial lifetime, τ_p, is in ps. The partial lifetime takes into consideration the branching ratio of the γ-ray transition with respect to the total γ decay of the state, as well as the internal conversion coefficient, α (outlined in the subsequent section):

$$\tau_p = \frac{\tau_t \cdot (1+\alpha)}{\mathrm{BR}} \tag{1.41}$$

where τ_t is the total lifetime, and BR is the branching ratio for the γ-ray transition of interest. If the transition is a mixed multipolarity, the mixing ratio, δ, must also be considered:

$$b(E2) = \frac{\delta^2}{1+\delta^2} \tag{1.42}$$

is used in Sections 4.2 and 5.3 to scale the $B(E2)$ based on the multipolarity mixing ratio between the $E2$ and $M1$ transition.

Equation 1.40 is often compared to the single-particle estimate established by Weisskopf (Equation 1.43), and the ratio between the measured $B(E2)$ to the estimated carries Weisskopf units, or W.u. for short.

$$B(E2)_W = 0.0594 A^{4/3} e^2 fm^4 \tag{1.43}$$

As an example of enhanced electric quadrupole strength, the ground state transition of the first excited 2^+ in ^{116}Sn is a pure $E2$ and the $B(E2)$ value is about 10 W.u. which is often the case for near magic nuclei. This suggests weak collectivity of the first $J = 2^+$ state which is considered as a breaking of a pair of neutrons. However, a larger $B(E2)$ value is observed in the $2^+ \rightarrow 0^+$ transition belonging to the 2p-2h configuration is over 40 W.u. [20]. This enhanced strength suggests deformation associated with a greater electric quadrupole moment and collective motion of the nucleons. As the enhanced $B(E2)$ values are a signature of deformation, they are of interest in the present work to further establish the known 2p-2h states in ^{118}Sn.

1.3.5 Internal Conversion

Another electromagnetic process which takes place between an initial and final state within a nucleus, and that competes with γ decay, is called *internal conversion*. This decay process involves a tightly bound, inner-orbital electron being ejected from the atom (unlike being produced within the nucleus via the weak interaction in β decay) rather than the emission of a γ ray [1, 14]. These innermost electrons spend a considerable amount of time within the nuclear volume. If an excited nucleus de-excites, the change in the electromagnetic field can impart this excess decay energy to one of these close-proximity electrons. The kinetic energy of the ejected electron is

$$T_e = \Delta E - B_{e^-} \tag{1.44}$$

where B_{e^-} is the atomic binding energy of the electron, and $\Delta E \approx E_\gamma$ as previously identified in the γ-decay energetics. Unlike γ decay, internal conversion occurs with a $J_i = J_f = 0$ transition. For these types of transitions, only an electric monopole, $E0$, is allowed. It is also possible for $E0$ transitions to also be measured between $J_i = J_f$ states that are not 0.

A significant fingerprint of shape deformation in nuclei is an enhanced $E0$ transition strength between low-lying excited 0^+ states. Similarly to the enhanced $B(E2)$ value used to identify shape coexistence, $E0$ strength is related to the difference in the mean-square charge radii between two mixed low-lying 0^+ states and thus a change in shape [21]. This can be a very important measurement in determining the configuration mixing between two low-lying 0^+ states. The reduced $E0$ transition probability, $B(E0)$, is

$$B(E0) = \rho^2(E0)e^2R^4 \tag{1.45}$$

where e is the electric charge and R is the nuclear radius. The greater the $B(E0)$, the greater the mixing between the two states, and/or the greater the difference in the mean-square charge radii between the two states. The factor, $\rho(E0)$, is the monopole transition strength,

$$\rho(E0) = \frac{\langle \psi_i || E0 || \psi_f \rangle}{eR^2}, \tag{1.46}$$

which, like for the $B(E2)$, shows the relationship to the monopole matrix element which carries the information about the nuclear structure. Methods for obtaining the $\rho^2(E0)$ are expressed in Reference [21] and will be further discussed in Section 5.

Another importance of understanding internal conversion for the works presented here is related to decay branching ratios for the transition probabilities. Essentially, internal conversion contributes to the total decay probability of an excited state, shown in Equation 1.47, and when not measured, or simply neglected, the absolute branching fraction of a γ ray depopulating that excited state will appear to be faster that it truly is.

$$\lambda_{tot} = \lambda_\gamma + \lambda_{e^-} \tag{1.47}$$

A useful term called the *internal conversion coefficient*, α, is defined as

$$\alpha = \frac{\lambda_{e^-}}{\lambda_\gamma} \tag{1.48}$$

such that

$$\lambda_{tot} = \lambda_\gamma(1+\alpha). \tag{1.49}$$

For certain known transitions, α coefficients have been previously measured and are useful for determining quantities such as $\log ft$ values and γ-ray transition probabilities to account for the intensity lost due to internal conversion. Fortunately, these coefficients can also be estimated from phenomenological calculations for transitions that have no previous measurements and the ratio of the calculated values to the measured α coefficients are within 5 % [22].

Further reading on the theory of internal conversion can be found in texts such as References [1, 13, 14]. However, the key takeaways are that the $E0$ transitions between $J = 0^+$ states are an important measurement in determining shape coexistence and that α coefficient is inversely proportional to $E^{L+5/2}$ for electric transitions and $E^{L+3/2}$ for magnetic [1]. It is therefore more probable for internal conversion to occur only at small transition energies and lower multipolarities.

1.3.6 Angular Correlations

For the evaluation of theoretical predictions using nuclear models, knowledge of the multipole character of the electromagnetic transition is very important. The energy and intensity of a γ ray that is measured in γ decay does not provide information on the multipolarity or type of transition (electric or magnetic) [1]. Even if the spin and parity of both the initial and final states are known, the multipole character can only be restricted by the selection rules—certainty of the multipolarity can be given if J_i or $J_f = 0$ with the other being greater than 0. However, there is an angular distribution associated with the character of the γ-ray transition that can be exploited to determine J.

Considering a simple dipole transition between a $J_i = 1$ to $J_f = 0$, the transition certainly has $L = 1$. Each state, however, has $m_J = 2J+1$ substates, where m_J are the magnetic substates and J is the orbital angular momentum. Therefore, $m_i = 1, 0, -1$ and $m_f = 0$ in this example and as shown in Figure 1.6. For a classical dipole, the probability of emitting a transition between $m_i = m_f = 0$ varies as $\sin^2\theta$, whereas for $m_i = \pm 1$, the emission varies as $\frac{1}{2}(1+\cos^2\theta)$ [1]. Under normal conditions, the m-states are all equal in energy. With a strong magnetic field present, these m-states are separated with transition energies $E+\Delta E$, E and $E-\Delta E$ for J_i. This is essentially the same as the Zeeman effect in atoms. The splitting is unfortunately not resolvable with γ-ray detectors, even when using a very powerful magnet, and the angular distributions of each substate sum together to an observed isotropic distribution that provides no information on the multipolarity:

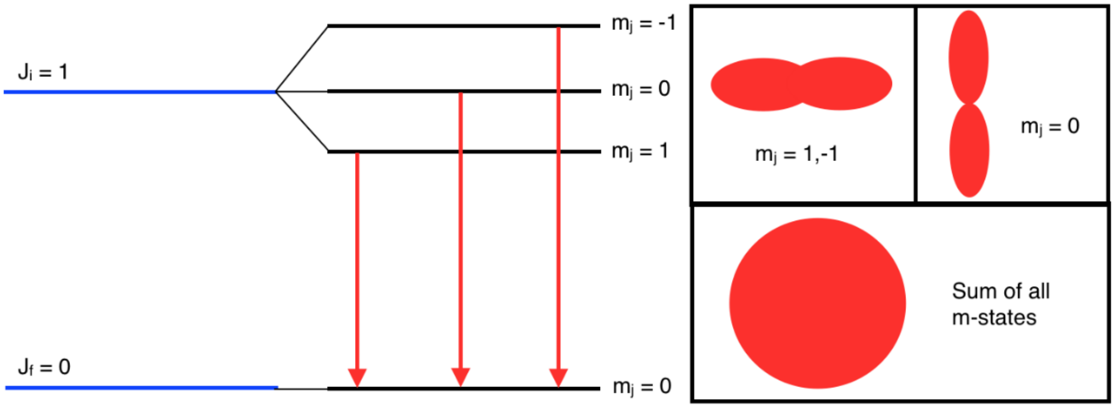

Figure 1.6: An example of a pure dipole radiation where $L = 1$. The $J_i = 1$ state consists of $m_J = 0, \pm 1$ substates which each produce an angular distribution. However, these states are not resolvable and an isotropic distribution is observed, shown on the right. Reprinted with permission of Reference [23].

$$W(\theta) \propto \frac{1}{3}[\frac{1}{2}(1+\cos^2\theta)] + \frac{1}{3}(\sin^2\theta) + \frac{1}{3}[\frac{1}{2}(1+\cos^2\theta)] \tag{1.50}$$

is the angular distribution for the dipole example with equal weight, $\frac{1}{3}$, given to each of the m-states being populated.

A method for establishing an anisotropic distribution from which the multipole character can be measured is an *angular correlation*. It requires two consecutive γ-ray transitions and two γ-ray detectors that can be positioned with a varying angle between them. Following the simple dipole example, a second level of $J = 0$ is used to describe the angular correlation of a $0 \to 1 \to 0$ cascade shown in Figure 1.7—note that the figure is taken from a reference which uses I instead of J for the spin of a state. In this example, γ_1 is measured in the first detector, D_1, which is taken to be along the z-axis such that γ_2 measured in the second detector, D_2 at an angle, θ_2 between the two detectors. It should be pointed out that the greater number of angles between detector pairs, the smoother the angular correlation plot will be. If the z-axis is defined to have $\theta = 0$, then the $\sin^2\theta$ term for the $m_0 \to m_i = 0$ is simply zero and the $m_i = 0$ substate for $J_i = 1$ is not observed to be populated. This leaves the angular distribution from Equation 1.50 for γ_2 as:

$$W(\theta) \propto 1+\cos^2\theta. \tag{1.51}$$

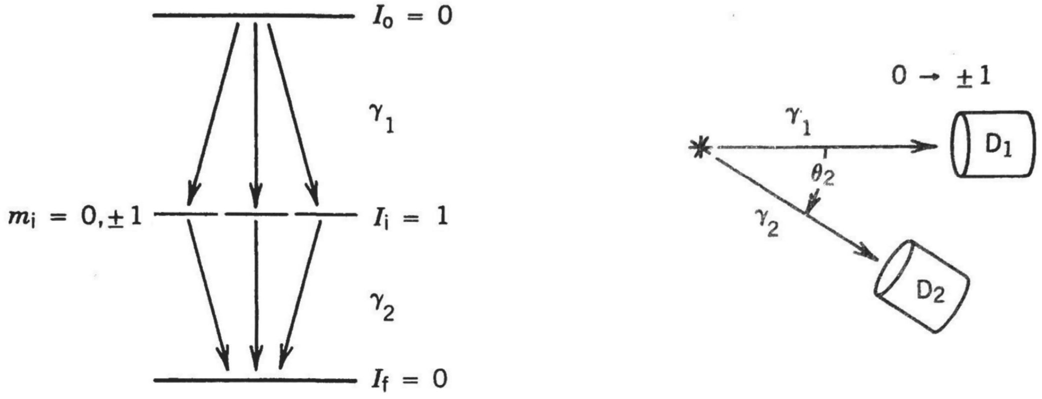

Figure 1.7: An example of an cascade for which angular correlations can be made is shown on the left. The first transition, γ_1, is measured in detector 1, D_1, (shown on the right) which is set to be along the $\theta = 0$ z-axis. The second transition, γ_2, is then measured in detector 2, D_2. By varying the angle, θ_2, between the detector pairs, and angular correlation can be produced. The corresponding plot is then fit with Equation 1.52 to establish the spin, J of the state of interest. Reprinted with permission from Reference [1].

While this is specifically for the case of a pure dipole radiation, the general form for an angular correlation is

$$W(\theta) = 1 + \sum_{k=1}^{L} a_{2k} \cos^{2k} \theta \tag{1.52}$$

which consists of even powers of $\cos\theta$ and the coefficients, a_{2k}, depend on the spins of the initial and final states, J_i and J_f, respectively, and the multipolarity, L, of the γ ray.

Considering the selection rules and transition probabilities discussed in the previous sections, there are often transitions observed with a mixture of $M1$ and $E2$ and defined by Equation 1.38. The value of the mixing ratio, δ, changes the values of the a_2 and a_4 coefficients and by fitting an angular correlation plot for these coefficients with Equation 1.52, it is possible to determine δ.

Lastly, while angular correlations prove useful to identifying the spins of states, the parity cannot be determined with this method—aside from an educated guess with the help of the selection rules. There are methods to determine the parity, however these were not used in the present studies and will not be discussed. It is, however, very helpful to know, from previous studies, the parity and the spin of one of the states used in the angular correlation to restrict the possible spins of the unknown state.

1.4 γ Ray Interaction with Matter

When a nucleus undergoes γ decay, the high-energy photons lose their energy to their surroundings in mainly three distinct ways—photoelectric absorption, Compton scattering, and pair production [24]. These processes result in the transfer of γ-ray energy to an electron in an atom or, in the case of pair production, to creating an electron-positron pair.

In the case where a γ-ray photon imparts all of its energy in an atom, an electron will be ejected with the energy of the γ ray, $h\nu$, minus the binding energy, E_b:

$$E_{e^-} = h\nu - E_b \tag{1.53}$$

This is called a *photoelectron* and is typically ejected from the K shell (innermost shell) [24]. For most γ decay measurements that provide information on nuclear structure, the photoelectrons which receive the complete transfer of energy from the γ ray are desirable and ultimately result in the measured electronic signal. However, as the energy of the photon increases, the probability of complete photoelectric absorption decreases as shown in Figure 1.8.

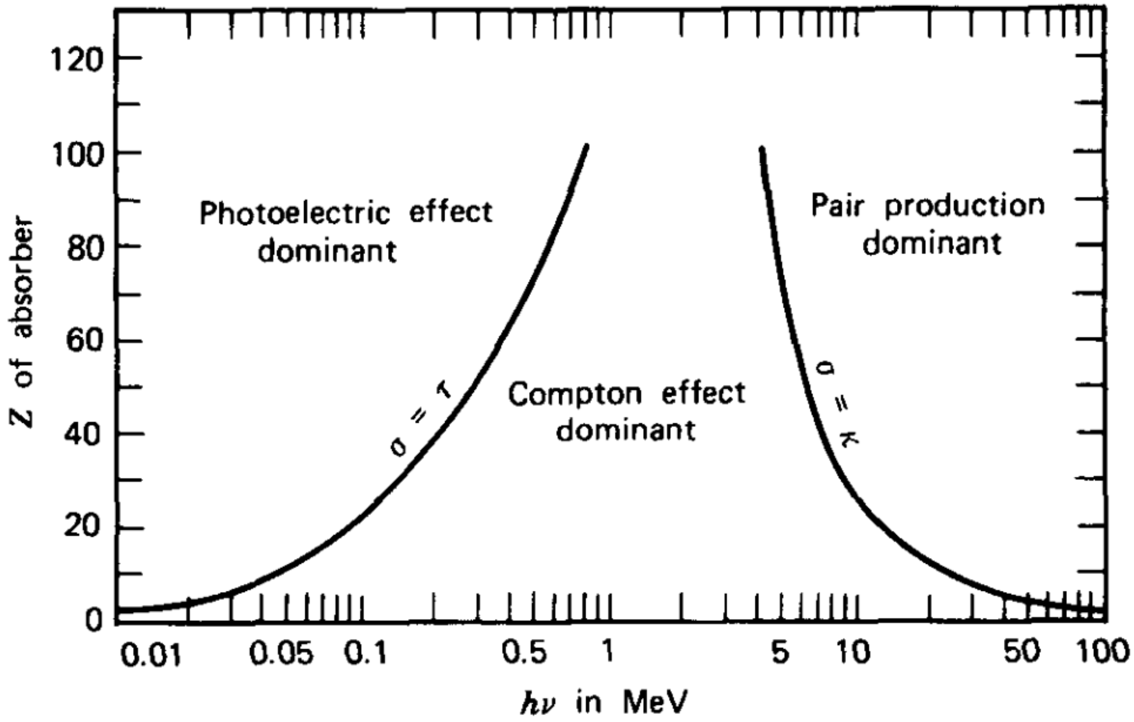

Figure 1.8: The dominant regions of the three major interactions of a γ ray in an absorber with atomic number, Z, and for photon energy, $h\nu$. The boundary lines indicate where the probability of the two adjacent interaction types are approximately equal. Reprinted with permission from Reference [24]

Typically, for γ rays with energy less than 200 keV, the photoelectric absorption is dominant in γ-ray detectors (e.g. germanium, $Z = 32$). However, γ decay often results in the emission of γ rays in excess of 200 keV. At these energies, Compton scattering is the most dominant process. In this process, the γ-ray photon transfers part of its energy to an atomic electron, and carries the remaining energy at a deflected angle, θ, from its initial direction. The deflected photon energy can be determined from the Planck relationship, $E = h\nu$ and relativistic energy $E = \sqrt{p^2c^2 + m_0^2c^4}$ to obtain

$$h\nu^{'} = \frac{h\nu}{1 + \frac{h\nu}{m_0c^2}(1 - \cos\theta)} \tag{1.54}$$

where $h\nu$ is the incoming photon energy, and m_0c^2 is the rest-mass energy of the electron. Even in the extreme case where $\theta = \pi$, some energy is still carried away by the scattered γ ray. The electron involved in the Compton scattering process can be treated like a photoelectron with only part of the γ-ray energy being measured. It is possible that the remaining energy of the deflected γ ray is absorbed by an atom in within the detector volume or that further Compton scattering events occur.

While Compton scattering typically is the most probable γ-ray interaction type, it is possible for a third process to occur if the energy of the γ-ray photon is greater than the rest mass energy of two electrons (1.022 Mev). In this case, the γ ray interacts with the coulomb field of the nucleus and is replaced by an electron-positron pair. The electron and positron share the excess energy above 1.022 MeV as kinetic energy. The positron subsequently annihilates with the emission of two 511 keV photons, which can both escape the medium (double escape), have one escape and one absorbed (single escape), or have both absorbed. Of course, it is possible for these annihilation photons to Compton scatter as well.

Chapter 2

Experiments

To populate and characterize excited states in ^{118}Sn, two very different and complimentary experiments were performed. The first utilized the β^- decay of ^{118}In which was produced as a Rare Isotope Beam (RIB) and is discussed in section 2.1, whereas the second utilized a high-flux thermal neutron beam to be captured on a stable ^{117}Sn target and is discussed in section 2.2. Both sets of data were processed and analyzed with the same computer software and techniques as described in section 2.3.

2.1 RIB Production at TRIUMF

A RIB of ^{118}In was produced using the Isotope Separator On-Line (ISOL) technique at the Isotope Separator and ACcelerator (ISAC) facility, shown in Fig. 2.1, at TRIUMF in Vancouver, Canada [25]. The ISOL technique consists of a high-energy primary production beam, a thick target, an ion source, a mass separator and a beam transport [26].

The high-energy beam of protons used to facilitate reactions for study is generated by the 480 MeV cyclotron at the heart of TRIUMF [27]. Negatively charged hydrogen ions are produced and delivered to the centre of the cyclotron in which they are accelerated to 75% of the speed of light in 0.3 ms and in an outward spiral trajectory. Graphite foil is used to strip the hydrogen atoms of their electrons to produce positively charged protons. Protons are deflected outwards due to the magnetic field and are directed to a proton beam line. In this experiment, 9.8 μA protons at 480 MeV were bombarded onto a uranium carbide (UC$_x$) production target.

Reactions of the protons on the UC$_x$ target include fragmentation, spallation and fission, which altogether yield nearly every isotopes up to the target's mass. Surface ionization of the products due to the heat generated in the reactions is a possibility—predominantly from the alkali elements. Thus, an electrostatic repeller is used to reduce unwanted ions contaminating the beam while allowing neutral ions to pass through to the ion source. The Ion-Guided Laser Ion Source (IG-LIS) was used to selectively ionize species of interest [28]. The ionization is typically done in a three-step excitation within a Radio Frequency Quadrupole (RFQ) which guides, or focuses, the ions towards the exit electrode after which are then mass separated.

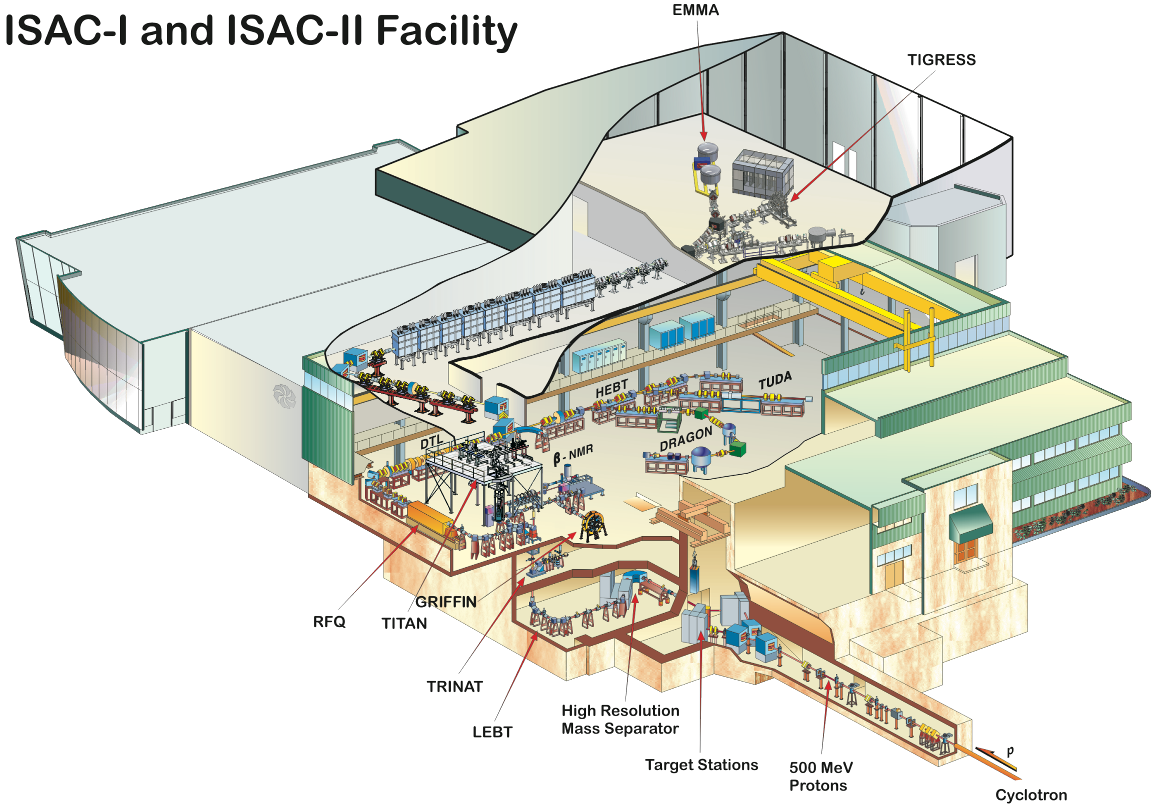

Figure 2.1: The layout of the ISAC facilities at TRIUMF. GRIFFIN is located in the low energy experimental hall, ISAC-I, shown in the bottom left. Adapted from Ref. [25].

The high resolution mass separator uses a constant magnetic field to steer the ions across a 45-degree bend. The mass-to-charge ratio dictates the trajectory and allows one to select the mass of interest using adjustable slits at the end of the separator. The resolving power of the mass separator is $M/\Delta M \approx 2000$ [29]. For this experiment, the ions with mass number $A = 118$ were separated and transported to the ISAC-I experimental hall. The RIB was implanted into the centre of the GRIFFIN array where the β-decay of ^{118}In was observed via the subsequent γ decay of excited states in the daughter nucleus of interest, ^{118}Sn.

2.1.1 GRIFFIN Array

The Gamma-Ray Infrastructure For Fundamental Investigations of Nuclei (GRIFFIN), shown in Fig. 2.2, is a relatively new γ-ray spectrometer which is comprised of up to 16 large-volume high-purity germanium (HPGe) clover detectors used to measure γ rays from the stopped RIB [30]. HPGe crystals are used for their excellent resolution in detecting γ rays, and GRIFFINS' 16 clover configuration of 4π coverage around the implantation chamber provides high efficiency [31]. A full suite of ancillary detectors can be coupled with the HPGe detectors to further enhance the capabilities of GRIFFIN.

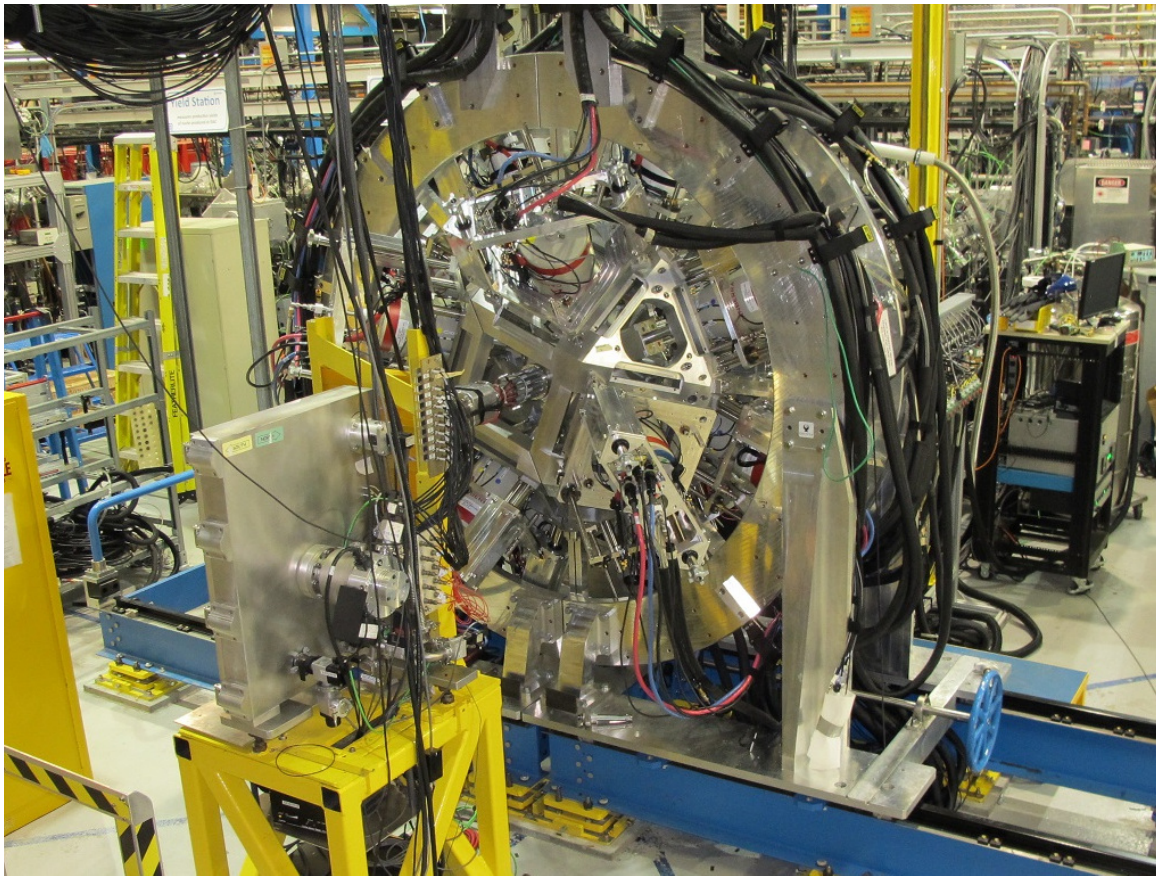

Figure 2.2: Shown is the GRIFFIN spectrometer which is stationed in the ISAC-I hall. On the left side is the lead box which stores the beam-implanted Mylar tape to contain γ rays from the remaining β-decaying species that may be present on the tape.

GRIFFIN is arranged in a rhombicuboctahedron which provides 18 square faces—16 for the HPGe clover detectors and two for the beam line and Mylar tape system—and eight triangular faces—used for the ancillary cerium-doped lanthanum bromide ($LaBr_3(Ce)$) detectors. This allows for full 4π coverage of the chamber in which the beam is stopped at the centre on a strip of Mylar tape.

The Mylar tape system consists of a $\sim$135 m continuous loop with a thin layer of iron oxide on one side [30]—much like what is used in video cassettes. The RIB is implanted onto the tape for a desired amount of time, followed by an amount of time to observe the decays during which the beam is turned off. The contaminated tape is then cycled out into a lead shielded box at the same time as a fresh strip of tape is introduced into the detector chamber for another set time of implantation. The repeated implantation and decay times, also called cycle times, are generally user defined to maximize the population of excited states of interest or to limit unwanted isobars present in the same beam.

2.1.2 HPGe Detectors

Each of the 16 clover detectors that make up the essence of GRIFFIN consist of four n-type HPGe crystals which are each 60 mm in diameter and 90 mm in length [31]. The crystals are machined for a close-packed clover, shown in Fig. 2.3, and their outer edges are tapered over the first 30 mm for close-packing of neighbouring clovers. Germanium is a semiconductor material and n-type refers to the HPGe crystals containing donor impurities after fabrication [24].

The semiconductor property that makes germanium excellent for γ-ray spectroscopy is the small energy of 2.96 eV to create an electron-hole pair [24]. Although this is only true when cooled to 77 K with liquid nitrogen, this low energy for electron-hole production is several orders of magnitude smaller than the typical γ ray (10 keV to 10 MeV). The number of electron-hole pairs generated from a single γ ray correspond to the γ-ray energy when fully absorbed and the statistical fluctuation in the measured current from the drifting electron-hole pairs is minimal. This leads to an excellent energy resolution necessary to resolve many of the γ rays emitted in a nuclear structure experiment.

The full-width at half-maximum (FWHM) energy resolution for the GRIFFIN HPGe crystals are averaged across all 64 crystals to be 1.89(6) keV at 1332.5 keV from Ref. [31]. This will naturally increase when all events recorded from each crystal are added together due to imperfect alignment of the energy response between each crystal. This is detailed in section 3.

Another property of germanium that makes it very useful to γ-ray spectroscopy, is the relatively large atomic number, $Z = 32$. This is directly related to the number of electrons each germanium atom has which in turn provides the incoming γ rays more to interact with. Ultimately, the higher Z a material has, the more efficient it is to absorb a high-energy photon. The efficiency for the entire GRIFFIN array of 64 crystals positioned at 11 cm from the centre of the chamber is given as 10.06(11)% at 1 MeV [30]. To further enhance the efficiency, a technique called *addback* uses the full clover volume. This technique adds events detected by the crystals in the same clover when

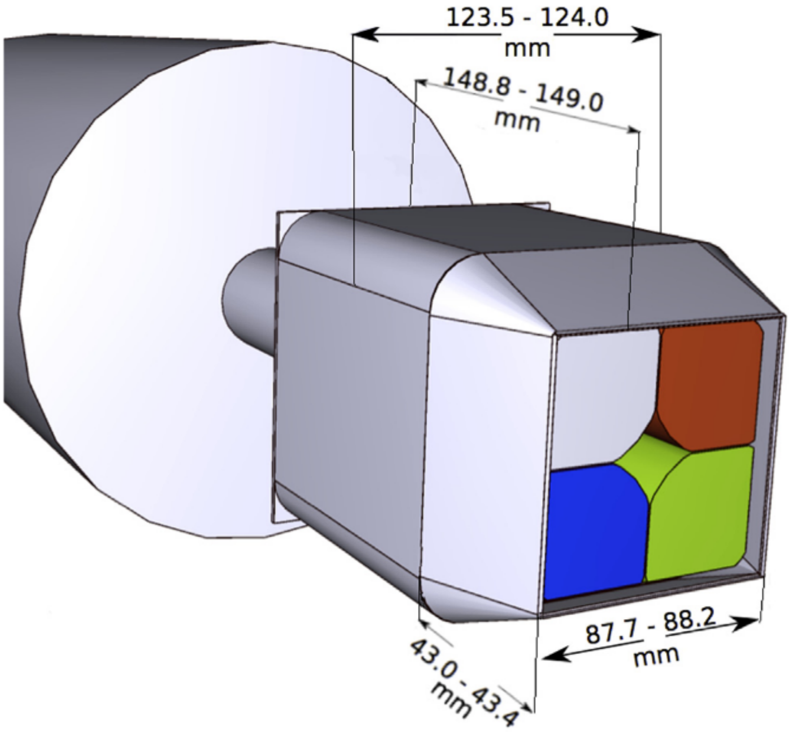

Figure 2.3: Schematic of the GRIFFIN HPGe clover detector. The colours represent the four different HPGe crystals used to detect the γ rays. Reprinted from Ref. [31], with permission from Elsevier.

they occur within 300 ns to recover the full energy of γ rays which may have Compton scattered into adjacent crystals. At 1 MeV, the addback efficiency is 14.20(16)% [30].

Combining the small energy required to produce electron-hole pairs, large Z of germanium and the significant crystal volume, the HPGe crystals used in GRIFFIN offer a powerful tool for γ-ray spectroscopy.

2.1.3 SCEPTAR

The studies of interest that utilize GRIFFIN often involve the emission of a β particle (electron or positron) which can be detected and used to isolate the γ rays associated with the β particles. This β-tagging reduces contaminants and can be achieved with the ancillary SCintillating Electron Positron Tagging ARay (SCEPTAR). SCEPTAR is mounted in the vacuum chamber and consists of 20 plastic scintillators—an upstream half and a downstream half each consisting of 10 scintillators made from polyvinyl-toluene based Saint Gobain BC404 [32]. The scintillators are connected to ultra-violet transmitting (UVT) acrylic light guides that are coupled to photomultiplier tubes (PMTs) located on the outside of the outside of the beam tube [30].

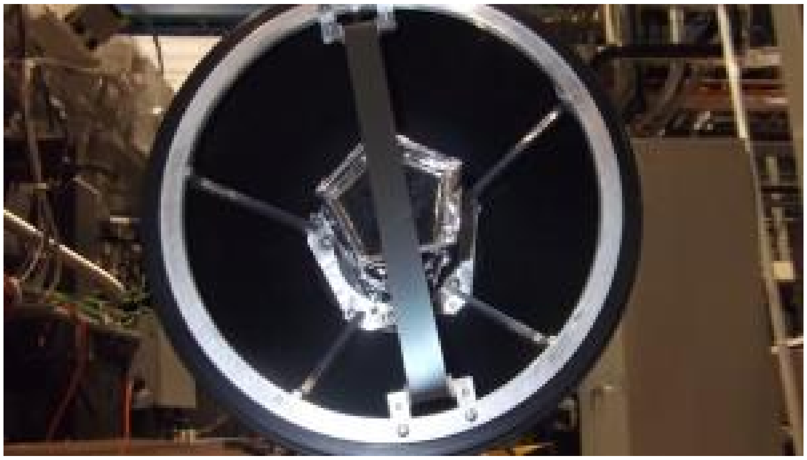

Figure 2.4: Shown here is the movable Mylar tape on which the RIB is implanted, half of SCEPTAR (behind the tape) wrapped in foil, and half of the Delrin shield (outer, black hemisphere).

SCEPTAR offers 80% of the solid angle and as such provides 80% efficiency for β-particle detection [30, 32]. It is also possible to use either the upstream or downstream half of SCEPTAR in conjunction with another ancillary detector within the chamber.

2.1.4 Compton suppression BGOs

As the Compton continuum of partially detected γ rays makes up much of the γ-ray spectrum, ancillary detectors can be used to suppress these events to enhance the peak-to-total background. At the time of this experiment, there were no Compton suppression measures in place, aside from the partial recovery of scattered events using the addback method.

Since this experiment, Compton suppression shields have been added to the GRIFFIN array [30]. These are made from bismuth germanate (BGO) and consist of four front shields, four side shields and two back catchers for each HPGe clover. BGO is used for its high efficiency, a result of being a high Z material, however, the resolution is very poor. When used, coincidence between a BGO event and any event with its corresponding clover are omitted from the γ-ray spectra. The geometry allows for the HPGe detectors to be positioned with the BGO shields withdrawn so that the HPGe are positioned in a close-packed formation 110 mm from the centre of the chamber for maximum efficiency. The HPGe can also be withdrawn to 145 mm so that the BGO shields are at 110 mm from the centre of the chamber and offer maximal suppression and optimal peak-to-total detection.

2.1.5 Other Ancillary Detectors

The low energy physics studied with GRIFFIN can vary from one experiment to the next. It is thus important to have a modular design for the detector array that allows for specific research proposals. Although these ancillary detectors were not used for the purpose of this research, it is useful to discuss for a complete understanding of GRIFFIN's capabilities.

The Zero-Degree Scintillator (ZDS) detector, or the fast β scintillator, offers the same β-tagging that half of SCEPTAR with a similar efficiency of $\sim$40%. The advantage of the ZDS detectors are their fast timing response which can be useful when measuring life-times of excited states when used in conjunction with the $LaBr_3$(Ce) γ-ray detectors [30].

Both the $LaBr_3$(Ce) and ZDS signals output through logic modules that provide a start and stop input signal to the Time-to-Amplitude Converter (TAC) module and life-time measurements of excited states down to 10 ps can be achieved. The $LaBr_3$(Ce) are also scintillators and have a combined absolute efficiency of 1.8(1)% at 1 MeV for all eight detectors [30]. BGOs are also used with the $LaBr_3$(Ce) for the same reason as mentioned in the previous section.

Competing with γ-ray emission, internal conversion is the emission of an electron which carries away the transition energy minus the electron's binding energy. While these conversion electrons can be detected by SCEPTAR or ZDS, the poor resolution of the plastic scintillators leaves no evidence of internal conversion taking place. The observation of conversion electrons is often the subject of study when measuring electric monopole ($E0$) transitions where a γ-ray emission is forbidden. For such experiments, the Pentagonal Array for Conversion Electron Spectroscopy (PACES) are a set of five lithium-drifted silicon (Si(Li)) semiconductor detectors which are mounted in the upstream side of the vacuum chamber and cooled with LN_2. One HPGe clover is necessarily removed for the LN_2 dewer. The simulated efficiency at 1 MeV is $\sim$4% [30].

Lastly, GRIFFIN can also couple to the DEuterated SCintillator Array for Neutron Tagging (DESCANT) which can be useful for β-delayed neutron emission [30, 33]. The importance of β-delayed neutron emission studies extends from the astrophysical r-process to stable operation of nuclear reactors. DESCANT consists of up to 70 scintillating detectors, each filled with 2 L of deuterated benzene [33]. It couples to the GRIFFIN array on the downstream side, replacing four of the HPGe clover detectors and maintains a $\sim$27% efficiency for detecting neutrons over 1-5 MeV [34].

2.1.6 Digital Acquisition

The GRIFFIN data acquisition (DAQ) system is set of digital electronics which were custom-designed to operate with each HPGe crystal capable of counting at a rate of up to 50 kHz [35]. The DAQ system consists of GRIF-16 digitizers—16-channel, 14-bit, 100MHz sampling analogue-to-digital converter (ADC) which read the analogue signals from the HPGe and SCEPTAR detectors—lower level collectors that connect directly to the ADCs and relay the signals to the master level collectors which determine what data is rejected and what is written to disk, and the GRIFFIN Clock (GRIF-CLK) modules which each house a chip-sized atomic clock (CSAC) that produces a 10 MHz reference signal and fanned out to all collectors and digitizers in the DAQ system for precise synchronization [35].

2.2 Neutron Capture at the Institut Laue-Langevin

To study excited states in nuclei, one must explore various mechanisms for populating specific states of interest since no single reaction can populate all excited states. Where the RIBs produced at TRIUMF primarily β-decay—the states which can be populated in the daughter nucleus are limited based on the β-decay selection rules as well as the Q-value—thermal neutron capture at the Institut Laue-Langevin (ILL) in Grenoble, France, only populates states at the neutron separation energy, S_n, which then decay through many levels via γ-ray emission to the ground state [1]. The principles behind thermal neutron capture are discussed in Section 5.1.

At the ILL, the most intense continuous flux of neutrons (10^{15} n/(cm^2·s) in the reactor moderator) in the world is produced from the fission of highly-enriched ^{235}U [36]. The research reactor operates at 58 MW and a collimated pencil-like beam (1.5 cm in diameter) of neutrons with a flux of 10^8 n/(cm^2·s) [36, 37] is delivered to many experimental stations throughout the facility.

2.2.1 Research Reactor

The fission reaction at ILL's research reactor uses a 10-kg single fuel element of highly-enriched ^{235}U [38]. Submerged in heavy water (D_2O) for cooling, the fission produces 58 MW of heat that is removed through heat-exchange between the D_2O and light water (H_2O) in a nearby river. The D_2O vessel in which the core is situated is contained in an pool of H_2O used for shielding the neutron and γ radiation generated by the fission process.

The neutrons produced in fission are emitted with an average energy of 2 MeV (20,000 km/s) and need to be slowed by a moderator in order for the fission to maintain the chain reaction. This slowing, or thermalizing, is also necessary to supply the neutrons to most of the research instruments. The D_2O not only cools the reactor, but serves as the moderator, slowing the neutrons down to 0.025 eV (2.2 km/s). These thermal neutrons, are used in the neutron capture experiment presented in this work.

The thermal neutrons produced in the reactor can be delivered to various experimental halls and instruments. Here, the neutrons are delivered via the H22 thermal neutron guide to the ILL7 neutron guide hall [37, 39] in which the FIssion Product Prompt γ-ray Spectrometer (FIPPS) is located.

2.2.2 FIPPS array

The FIssion Product Prompt γ-ray Spectrometer (FIPPS) array is the γ-ray spectrometer used in thermal neutron capture experiments at the ILL. A target is mounted in the centre chamber of FIPPS on which the neutron capture, $^{A}X(n,\gamma)^{A+1}X$, populates the isotope of interest, ^{A+1}X, in an excited state at the neutron separation energy. The excited nucleus releases energy via γ-ray emission which can be detected by the FIPPS array. FIPPS consists of eight HPGe clover-type detectors and can be coupled with ancillary detectors to enhance its capabilities. Like GRIFFIN, FIPPS is a modular design with the capabilities of a rhombicuboctahedral geometry in which 16 HPGe clover detectors can be mounted in the square faces, and eight $LaBr_3$(Ce) scintillator detectors can be mounted in

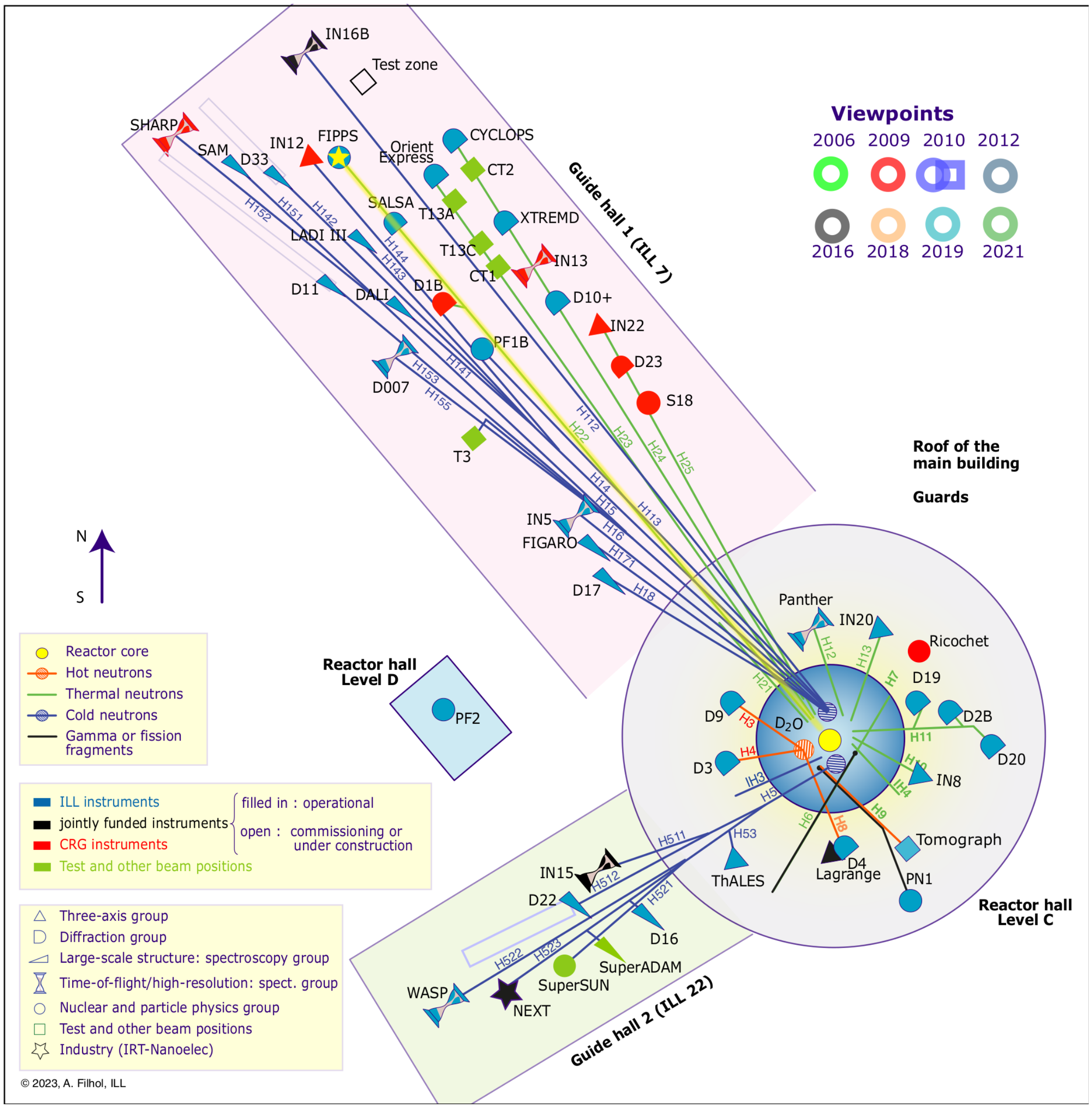

Figure 2.5: Schematic layout of the neutron guides and instruments used at ILL. Highlighted in yellow is the thermal neutron guide, H22, used to transport neutrons to the FIPPS array (marked with a yellow star). Taken from Ref. [40]

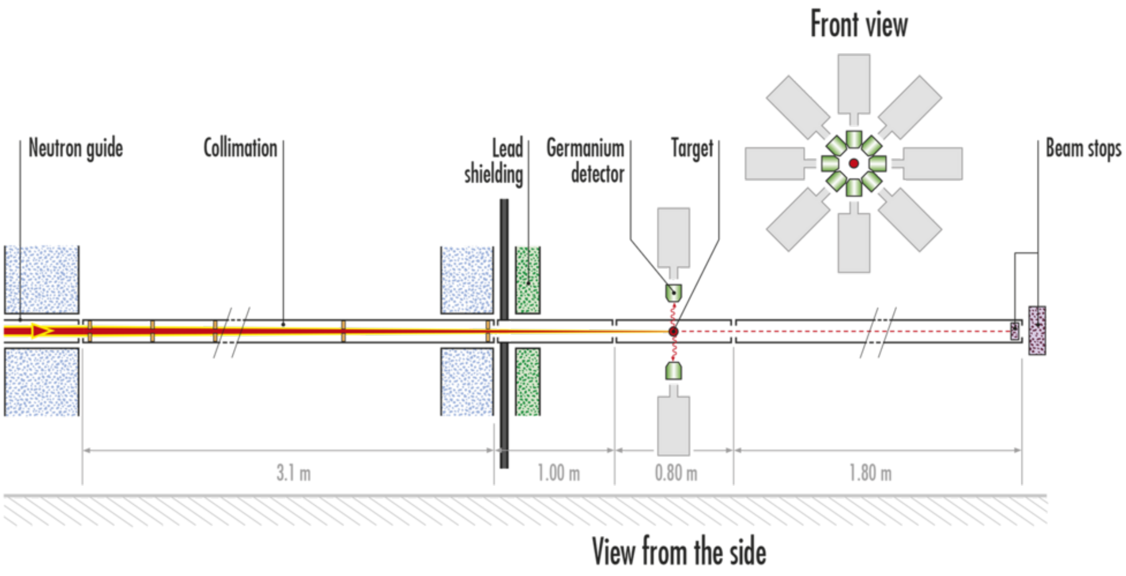

Figure 2.6: Side view schematic of neutron guide and collimation used to create a 1 cm diameter neutron beam at the target position. Taken from Ref. [43]

the triangular faces. The main difference is that FIPPS consists of eight HPGe detectors in a central ring and are positioned 90 mm from the target compared to 110 mm for GRIFFIN. The difference in distance is due to the FIPPS' HPGe crystals being slightly smaller than GRIFFIN's—50 mm in diameter and 80 mm in length before tapering [37] compared to 60 mm and 90 mm, respectively.

At the centre of the array in the vacuum chamber, a target of interest can be mounted along the neutron beamline. To ensure the neutron beam interacts with the target, the beam is collimated to a beam diameter of ∼1.5 cm. This is done through a series of apertures made of natural boron carbide backed with 5 cm of lead to absorb beam-related γ-ray background [37]. At the aperture closest to the detector, enriched ^{6}LiF is used. Both boron and ^{6}Li are excellent at absorbing thermal neutrons without the production of any significant background γ-ray radiation [41, 42].

2.2.3 HPGe Detectors

The 32 HPGe crystals used in the eight FIPPS clovers that form the central ring around the beam line are, like GRIFFIN, n-type semiconductors. They operate as previously discussed in section 2.1.2. In the neutron capture experiment that is the subject of this work, eight additional HPGe clover detectors were borrowed from Horia Hulubei National Institute for Physics and Nuclear Engineering (IFIN-HH), in Bucharest, Romania. This was to improve the total photopeak efficiency.

As with GRIFFIN, the excellent energy resolution of the FIPPS (and IFIN) HPGe detectors is very important in identifying γ rays with nearly the same energies. The FWHM was experimentally determined to be 2.41(6) keV at 1.4 MeV and 4.94(10) keV at 9.3 MeV for singles. Using addback, the FWHM was determined to be 2.64(7) keV at 1.4 MeV and 6.90(11) keV at 9.3 MeV.

The efficiency of the FIPPS array, without IFIN, is given as 4% at 1.4 MeV for singles and 5% using addback [37]. From the current experimental data presented in section 5, the efficiency at 1.4 MeV for the full array including the IFIN detectors is 6.3(2)% and 9.4(3)% for singles and addback, respectively. In the experiment, one IFIN clover, one IFIN crystal and two FIPPS crystals were not used in the analysis due to poor energy responses.

2.2.4 Compton Suppression

Similarly to the GRIFFIN setup, shields were not available for the FIPPS detectors at the time, but have since been added [44, 45]. This allows FIPPS to operate in the maximal efficiency and the enhanced peak-to-total mode much like the GRIFFIN array. The borrowed IFIN HPGe detectors did, however, have BGO shields for Compton suppression and were positioned 200 mm from the target. The increase in distance was to accommodate the BGO shields, but this also decreased the efficiency. Since the statistics were dominated by the nearer-to-the-target FIPPS detectors, and addback, which was employed, recovers many of the Compton scattering events, the suppressed data was not analyzed.

The BGO Compton suppression shields on the IFIN detectors and the newly installed shields on FIPPS have the same design as outlined in section 2.1.4.

2.2.5 Ancillary Detectors

FIPPS is designed to be modular and has the capabilities of fast-timing measurements with a set of $LaBr_3$(Ce) scintillator detectors [39, 46] similar to GRIFFIN's. Lifetime measurements have been made with the FIPPS array in recent studies [46]. These detectors were unavailable during the present experiment. However, it should be mentioned that there is access to a set of $LaBr_3$(Ce) which would be beneficial to measuring lifetimes of states populated in thermal neutron reactions.

2.2.6 Digital Acquisition Hardware

The signals from the detectors are processed with eight-channel CAEN V1724 ADCs which, like the GRIF-16 cards, have a 100 MHz sampling frequency. Each channel is capable of 10 kHz count rates [37].

2.3 Data Sorting

For both the β-decay of ^{118}In and ^{117}Sn$(n,\gamma)^{118}$Sn experiments, the data collected was sorted with GRSISort V3.1.3.5 [47] and V4.0.0.2 [48], respectively. GRSISort works off of the ROOT framework [49] to sort the raw data into fragments which are stored in *fragment trees*. These fragment trees are then sorted into time-ordered physics events in *analysis trees* which are used to make histograms and matrices with scripts written in C++.

As the detector systems between the two experiments are nearly the same, the following chapter on data analysis applies to both setups unless otherwise specified.

Chapter 3

Analysis

After the collected data is sorted into analysis trees, calibrations must be made such that the charge collected by each HPGe crystal corresponds to the energy of the γ ray that induced the charge. This process is called gain matching and requires an initial linear gain match followed by corrections of the ADCs' non-linear response, cross-talk between adjacent crystals within the same clover, and potentially pile-up. These corrections ensure a maximal energy resolution when adding all crystals together.

3.1 Energy Calibration

The energy response for each crystal can be determined using any source with well known γ-ray energies. In an ideal system, the detectors would require one calibration that would serve for the entire experiment and beyond. However, due to gain drifts—fluctuations in the energy response over time—it was necessary to calibrate the energy on a run-by-run basis. Gain drifts were observed in both the GRIFFIN and FIPPS data sets and easily corrected for as ^{118}Sn has many well known γ rays with precise energy measurements.

The gain matching was performed using a linear gain match between two γ-ray photopeaks. While this provided calibrated photopeaks of the two energies used for all HPGe detectors as shown in Figure 3.1, the photopeaks between and beyond these γ-ray energies deviated slightly from known literature values as shown in Figure 3.2. This is due to the ADCs having a non-linear energy response, as well as a non-uniform response between each ADC. To achieve the best possible resolution, the ADC non-linearity must be corrected.

3.1.1 ADC Non-Linearities

In order to account for the energy non-linearities exhibited by each ADC, all well known γ-ray energies from literature that could be identified in the γ-ray spectrum for ^{118}Sn were used. This method was similarly performed for both experiments where the literature values were compared to the measured photopeak centroids in the experimental γ-ray spectrum. The difference in these values established the residuals for the literature energies which were then applied to the calibration

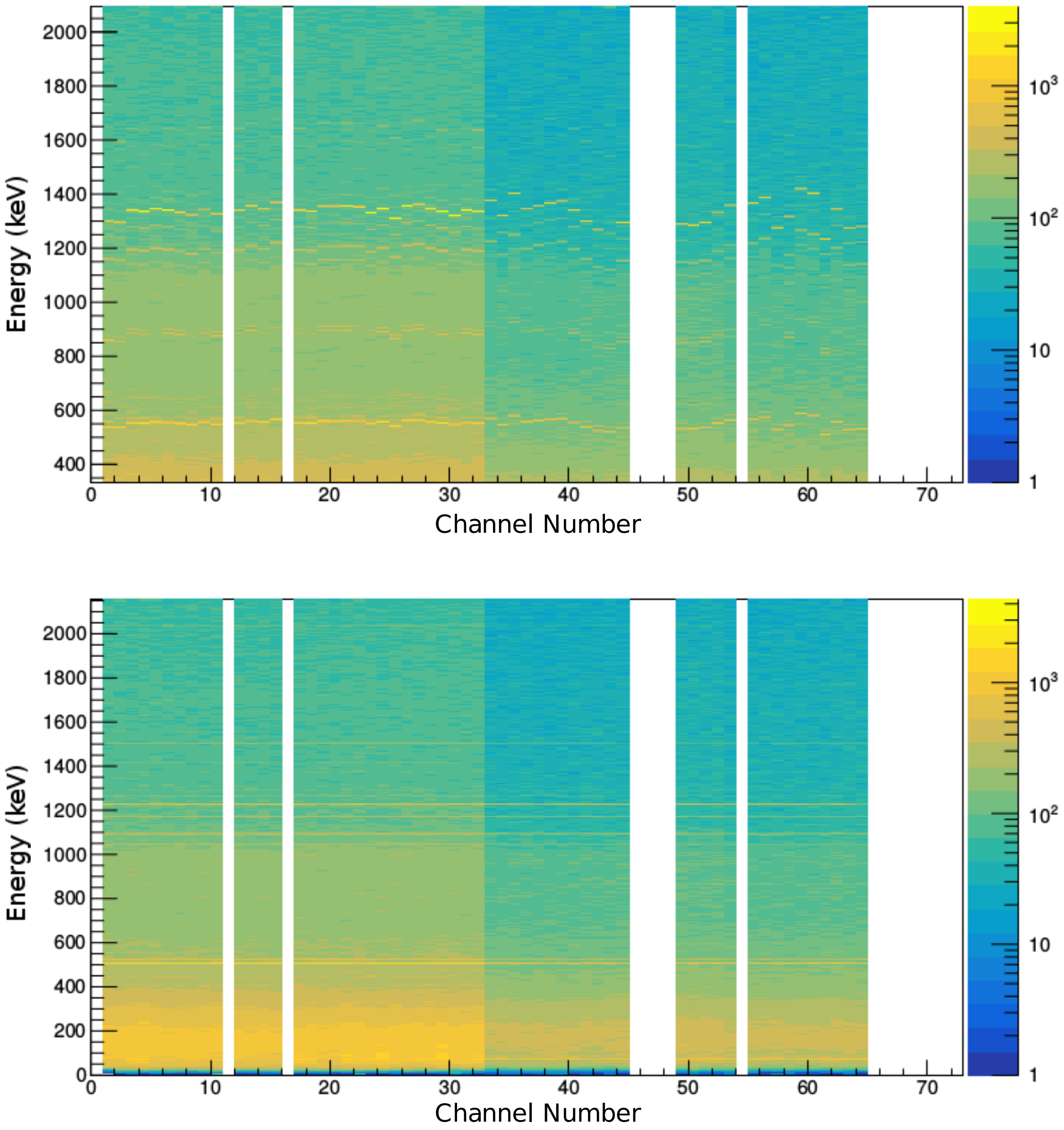

Figure 3.1: Example of calibrating ^{118}Sn data from the neutron capture experiment. (Top) A rough calibration of the charge collected to the γ-ray energy for each of the 64 HPGe crystals. (Bottom) Linear calibration between a 511-keV annihilation peak and the 1229.6-keV γ-ray transition of the first excited 2^+ to the ground state. The first 32 channel numbers correspond to the FIPPS HPGe crystals, and the last 32 correspond to the IFIN HPGe crystals. Two FIPPS crystals, one IFIN clover and one IFIN crystal were omitted in analysis due to poor energy response.

file. An example of one of the ADC residual plots for a full clover is shown in Figure 3.3 from the FIPPS array. Since the energy range for neutron capture extends to the neutron separation energy, 9326.42(13) keV in ^{118}Sn [50], there is a large deviation from the initial measured 1229-keV

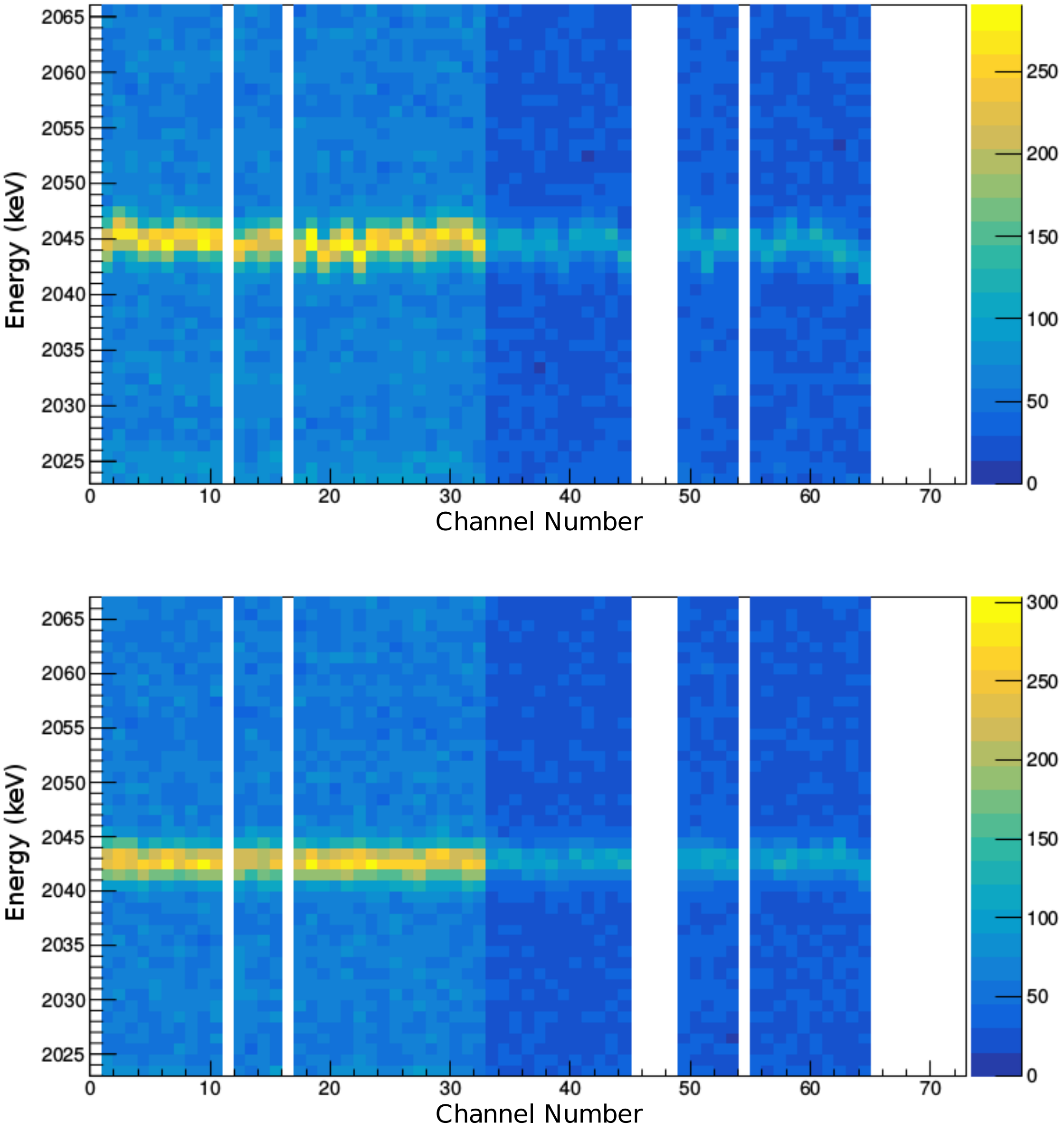

Figure 3.2: (Top) From the same calibration in the bottom of Figure 3.1, the well known 2042-keV transition from the second 2^+ to the ground state in ^{118}Sn shows a poor alignment of the HPGe crystals due to the non-linear behaviour of the ADCs. (Bottom) After correcting the non-linear response, the alignment is greatly improved.

photopeak used in linear calibration to the measured 9326-keV photopeak used in the non-linear residuals.

The ADC non-linear residuals were assumed to remain constant for the entire experiment. Any gain drift could then be corrected by a simple linear gain match with the set of determined residuals from the ^{118}Sn data applied. This was also done for the β-decay experiment, although the energy range only extended up to 3057 keV.

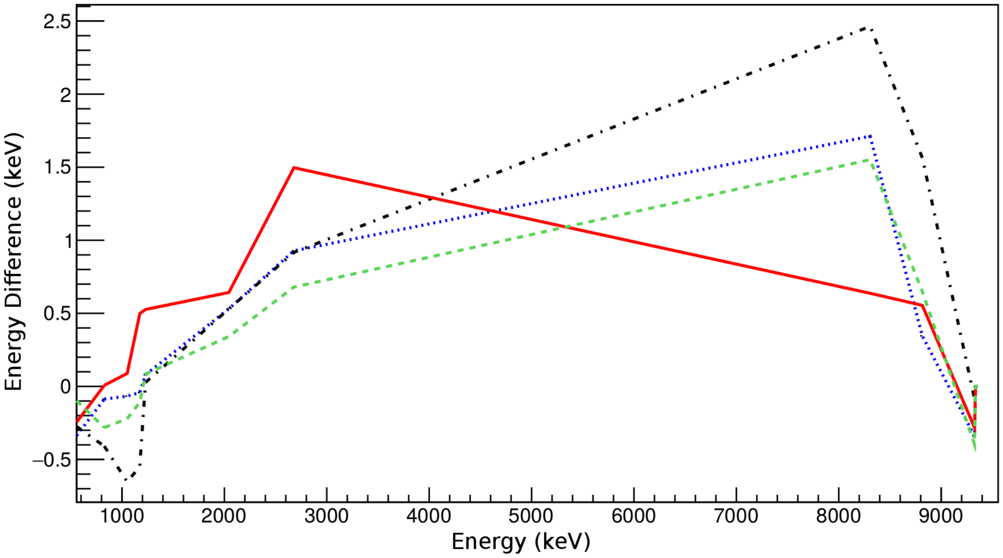

Figure 3.3: Example of a non-linearity residual plot for one of the FIPPS clovers in which well known literature values of γ-ray transitions were compared to the photopeak centroids in ^{118}Sn from the neutron capture data. Each colour represents one crystal from the same clover as the others. The residuals were used to correct the energy response of the corresponding HPGe channel number. Further corrections were necessary to the high energy region as there were no known transitions in the 3–8 MeV range that could be used.

The alignment of the HPGe crystals was consistent throughout the entire energy range in both experimental data sets after the ADC non-linearity corrections were made. For the β-decay data obtained with GRIFFIN, the residuals were sufficient for the entire energy range and no further gain corrections were necessary. However, in the neutron capture data obtained with FIPPS there were no well known γ rays that could be used in the region of 3–8 MeV which led to uncertainty in the peak energy. The only photopeaks which could be used in calibrating the high energy region were from the transitions of the capture state at 9326-keV directly to the ground state and the single and double escape peaks from the same transition—8815 keV and 8304 keV, respectively. As a result, the photopeak centroids were off by as much as 1.5 keV in the 4–8-MeV range. Further corrections to the FIPPS data were made by using summed runs to enhance the statistics in the spectrum and by making use of contaminant photopeaks from the neutron capture on the natural Ge in the detectors, and ^{56}Fe and ^{27}Al in the framing for the array and facility. The γ rays from these contaminant reactions provided an additional 10 photopeaks from 4.2 MeV to 8.5 MeV. These transitions are summarized in Table 3.1.

In both experiments, systematic uncertainty on the energy calibration was determined using the measured photopeak centroids of well known γ-ray energies from the experimental data as well as

Table 3.1: To check the energy calibrations for the neutron capture data in the 4–8 MeV region, contaminant γ-ray transitions were identified from the thermal neutron capture reaction with ^{A}X material present in the Ge [51, 52, 53, 54] detectors and building material commonly used—Al [55] and Fe [56]. The experimentally measured energies, E_{exp}, are in good agreement with the literature values, E_{lit}, indicating the spectra are correctly calibrated. The measured uncertainty comes directly from the fit with no systematic uncertainty given.

^{A}X	E_{lit} [keV]	E_{exp} [keV]
^{27}Al	4259.539(8)	4259.67(14)
	7724.034(7)	7724.33(2)
^{56}Fe	7631.18(10)	7631.28(10)
	7645.58(5)	7645.67(10)
^{70}Ge	5817.15(4)	5816.98(10)
	6707.45(4)	6707.50(10)
^{72}Ge	6390.17(4)	6390.26(5)
^{73}Ge	7260.13(4)	7260.27(16)
	8498.64(4)	8498.6(3)
^{74}Ge	6252.24(11)	6252.22(5)

standard sources—^{56,60}Co, ^{133}Ba, and ^{152}Eu for the β-decay data, and ^{152}Eu and $^{27}\mathrm{Al}(n,\gamma)^{28}\mathrm{Al}$ for the neutron capture data. The systematic uncertainties of 0.20 keV and 0.25 keV were used for the energies measured with GRIFFIN and FIPPS, respectively.

3.1.2 Cross-Talk

Cross-talk is an issue related to the close-packing of the HPGe crystals in a clover in which the energy deposited by a γ ray in one detector modifies the observed energy of a coincident event in an adjacent crystal of the same clover [30]. This has a significant effect on the photopeak resolution and peak shape of a deposited γ ray such that corrections need to be made. Cross-talk is significantly more noticeable when using addback since this technique recovers Compton-scattered γ rays between adjacent crystals within the same clover.

A method for correcting cross-talk has been developed and is outlined in References [30, 57]. This method works by fitting the Compton-scattered diagonal lines observed in γ-γ coincidence matrices for each HPGe crystal combination to establish coefficients which determine how much the energy deposited in the first crystal changes the energy observed in the second crystal. This was a necessary step in producing addback photopeaks with the best possible resolution as shown for an extreme-case crystal-pair combination in Figure 3.4.

3.2 Efficiency

Many of the experimental measurements rely on the characterization of the detector efficiency. The efficiency is a measure of the probability of a γ ray being fully detected in one of the HPGe crystals

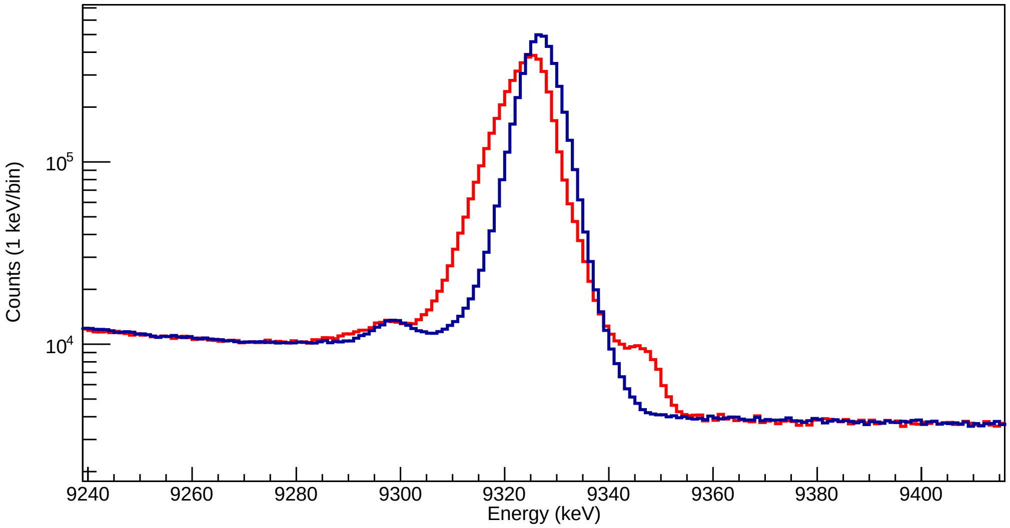

Figure 3.4: Shown is an addback photopeak of the entire FIPPS array comparing the effects of cross-talk (Red) to a cross-talk corrected photopeak (Blue). Not only does the cross-talk increase the peak width, here it also introduces the appearance of an extra photopeak at the high-energy side. The photopeak is from the decay of the 9326-keV neutron capture state directly to the ground state from the neutron capture experiment.

or a full clover when using addback. The efficiency can be determined by using standard sources which have well defined half-lives, γ-ray intensities, and a known activity. With these values, the expected number of events for each known source can be calculated and compared to the actual number events measured by the detector array. The efficiency is then,

$$\varepsilon_\gamma = \frac{A_\gamma}{N_\gamma} \tag{3.1}$$

where ε_γ is the measured efficiency, A_γ is the number of counts in a photopeak, and N_γ is the expected number of events for the same γ ray. This was performed for a range of well-known γ-ray transitions in the standard sources which were also used in determining the systematic uncertainty on the peak centroids. These were ^{56,60}Co, ^{133}Ba, and ^{152}Eu for the GRIFFIN array and ^{152}Eu and ^{27}Al(n,γ) for the FIPPS array. The energy range of the sources used with GRIFFIN extend from 81 keV (^{133}Ba) to 3273 keV (^{56}Co). The energy range of the sources used with FIPPS extend from 31 keV to 7724 keV (^{27}Al).

3.2.1 Efficiency Curves

In order to parameterize the efficiency of the detector arrays, the photopeaks of well known γ-ray transitions from standard sources (^{56,60}Co, ^{133}Ba, and ^{152}Eu for GRIFFIN and ^{152}Eu and ^{27}Al(n,γ) for the FIPPS) were measured for their peak area and then compared to the expected number of events based on the decay half-life, the time the source was measured for, and the intensity of the γ rays measured. All energy calibrations were applied to ensure the peak shape was fit well, and summing corrections were taken into account. The resulting efficiency (obtained with Eq. 3.1) corresponding to each γ ray measured in singles and addback were plotted and fit with with a 6^{th} order polynomial for the GRIFFIN data and a 5^{th} order polynomial for the FIPPS data. These fits are shown in Figures 3.5 and 3.6 for the GRIFFIN array and for the FIPPS array, respectively. These efficiency curves allow for interpolating the efficiency for any γ-ray energies that may be observed.

For the present experiments, only the relative efficiency curves were obtained. The relative efficiency does not account for timing losses throughout the experiment and may not indicate the actual, or absolute, efficiency of the detector. The curve produced from the relative efficiency, and the corresponding parameters from the fit, is identical to the absolute efficiency curve aside from a constant scale factor of the entire curve.

3.2.2 Summing Corrections

In the case that two or more γ rays are detected in the same HPGe crystal or clover within a narrow time window, the signals generated appear as if there was a single γ-ray event in the DAQ's output. This is called true coincident summing and is dependent on the cascading γ-ray transitions such that the efficiencies can vary from one decaying nucleus to the next. This affect is greater for larger detector volumes and evident in addback mode.

There are two types of coincident summing that lead to inaccurate photopeak detection called *summing out*, and *summing in*. In a simple level scheme, shown in Figure 3.7, summing out refers to at least two events, A and B, that are detected simultaneously in the same detector—this can be all of A and any amount of B as shown in Figure 3.8. In the case of measuring the intensity of A, this coincident signal from the same detector will have the affect of one event being taken out from A (hence summing *out*). In the case where there is a third γ-ray transition, C, that is parallel to A and B and equal to their sum, there is a potential for summing in. Summing in refers to the detection of a cascade of at least two γ-ray transitions that are fully detected in the same detector. This will produce a signal that is indistinguishable from C such that the photopeak will appear to have an extra event in it (hence summing *in*).

To correct for these summing events, an empirical technique that makes use of the symmetry of angular correlations about 90° was developed with the GRIFFIN array [30] and is discussed in greater detail in [57]. Highlighted in Figure 3.8, a simple description is that the probability of a γ ray emitted at $\theta = 0^\circ$ with respect to a coincident γ ray is equal to the probability of the two coincident γ rays being emitted at $\theta = 180^\circ$ with respect to each other. The angular coverage of both GRIFFIN and FIPPS allow for the experimenter to calculate the amount of summing which occurs at an angle of $\theta = 0^\circ$ between the two γ rays, A and B, by measuring the amount of B at $\theta = 180^\circ$ from A. In this sense, a matrix is filled with γ-ray coincidences in which the second γ-ray event is required to be detected in the HPGe crystal, or clover for addback, at $\theta = 180^\circ$ from the detector in which the first γ-ray event is detected.

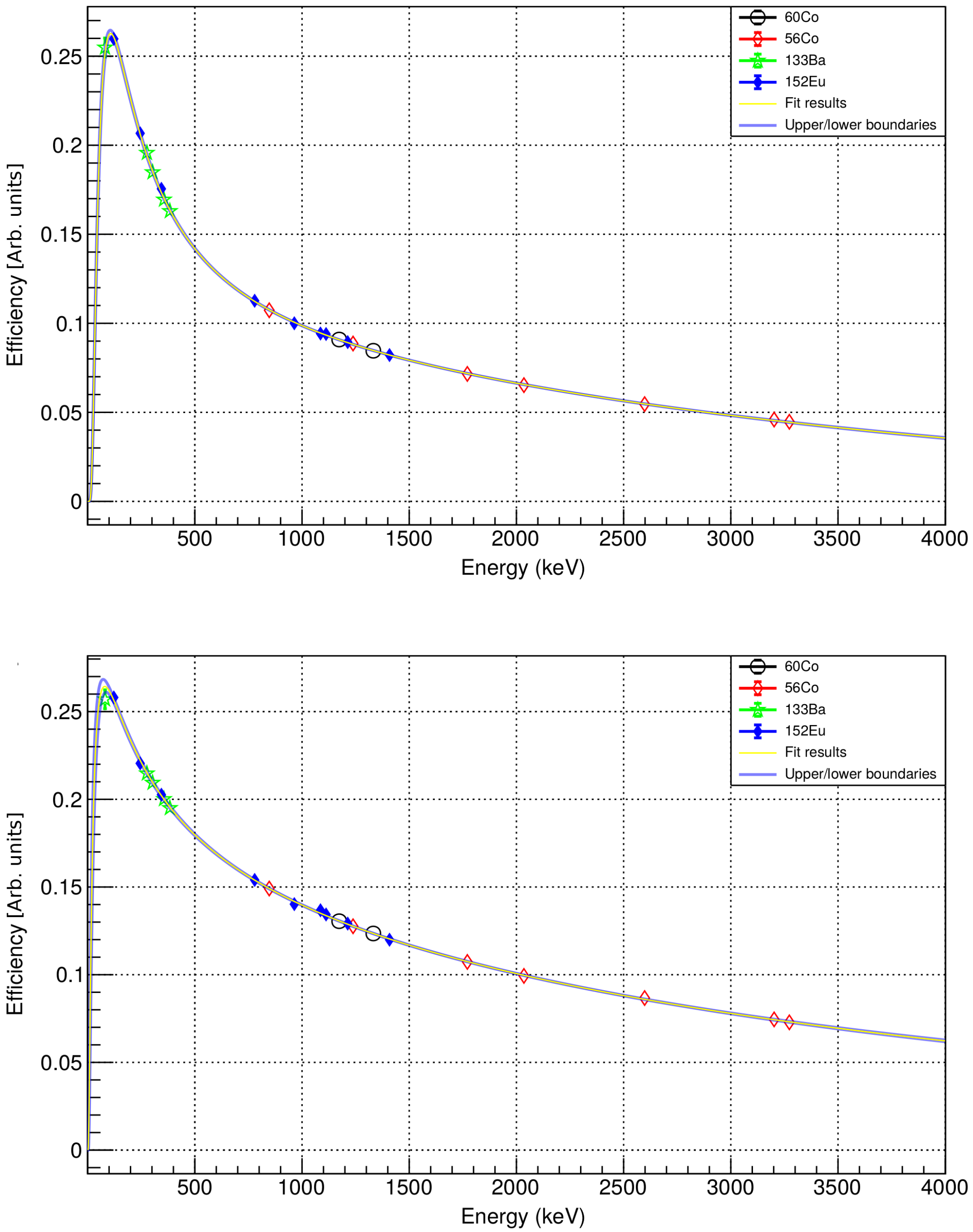

Figure 3.5: The relative efficiency curves for γ-ray singles (top) and addback (bottom) for the GRIFFIN array. The sources were scaled to fit to ^{60}Co and minimize the χ^2. The reduced χ^2 was 1.81 for singles and 1.51 for addback.

The amount of summing out of A is determined by gating on A in the 180° coincident matrix and integrating over the entire projection. This amount of summing out that was lost, is added back to the

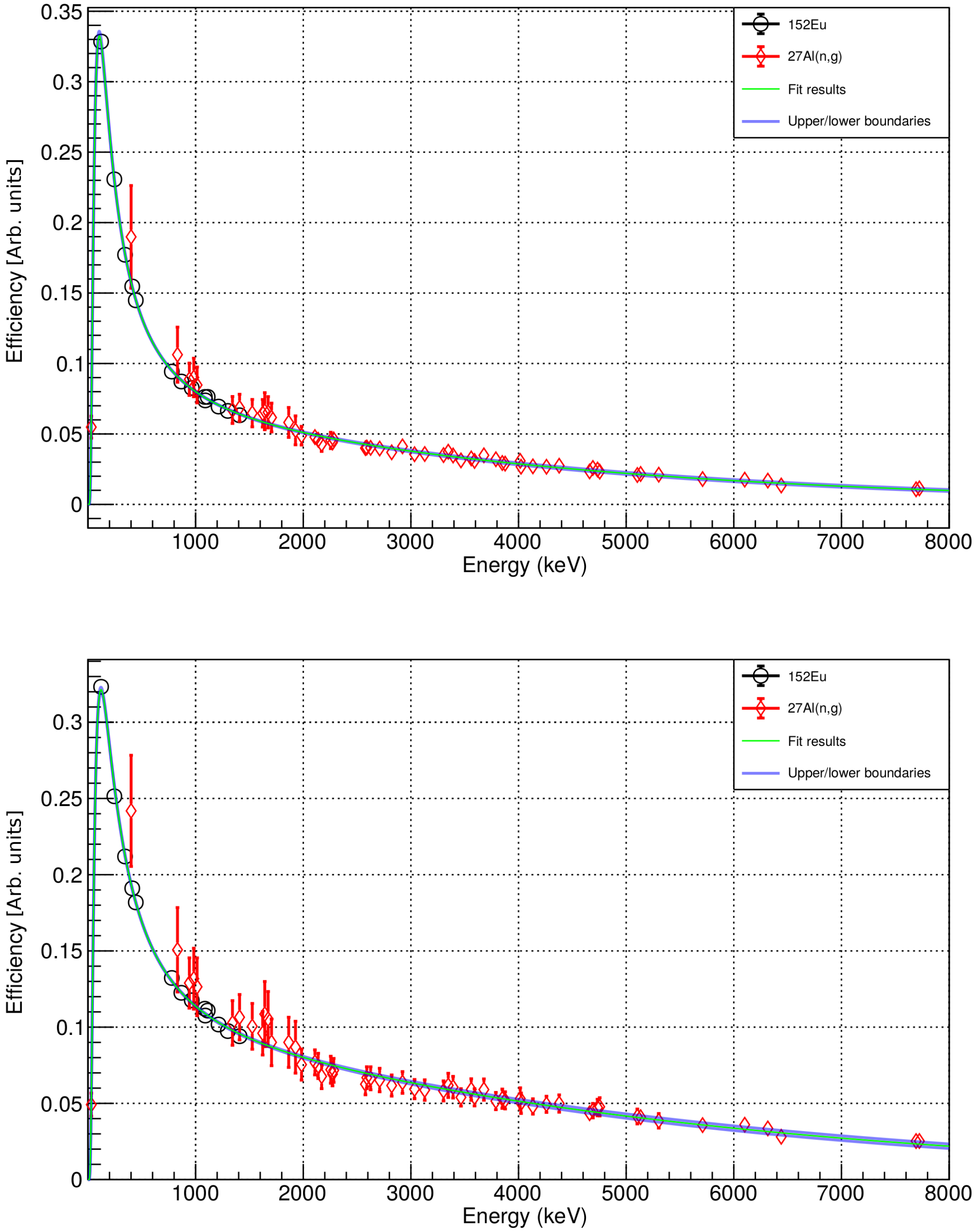

Figure 3.6: The relative efficiency curves for γ-ray singles (top) and addback (bottom) for the FIPPS array. The ^{27}Al($(n,\gamma)^{28}$Al γ-ray events were scaled to fit to ^{152}Eu. The reduced χ^2 was 0.60 for singles and 0.92 for addback. The large error bars on the ^{28}Al efficiencies is due to the large uncertainty of 10% on these intensities [55].

total events of A. To avoid over compensating for the summing out, a projection on the background near A is also integrated and subtracted.

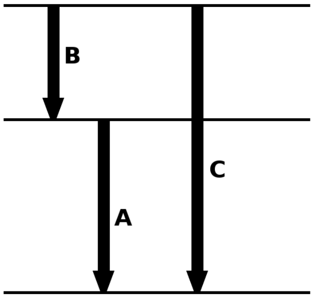

Figure 3.7: A simple level scheme to help describe summing in and summing out. Summing in refers to the number of events in the peak area of *C* that are due to the summing of *A* and *B* within the same detector. Summing out refers to the events lost in *A* due to the summing with any amount (partial or full) of *B* in the same detector, and vice versa.

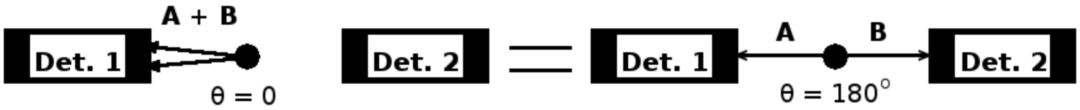

Figure 3.8: Schematic of true coincident γ-ray events, *A* and *B*, both interacting with the same detector with $\theta = 0°$ compared to when *a* is detected at 180° from *B*. The have equal probabilities, allowing for an empirical way to determine the summing at $\theta = 0°$ by observing the $\theta = 180°$ coincidence events.

The amount of summing in of *C*, shown in Figure 3.7, is also determined by by gating on *A* in the 180° coincident matrix (or similarly *B*). In this projection, the photopeak area of *B* (or similarly *A*) is measured and subtracted from the total events of *C*.

3.3 Intensity Measurements

3.3.1 γ-Singles Data

Much of the measured quantities require the characterization of the detectors' efficiencies as described in the previous section. The intensity of a γ ray, for instance, is a measure of how frequently that γ ray is emitted in a given experiment. It is thus necessary to know the efficiency for detecting that γ-ray energy to truly know how many times it was emitted throughout the experiment. The intensity is given as,

$$I_\gamma = \frac{A_\gamma + N_{\text{sum out}} - N_{\text{sum in}}}{\varepsilon_\gamma}, \tag{3.2}$$

where A_γ is the peak area, $N_{\text{sum out}}$ and $N_{\text{sum in}}$ are the number of events lost and gained due to summing out and summing in, respectively, and ε_γ is the total detector efficiency at that γ-ray's energy.

The intensities for many transitions can be measured by fitting the photopeaks in the singles spectrum and using Equation 3.2. As mentioned in the previous section, a relative efficiency curve was obtained and the efficiency used in Equation 3.1 may not describe the actual intensity of the γ ray. However, the relative efficiency still suffices for relative intensity measurements in the present experiments:

$$I_{\gamma,\mathrm{rel}} = \frac{I_\gamma}{I_{1230}}. \tag{3.3}$$

In this equation, I_γ is the intensity from Equation 3.2, and I_{1230} is the intensity of the most intense transition—1230 keV is the most intense transition in the γ decay of ^{118}Sn in both of the experiments presented here.

3.3.2 γ-γ Coincidences

Although the efficiency of both the GRIFFIN and FIPPS arrays are excellent for detecting γ-ray events, there are often transitions with very little intensity that are buried under the background associated with Compton scattered events. Furthermore, the added γ-ray events from all 64 HPGe crystals produce γ-singles spectra and from these spectra, it is impossible to fully understand the placement of the observed γ rays to a level scheme. For these reasons, it is necessary to produce a γ-γ coincidence matrix of time correlated events that can be used to identify weak transitions, and place them.

The γ-γ coincidence matrix consists of a prompt time window, 320 ns with GRIFFIN and 250 ns with FIPPS, that defines the coincident time between two γ rays. There are random coincidence events present in the prompt window, and so it is necessary to subtract these. For both experiments, a time window between between 1000 ns and 2000 ns was used to ensure the events are uncorrelated. These time windows for FIPPS are shown in Figure 3.9.

Using the γ-γ-matrix, shown in Figure 3.10, consists of placing an energy window, or gate, around a photopeak of interest on the x-axis, and then projecting the y-axis to a 1-D histogram. The resulting histogram reveals transitions that are in coincidence with the gated photopeak and is used to place the γ rays and measure the intensity of transitions not observed in the singles spectrum.

3.3.3 γ-γ Coincidence Data

It is often the case that a γ-ray photopeak cannot be observed or cleanly fit in the singles spectrum. This could be due to the γ ray having a weak intensity compared to the Compton background or compared to a neighbouring photopeak with much greater intensity. However, intensities can still be measured by using a γ-γ coincidence matrix to clearly resolve and fit the peak of interest. Two commonly used methods to extract intensities are gating from below and gating from above.

Gating from below is a method in which the γ-ray intensity can be directly measured by gating on a transition, with a known branching ratio, that depopulates the level that the γ ray of interest feeds into. For instance, in Figure 3.7, gating on A will result in a projected spectrum with a photopeak, corresponding to B, of peak area, N_B. The intensity is

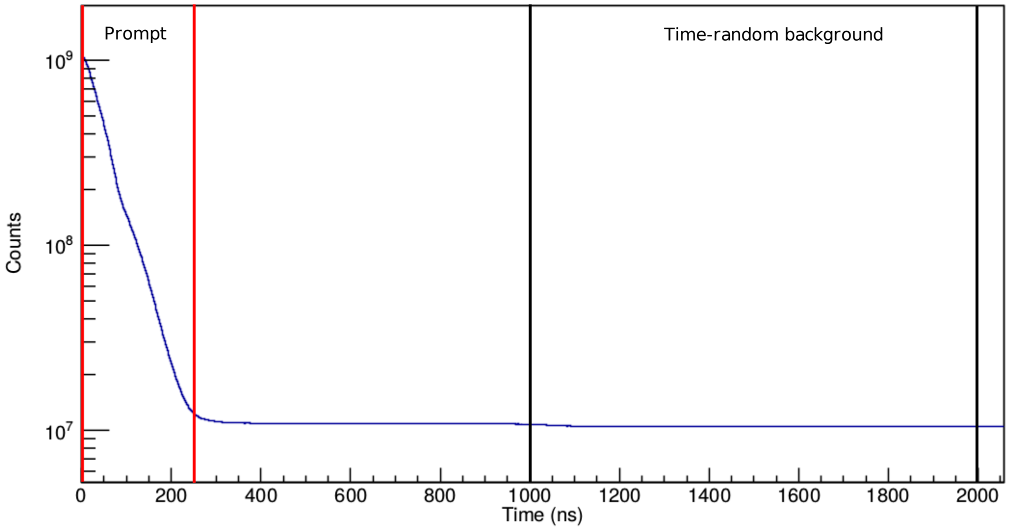

Figure 3.9: The timing between two coincident γ-ray events in the FIPPS data show two general regions. The initial 250 ns contains the *true* coincident γ rays labeled *prompt* while at times greater than 300 ns, the events are considered to be *random* background coincidences. The random coincidences are subtracted from the prompt to produce a time-random background subtracted γ-γ matrix shown in Figure 3.10.

$$I_B = \frac{N_B}{\eta \varepsilon_B \varepsilon_A BR_A} \tag{3.4}$$

where ε is the efficiencies for A and B, BR_A is the branching ratio for A, and η is a normalization constant. In this example, where A is the only transition which depopulates the level, $BR_A = 1$. The constant, η is determined from known intensities that can be easily measured from the singles spectrum. This is achieved by swapping I_B with η.

Intensities for transitions which feed the ground state cannot be measured using this method. If the transition is observed only in γ-γ coincidences, it would be from gating on a γ-ray transition directly above. Using Figure 3.7 again, this would be a gate on B to project a spectrum with a photopeak corresponding to A. In this simple scheme, knowing the intensity of B is enough to get the intensity of A if the level from which A is depopulating is only populated by B. However, this method can get complicated very quickly when looking at a more realistic level scheme. The state which A originates from can be directly populated from β decay or from many γ decays from high-lying states to the state which A originates from.

3.3.4 Branching Ratios

If the intensities of all γ-ray transitions which decay from a level are known, as well as any corresponding internal conversion coefficients, the branching ratios can be determined. Branching ratios

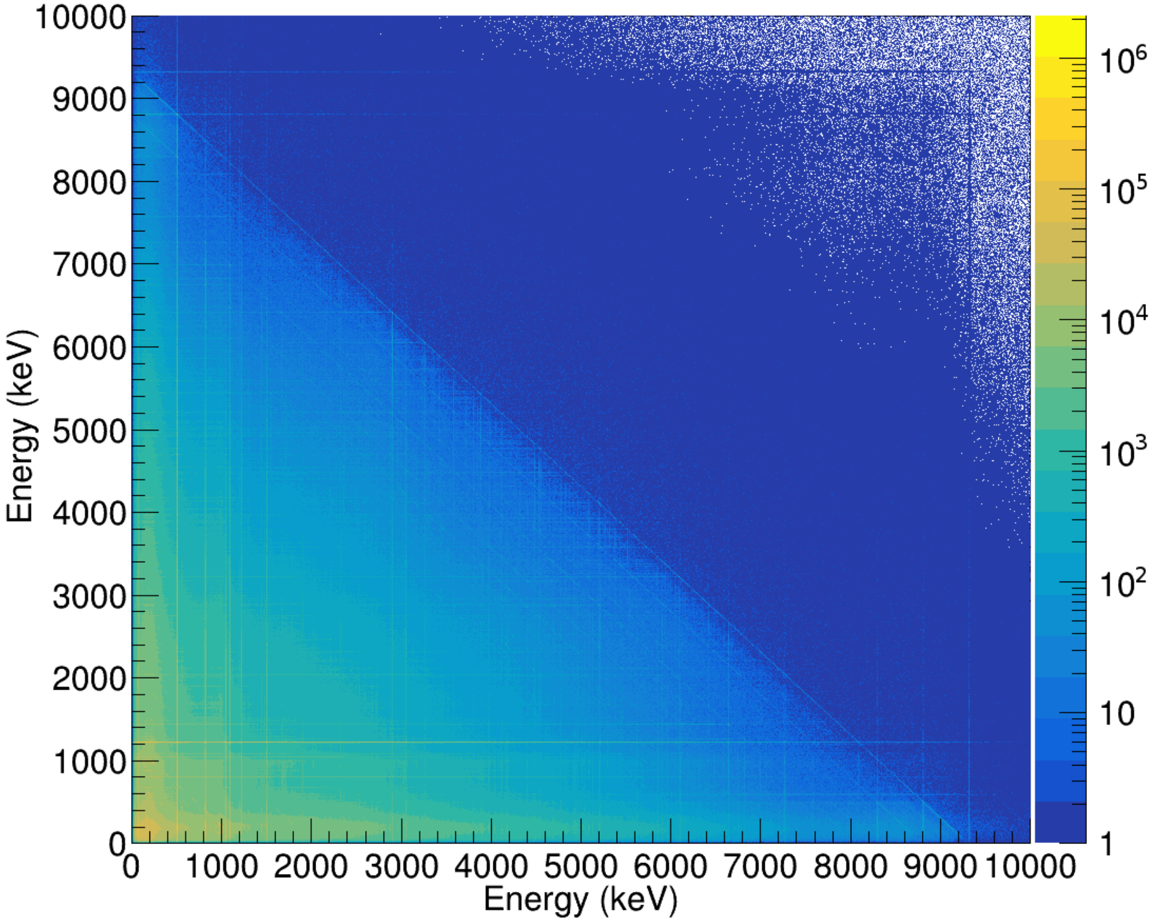

Figure 3.10: A 2-D time-random background subtracted γ-γ coincidence matrix produced from the FIPPS data. By selecting a narrow energy range on one axis and projecting the other axis, a 1-D histogram reveals the γ-ray transitions which are in coincidence with the gated transition.

of excited states are important to measure as they offer a comparison to other studies which populate the same excited state since the branching ratios are independent from how the state was populated, and they provide useful information in the study of nuclear structure related to transition probabilities and the mixing between different states.

$$BR_\gamma = \frac{I_\gamma}{I_{total}} \tag{3.5}$$

Here, the branching ratio of a γ-ray transition is defined by the intensity of that γ ray, I_γ, divided by the total γ intensity, I_{total}, which decays from the excited state. In the following analysis sections for the present studies, branching ratios are used to compare different experimental results, used in determining partial lifetimes for measuring $B(E2)$ values, and used in comparing the ground-state branching of select states of interest.

Chapter 4

β-Decay Results

The experiment carried out at TRIUMF observed the β^- decay of ^{118}In occurring from the 1^+ ground state ($t_{1/2}$ = 5.0(5) s), and the 5^+ ($t_{1/2}$ = 4.45(5) min) and 8^- ($t_{1/2}$ = 8.5(3) s) isomeric states. Based on the β-decay selection rules, discussed in section 1.2, and previous studies on the β^- decay of ^{118}In [58, 59, 60], the states of interest in the daughter, ^{118}Sn, are primarily populated via the 5^+ isomer.

The Q-value in the ground state to ground state β-decay of ^{118}In to ^{118}Sn is 4.425(8) MeV. This energy represents the highest energy state that could be able to be populated in ^{118}Sn, if such a state exists. The 5^+, being an isomeric state, is ≈60 keV above the Q-value [60].

Since the half-life of the 5^+ isomer is 4.45 min, it was easy to isolate from the shorter lived 1^+ and 8^- states with half-lives of 5 s and 8.5 s, respectively. The cycle time was set to measure 5 s of background, 5 min of beam implantation, and 5 min of beam decay. There is then a 1.5 s tape move to start a new cycle. Nearly 99% of the 8^- isomer, decays internally to the 5^+ isomer by emitting a 138.5 keV γ ray. Furthermore 95% of the ^{118}In ground state decays directly to the ground state in ^{118}Sn. However, to ensure there is virtually no contamination from these β-decaying states, analysis was performed only on the data obtained during the beam decay cycle with the first 25 s omitted. Removing the first 25 s further removed the 1^+ ground state by five half-lives, and the 8^- isomer by three half-lives.

The total run time was 80 min during which 2×10^9 γ-singles and 1×10^9 γ-γ coincidence events were recorded. With the high rate of implantation and low number of isobaric contamination in the decay cycle, SCEPTAR was not used to produce β-γ coincidences as this would reduce statistics due to the 80% efficiency of SCEPTAR. The data was analyzed using the addback technique, and the level scheme was built using a γ-γ coincidence matrix.

The results on the low-lying levels populated in the present experiment have been published in Physical Review C [61] and presented in Appendix A.

4.1 Literature Review

The semi-magic Sn isotopes have been the subject of many theoretical and experimental studies as they offer a strong foundation to the study of nuclear structure in the $Z = 50$ region. The focus of this β-decay study on ^{118}Sn is the proton two-particle two-hole, 2p-2h, intruder band which gives rise to shape coexistence in the mid-shell Sn isotopes [4,62,63]. Shape coexistence is a phenomenon that has been observed in many regions of the nuclear chart and is defined as a nucleus having two or more distinct shapes at similar excitation energies [4]. Past studies on the stable, even-even Sn isotopes have shown that the transitions within the 2p-2h band have enhanced $B(E2)$ values, as a result of their collective structure, compared to the normal configuration transitions from the single particle excitations. In the case of the even-even Sn nuclei, the normal configuration is spherical, whereas the 2p-2h likely takes a prolate shape [64]. However, it is not so easy to distinguish the two as there is considerable amount of mixing between the two configurations.

In a recent study of ^{116}Sn, the previous suggested 2p-2h 0_2^+ bandhead at 1757 keV is in fact strongly mixed with the intruder band, but it is the 0_3^+ that should be considered the bandhead [46, 65]. This is based on the much more enhanced $B(E2; 2_2^+ \rightarrow 0_3^+) = 99.7(84)$ W.u. of a 85 keV transition connecting the 2_2^+ to the 0_3^+ compared to the $B(E2; 2_2^+ \rightarrow 0_2^+) = 44.4(28)$ W.u. of a 355 keV transition connecting the 2_2^+ to the 0_2^+. Furthermore, *sd* IBM-2 calculations were performed to test the collectivity and mixing of the observed intruder states [46]. It was concluded that the 0_3^+ in ^{116}Sn is best described as the bandhead of the 2p-2h band.

In the case of ^{118}Sn, observations of the states owing to 2p-2h excitations have been made in several studies [58, 59, 60, 63, 66, 67]. The same story of the 2.057-MeV, 0_3^+ being described as the 2p-2h bandhead is not likely as the energy of this state is higher than the 2.043-MeV, 2_2^+ state belonging to the 2p-2h band, shown in Figure 1.1. However, the character of the 2p-2h band is difficult to characterize due to strong mixing between many of the states with the same spin, J [61].

A discrepancy between two γ-ray spectroscopy studies performed in the late 80s [58,66] which leads to an inaccurate degree of collectivity of the 2.043-MeV 2^+ intruder state is examined in the present research. These studies offer the greatest source of γ-ray transitions used to build the level scheme for ^{118}Sn and in determining their $B(E2)$ values. The 2_2^+ state at 2.043 MeV was populated in a β-decay study of the 5^+ isomer of ^{118}In [58]. A 285.22(11)-keV transition from the 2_3^+ state of 2.328 MeV is observed to populate the 2_2^+ 2.043-MeV level. While they also observed the 528-keV γ-ray transition from the 2p-2h 0_2^+ at 1.758 MeV, there was no observation for the $2_2^+ \rightarrow 0_2^+$ transition. This is likely due to the energy being nearly that of the $2_3^+ \rightarrow 2_2^+$ transition (284.66(12) keV) and there were no γ-γ-coincidences used to isolate these transitions.

In a neutron scattering study, ^{118}Sn$(n, n'\gamma)$, a 284.66(12)-keV transition was placed from the 2043-keV level to the 2p-2h 0_2^+ bandhead with no observation of the 285.22(11)-keV transition despite populating the 2.328-MeV level from which it originates [66].

Given the similar energies (less than 1 keV), it is understandably likely that these transitions were placed as one, rather than as two. While the intensity of the 284.66(12)-keV and 285.22(11)-

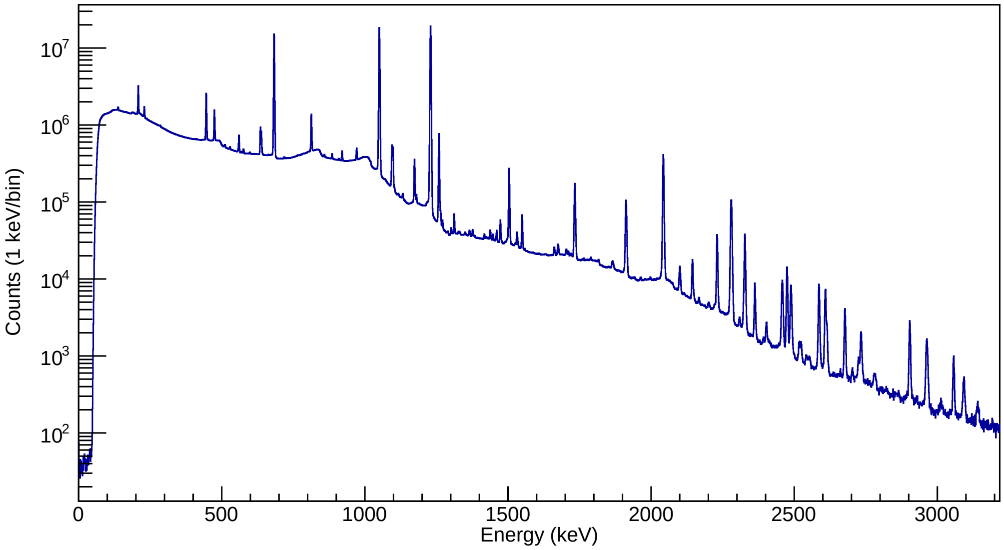

Figure 4.1: Addback singles spectrum obtained from the β-decay of the 5^+ isomer in ^{118}In.

keV transitions are fairly weak, the missing, or additional intensity of one or both transitions can change how the states they originate from are described. It is thus important to examine all possible transitions based on γ-ray selection rules by using γ-γ coincidence techniques outlined in Section 3.3.2.

4.2 γ-ray Analysis

The γ-decay of excited states in ^{118}Sn that were populated in the β-decay of the 5^+ isomer of ^{118}In was analyzed using addback, both in singles and in γ-γ coincidences. In total, 23 levels were identified with one being newly placed at 3397.46(13) keV. From these levels, 99 γ-ray transitions were placed with 43 being newly observed. The energies and their intensities are presented in Table 4.1.

The strongest γ-ray intensities were generally obtained from the addback singles spectrum, shown in Figure 4.1. Many of the transitions were only observed in γ-γ coincidence which was also used to resolve any overlapping photopeaks and resolve discrepancies from previous works. Discrepancies from previous studies are discussed in subsequent sections, although the majority of energies and intensities are comparable to the those measured in the same β-decay study of the 5^+ isomer in ^{118}In performed by Raman *et al.* [58]. Of note, the 284.66-keV and 285.22-keV transitions are resolved and their intensities determined, as well as two of the γ-ray transitions observed and placed by Raman are not identified in the present experiment, and several transitions' intensities measured by Raman differ by more than three standard deviations. These are all discussed in the subsequent sections.

Another important topic of discussion is the spin assignment for several levels that were previously unassigned. Logft values, γ-decay selection rules and angular correlations were all used to establish the spins and parities of the states.

Table 4.1: Levels in ^{118}Sn populated by the β^- decay of the 5^+ isomer of ^{118}In ($E_x = 60$ keV, $T_{1/2} =$ 4.45 min). The relative intensity of the observed transitions, I_γ, are compared to the previous β^- decay study [58], and the branching ratios, BR_γ, and $B(E2)$ values are compared to the ENSDF [50].

E_{level} [keV]	$J_i^\pi \rightarrow J_f^\pi$	E_γ [keV]	I_γ	$BR_{\gamma,rel}$	I_γ Ref. [58]	$BR_{\gamma,rel}$ Ref. [50]
1229.50(10)	$2_1^+ \rightarrow 0_1^+$	1229.57(20)	100	100	100	100
1758.24(14)	$0_2^+ \rightarrow 2_1^+$	528.70(20)	0.129(4)	100		100
2042.62(10)	$2_2^+ \rightarrow 0_2^+$	284.52(20)	0.051(7)	1.31(17)		2.5(2)
	$2_2^+ \rightarrow 2_1^+$	813.11(21)	3.91(9)	100.0(23)	3.88(12)	100.0(24)
	$2_2^+ \rightarrow 0_1^+$	2042.70(22)	3.27(10)	83.6(26)	3.63(8)	92.2(25)
2280.21(11)	$4_1^+ \rightarrow 2_2^+$	237.80(22)	0.050(4)	0.058(5)	0.04(2)	0.05(2)
	$4_1^+ \rightarrow 2_1^+$	1050.54(20)	85(2)	100.0(26)	84.4(26)	100(3)
2324.29(21)	$3_1^- \rightarrow 2_1^+$	1094.98(63)	1.46(7)	100(5)	1.5(5)	100(4)
	$3_1^- \rightarrow 0_1^+$	2323.9(3)	0.0148(13)	1.02(9)		1.1(1)
2327.73(12)	$2_3^+ \rightarrow 2_2^+$	285.26(22)	0.038(14)	2.3(8)	0.081(10)	5.1(6)
	$2_3^+ \rightarrow 0_2^+$	569.39(20)	0.041(2)	2.40(14)		
	$2_3^+ \rightarrow 2_1^+$	1098.2(6)	1.70(7)	100(4)	1.6(3)	100(19)
	$2_3^+ \rightarrow 0_1^+$	2327.7(6)	0.326(13)	19.1(8)	0.374(12)	23.4(8)
2403.05(11)	$2_4^+ \rightarrow 2_2^+$	360.67(22)	0.0121(18)	0.91(13)		1.8(2)
	$2_4^+ \rightarrow 0_2^+$	644.73(20)	0.0190(8)	1.44(6)		
	$2_4^+ \rightarrow 2_1^+$	1173.44(22)	1.32(3)	100.0(26)	1.43(5)	100(3)
	$2_4^+ \rightarrow 0_1^+$	2403.05(22)	0.0029(3)	0.222(20)		
2488.59(11)	$4_2^+ \rightarrow 4_1^+$	208.46(21)	3.96(8)	60.3(12)	2.71(8)	52(7)
	$4_2^+ \rightarrow 2_2^+$	445.90(21)	6.56(14)	100.0(22)	5.76(17)	100(3)
	$4_2^+ \rightarrow 2_1^+$	1259.11(22)	3.87(10)	59.2(16)	3.99(12)	67(3)
2677.10(11)	$2_5^+ \rightarrow 2_1^+$	1447.51(21)	0.035(3)	87(6)	0.047(5)	86(4)
	$2_5^+ \rightarrow 0_1^+$	2677.18(20)	0.0405(25)	100(6)	0.039(5)	100(4)
2733.53(11)	$4_3^+ \rightarrow 4_1^+$	452.7(3)	0.098(11)	6.2(7)		
	$4_3^+ \rightarrow 2_2^+$	690.89(21)	0.0199(18)	1.26(12)		
	$4_3^+ \rightarrow 2_1^+$	1504.0(3)	1.58(4)	100(3)	1.65(5)	100
2878.4(3)	(5^-)[1] $\rightarrow 4_2^+$	598.2(3)	0.067(6)	100	0.069(11)	100(3)

---

[1] Listed as (4,5,6$^+$) in [50] but suggested to be 5^- in Ref. [66, 68]. A 5^- assignment also fits with the logft value in Table 4.2.

Table I.(*Continued*).

E_{level} [keV]	$J_i^\pi \rightarrow J_f^\pi$	E_γ [keV]	I_γ	$BR_{\gamma,rel}$	I_γ Ref. [58]	$BR_{\gamma,rel}$ Ref. [50]
2903.53(12)	$2_6^+ \rightarrow 2_1^+$	1673.76(28)	0.0216(17)	67(7)		37(2)
	$2_6^+ \rightarrow 0_1^+$	2903.46(21)	0.0324(24)	100(7)	0.028(9)[2]	100(4)
2963.04(12)	$4_4^+ \rightarrow 4_3^+$	229.6(4)	1.06(5)	1.80(8)	0.783(24)	1.38(4)
	$4_4^+ \rightarrow 2_5^+$	286.02(20)	0.0371(17)	0.063(3)		
	$4_4^+ \rightarrow 4_2^+$	474.5(3)	3.10(7)	5.26(16)	3.00(10)	5.30(18)
	$4_4^+ \rightarrow 2_4^+$	560.04(20)	1.161(26)	1.97(4)	0.99(4)	1.75(7)
	$4_4^+ \rightarrow 2_3^+$	635.2(3)	1.73(4)	2.94(7)	1.77(6)	3.13(11)
	$4_4^+ \rightarrow 3_1^-$	638.4(3)	1.60(4)	2.72(6)	1.37(4)	2.42(7)
	$4_4^+ \rightarrow 4_1^+$	682.94(20)	59.0(13)	100.0(23)	56.6(17)	100(3)
	$4_4^+ \rightarrow 2_2^+$	920.4(3)	0.476(12)	0.807(20)	0.506(21)	0.89(4)
	$4_4^+ \rightarrow 2_1^+$	1733.56(22)	0.446(13)	0.76(5)		
2999.12(18)	$6_1^+ \rightarrow 4_2^+$	510.88(21)	0.094(8)	100(8)	0.13(2)	100(17)
	$6_1^+ \rightarrow 4_1^+$	718.57(21)	0.090(7)	96(7)	0.076(13)	60(3)
3056.88(14)	$2_7^+ \rightarrow 0_1^+$	3056.90(22)	0.0108(11)	100		100(4)
3374.10(11)	$4_5^+ \rightarrow 4_4^+$	411.16(22)	0.045(5)	8.2(9)	0.037(7)	4.6(9)
	$4_5^+ \rightarrow 2_6^+$	470.66(22)	0.00084(6)	0.154(10)		
	$4_5^+ \rightarrow 4_3^+$	640.50(21)	0.0222(11)	4.05(20)		
	$4_5^+ \rightarrow 2_5^+$	696.87(22)	0.0067(12)	1.23(23)		
	$4_5^+ \rightarrow 4_2^+$	885.43(20)	0.259(7)	47.3(12)	0.264(20)	33(3)
	$4_5^+ \rightarrow 2_4^+$	971.0(3)	0.139(6)	25.4(10)	0.35(6)	44(8)
	$4_5^+ \rightarrow 2_3^+$	1046.31(21)	0.070(7)	12.8(13)		
	$4_5^+ \rightarrow 4_1^+$	1094.10(20)	0.548(23)	100(4)	0.805(20)	100(3)
	$4_5^+ \rightarrow 2_2^+$	1331.3(3)	0.0127(18)	2.3(3)		
	$4_5^+ \rightarrow 2_1^+$	2144.64(21)	0.108(11)	19.7(20)	0.121(5)	15.0(6)
3397.46(13)	$4_6^+ \rightarrow 4_3^+$	663.92(20)	0.0338(16)	43.0(20)		
	$4_6^+ \rightarrow 4_2^+$	908.72(20)	0.079(4)	100(5)		
	$4_6^+ \rightarrow 2_4^+$	994.18(22)	0.0166(11)	21.1(14)		
	$4_6^+ \rightarrow 2_3^+$	1070.06(23)	0.035(3)	45(4)		
	$4_6^+ \rightarrow 4_1^+$	1117.3(3)	0.043(4)	54(5)		
	$4_6^+ \rightarrow 2_1^+$	2168.3(4)	0.008(3)	10(4)		
3460.21(11)	$4_7^+ \rightarrow 2_7^+$	403.41(22)	0.0047(4)	1.20(10)		
	$4_7^+ \rightarrow 2_6^+$	556.54(21)	0.0064(4)	1.64(11)		

---

[2] Observed by Raman, but not placed in level scheme.

Table I.(*Continued*).

E_{level} [keV]	$J_i^\pi \to J_f^\pi$	E_γ [keV]	I_γ	$BR_{\gamma,rel}$	I_γ Ref. [58]	$BR_{\gamma,rel}$ Ref. [50]
	$4_7^+ \to 4_3^+$	726.62(21)	0.019(1)	4.93(27)		
	$4_7^+ \to 2_5^+$	783.10(22)	0.024(4)	6.0(11)		
	$4_7^+ \to 4_2^+$	971.6(6)	0.39(3)	100(8)	0.32(7)	96(21)
	$4_7^+ \to 2_4^+$	1057.15(22)	0.0148(10)	3.79(26)		
	$4_7^+ \to 2_3^+$	1132.42(20)	0.090(3)	23.1(8)	0.099(9)	30(3)
	$4_7^+ \to 4_1^+$	1180.21(20)	0.159(9)	40.7(23)	0.163(10)	49(3)
	$4_7^+ \to 2_2^+$	1417.57(21)	0.0240(15)	6.1(4)	0.027(5)	8(2)
	$4_7^+ \to 2_1^+$	2230.7(9)	0.280(11)	71.4(28)	0.333(11)	100(3)
3592.15(11)	$4_8^+ \to 2_7^+$	535.21(22)	0.0036(3)	1.37(11)		
	$4_8^+ \to 4_3^+$	858.52(21)	0.108(4)	41.2(16)	0.117(20)	42(7)
	$4_8^+ \to 2_5^+$	915.20(22)	0.0034(6)	1.30(26)		
	$4_8^+ \to 4_2^+$	1103.37(21)	0.083(7)	31.5(27)		
	$4_8^+ \to 2_3^+$	1189.25(22)	0.0140(8)	5.31(29)		
	$4_8^+ \to 2_3^+$	1264.34(20)	0.051(6)	19.4(24)		
	$4_8^+ \to 4_1^+$	1312.1(6)	0.181(6)	68.7(23)	0.187(9)	67(3)
	$4_8^+ \to 2_2^+$	1549.52(20)	0.264(8)	100.0(29)	0.281(12)	100(4)
	$4_8^+ \to 2_1^+$	2362.79(21)	0.064(3)	24.1(12)	0.068(4)	24(1)
3704.34(11)	$4_9^+ \to 2_6^+$	800.76(20)	0.0168(9)	12.3(7)		
	$4_9^+ \to 4_3^+$	970.80(21)	0.110(5)	81(3)		
	$4_9^+ \to 2_5^+$	1027.16(22)	0.0043(8)	3.2(6)		
	$4_9^+ \to 4_2^+$	1215.71(21)	0.030(3)	22.4(23)		
	$4_9^+ \to 2_4^+$	1301.37(20)	0.0411(18)	30.3(14)	0.056(6)	37(4)
	$4_9^+ \to 2_3^+$	1376.65(20)	0.0265(24)	19.5(18)	0.038(5)	25(3)
	$4_9^+ \to 4_1^+$	1424.1(3)	0.019(4)	27(6)	0.021(5)	14(3)
	$4_9^+ \to 2_2^+$	1661.57(21)	0.0292(24)	21.5(18)	0.041(6)	27(4)
	$4_9^+ \to 2_1^+$	2475.06(20)	0.136(7)	100(5)	0.150(7)	100(5)
3753.74(14)	$4_{10}^+ \to 4_3^+$	1020.14(20)	0.070(3)	39.0(17)		
	$4_{10}^+ \to 4_2^+$	1265.14(20)	0.064(6)	36(3)	0.138(9)	78(5)
	$4_{10}^+ \to 4_1^+$	1473.55(21)	0.179(6)	100(3)	0.177(8)	100(5)
	$4_{10}^+ \to 2_2^+$	1711.16(22)	0.0178(16)	9.9(9)		
	$4_{10}^+ \to 2_1^+$	2524.3(3)	0.0061(11)	3.4(6)		
3816.19(15)	$4_{11}^+ \to 2_6^+$	912.6(3)	0.00150(18)	1.72(21)		
	$4_{11}^+ \to 4_3^+$	1082.8(3)	0.0063(6)	7.2(7)		
	$4_{11}^+ \to 4_2^+$	1327.66(22)	0.0190(22)	21.8(26)		

Table I.(*Continued*).

E_{level} [keV]	$J_i^\pi \rightarrow J_f^\pi$	E_γ [keV]	I_γ	$BR_{\gamma,rel}$	I_γ Ref. [58]	$BR_{\gamma,rel}$ Ref. [50]
	$4_{11}^+ \rightarrow 4_1^+$	1536.1(4)	0.0069(12)	7.9(14)		
	$4_{11}^+ \rightarrow 2_1^+$	2586.57(21)	0.087(5)	100(6)	0.096(6)	100
3838.33(16)	$4_{12}^+ \rightarrow 2_6^+$	934.7(3)	0.00085(15)	1.06(20)		
	$4_{12}^+ \rightarrow 4_3^+$	1104.5(3)	0.0030(12)	3.8(15)		
	$4_{12}^+ \rightarrow 4_2^+$	1350.2(4)	0.0081(16)	10.2(21)		
	$4_{12}^+ \rightarrow 4_1^+$	1558.0(3)	0.0144(24)	18(3)		
	$4_{12}^+ \rightarrow 2_1^+$	2608.96(21)	0.080(4)	100(5)	0.086(6)	100

4.2.1 285 keV Triplet

As indicated in the previous section, the evaluated intensities of the 284.66-keV and 285.22-keV γ-ray transitions were expected to be grouped together and needed a thorough investigation to decouple them. The reduction in intensity for these transitions leads to a reduction in their corresponding $B(E2)$ values, and the magnitude of this change can have implications on how the states are characterized.

Using a variety of gates from above, it was determined that there was, in fact, a triplet at 285.2 keV corresponding to 284.52(20)-keV and 285.26(22)-keV—the previously identified transitions—as well as a newly identified 286.02(20)-keV transition depopulating the 2963-keV level. The gates used to separate these transitions are highlighted in Figure 4.2 with the overlay of all three shown in Figure 4.3.

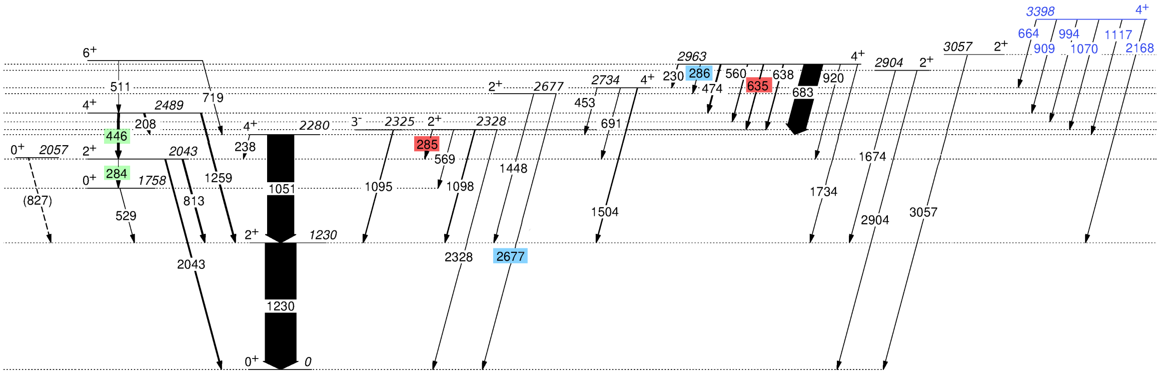

Figure 4.2: Partial level scheme of the low-lying levels populated in the present β-decay experiment. Highlighted are the gates used (446 in green, 635 in red, and 2677 in blue) to determine the placement of each of the $\approx$ 285-keV transitions that make up the triplet.

The 286.02-keV transition was easily identified by gating below on the 2677-keV transition. This isolated the 286.02-keV transition from the other two. The other two are in coincidence with each other and were harder to isolate due to the Compton edge at ≈284 keV from the relatively intense 446-keV transition that feeds the 2^+_2 from the 4^+_2. This made it nearly impossible to measure the intensities from below.

The 284.52-keV transition was isolated by gating above on the 446-keV transition. From the projection of the 446-keV gate, the branching ratio was first determined for the transitions depopulating the 2043-keV level: 284.52 keV, 813 keV and 2043 keV. The total intensity populating the 2043-keV level was also determined to calculate the intensity of these three transitions based on their branching ratios.

Similarly for the 285.26-keV transition, gating from above was necessary. This was achieved by placing a gate on the 635-keV from the 2963-keV level. Although the 285.26-keV transition feeds the 2043-keV level that the 284.52-keV transition comes from, the branching fraction of the 284.52-keV is only 0.7(1)%. The uncertainty on the branching ratio for the 285.26-keV transition is already 35% and the small difference in intensity gained by including the 284.26-keV in the total was ignored.

4.2.2 Literature Discrepancies

The intensity values obtained in this experiment are generally in line with the reported values by Raman [58] and presented in Table 4.1. However, there are also several that have very different values that will be discussed. It should be noted that there is also good agreement with similar β-decay studies [59, 60], but these offer much fewer comparisons.

The discrepancies with the easiest explanation stem from being able to resolve doublets and triplets through γ-γ coincidences. For instance, Raman identified a 1265.14-keV transition from the 3753-keV level with an intensity of 0.138(9). This transition was identified as a doublet consisting of the same energy of 1265.14 keV, but with an intensity of 0.064(6). A second transition of 1264.34 keV was also identified to come from the 3592-keV level with an intensity of 0.051(6). The sum of these intensities is in line with the singly placed γ-ray by Raman.

A 971.0-keV transition was placed twice by Raman. The summed intensity of the doublet was split based on the intensity balance of the 2^+ 2403-keV level as this state is not expected to have direct β feeding. The remaining intensity went to the other transition of the same energy that feeds the 2488-keV level. In the present experiment, a triplet at 971.0 keV was identified to consist of the previously identified γ-ray transitions, as well as a 970.8 keV transition from the 3704-keV level. The summed intensities are consistent with the summed intensity from Raman.

At ≈1095 keV, a doublet of 1094.1 keV and 1094.98 keV was resolved with the former populating the 2280-keV level. This was identified by placing a gate on the 1050-keV γ-ray transition in the γ-γ coincidence matrix and an intensity of 0.548(23) was determined. The latter feeds the 2^+_1 1229-keV level from a 3^- 2325-keV level and is in good agreement with Raman's measured inten-

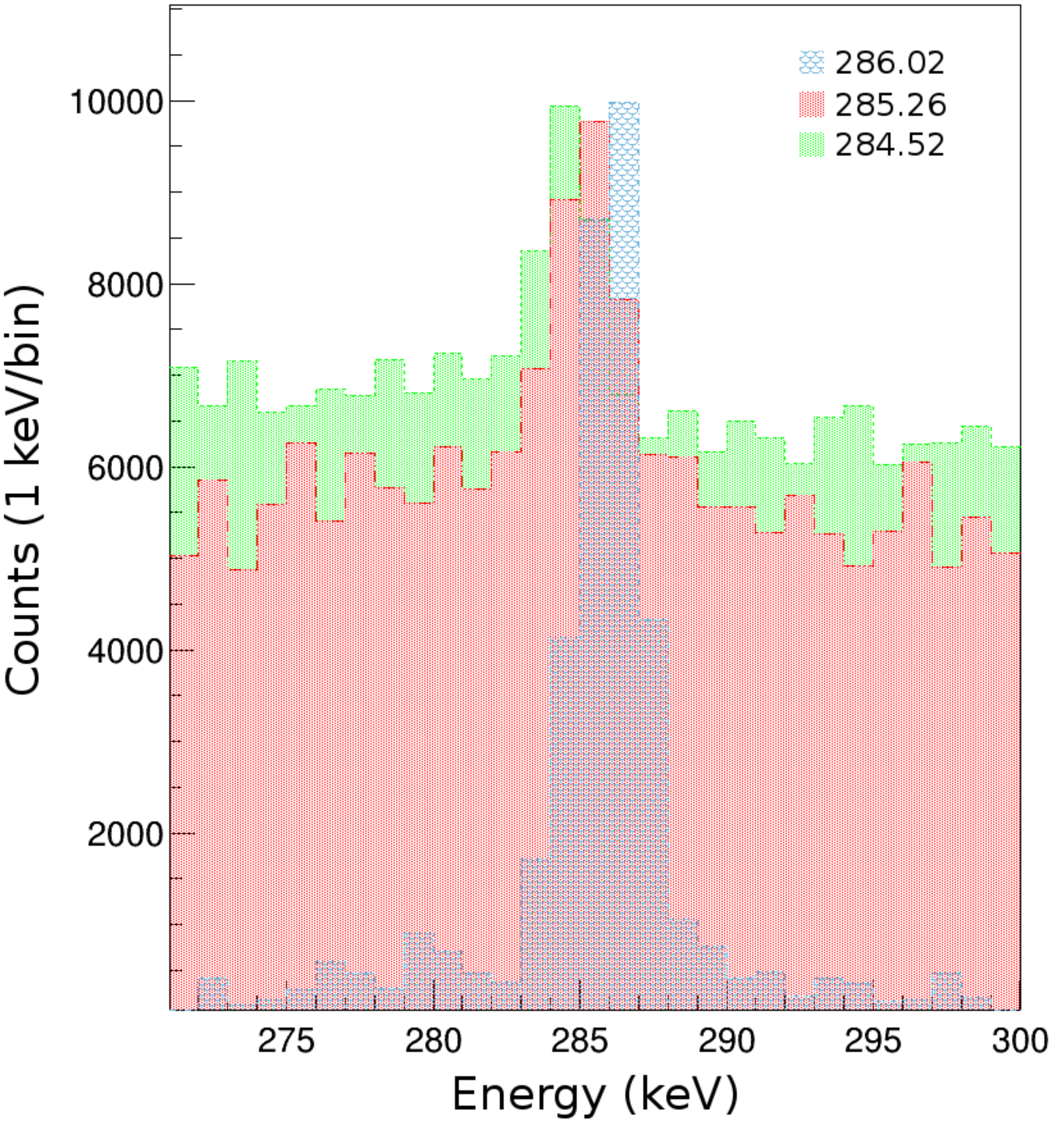

Figure 4.3: Overlay of the triplet showing the slight centroid shift from one gate to the next. The colours are described in Figure 4.2. The photopeaks are scaled to the projection with 284.5 keV making the counts arbitrary. The 286-keV peak is projected from a 2677-keV gate, the 285.26-keV peak is projected from a 635-keV gate, and the 284.52-keV peak is projected from a 446-keV gate.

sity. However, it is unclear how Raman measured the 1094.1-keV transition intensity as 0.805(20) without γ-γ coincidence.

Two placed transitions by Raman, 756-keV and 1116-keV, were assigned to a level at 3159 keV. Neither the transitions nor the level were observed in the present experiment.

Lastly, a 1733.56-keV transition from the 2963-keV level was not placed by Raman, but was placed in other β-decay studies [59,60,69]. A large fraction of the singles intensity in this photopeak is from the summed transitions of the 683-keV and 1050-keV γ-ray transitions. Taking summing corrections into account, the intensities were in good agreement with these other studies.

4.2.3 Logft Values and Spin Assignment

From the β-decay selection rules, there are some predictive qualities for determining the spin of a state that is populated in the daughter nucleus directly from the β-decay of the parent nucleus. The value used for determining the spin is the logft value and is discussed in Section 1.2. Furthermore, the γ-decay selection rules can also be applied to help with assigning a spin.

The measured logft values were determined using the NNDC LOGFT calculator [70]. First, the β-decay feeding intensity was calculated through an intensity balance of the total γ-ray intensity depopulating a level minus the total γ-ray intensity populating that level. The difference is then the amount of β-decay feeding to that level. For transitions less than 500 keV, the internal conversion coefficient was calculated to determine the missing intensity associated with the transition decaying via internal conversion. These were calculated using BrIcc Conversion Coefficient Calculator [71].

The calculated logft values, shown in Table 4.2, are in good agreement with the values in the nuclear datasheets [50]. The discrepancies in which the present values are greater than the literature values can be explained by the observation of more γ-ray transitions, and thus more intensity, feeding the levels. This leads to a lower β-decay intensity to the given states.

The majority of the levels populated directly through β-decay are assigned as 4^+ which is expected. Only five of these levels were previously unassigned spin—one of which is the newly observed 3397 keV level.

The 2878-keV level was previously given a spin of $J = (4,5,6^+)$. However, based on two studies [66,68], the suggested spin is a 5^-. This is in line with the calculated log$ft = 7.9(5)$ as well as the observation of only one transition from this state feeding the 4^+_1.

A newly identified level at 3397 keV was assigned a spin of $J = 4^+$ based on the log$ft = 6.70(3)$ as well as transitions feeding both 2^+ and 4^+ states.

The 3753-keV level was previously assigned a spin of $J = (4,5,6)$ by Raman. They identified only two transitions from this state feeding states with a spin of $J = 4^+$. In the present experiment, two more transitions both feeding 2^+ states suggest a spin of $J = 4^+$ which also is in line with the log$ft = 5.88(4)$.

The 3816-keV level was previously given a spin of $J = (1^+,2^+,3^+)$ with one ^{117}Sn(d,p)^{118}Sn study assigning it a $J = 2$ [72]. Based on the log$ft = 6.19(6)$ and the transitions depopulating this state feeding states with $J = 2^+,4^+$, it is assigned as a 4^+.

Table 4.2: The β feeding intensity, I_{β^-}, and $\log(ft)$ values obtained in the present experiment and compared to the Evaluated Nuclear Data File [50].

$5^+ \to J^\pi$	Energy [keV]	$I_{\beta^-}\%$	$\log ft$	$I_{\beta^-}\%$	$\log ft$
		This work		Ref. [50]	
4^+	2280.21	19.7(24)	5.92(6)	22(3)	5.83(6)
4^+	2488.59	10.24(20)	6.033(18)	8.5(4)	6.058(23)
4^+	2733.53	0.17(6)	7.58(16)	0.67(7)	6.90(4)
(5^-)	2878.4	0.065(6)	7.9(5)	0.066(11)	7.78(8)
2^+	2903.53	0.027(3)	10.08(6)	-	-
4^+	2963.04	66.2(8)	4.752(8)	62(3)	4.712(24)
6^+	2999.12	0.178(10)	7.28(4)	0.198(24)	7.17(6)
2^+	3056.88	0.0021(11)	10.84(22)	-	-
4^+	3374.10	1.17(3)	5.98(3)	1.51(8)	5.78(3)
4^+	3397.46	0.207(8)	6.70(3)	-	-
4^+	3460.21	0.98(3)	5.93(3)	0.90(8)	5.87(5)
4^+	3592.15	0.733(14)	5.83(4)	0.63(4)	5.79(4)
4^+	3704.34	0.398(10)	5.89(4)	0.294(16)	5.89(3)
4^+	3753.74	0.325(9)	5.88(4)	0.302(15)	5.77(3)
4^+	3816.19	0.117(6)	6.19(6)	0.092(7)	6.14(4)
4^+	3838.33	0.102(5)	6.19(5)	0.083(7)	6.13(5)

Lastly, the 3838-keV level was previously assigned a spin of $J = 4$ with out the parity. The $\log ft = 6.19(5)$ suggests there is no change in parity and the appropriate assignment is a positive parity state, $J = 4^+$.

4.2.4 Angular Correlations

While angular correlations can be used to determine the spin of a state, the statistics necessary in this experiment were insufficient for the unassigned states discussed in the previous section. However, angular correlations were performed for a selection of states with sufficient statistics to determine the mixing ratios (see Section 1.3.6 for more information) and compare them to the literature values.

The importance in determining the mixing ratio is related to understanding the transition probability for a specific radiation type ($E1, E2, E3..., M1, M2, M3...$ etc.) and, in the case of this study, the $B(E2)$ values. From the Weisskopf estimates discussed in Section 1.3.2, when allowed, an $E2$ transition will compete with an $M1$ transition. When calculating the $B(E2)$ value, the branching fraction of the $E2$ to the $M1$ is necessary:

$$b(E2) = \frac{\delta^2}{1+\delta^2} \tag{4.1}$$

where δ is the mixing ratio defined in Section 1.3.2. In this experiment, it was possible to measure the mixing ratio of five transitions shown in Table 4.3.

Table 4.3: The angular correlations made in this study are summarized by the transition gated on, $E_{\gamma 1}$, and the corresponding transition, $E_{\gamma 2}$, used to make the angular correlation (eg. Figure 5.10a).

$E_{\gamma 1}$ [keV]	$E_{\gamma 2}$ [keV]	$J_2 \to J_1 \to J_0$	χ^2_ν	δ	δ [50]
1230	813	$2^+_2 \to 2^+_1 \to 0^+_1$	1.39	-2.28(7)	-2.34(16)
	1098	$2^+_3 \to 2^+_1 \to 0^+_1$	0.86	-14(4)	56(31)[3]
	1173	$2^+_4 \to 2^+_1 \to 0^+_1$	1.21	0.85(3)	1.07(9)
1050	208	$4^+_2 \to 4^+_1 \to 2^+_1$	1.36	-0.19(4)	-0.17(4)
	683	$4^+_4 \to 4^+_1 \to 2^+_1$	0.427	0.224(6)	0.09(5)

The angular correlations require normalizing due to an unequal number of detector pairs that make up each of the angles as shown in Table 4.4. It is possible to obtain a normalized angular correlation using the detector weights listed for each angle. However, the efficiency and positions can vary slightly from detector to detector which is difficult to account for. A method called *event-mixing* is used, instead, to eliminate the need to establish individual detector efficiencies. This normalization method makes use of the time-random coincidences from which the uncorrelated γ-γ coincidence events that correspond to the angular correlation of interest are measured. The timing window for the event-mixed events was 1000–2000 ns whereas the true-coincident events had time differences of less than 320 ns. For the $4^+_1 \to 2^+_1 \to 0^+_1$ cascade (1050-keV → 1230-keV), the peak area of the 1050-keV are shown in Figures 4.4 and 4.5, for 1230-keV prompt and event mixed gates, respectively.

The 64 HPGe detectors provide 51 unique angle pairs between correlated γ-ray events (not including the 0° pair). The detectors are not point-like sources, and the distribution and efficiencies of the detectors are not the same from one detector to the next. These factors lead to an attenuation of the asymmetry that is observed in the angular distribution and have to be accounted for when determining the mixing ratios. Fitting an angular correlation (such as shown in the top plot in Figure 4.6) using Equation 1.50, the a_2 and a_4 coefficients that are determined are attenuated and need correcting.

The attenuation is energy dependent and the correction factors were obtained using values from Method 4 in the GRIFFIN angular correlation analysis techniques study [73]. This method takes advantage of the characterization of scaling parameters that were determined to have a smooth evolution with respect to the cascade γ-ray energies. While this method ultimately held true for the present experiment, the detector setup in their study did not include the Delrin shield which was used in the present experiment. A distinct set of simulations, which included the Delrin shield, were performed for several combinations of γ-ray energies as outlined in Method 2 to determine if the Delrin shield modifies the scaling parameters by any significant amount. The difference between these values were at most 1% which was below the uncertainty in the angular correlation fit parameters.

Table 4.4: The 52 angles between detector pairs of the 64 GRIFFIN HPGe crystals. The angle, in degrees, and the weights, which represent the number of detector pairs for the given angle, are listed.

Angle (degrees)	Weight	Angle (degrees)	Weight
0	64	91.5	128
18.8	128	93.8	48
25.6	64	93.8	64
26.7	64	97	64
31.9	64	101.3	64
33.7	48	103.6	96
44.4	128	106.9	64
46.8	96	109.1	96
48.6	128	110.1	64
49.8	96	112.5	64
53.8	48	113.4	64
60.2	96	115	96
62.7	48	116.9	64
63.1	64	117.3	48
65	96	119.8	96
66.5	64	126.2	48
67.5	64	130.2	96
69.9	64	131.4	128
70.9	96	133.2	96
73.1	64	135.6	128
76.4	96	146.3	48
78.7	64	148.1	64
83	64	152.3	64
86.2	64	154.4	64
86.2	48	160.2	128
88.5	128	180	64

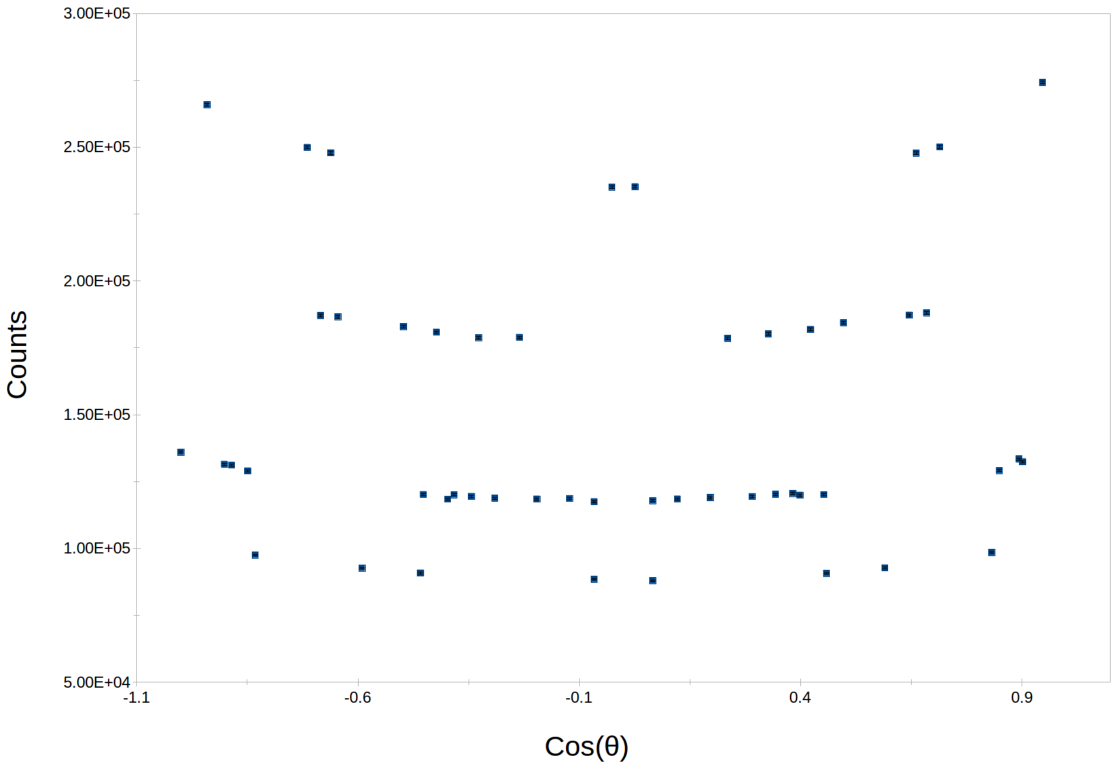

Figure 4.4: The number of true coincidence events in the peak area of the 1050-keV γ ray in prompt coincidence with the 1230-keV γ ray at each of the angles between detector pairs.

The angular correlations are fit for a series of mixing ratios, δ, by fixing the a_2 and a_4 parameters of Equation 1.52 to the theoretical values corresponding to each given mixing ratio. The theoretical a_2 and a_4 values are first scaled by the attenuation factors and the resulting χ^2 for each angular correlation is plotted with respect to δ. The minimum corresponds with the most likely δ value for the transition type.

In general, the experimental values agree with the literature values in the Nuclear Datasheets [50]. For each of the angular correlations presented in Table 4.3, the angular correlation plot and its corresponding χ^2 minimization plot are shown in Figures 5.10–4.10. The one value that differs greatly when considering the branching fraction is for the 683-keV γ-ray transition. The literature value of $\delta = 0.09(5)$ does show a large uncertainty, but still differs by more than two standard deviations from the present experimental measurement of $\delta = 0.224(6)$. The angular correlation and the χ^2 minimization plot to extract the mixing ratio is shown in Figure 4.10. When considering the $B(E2)$ value, the branching fraction from the measured mixing ratio is nearly six times greater than the literature value.

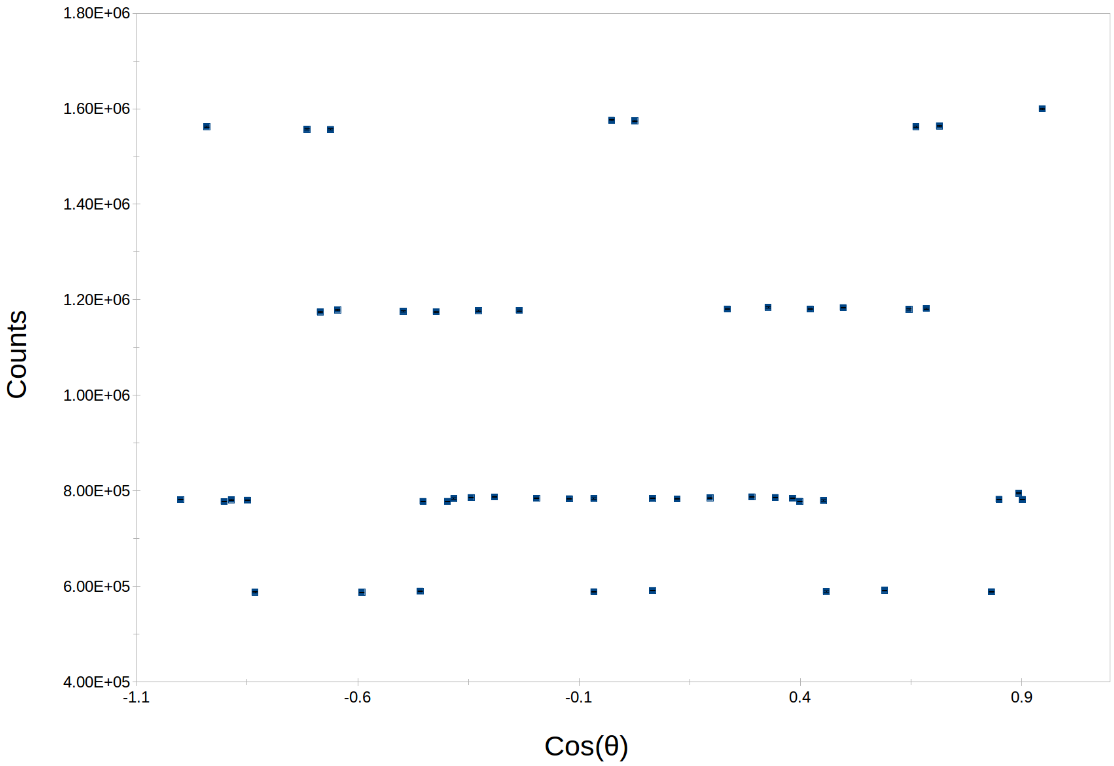

Figure 4.5: The number of uncorrelated events in the peak area of the 1050-keV γ ray in the event-mixing coincidence with the 1230-keV γ ray at each of the angles between detector pairs. These events are used to normlize the prompt events.

4.3 Theoretical Description

In previous studies on the intruder band in the ^{114,116}Sn isotopes [46, 74], interacting boson model, *sd* IBM-2, calculations with mixing were performed, by Dr. Mark Spieker, to compliment the experimental data and to better understand the degree of mixing between normal and intruder configurations. The '2' in IBM-2 indicates that protons and neutrons are treated separately, and the *sd* indicates that pairs of protons or pairs of neutrons couple to $J = 0$ and $J = 2$ for s-bosons and d-bosons, respectively [75]. The same theoretical approach used in their studies [46, 74] was applied to the ^{118}Sn results to help in characterizing certain low-lying states as normal or intruder. The specifics on the calculations and parameters are provided in Ref. [61] and the references within.

The IBM-2 parameters were adopted from Ref. [76] for the corresponding 0p-4h ^{114}Pd isotope [76]. This was done as the yrast band of the 0p-4h Pd isotopes has a similar $B(E2)$ strength to the 2p-2h intruder band in the Sn isotopes compared to the known 4p-0h Xe isotopes which have even greater $B(E2)$ strength. With these initial parameters in mind, subtle changes were made to ensure the low-lying energies and $B(E2)$ strengths were in line with experimental observations.

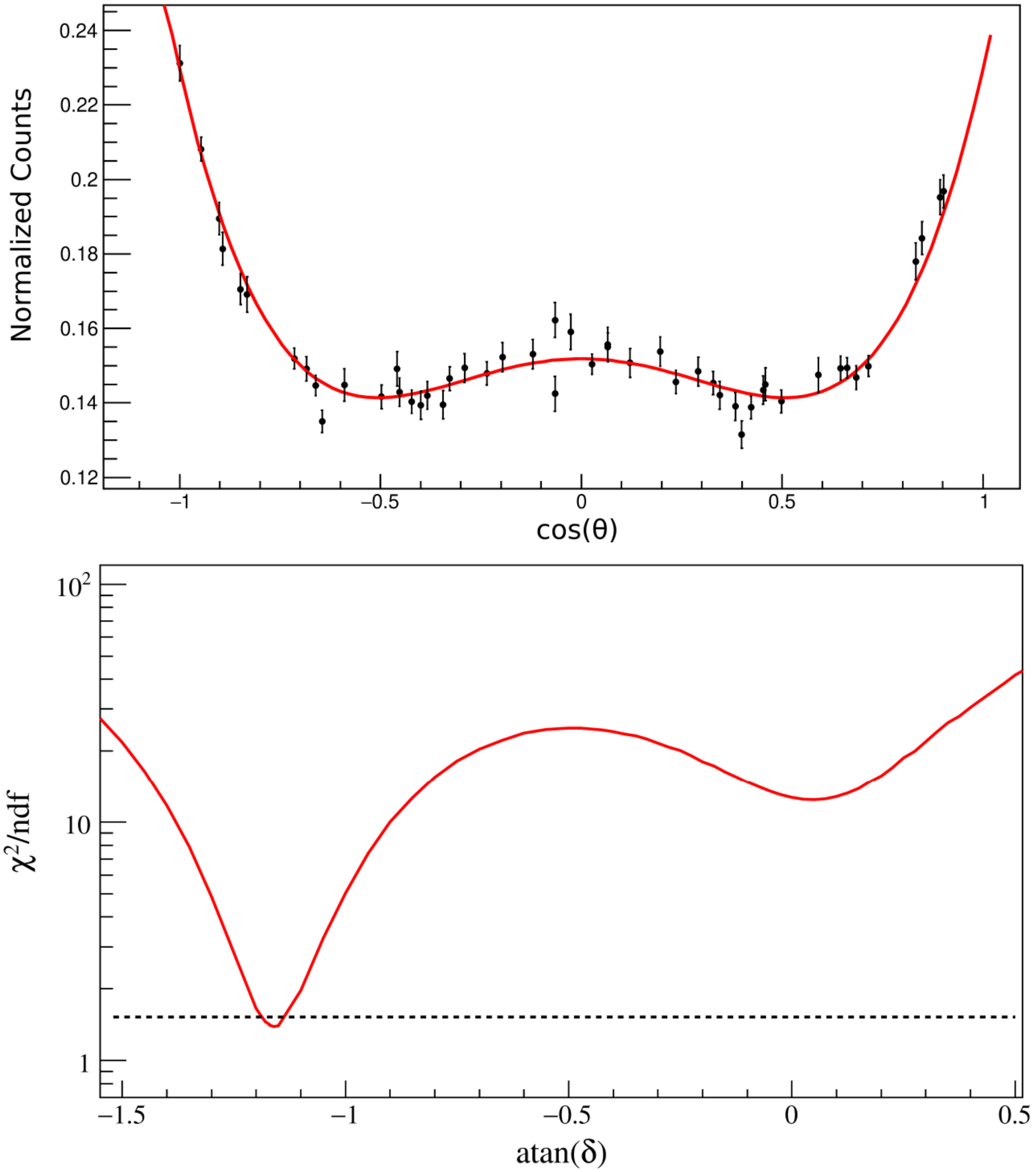

Figure 4.6: The measured angular correlation (top) of the $2_2^+ \rightarrow 2_1^+ \rightarrow 0_1^+$ transition which corresponds to a gate on the 1230 keV transition and the event-mixed-normalized peak area of the coincident transition, 813 keV from the 2043-keV, 2^+ level. This was performed for each of the 51 unique angles between detector pairs of the GRIFFIN array. The χ_ν^2 was 1.39 and the mixing ratio was determined with a χ^2 minimization plot (bottom) to be $\delta = -2.28(7)$.

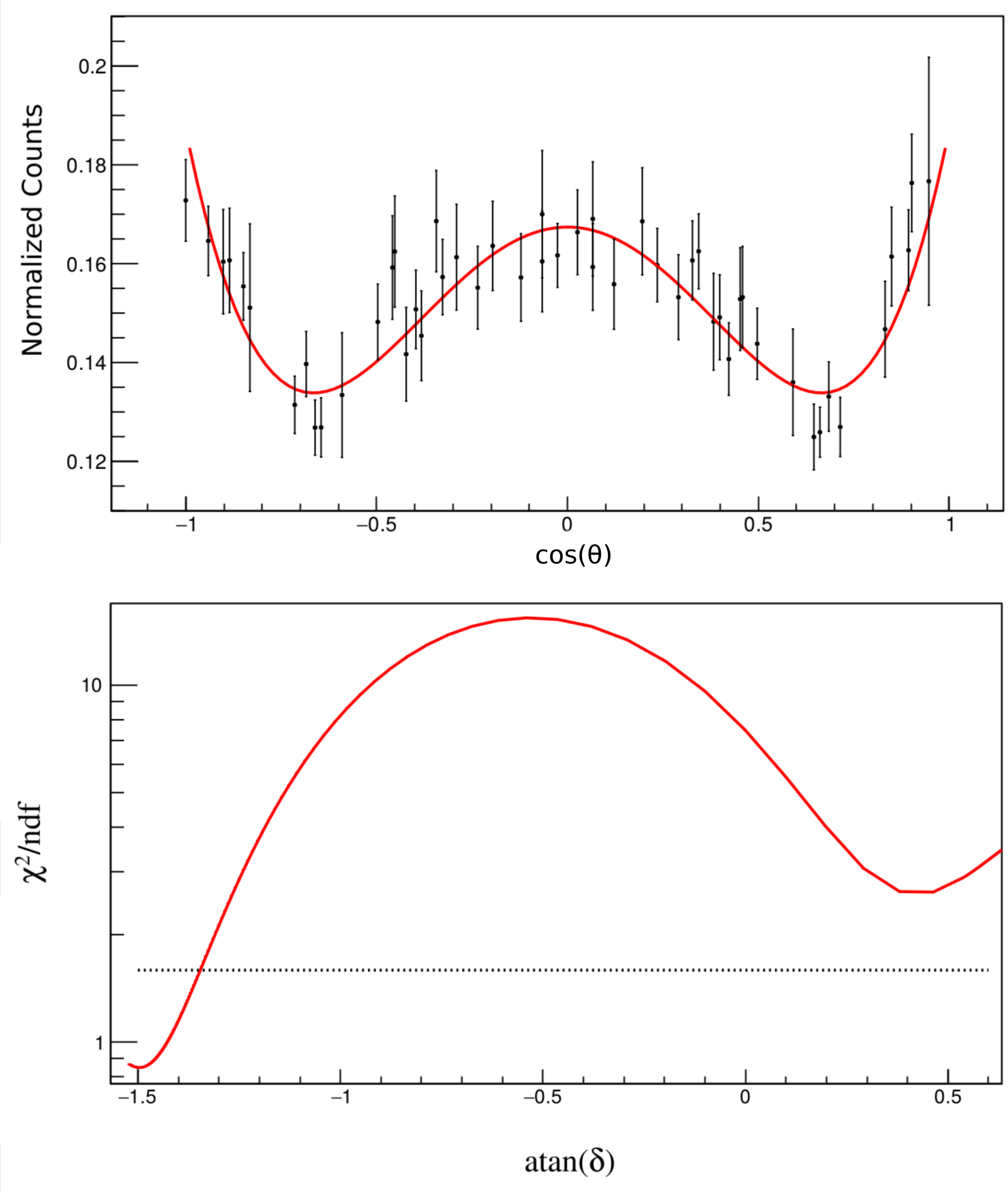

Figure 4.7: The measured angular correlation (top) of the $2_3^+ \rightarrow 2_1^+ \rightarrow 0_1^+$ transition which corresponds to a gate on the 1230 keV transition and the event-mixed-normalized peak area of the coincident transition, 1098 keV from the 2328-keV, 2^+ level. This was performed for each of the 51 unique angles between detector pairs of the GRIFFIN array. The χ_ν^2 was 0.86 and the mixing ratio was determined with a χ^2 minimization plot (bottom) to be $\delta = -14(4)$.

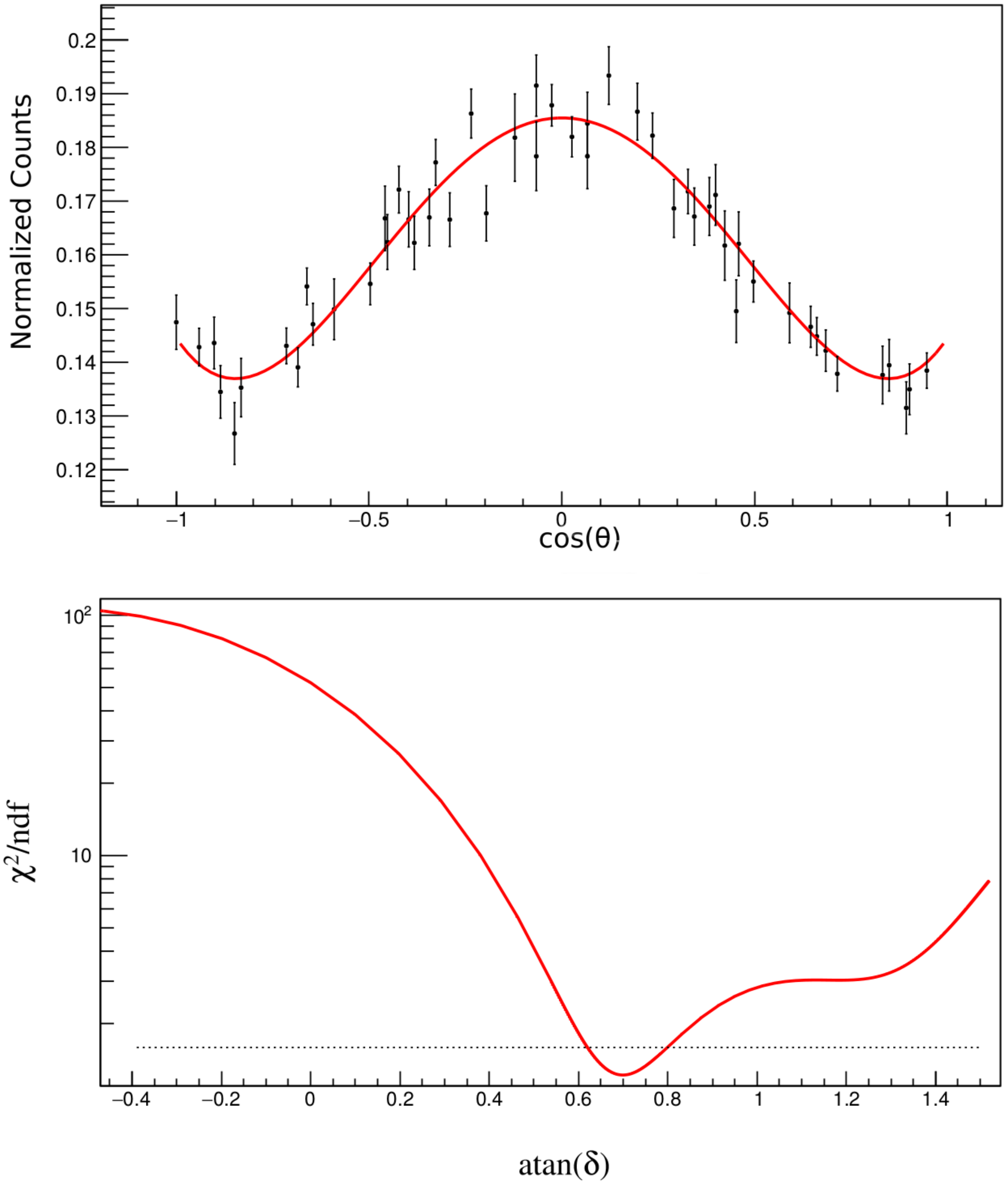

Figure 4.8: The measured angular correlation (top) of the $2_4^+ \rightarrow 2_1^+ \rightarrow 0_1^+$ transition which corresponds to a gate on the 1230 keV transition and the event-mixed-normalized peak area of the coincident transition, 1173 keV from the 2403-keV, 2^+ level. This was performed for each of the 51 unique angles between detector pairs of the GRIFFIN array. The χ_ν^2 was 1.21 and the mixing ratio was determined with a χ^2 minimization plot (bottom) to be $\delta = 0.85(3)$.

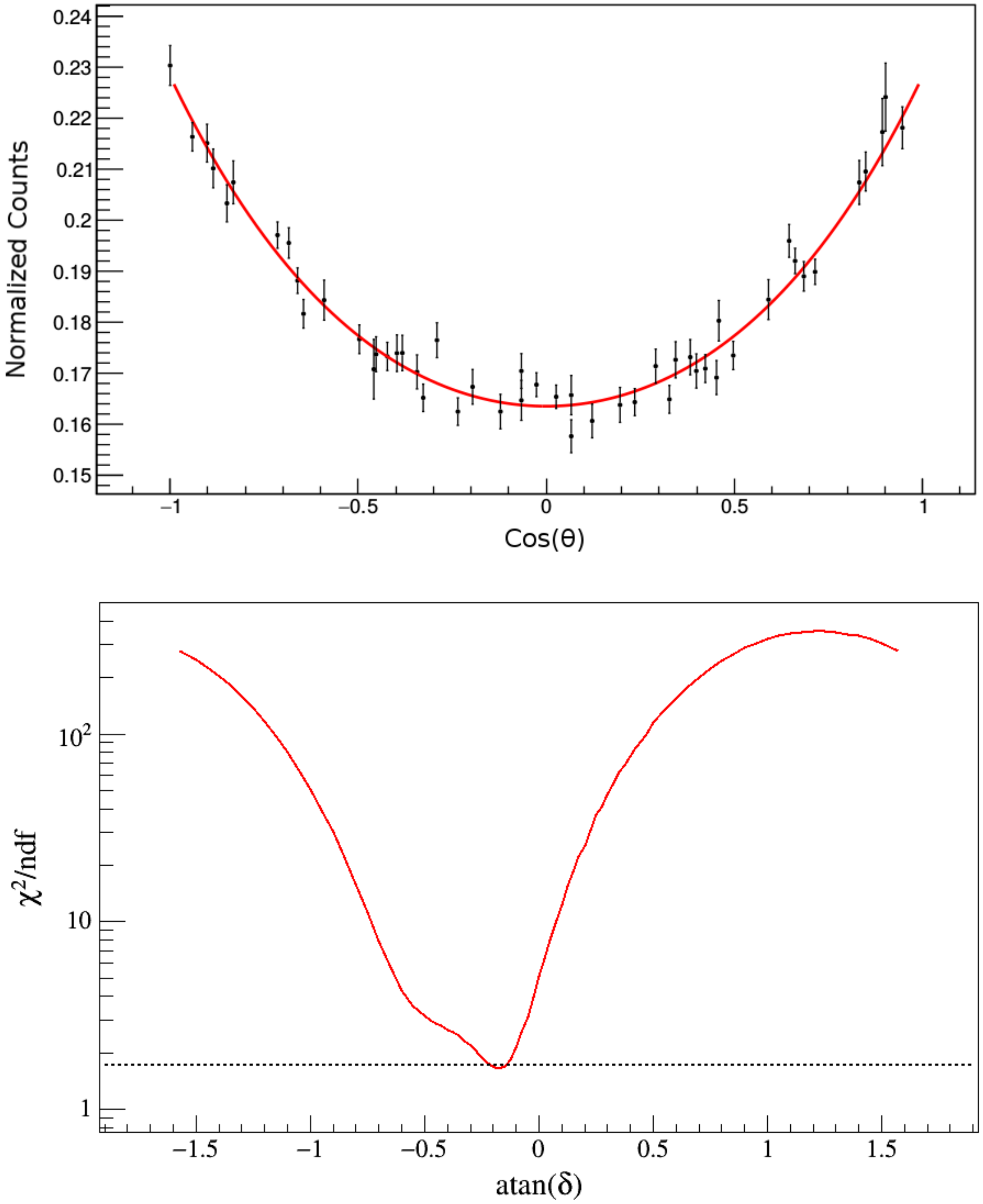

Figure 4.9: The measured angular correlation (top) of the $4_2^+ \rightarrow 4_1^+ \rightarrow 2_1^+$ transition which corresponds to a gate on the 1050 keV transition and the event-mixed-normalized peak area of the coincident transition, 208 keV from the 2488-keV, 2^+ level. This was performed for each of the 51 unique angles between detector pairs of the GRIFFIN array. The χ_ν^2 was 1.36 and the mixing ratio was determined with a χ^2 minimization plot (bottom) to be $\delta = -0.19(4)$.

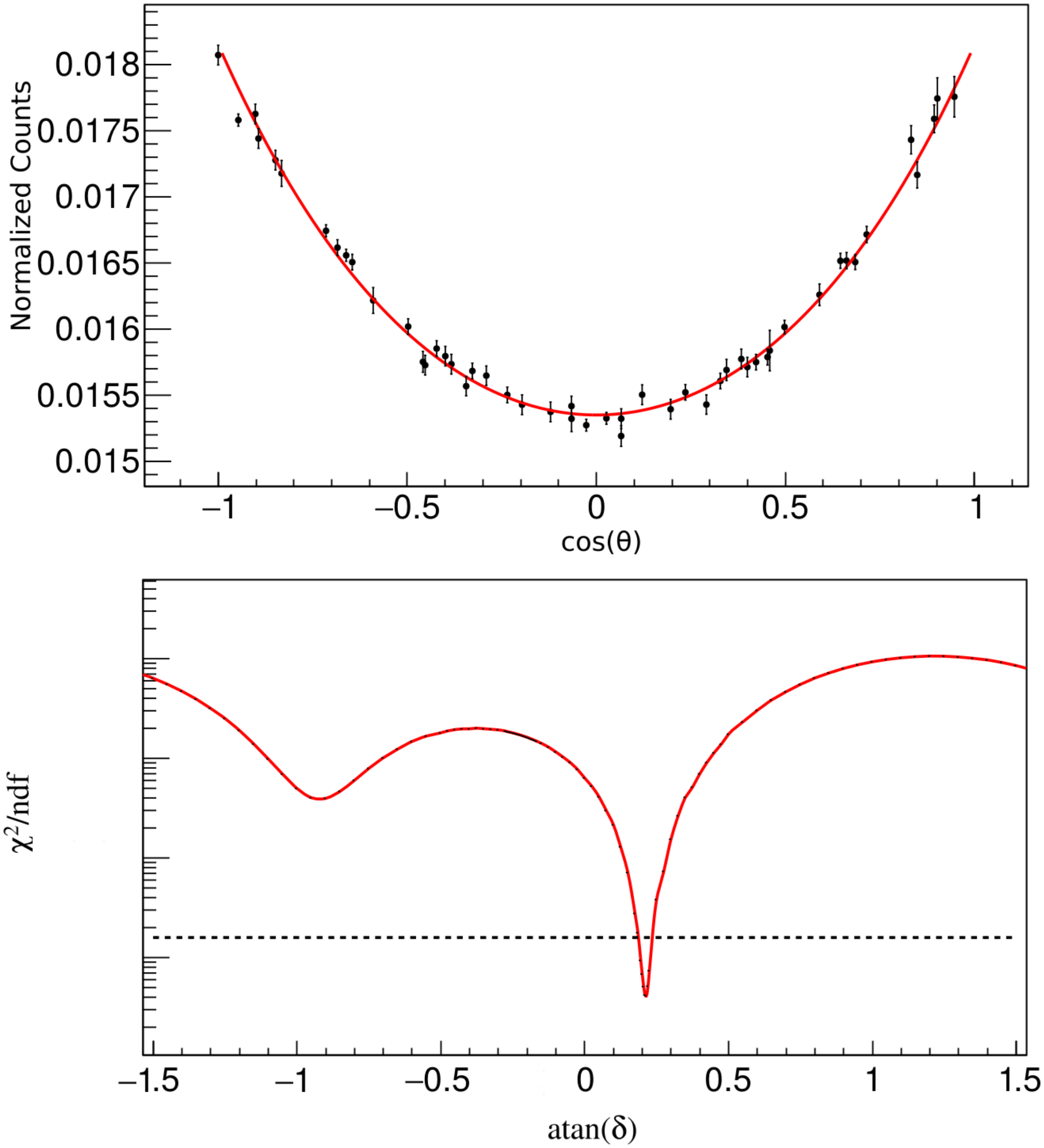

Figure 4.10: The measured angular correlation (top) of the $4_4^+ \rightarrow 4_1^+ \rightarrow 2_1^+$ transition which corresponds to a gate on the 1050 keV transition and the event-mixed-normalized peak area of the coincident transition, 683 keV from the 2963-keV, 2^+ level. This was performed for each of the 51 unique angles between detector pairs of the GRIFFIN array. The χ_ν^2 was 0.43 and the mixing ratio was determined with a χ^2 minimization plot (bottom) to be $\delta = 0.224(6)$.

As with the previous studies [46, 74], the results, shown in Table 4.5, highlight the difficulty in confining low-lying states to one specific configuration. Rather, many of the intruder states are highly mixed with the normal configuration, and vice versa.

The reassignment of the intruder bandhead in ^{116}Sn as the 0_3^+ [65] was not an expected result and the investigation of the intruder band in the present experiment, with support from the IBM-2 calculations, does not find the same result in ^{118}Sn.

Table 4.5: The *sd* IBM-2 calculations used to predict the energy and reduced $E2$ transition probabilities, $B(E2)$, for selected states are compared to the preset experimental values. The lifetimes and mixing ratios, δ, were taken from the ENSDF [50]. The suggested intruder states are indicated with #, whereas the states with normal configuration are marked with †.

$J_i^\pi \to J_f^\pi$	E_x [keV]	$E_{x,IBM}$ [keV]	$B(E2)_{exp}$ [W.u.]	$B(E2)_{IBM}$ [W.u.]
$2_1^+ \to 0_1^+$	1230	$1231^{\dagger}$	12.1(5)	10
$0_2^+ \to 2_1^+$	1758	$1714^{\#}$	19(3)	16
$2_2^+ \to 0_1^+$	2043	$2098^{\#}$	0.072(10)	0.008
$\to 2_1^+$			7.2(10)	0.13
$\to 0_2^+$			21(4)	35
$0_3^+ \to 2_1^+$	2057	$2099^{\dagger}$		10
$\to 2_2^+$				11
$4_1^+ \to 2_1^+$	2280	$2270^{\dagger}$	17(3)	19
$\to 2_2^+$			16(3)	18
$2_3^+ \to 0_1^+$	2328	$2256^{\#}$	< 0.19	0.00010
$\to 2_1^+$			< 42	16
$\to 0_2^+$			< 26	0.5
$\to 2_2^+$			< 762	29
$2_4^+ \to 0_1^+$	2403	$2728^{\dagger}$	0.0025(11)	0.0002
$\to 2_1^+$			17(7)	4
$\to 0_2^+$			12(5)	0.05
$\to 2_2^+$			< 81	26
$\to 2_3^+$				0.6
$4_2^+ \to 2_1^+$	2489	$2702^{\#}$	< 2.5	1.2
$\to 2_2^+$			< 764	39
$\to 4_1^+$			< 673	0.3
$4_3^+ \to 2_1^+$	2733	$2903^{\#}$	4^{+5}_{-4}	0.014
$\to 2_2^+$			3(3)	0.09
$\to 4_1^+$			100^{+120}_{-100}	19
$\to 2_3^+$				28
$\to 4_2^+$				12
$6_1^+ \to 4_1^+$	3000	$3034^{\#}$		42
$\to 4_2^+$				20

4.4 Discussion

The β-decay of the 5^+ isomer in ^{118}In proved to be a successful experiment in populating the low-lying states of the intruder band that give rise to shape coexistence. With the use of the GRIFFIN spectrometer, 43 transitions, from the 99 that were observed, are newly identified. Furthermore, one level, from the 23 observed, was newly identified to be directly populated from the β-decay.

Of interest, the discrepancies between the previously identified 284.5 keV [66] and 285.3 keV [58] and their reported intensities have been corrected with the γ-γ-coincidence technique to isolate what turned out to be a triplet—284.5 keV, 285.3 keV, and 286.0 keV. The importance of resolving the intensities of these transitions is related to the $B(E2)$ value of the 284.5 keV transition which originates from the 2_2^+ intruder state. The reduction in intensity from 39(7) W.u. to 21(4) W.u. suggests less collectivity, although this is not entirely supported in the IBM-2 calculations. The $B(E2)$ strength of the 2_2^+, however, could be fragmented with the $2_{3,4}^+$ states.

Generally, the comparisons of the present experiment with the IBM-2 calculations are in good agreement. There is support for keeping the 0_2^+ as the intruder bandhead, unlike the reassignment of 0_3^+ in ^{116}Sn as the intruder bandhead. The strong mixing that is observed between the similar states makes it difficult to give structure labels to many of the states with confidence. To further the conversation of configuration mixing in ^{118}Sn, more lifetime measurements are necessary as well as the mixing ratios that angular correlations can provide.

Chapter 5

Thermal Neutron Capture Results

The thermal neutron capture experiment, ^{117}Sn$(n,\gamma)^{118}$Sn, was successfully performed at the Institut Laue-Langevin (ILL) at which a collimated thermal neutron beam with a flux of 1×10^8 n cm^{-2} s^{-1} bombarded a 300 mg, 92.8% isotopically enriched ^{117}Sn target. Thermal neutrons are defined as having, on average, the kinetic energy corresponding with the ambient room temperature, $T =$ 290 K, such that $kT = 0.025$ eV [1]. The absorption cross section for thermal neutrons on ^{117}Sn is 1.3(2) b [77]. Of the target's remaining 7.2%, the dominant reactions were neutron captures on the ^{115}Sn and ^{119}Sn isotopes which have 0.34% and 8.59% natural abundances due to the large thermal neutron capture cross sections of 30(7) b and 2.2(5) b, respectively [77]. However, these only amounted to approximately 0.8% and 1% of the total events and were not of significance in the γ-ray analysis.

The neutron capture reaction ran for two and a half days and populated states in ^{118}Sn at the neutron separation energy of 9.326 MeV [50]. A total of 3×10^{10} γ-γ coincidence events were recorded with the FIPPS array. Similarly to the β-decay analysis with GRIFFIN, only the addback events were used in the γ-singles and γ-γ coincidence analysis.

5.1 Thermal Neutron Capture

Thermal neutron capture experiments directly populate excited states at the neutron separation energy, S_n, from which subsequent γ-decay can populate many energy levels within a narrow spin and parity range, and without preference for structure [2]. Neutron capture can be considered as a reaction which yields a compound nucleus that decays to some final state,

$$^{A}X + n \rightarrow {}^{A+1}X^{*} \rightarrow \text{final state.} \tag{5.1}$$

The compound nucleus, $^{A+1}X^{*}$, is simply the target nucleus, ^{A}X, plus the neutron, n, and its binding energy which is effectively the separation energy (there is some negligible recoil energy as well) [78]. This process, shown in Figure 5.1, makes for an excellent study to the understanding of nuclear structure as the decay of the compound state to the ground state is typically by way of intermediate states [79]. Furthermore, this offers a nearly complete level scheme within the confines of the γ-decay selection rules [1].

The energy of thermal neutrons is $\approx$0.025 eV, at which neutron capture most frequently occurs, and at these low energies, only neutrons with zero orbital angular momentum, $l = 0$, (called s-waves) need to be considered. This implies that the capture state, which can be thought of a continuum of unresolvable individual states of the compound nucleus [1], can be formed by coupling the ground spin of the target nucleus, J_A, to the intrinsic spin of the neutron, $s = \pm\frac{1}{2}$. The parity in s-wave capture remains unchanged in the capture state to that of the target's ground state. Provided the target's ground state spin and parity is known, the capture state's spin and parity, J_{A+1} and π, are given by,

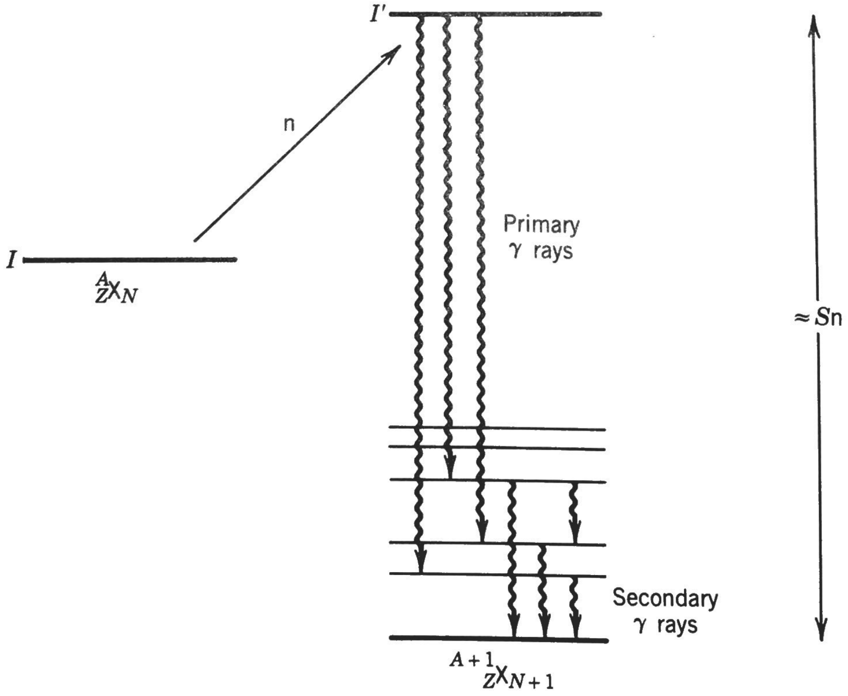

Figure 5.1: Thermal neutron capture on a target $^{A}_{Z}X_N$ populates a capture state at the neutron separation energy, S_n, in the $^{A+1}_{Z}X_{N+1}$ nucleus. The emission of primary γ rays, and subsequent secondary γ rays are shown. Note that angular momentum is given as I, rather than J in this figure. Reprinted with permission from Reference [1].

$$J_{A+1} = J_A \pm \frac{1}{2}, \tag{5.2}$$

and

$$\pi_{A+1} = \pi_A, \tag{5.3}$$

respectively.

From the γ-decay selection rules, expectations of the transition type can be made. For instance, the most probable electromagnetic radiation types, according to the single particle estimates, are electric and magnetic dipole, $E1$ and $M1$, transitions. Magnetic dipole radiation is about 100 times less likely than electric dipole, but should still be considered [1]. Thus, constraints can be placed on the values of J^{π} that can be populated from the primary γ rays which originate from the capture state without knowledge of the configuration of these states. However, secondary γ ray transitions will inevitably populate lower-lying states based on structure, as well as the selection rules.

In the present experiment, the target, ^{117}Sn has a ground state spin and parity, $J^{\pi} = \frac{1}{2}^{+}$, yielding a capture state in ^{118}Sn of 0^{+} or 1^{+}. Based on this information, primary transitions to states with $J = 0, 1,$ and 2 with either + or - parity were expected.

5.2 Literature Review

As with the present β-decay study of ^{118}In discussed in Section 4, review of previous studies on the Sn isotopes, as well as neighbouring nuclei, were necessary to realize the opportunity to identify exciting phenomena in ^{118}Sn via thermal neutron capture. Particularly of interest are states belonging to a collective quadrupole resonance-like mode which were theoretically predicted to occur in the even-even Sn isotopes in the 3–5 MeV range [80]. Many newly-observed levels were placed in this energy region and will be discussed in the subsequent sections. Furthermore, low-lying $J = 0^{+}$ states were populated and the mixing between these states has importance to shape coexistence, which was explored in the β-decay study presented in Section 4.

5.2.1 Resonances in Nuclei — Pygmy Quadrupole Resonances

Resonances in nuclei have been known to exist since the 1940s when the description of the GDR as a dipole oscillation of the protons against the neutrons was first made and the near-Lorentzian shape of the resonance was established [81]. These GDR excitations exist above the particle separation energies and exhaust nearly 100% of the energy-weighted sum rule (EWSR) for isovector electric dipole ($E1$) transitions. The EWSR is approximately

$$\int_{0}^{\infty} \sigma(E)dE \;=\; 60\frac{NZ}{A}\text{MeV mb} \tag{5.4}$$

where σ is the GDR cross section for a given reaction in units of millibarns (mb), energy, E is in MeV and N, Z, and A are the neutron, proton and mass numbers, respectively [82]. Any remaining $E1$ strength not attributed to the GDR would then be rather small and the term Pygmy Dipole Resonances (PDR) was first designated in 1969 [83]. Now, low-lying dipole states below the GDR, forming a resonance-like structure, are a common feature of nuclei with neutron excess and have a strength of a few percent of the EWSR [8]. Many theoretical and experimental works since the 1970s have shown the existence of PDR states below the separation energy [9, 81, 82, 84] and have been described as neutron skin oscillations against a proton-neutron core [12, 80].

The description of the PDR is still debated as there seems to be questions pertaining to the collectivity of these states. Macroscopic models imply a collective behaviour of the nucleons, and microscopic models conclude two modes—a higher-lying isovector-dominant mode that is not as collective as a lower-lying isoscalar-dominant mode [8]. The lower-lying part is thought as the "real PDR", being distinct from the GDR [10]. An unclear understanding on the isospin mixing of the PDR makes the simplistic picture of a neutron skin oscillation not entirely realistic, yet prompts the question of higher multipolarities such as quadrupole states.

A higher multipolarity Pygmy Quadrupole Resonance (PQR) was proposed based on the description of the PDR as an oscillating neutron skin that gives rise to a grouping of $J = 1^-$ electric dipole states below the neutron separation energy. It was theoretically predicted that the PQR region lies between 3–5 MeV as a grouping of $J = 2^+$ states [80]. Since, two recent studies on ^{112,114}Sn [11] and ^{124}Sn [12] have identified a resonance-like structure of 2^+ states in the 3–5 MeV region, believed to be attributed to the PQR. In these studies, theoretical calculations were also performed (energy-density functional and three-phonon quasiparticle-phonon model theory). With support from the experimental data, the theoretical calculations suggest a low-energy quadrupole mode occurring as a quadrupole-type oscillation of the neutron skin. Similarly to the PDR, an isoscalar-dominant mode at lower-lying energies is observed to be separate from a higher-lying isovector-dominant mode. This splitting is based on the observation of lower-lying PQR states predominantly populated in hadronic scattering which favours the excitations of the surface modes, whereas both low-lying and high-lying states were observed with nuclear resonance fluorescence (NRF) which primarily populates $J = 1^-, 1^+$ and 2^+ states [11, 12, 84]. This gives reason to believe the lower-lying PQR states (and PDR states for that matter) are a result of surface oscillations. Furthermore, one possible signature of the PQR states identified in these studies is an enhanced ground-state branching ratio, shown in Figure 5.2 and 5.3.

The branching ratio of the γ decay to the ground state is defined as

$$b_0 = \Gamma_0/\Gamma, \tag{5.5}$$

where Γ_0 is the ground-state decay intensity and Γ is the total intensity observed to decay from the level of interest. For example, $b_0 = 1$ would indicate only the ground-state decay is observed, whereas $b_0 = 0.5$ would mean half of the total decay is directly to the ground state.

To populate $J = 2^+$ states in ^{118}Sn that could be part of the PQR, thermal neutron capture was performed for its unbiased population of various nuclear structure. The capture state is a continuum of predominantly $J = 1^+$ states that were expected to populate low spin states, including $J = 2^+$. The levels populated in the 3–5 MeV region of interest were measured for their ground-state branching ratio as a means to compare to the previous studies on the ^{112,114,124}Sn isotopes. These results are shown and discussed in the following sections.

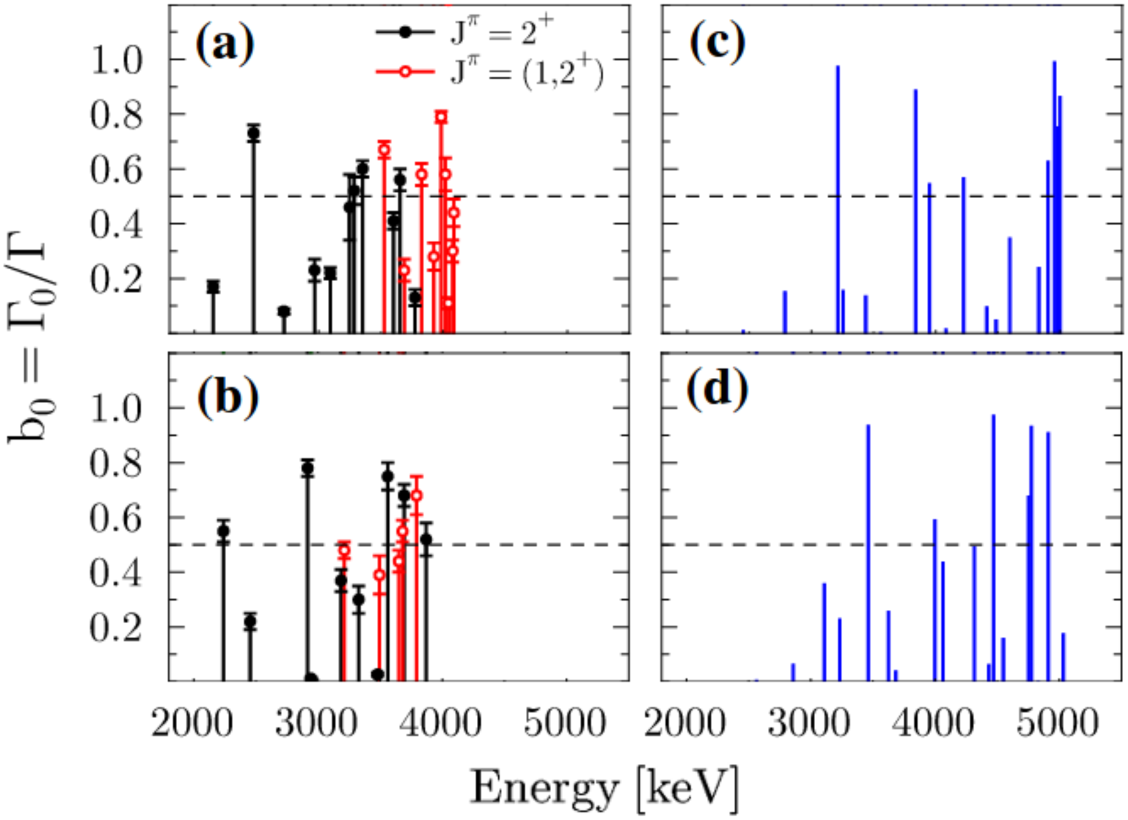

Figure 5.2: The experimental absolute ground-state branching fraction of 2^+ states (black) and tentatively assigned (1, 2^+) states (red) in the proposed PQR region for ^{112}Sn (a) and ^{114}Sn (b). The blue lines in (c) and (d) are theoretical predictions using energy-density functional (EDF) and three-phonon quasiparticle-phonon model (QPM) which show a good agreement in reproducing the *E*2 distributions. These enhanced ground-state branching ratios are a potential signature of the PQR states. Adapted, with permission from Reference [11].

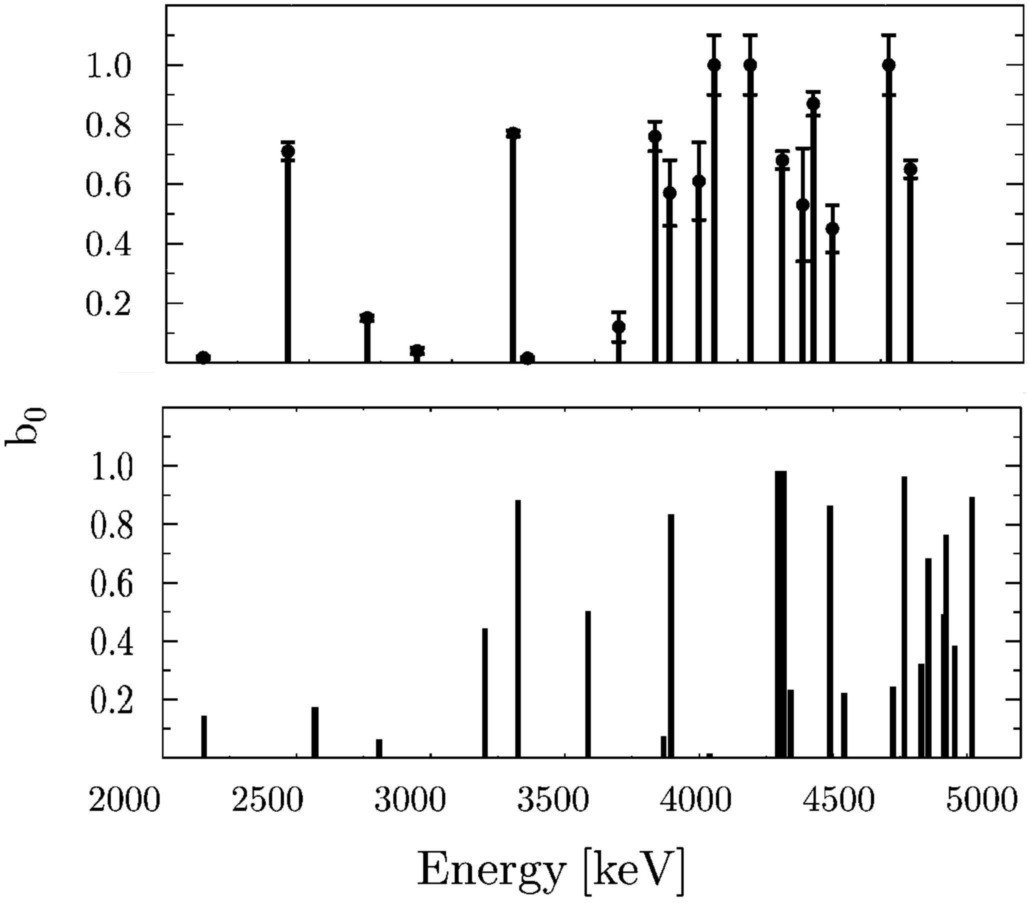

Figure 5.3: The same as Figure 5.2 with the experimental absolute ground-state branching fraction of 2^+ states (top) for ^{124}Sn. The theoretical QPM (bottom) calculations similarly show good agreement in the ground-state feeding and $E2$ distributions. Adapted, with permission from Reference [12].

5.2.2 Low-Lying 0^+ States

While the topic of PQR was the main motivating factor in running the neutron capture experiment, observations of low-lying $J = 0^+$ states were expected and also explored. The $E0$ transitions between 0^+ states are not observed with γ-ray spectroscopy as indicated in Section 1.3. However, indirect measurements of the $E0$ transition strength can be made with the right circumstances as described in Reference [21] and the references within. In the case that an excited 0^+ state decays to both a 0^+ and a 2^+ (example in Figure 5.4), a quantity relating the intensities of the $E0$ and $E2$ K-conversion electron components ($I_K(E0)$ and $I_K(E2)$, respectively) can be measured:

$$q^2(E0/E2) = \frac{I_K(E0)}{I_K(E2)}. \tag{5.6}$$

The value obtained can be used to calculate a ratio of the $E0$ to the $E2$ reduced transition probabilities,

$$X(E0/E2) = 2.54 \times 10^9 A^{4/3} \times q^2(E0/E2) \times \frac{\alpha_K(E2)}{\Omega_K(E0)} \times E_\gamma^5, \tag{5.7}$$

where $\alpha_K(E2)$ is the K-conversion coefficient for the $E2$ transition and $\Omega_K(E0)$ is the electronic factor for the K-conversion electron of the $E0$ transition. The ratio is defined as:

$$X(E0/E2) \equiv \frac{B(E0)}{B(E2)} = \frac{\rho^2(E0)e^2R^4}{B(E2)}. \tag{5.8}$$

As previously mentioned, $\rho^2(E0)$ values are related to the decay probability and are of importance to the understanding of shape coexistence. Where the $B(E2)$ values are a measure of deformation, enhanced $\rho^2(E0)$ values for $J_i = J_f = 0$ indicate a mixing of configurations with different mean square charge radii [4]. Thus, providing a measure of shape coexistence. Observations of $E0$ transitions require conversion electron detectors, such as the Pentagonal Array for Conversion Electron Spectroscopy (PACES) used with GRIFFIN [30] which were not used in either of the present experiments. Furthermore, the lifetime of the states are necessary to obtain the $\rho^2(E0)$ values which are often lacking in the current experimental information. It is noted that since $\rho^2(E0)$ values are often on the order of 10^{-3} to 10^{-1}, the value reported is $10^3 \times \rho^2(E0)$.

The 0^+ state in ^{118}Sn that has been investigated for $E0$ transition strength in the present experiment is the 2057-keV level which was populated directly from the neutron capture state via a 7269-keV γ-ray transition. The 2057-keV level decays by a pure $E2$ transition of 827 keV and feeds the first excited 2^+ at 1230 keV (shown in Figure 5.4). An $E0$ transition of 299 keV to the second 0^+ at 1758 keV has been previously identified [85] and the lower limit of the $10^3 \times \rho^2(E0)$ is 36 [21]. The lower limit is due to an upper limit on the half-life of 200 ps for the 2057-keV level [86]. A more recent measurement placed a lower limit of 0.7 ps on the half-life [87]. However, this is likely too small since the $10^3 \times \rho^2(E0)$ is inversely proportional to the half-life and 0.7 ps would give a $10^3 \times \rho^2(E0)$ of over 10000. For example, the neighbouring ^{116}Sn has a half-life of 160(20) ps for the third 0^+ and a $10^3 \times \rho^2(E0)$ of 86(16) for the 271 keV $E0$ transition to the second 0^+ [21]. The

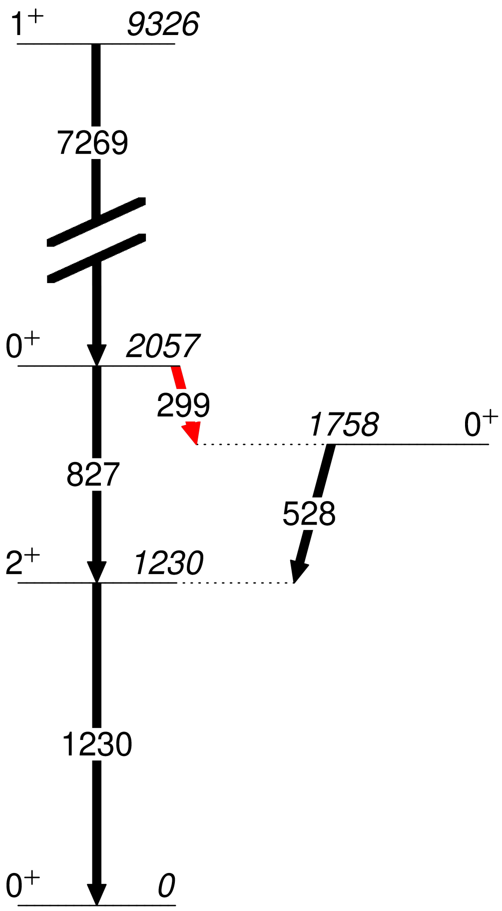

Figure 5.4: A partial level scheme showing the first two excited 0^+ states and the γ-ray transitions (black) and an unobserved $E0$ transition (red) which connects the 0^+ states via internal conversion decay. The intensity of the 299-keV $E0$ is determined from gating above on the 7269-keV transition and assuming any amount of 528 keV is due to the number of 299-keV events.

measurement of the $E0$ transition strength between the 2057-keV, 0_3^+ state and the 1758-keV, 0_2^+ state is described in the following section and discussed with respect to previous values.

5.3 γ-ray Analysis

The γ-decay observed in the ^{117}Sn(n,γ) reaction originated from the capture state of the compound nucleus, ^{118}Sn. From the capture state, 75 primary γ-ray transitions were identified populating 74 excited states and the ground state. There were 349 secondary transitions observed for a total of 424 γ-ray transitions. Of the total observed, 358 were newly placed to the level scheme. Furthermore, 96 energy levels were identified with 46 being newly placed to the level scheme. These findings are listed, along with their relative intensities and branching ratios, in Table 5.1.

Table 5.1: Observed levels and transitions from the present ^{117}Sn$(n,\gamma)^{118}$Sn experiment. Levels were fit to the energies of the γ-ray transitions to establish the energies with the recoil energy taken into account. The energies in bold are the newly placed transitions and levels which are not in the current evaluation from the ENSDF [50]. Note that the transitions originating from newly placed levels are not in bold. Spins of newly placed states are given based on γ-decay selection rules. Branching ratios are compared to a previous high-statistics study involving β decay of the 5^+ isomer of ^{118}In [61].

E_{level} (keV)	J_i^π	J_f^π	E_γ (keV)	I_γ	BR_γ	BR_γ [61]
1229.50(7)	2^+	0^+	1229.7(3)	100	100	100
1758.08(9)	0^+	2^+	528.9(3)	6.5(2)	100	100
2042.67(8)	2^+	0^+	284.5(3)	0.12(3)	1.1(3)	1.31(17)
		2^+	813.3(3)	11.3(4)	100(3)	100.0(23)
		0^+	2042.9(3)	8.3(3)	74(3)	83.6(26)
2056.66(9)	0^+	2^+	827.3(3)	5.26(18)	100	
2280.23(14)	4^+	2^+	1050.7(3)	5.31(17)	100	100
2321.1(2)	5^-	4^+	41.0(3)	-	100(3)	
		2^+	1091.5(3)	-	8.6(9)	
2324.77(10)	3^-	2^+	1095.2(3)	9.1(3)	100	100(5)
2327.82(9)	2^+	2^+	285.2(3)	0.156(19)	1.69(20)	2.3(8)
		0^+	569.6(3)	0.255(12)	2.76(13)	
		2^+	1098.4(3)	9.2(3)	100(4)	100(4)
		0^+	2328.0(3)	1.52(8)	16.6(8)	19.1(8)
2403.01(9)	2^+	2^+	360.4(3)	0.102(9)	1.29(12)	0.91(13)
		0^+	644.8(3)	0.108(9)	1.36(11)	
		2^+	1173.7(3)	7.9(4)	100(4)	100.0(26)
2488.57(14)	4^+	4^+	208.6(3)	0.372(13)	47.3(16)	60.3(12)
		2^+	446.0(3)	0.79(5)	100(6)	100.0(22)
		2^+	1259.1(3)	0.54(9)	69(12)	59.2(16)
2496.78(12)	0^+	2^+	1267.6(3)	2.55(11)	100	
2677.20(10)	2^+	2^+	**274.2(3)**	0.073(5)	2.8(2)	
		2^+	**349.4(3)**	0.063(8)	2.4(3)	
		0^+	620.5(3)	0.016(4)	0.62(17)	
		0^+	918.8(3)	0.108(9)	4.1(3)	
		2^+	1447.7(3)	2.36(9)	90(5)	87(6)

Continuation of Table 1

E_{level} (keV)	J_i^π	J_f^π	E_γ (keV)	I_γ	BR_γ	BR_γ [61]
		0^+	2677.3(3)	2.61(13)	100(5)	100(6)
2733.6(3)	4^+	2^+	1504.1(3)	0.92(4)	100	
2737.89(10)	1^+	2^+	**410.0(3)**	0.41(3)	9.4(6)	
		0^+	**979.7(3)**	0.020(6)	0.46(14)	
		2^+	1508.4(3)	4.37(16)	100(4)	
		0^+	2738.0(3)	1.30(11)	30(2)	
2773.92(17)	4^-	3^-	449.1(3)	0.323(14)	42.1(18)	
		5^-	452.8(3)	0.77(3)	100(4)	
2903.78(11)	2^+	0^+	**846.8(3)**	0.017(7)	0.6(2)	
		2^+	**861.0(3)**	0.125(19)	4.4(7)	
		2^+	1674.2(3)	0.99(6)	35(2)	67(7)
		0^+	2903.9(3)	2.83(14)	100(5)	100(7)
2929.6(3)	0^+	2^+	**886.9(7)**	0.095(14)	11.6(17)	
		2^+	1700.1(3)	0.82(8)	100(9)	
2963.25(18)	4^+	4^+	474.6(5)	0.019(9)	5(2)	5.26(16)
		2^+	559.9(3)	0.011(5)	2.8(11)	1.97(4)
		2^+	635.9(4)	0.026(7)	6.4(16)	2.94(7)
		3^-	638.5(4)	0.013(4)	3.1(11)	2.72(6)
		4^+	683.1(3)	0.406(9)	100(2)	100.0(23)
3057.15(17)	2^+	0^+	**1298.5(3)**	0.181(6)	13.0(4)	
		2^+	1827.4(3)	0.315(3)	22.7(18)	
		0^+	3057.2(3)	1.39(9)	100((7)	
3089.3(4)	$(5)^+$	4^+	809.0(3)	0.359(7)	100	
3137.35(3)	0^+	2^+	1907.7(3)	0.85(6)	100	
3215.87(18)	(0^+)	2^+	888.3(3)	0.31(2)	74(5)	
		2^+	1173.6(3)	0.33(3)	78(7)	
		2^+	1986.7(3)	0.42(4)	100(9)	
3228.27(14)	2^+	2^+	**550.9(3)**	0.086(7)	7.5(6)	
		3^-	**903.3(3)**	0.138(5)	12.00(4)	
		0^+	**1171.7(3)**	0.18(3)	15(2)	
		2^+	**1185.5(3)**	0.191(13)	16.6(11)	
		2^+	**1998.1(3)**	0.82(8)	71(7)	
		0^+	3228.3(5)	1.15(6)	100(5)	
3262.33(19)	3^+	4^+	**773.5(3)**	0.017(6)	2.2(7)	
		4^+	**982.06(3)**	0.15(5)	20(6)	

Continuation of Table 1

E_{level} (keV)	J_i^π	J_f^π	E_γ (keV)	I_γ	BR_γ	BR_γ [61]
		2^+	1219.6(3)	0.76(5)	100(6)	
3270.47(17)	1	0^+	**1213.8(3)**	0.042(5)	2.2(3)	
		0^+	**1512.3(3)**	0.107(9)	5.6(5)	
		2^+	**2040.6(3)**	0.06(3)	3.3(14)	
		0^+	3270.7(3)	1.91(8)	100(4)	
3308.39(14)	2^+	2^+	**631.3(3)**	0.026(7)	3.4(9)	
		2^+	**905.3(3)**	0.138(5)	17.5(6)	
		3^-	**983.8(3)**	0.081(3)	10.3(3)	
		0^+	**1251.6(3)**	0.089(5)	11.3(6)	
		2^+	2078.8(3)	0.79(4)	100(5)	
		0^+	3308.2(3)	0.197(13)	25.0(16)	
3352.9(2)	$0^{(+)}$	2^+	1025.1(3)	0.110(13)	19(2)	
		2^+	1310.2(3)	0.152(14)	26(3)	
		2^+	2123.4(3)	0.58(8)	100(13)	
3355.59(13)	2^+	2^+	**452.0(3)**	0.014(3)	2.4(4)	
		2^+	**678.4(3)**	0.057(10)	9.8(17)	
		4^+	**867.1(3)**	0.027(11)	3.7(15)	
		2^+	**952.5(3)**	0.124(8)	17.0(10)	
		0^+	**1298.8(3)**	0.200(7)	27.5(9)	
		2^+	**1312.9(3)**	0.149(14)	20(2)	
		2^+	2126.2(3)	0.73(9)	100(13)	
		0^+	3355.9(3)	0.20(3)	27(4)	
3375.49(12)	(1)	1^+	637.8(3)	0.058(3)	8.5(5)	
		2^+	698.5(3)	0.027(6)	3.9(8)	
		2^+	972.4(3)	0.160(6)	23.4(8)	
		2^+	1047.8(3)	0.68(5)	100(7)	
		0^+	1318.8(3)	0.158(7)	23.0(10)	
		2^+	1333.0(3)	0.057(8)	8.3(12)	
		0^+	1617.4(3)	0.142(5)	20.7(8)	
		2^+	2146.1(3)	0.237(15)	35(2)	
3426.9(2)	3^+	3^-	**1102.2(3)**	0.075(3)	23.8(10)	
		2^+	1384.0(3)	0.154(11)	63(5)	
		2^+	2197.6(3)	0.32(3)	100(9)	
3450.4(3)	$4^-,5^-$	4^+	487.05(3)	0.126(7)	100(5)	
		4^+	961.9(3)	0.039(11)	31(9)	

Continuation of Table 1

E_{level} (keV)	J_i^π	J_f^π	E_γ (keV)	I_γ	BR_γ	BR_γ [61]
3462.49(13)	$(1^-, 2^+)$	2^+	**558.7(3)**	0.011(5)	1.2(5)	
		1^+	**724.6(3)**	0.056(4)	5.9(4)	
		2^+	**785.3(4)**	0.027(6)	2.8(7)	
		2^+	**1059.3(3)**	0.024(4)	2.5(4)	
		3^-	**1137.9(3)**	0.297(9)	31.0(9)	
		0^+	**1405.6(3)**	0.036(4)	3.8(4)	
		2^+	1419.7(3)	0.96(6)	100(6)	
		2^+	**2232.8(3)**	0.089(4)	9.3(4)	
3554.1(3)	(3, 4)	4^+	590.9(3)	0.025(4)	100(17)	
		2^+	650.3(3)	0.009(2)	35(10)	
3636.49(18)	$(1^-, 2^+)$	2^+	**1308.3(3)**	0.069(8)	16.00(18)	
		3^-	**1311.7(3)**	0.251(8)	59(2)	
		0^+	**3636.6(3)**	0.43(3)	100(8)	
3673.46(18)	4^+	4^+	**710.2(4)**	0.009(4)	3.8(18)	
		2^+	**769.7(3)**	0.035(3)	15.6(15)	
		4^-	**899.7(3)**	0.032(6)	14(3)	
		2^+	**1345.6(3)**	0.082(8)	37(3)	
		4^+	1393.3(3)	0.043(6)	19(3)	
		2^+	2443.8(4)	0.22(3)	100(15)	
3690.4(3)	(5^-)	4^-	916.5(3)	0.093(10)	53(6)	
		3^-	1365.6(3)	0.176(8)	100(4)	
3695.98(14)	$1, 2^+$	0^+	**1639.5(3)**	0.185(7)	28.3(11)	
		2^+	**1653.3(3)**	0.115(10)	17.6(15)	
		0^+	**1937.9(3)**	0.108(5)	16.5(8)	
		2^+	2466.6(3)	0.339(18)	52(3)	
		0^+	3696.5(3)	0.65(16)	100(3)	
3699.31(17)	$(1^-, 2^+)$	1^+	961.3(3)	0.256(10)	49.4(18)	
		3^-	1374.6(3)	0.520(13)	100(3)	
		4^+	1418.4(3)	0.033(3)	6.3(6)	
		0^+	3699.7(3)	0.12(3)	23(5)	
3709.99(19)	$(1^-, 2^+)$	2^+	806.3(3)	0.016(2)	11.3(17)	
		1^+	972.1(3)	0.142(5)	100(4)	
		3^-	1385.3(3)	0.126(5)	89(4)	
		0^+	1653.2(3)	0.030(4)	21(3)	
		0^+	1951.9(3)	0.016(3)	11.3(17)	

Continuation of Table 1

E_{level} (keV)	J_i^π	J_f^π	E_γ (keV)	I_γ	BR_γ	BR_γ [61]
3737.66(19)	$(1, 2^+)$	2^+	834.2(3)	0.057(3)	55(3)	
		1^+	1000.0(3)	0.105(5)	100(4)	
		0^+	1240.9(3)	0.088(5)	84(5)	
		0^+	3736.6(3)	0.077(7)	74(7)	
3761.98(13)	$(1^-, 2^+)$	2^+	**1358.8(3)**	0.015(2)	1.07(18)	
		2^+	**1434.1(3)**	0.069(8)	5.1(6)	
		3^-	**1437.1(3)**	0.211(9)	15.6(7)	
		2^+	**1719.2(3)**	0.31(2)	22.5(14)	
		2^+	2532.3(3)	1.35(6)	100(5)	
		0^+	**3762.2(3)**	-	2.9(4)	
3770.8(2)	(4^+)	4^+	**1037.1(3)**	0.046(3)	69(4)	
		2^+	**1367.7(3)**	0.0232(14)	78(5)	
		4^+	**1490.6(3)**	0.067(6)	100(9)	
3816.17(3)	(4^+)	4^+	1327.8(3)	0.030(4)	9.1(13)	21.8(26)
		4^+	1535.4(3)	0.0213(3)	6.5(8)	7.9(14)
		2^+	2586.9(3)	0.33(4)	100(11)	100(6)
3847.12(13)	$(1^-, 2^+)$	2^+	943.3(3)	0.019(5)	10(2)	
		1^+	1109.2(3)	0.016(4)	9(2)	
		2^+	1169.9(3)	0.022(6)	11.5(3)	
		2^+	1443.9(3)	0.0461(3)	24.2(16)	
		3^-	1522.3(3)	0.190(6)	100(3)	
		0^+	1790.2(3)	0.028(3)	14.8(17)	
		2^+	1804.0(4)	0.039(5)	20(3)	
		2^+	2617.2(3)	0.15(2)	76(13)	
		0^+	3847.6(3)	0.066(9)	35(5)	
3856.75(15)	2^+	2^+	**1179.4(4)**	0.038(10)	9(2)	
		0^+	**1359.5(3)**	0.070(5)	16.3(11)	
		4^+	**1577.3(3)**	0.018(3)	4.1(7)	
		0^+	**1799.5(4)**	0.016(3)	3.8(8)	
		2^+	2627.1(3)	0.134(8)	30.8(19)	
		0^+	3857.0(3)	0.43(3)	100(6)	
3881.91(3)	(2^-)	3^-	1556.9(3)	0.710(18)	100	
3959.07(18)	$1^-, 2^+$	1^+	1221.2(3)	0.210(10)	100(5)	
		3^-	1634.0(3)	0.037(3)	17.5(13)	
		2^+	2729.8(3)	0.180(6)	86(3)	

Continuation of Table 1

E_{level} (keV)	J_i^π	J_f^π	E_γ (keV)	I_γ	BR_γ	BR_γ [61]
		0^+	3959.0(3)	0.070(9)	33(4)	
3994.48(19)	1^-, 2^+	2^+	**1317.3(3)**	0.022(3)	11.6(17)	
		2^+	**1666.6(3)**	0.092(10)	49(5)	
		3^-	**1669.9(3)**	0.026(4)	14(2)	
		2^+	**1951.7(3)**	0.19(3)	100(15)	
4014.7(3)	(2^-)	3^-	1689.7(3)	0.218(11)	100	
4023.94(15)	(2^+)	2^+	1120.3(3)	0.016(2)	17(2)	
		2^+	1346.7(3)	0.018(3)	19(3)	
		4^+	1535.1(3)	0.035(6)	37(7)	
		3^-	1699.1(3)	0.060(6)	63(6)	
		0^+	1967.3(3)	0.030(3)	31(4)	
		0^+	2265.7(3)	0.095(4)	100(4)	
4028.37(19)	(3^+)	2^+	1124.5(3)	0.013(2)	5.3(9)	
		1^+	1290.4(3)	0.251(10)	100(4)	
		2^+	1351.0(3)	0.051(4)	19.5(17)	
4034.41(19)	(3)	2^+	1130.6(3)	0.0201(3)	10.9(14)	
		2^+	1357.0(3)	0.0206(3)	11.2(16)	
		2^+	1706.4(3)	0.183(15)	100(8)	
4044.62(8)	$(1^+, 2^+, 3^+)$	2^+	2815.1(3)	0.313(14)	100	
4108.88(17)	2^-	2^+	**1051.3(3)**	0.044(6)	3.6(5)	
		4^-	**1334.7(3)**	0.065(5)	5.3(4)	
		1^+	**1371.3(3)**	0.038(3)	3.1(3)	
		2^+	**1706.2(3)**	0.056(3)	4.6(3)	
		2^+	2879.0(3)	1.22(8)	100(4)	
4117.80(15)	(2^+)	4^+	1630.0(3)	0.056(7)	4.6(6)	
		2^+	1714.3(3)	0.074(5)	6.1(4)	
		0^+	2060.3(4)	0.016(3)	1.3(2)	
		2^+	2075.8(3)	0.209(18)	17.2(15)	
		2^+	2887.8(3)	1.22(6)	100(13)	
		0^+	4117.7(3)	0.64(4)	53(3)	
4126.48(19)	1^+, 2^+	2^+	2897.3(3)	0.71(3)	100(5)	
		0^+	4126.4(3)	0.55(4)	77(5)	
4191.57(17)	$(2^-, 3^-)$	4^-	1417.7(3)	0.028(6)	4.0(8)	
		2^+	1863.1(3)	0.259(19)	37(3)	
		3^-	1867.1(3)	0.060(4)	8.6(5)	

Continuation of Table 1

E_{level} (keV)	J_i^π	J_f^π	E_γ (keV)	I_γ	BR_γ	BR_γ [61]
		2^+	2961.8(3)	0.70(6)	100(8)	
4226.6(2)	$(1,\ 2^+)$	2^+	2996.5(3)	0.43(8)	100(19)	
		0^+	4227.0(3)	-	50(3)	
4288.2(3)	$(3,\ 4^+)$	2^+	**3058.4(3)**	0.31(3)	100	
4312.11(12)	$(1,\ 2^+)$	$(1^-,2^+)$	**550.1(3)**	0.067(4)	35(2)	
		$(1,\ 2^+)$	**936.2(3)**	0.179(10)	94(5)	
		2^+	**1003.6(3)**	0.020(4)	10(2)	
		1	**1041.6(3)**	0.019(4)	9.8(19)	
		2^+	**1083.7(3)**	0.0287(15)	15.1(8)	
		2^+	**1255.0(3)**	0.078(3)	41.0(17)	
		1^+	**1574.2(3)**	0.110(5)	58(3)	
		2^+	**1634.9(3)**	0.089(7)	47(4)	
		2^+	**1984.1(3)**	0.190(16)	100(9)	
		2^+	**2270.0(3)**	0.088(9)	46(5)	
		0^+	**2556.3(3)**	0.029(3)	15.5(14)	
		2^+	**3083.2(4)**	0.076(7)	40(4)	
4353.09(14)	$(1,\ 2^+)$	1	**1082.8(4)**	0.007(3)	3.6(15)	
		2^+	**1448.8(3)**	0.021(4)	1.9(4)	
		0^+	**2296.8(3)**	0.109(7)	9.9(6)	
		2^+	**2310.7(3)**	0.39(3)	36(3)	
		0^+	**2595.4(3)**	0.104(15)	9.5(14)	
		2^+	**3122.8(3)**	1.10(5)	100(5)	
		0^+	**4353.5(3)**	0.167(13)	15.2(12)	
4406.21(19)	$(1,\ 2^+)$	0^+	**1909.1(3)**	0.127(5)	22.2(9)	
		0^+	**2349.4(3)**	0.124(7)	21.7(12)	
		2^+	**3176.8(3)**	0.57(4)	100(8)	
4432.76(16)	$(1,2^+)$	0^+	1935.4(3)	0.044(3)	41(3)	
		0^+	2674.8(3)	0.060(5)	57(4)	
		2^+	3203.4(3)	0.071(13)	67(12)	
		0^+	4432.5(3)	0.106(9)	100(9)	
4481.33(16)	$(1,\ 2^+)$	0^+	**1984.3(3)**	0.037(3)	25(2)	
		0^+	**2722.8(3)**	0.073(4)	51(3)	
		2^+	**3252.0(3)**	0.017(4)	11.5(3)	
		0^+	**4481.3(3)**	0.144(18)	100(12)	
4536.15(18)	$(1,2^+)$	2^+	2493.4(3)	0.093(8)	24(2)	

Continuation of Table 1

E_{level} (keV)	J_i^π	J_f^π	E_γ (keV)	I_γ	BR_γ	BR_γ [61]
		0^+	2777.6(3)	0.148(5)	38.8(14)	
		0^+	4536.0(3)	0.38(3)	100(8)	
4540.8(3)	$(3,\ 4^+)$	2^+	**2212.9(3)**	0.119(10)	100(9)	
		2^+	**2498.2(4)**	0.042(7)	31(6)	
4544.50(15)	$(1,2^+)$	2^+	2141.4(3)	0.094(5)	17.0(9)	
		0^+	2487.8(3)	0.090(5)	16.3(8)	
		2^+	2501.6(3)	0.206(14)	37.1(3)	
		2^+	3314.9(3)	0.168(14)	30.2(3)	
		0^+	4544.6(3)	0.55(4)	100(7)	
4560.25(14)	$(1,2^+)$	2^+	1883.5(3)	0.014(4)	5.5(17)	
		2^+	2232.6(3)	0.044(5)	17.00(19)	
		0^+	2503.5(3)	0.133(10)	51(4)	
		0^+	2802.1(3)	0.242(8)	93(3)	
		2^+	3329.7(3)	0.261(11)	100(4)	
		0^+	4560.4(3)	0.207(13)	79(5)	
4585.00(14)	$(1,2^+)$	1^+	1847.1(3)	0.034(2)	26.8(19)	
		2^+	1907.7(3)	0.013(5)	11(4)	
		2^+	2181.7(3)	0.027(3)	22(2)	
		0^+	2528.5(3)	0.125(5)	100(4)	
		2^+	2542.7(4)	0.012(4)	10(3)	
		0^+	2827.1(3)	0.108(4)	87(4)	
4667.8(4)	$3^{(-)}$	1	1397.4(3)	0.191(6)	100.0(0)	
4673.78(17)	$(1,2^+)$	2^+	2270.1(4)	0.016(3)	6.6(12)	
		3^-	2348.9(3)	0.019(4)	7.9(16)	
		2^+	3444.4(3)	0.247(9)	100(4)	
		0^+	4673.4(3)	-	< 42	
4723.50(3)	$(1,2^+)$	2^+	3494.6(3)	0.255(15)	100(6)	
		0^+	4722.6(3)	-	35(10)	
4769.65(15)	$(2^-,3^+)$	2^+	1865.9(3)	0.042(11)	24(7)	
		4^-	1995.4(7)	0.016(7)	9(4)	
		1^+	2031.8(3)	0.159(7)	93(4)	
		2^+	2092.5(3)	0.031(9)	18(5)	
		2^+	2366.5(3)	0.172(5)	100(3)	
		2^+	2441.8(3)	0.136(12)	79(7)	
4834.14(7)	$(1,2^+)$	2^+	**2507.0(3)**	0.146(11)	51(4)	

Continuation of Table 1

E_{level} (keV)	J_i^π	J_f^π	E_γ (keV)	I_γ	BR_γ	BR_γ [61]
		2^+	**2792.4(3)**	0.055(18)	19(6)	
		2^+	**3605.2(3)**	0.111(10)	39(3)	
		0^+	**4834.0(4)**	0.286(18)	100(6)	
4848.02(19)	$(2^-,3^+)$	$1^+,2^+$	721.6(3)	0.048(6)	32(4)	
		$1,\ 2^+$	1151.9(3)	0.024(3)	15.8(17)	
		1	1577.6(3)	0.041(2)	26.6(14)	
		1^+	2110.1(3)	0.154(6)	100(4)	
4910.47(3)	$(3,\ 4^+)$	2^+	2507.5(3)	0.089(5)	35.5(18)	
		2^+	2582.6(3)	0.251(18)	100(7)	
4981.40(16)	$(1,2^+)$	2^+	2578.1(3)	0.020(2)	14.1(17)	
		2^+	2653.3(3)	0.036(5)	26(4)	
		0^+	2924.4(3)	0.056(4)	40(3)	
		2^+	2938.4(3)	0.060(8)	42(5)	
		2^+	3752.3(3)	0.141(11)	100(8)	
5089.70(15)	$(1,\ 2^+)$	0^+	2592.8(3)	0.014(3)	8.2(15)	
		2^+	3047.5(3)	0.117(9)	68(5)	
		0^+	3331.6(3)	0.039(3)	22.3(16)	
		2^+	3860.2(3)	0.173(8)	100(5)	
		0^+	5089.6(3)	0.09(2)	52(11)	
5119.30(18)	$(1,\ 2^+)$	2^+	**2215.7(5)**	0.009(2)	6.7(16)	
		0^+	**3062.5(3)**	0.075(3)	55(2)	
		2^+	**3076.5(3)**	0.130(9)	97(7)	
		0^+	**3360.5(4)**	0.011(2)	8.2(17)	
		2^+	**3890.2(3)**	0.135(13)	100(10)	
5123.9(4)	(3^+)	1^+	2385.9(3)	0.093(4)	100	
5152.3(2)	(3^+)	2^+	**1295.9(3)**	0.036(13)	43(16)	
		1	**1882.1(7)**	0.0241(19)	29(2)	
		1^+	**2414.5(3)**	0.084(13)	100(16)	
5193.38(17)	$(1,\ 2^+)$	2^+	**2790.3(3)**	0.028(3)	28(3)	
		0^+	**3435.0(3)**	0.009(3)	9(3)	
		2^+	**3964.7(3)**	0.080(14)	80(14)	
		0^+	**5193.0(3)**	0.10(4)	100(4)	
5232.82(19)	$(1,2^+)$	0^+	3176.3(3)	0.026(3)	26(3)	
		2^+	3190.3(3)	0.10(17)	100(17)	
		0^+	3474.6(3)	0.038(2)	38(2)	

Continuation of Table 1

E_{level} (keV)	J_i^π	J_f^π	E_γ (keV)	I_γ	BR_γ	BR_γ [61]
5244.00(19)	$(1,2^+)$	2^+	2840.6(3)	0.034(3)	66(5)	
		0^+	3486.4(3)	0.021(5)	41(9)	
		0^+	5244.0(3)	0.052(3)	100(5)	
5274.28(17)	$(1,2^+)$	0^+	3217.4(3)	0.034(3)	10.3(8)	
		2^+	3232.2(3)	0.073(7)	22(2)	
		2^+	4044.9(3)	0.33(2)	100(6)	
		0^+	5274.0(3)	0.094(5)	28(14)	
5323.49(18)	$(1,\ 2^+)$	2^+	2995.9(3)	0.064(5)	52(4)	
		0^+	3565.6(3)	0.0408(3)	33(2)	
		0^+	5323.1(3)	0.123(6)	100(5)	
5382.8(2)	$(1,\ 2^+)$	0^+	2886.6(3)	0.034(2)	15.1(10)	
		0^+	5382.6(3)	0.227(14)	100(6)	
5396.24(19)	$(1,2^+)$	0^+	2899.5(3)	0.020(19)	14.4(14)	
		0^+	3339.7(3)	0.038(3)	27.5(19)	
		0^+	5396.3(3)	0.139(8)	100(6)	
5524.9(2)	$(1,\ 2^+)$	2^+	4295.2(3)	0.040(9)	22(5)	
		0^+	5524.8(3)	0.178(8)	100(5)	
5549.3(2)	$(1,\ 2^+)$	2^+	4320.1(3)	0.107(7)	100(6)	
		0^+	5548.9(3)	-	70(20)	
5613.75(19)	$(1,2^+)$	2^+	3210.5(4)	0.007(2)	4.8(15)	
		2^+	4384.6(3)	0.143(7)	100(5)	
		0^+	5613.4(3)	0.043(5)	30(4)	
5851.40(16)	$(1,\ 2^+)$	$1,2^+$	2156.6(3)	0.0126(12)	3.4(3)	
		2^+	3450.0(4)	0.019(4)	5(1)	
		2^+	3808.3(3)	0.123(10)	33(3)	
		0^+	4093.8(3)	0.023(2)	6.3(5)	
		2^+	4620.7(3)	0.371(15)	100(4)	
		0^+	5850.2(3)	0.087(7)	23.6(19)	
6004.1(2)	$(1,\ 2^+)$	2^+	4774.4(3)	0.097(7)	100(7)	
		0^+	6004.0(3)	0.076(8)	78(8)	
6168.40(18)	$(1,\ 2^+)$	0^+	3673.1(4)	0.008(4)	6(3)	
		2^+	3766.7(4)	0.016(3)	12(2)	
		2^+	4124.9(3)	0.045(7)	33(5)	
		0^+	6167.9(3)	0.135(7)	100(5)	
6305.59(13)	$(1^-,\ 2^+)$	1^+	3567.7(3)	0.0123(17)	8.6(12)	

Continuation of Table 1

E_{level} (keV)	J_i^π	J_f^π	E_γ (keV)	I_γ	BR_γ	BR_γ [61]
		2^+	3904.2(3)	0.048(4)	34(3)	
		2^+	3977.6(3)	0.076(6)	54(5)	
		3^-	3981.5(4)	0.048(4)	34(3)	
		2^+	4262.2(3)	0.143(10)	100(7)	
		0^+	4548.1(3)	0.082(3)	57(2)	
		2^+	5075.2(3)	0.034(2)	23.8(14)	
		0^+	6305.5(3)	0.025(3)	17(2)	
9326.23(7)	$(0^+, 1^+)$	$(1^-, 2^+)$	3021.6(3)	0.41(7)	11.5(19)	
		$(1, 2^+)$	3158.2(3)	0.212(9)	6.0(3)	
		$(1, 2^+)$	3322.0(3)	0.148(1)	4.1(3)	
		$(1, 2^+)$	3475.7(3)	0.128(12)	3.6(3)	
		$(1, 2^+)$	3712.5(3)	0.199(11)	5.6(3)	
		$(1, 2^+)$	3776.7(3)	0.106(9)	2.98(3)	
		$(1, 2^+)$	3801.2(3)	0.305(13)	8.5(4)	
		$(1, 2^+)$	3930.3(3)	0.134(12)	3.8(3)	
		$(1, 2^+)$	3943.7(3)	0.16(2)	4.5(6)	
		$(1, 2^+)$	4002.8(3)	0.28(3)	7.7(7)	
		$(1, 2^+)$	4052.2(3)	0.54(5)	15.1(14)	
		$(1, 2^+)$	4082.4(3)	0.060(7)	1.7(2)	
		$(1, 2^+)$	4093.6(3)	0.073(10)	2.1(3)	
		$(1, 2^+)$	4117.8(3)	0.64(4)	17.9(12)	
		(3^+)	4133.0(3)	0.184(15)	5.1(4)	
		(3^+)	4174.2(3)	0.18(3)	4.9(8)	
		$(1, 2^+)$	4202.5(3)	0.0158(10)	0.44(3)	
		$(1, 2^+)$	4206.8(3)	0.139(12)	3.9(3)	
		$(1, 2^+)$	4236.9(3)	0.36(9)	10(3)	
		$(1, 2^+)$	4344.3(3)	0.15(2)	4.2(6)	
		$(1, 2^+)$	4491.2(3)	0.58(10)	16(3)	
		$(2^-, 3^+)$	4556.35(3)	0.39(2)	11.0(5)	
		$(1, 2^+)$	4601.7(3)	0.144(6)	4.07(18)	
		$(1, 2^+)$	4652.0(3)	0.210(16)	5.9(4)	
		$(1, 2^+)$	4741.4(3)	0.15(2)	4.3(6)	
		$(1, 2^+)$	4765.6(3)	0.74(5)	20.8(13)	
		$(1, 2^+)$	4781.6(3)	0.54(10)	15(3)	
		$(1, 2^+)$	4789.4(3)	0.59(11)	17(3)	

Continuation of Table 1

E_{level} (keV)	J_i^π	J_f^π	E_γ (keV)	I_γ	BR_γ	BR_γ [61]
		$(1,\ 2^+)$	4844.3(3)	0.119(6)	3.33(16)	
		$(1,\ 2^+)$	4893.0(3)	0.108(8)	3.0(2)	
		$(1,\ 2^+)$	4919.7(3)	0.459(19)	12.8(5)	
		$(1,\ 2^+)$	4973.4(3)	0.98(15)	27(4)	
		$(1,\ 2^+)$	5013.7(3)	0.80(14)	22(4)	
		(3)	5037.4(4)	0.119(4)	3.33(12)	
		$(1,\ 2^+)$	5099.5(3)	0.41(10)	11(3)	
		$(2^-,\ 3^-)$	5134.2(3)	0.52(8)	15(2)	
		$(1,\ 2^+)$	5200.0(3)	0.137(7)	3.85(18)	
		2^+	5208.4(3)	1.03(4)	28.9(11)	
		2^-	5217.2(3)	0.93(6)	25.9(17)	
		$(1^+,\ 2^+,\ 3^+)$	5281.2(3)	0.073(3)	2.04(8)	
		(3)	5291.4(3)	0.043(3)	1.21(8)	
		(3^+)	5297.4(3)	0.194(12)	5.4(3)	
		2^+	5302.0(3)	0.0166(15)	0.47(4)	
		$(1^-,\ 2^-)$	5311.1(3)	0.098(7)	2.75(18)	
		$(1^-,\ 2^+)$	5331.3(3)	0.064(3)	1.78(10)	
		$(1^-,\ 2^+)$	5366.7(3)	0.084(4)	2.34(11)	
		(2^-)	5444.0(3)	0.46(3)	13.00(9)	
		2^+	5469.0(3)	0.145(16)	4.1(5)	
		$(1^-,\ 2^+)$	5478.5(3)	0.126(10)	3.5(3)	
		$(1^-,\ 2^+)$	5563.8(3)	0.77(10)	22(3)	
		$(1,\ 2^+)$	5587.7(3)	0.032(12)	0.9(3)	
		$(1^-,\ 2^+)$	5626.4(3)	0.50(3)	13.9(9)	
		$(1^-,\ 2^+)$	5689.5(3)	0.20(14)	5.6(4)	
		$(1^-,\ 2^+)$	5738.7(3)	0.41(3)	11.4(10)	
		$(1,\ 2^+)$	5863.3(3)	0.34(3)	9.5(8)	
		2^+	5950.2(3)	0.147(11)	4.1(3)	
		2^+	5970.91(3)	0.34(4)	9.5(11)	
		$0^{(+)}$	5972.6(3)	0.29(3)	8.1(8)	
		1	6055.41(3)	0.61(3)	17.1(8)	
		2^+	6063.4(3)	0.0403(18)	1.13(5)	
		2^+	6096.9(3)	0.29(7)	8.0(19)	
		(0^+)	6109.8(5)	0.74(5)	20.7(14)	
		0^+	6188.6(3)	0.034(2)	0.94(6)	

Continuation of Table 1

E_{level} (keV)	J_i^π	J_f^π	E_γ (keV)	I_γ	BR_γ	BR_γ [61]
		2^+	6422.1(3)	1.13(9)	31.5(3)	
		1^+	6588.0(3)	0.147(15)	4.1(4)	
		2^+	6648.7(3)	0.93(7)	26.0(18)	
		0^+	6828.8(3)	0.41(3)	11.4(9)	
		2^+	6922.9(3)	0.113(9)	3.2(3)	
		2^+	6998.1(3)	0.32(2)	9.0(6)	
		3^-	7001.2(3)	0.0316(15)	0.89(4)	
		0^+	7269.2(3)	0.46(4)	12.8(11)	
		2^+	7283.0(3)	0.215(2)	6.0(6)	
		0^+	7568.0(3)	0.028(3)	0.78(9)	
		2^+	8096.7(3)	0.33(3)	9.1(8)	
		0^+	9326.2(3)	3.6(4)	100(11)	

The large number of high energy γ-ray transitions, notably in the 3–6 MeV range, made for a difficult analysis due to many single- and double-escape peaks, as well as many photopeaks that were comprised of more than one γ ray. It was often the case that escape peaks and real photopeaks overlapped making γ-γ coincidence analysis difficult as the gated peak yielded a projection with γ rays stemming from the escape peak component of the gated peak. Furthermore, with many peaks closely packed, it was a challenge to make background subtractions. The singles addback spectrum is shown in Figure 5.5 and Figure 5.6 to highlight the large number of peaks necessary to investigate.

Given that the most dominant primary transition is directly to the ground state, the capture state is considered to have spin $J = 1^+$. The 9326.2(3)-keV transition has a relative intensity (to the 1230-keV, $2_1^+ \to 0_1^+$ ground state transition) of 3.6(4)% which is nearly three times greater than the next most intense primary transition. This is in line with the findings of Y.E. Loginov et al. in a similar thermal neutron capture, ^{117}Sn(n,γ), experiment [88]. Their paper is the most comprehensive γ-ray analysis of the other previously known ^{117}Sn(n,γ) experiments that measured γ-ray energies [89, 90, 91]. In it, they observed 45 states and 162 γ-ray transitions which compare well to the present dataset. They also suggest the capture state as having spin, $J = 1$, with the capture state feeding the ground state with an intensity of 5.3(15)%. The works by Borzakov et al. similarly measured 5.7(8)% intensity to the ground state from the capture state [89].

The capture state, which is assumed to be a continuum of states at the neutron separation energy, was determined to be 9326.23(7) keV which is in good agreement with the neutron separation energy of 9326.42(13) keV [67]. The current evaluated neutron separation energy of 9326.3(14) [50] is also in good agreement, but is 20 years older and has a large uncertainty.

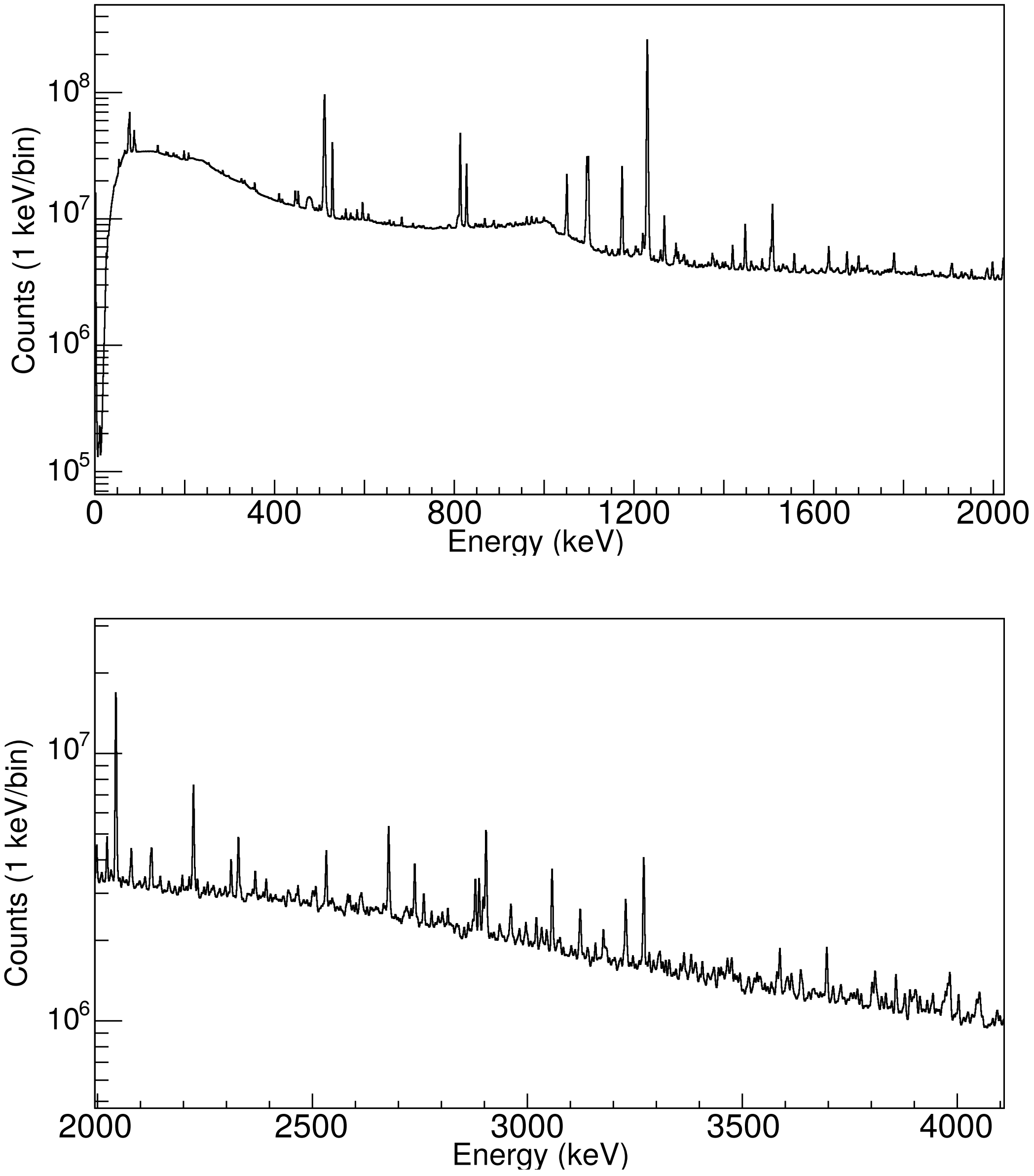

Figure 5.5: γ-ray spectrum of singles addback events for different energy regions is shown. Log scale was used to accentuate the weaker transitions.

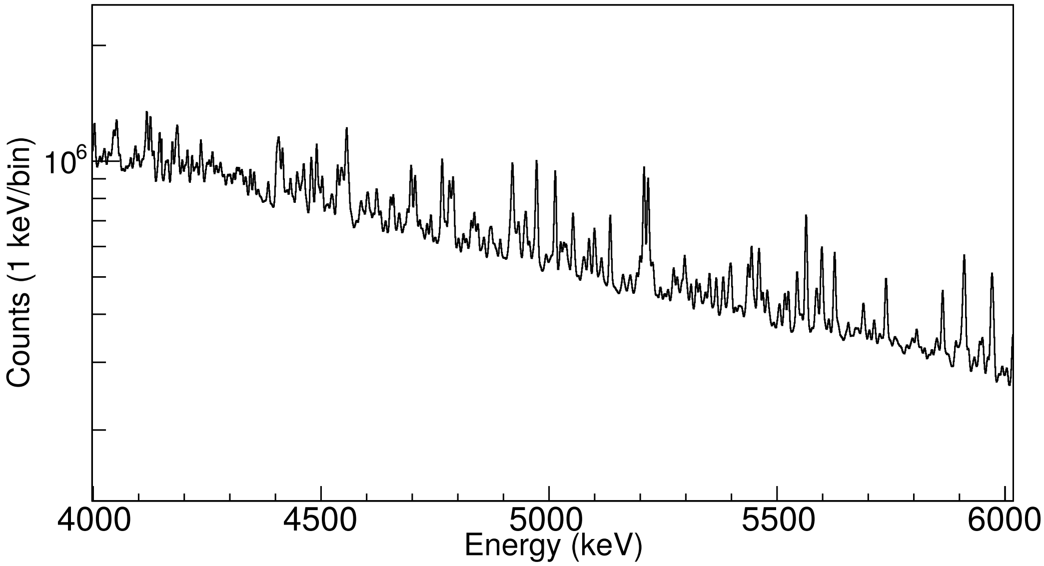

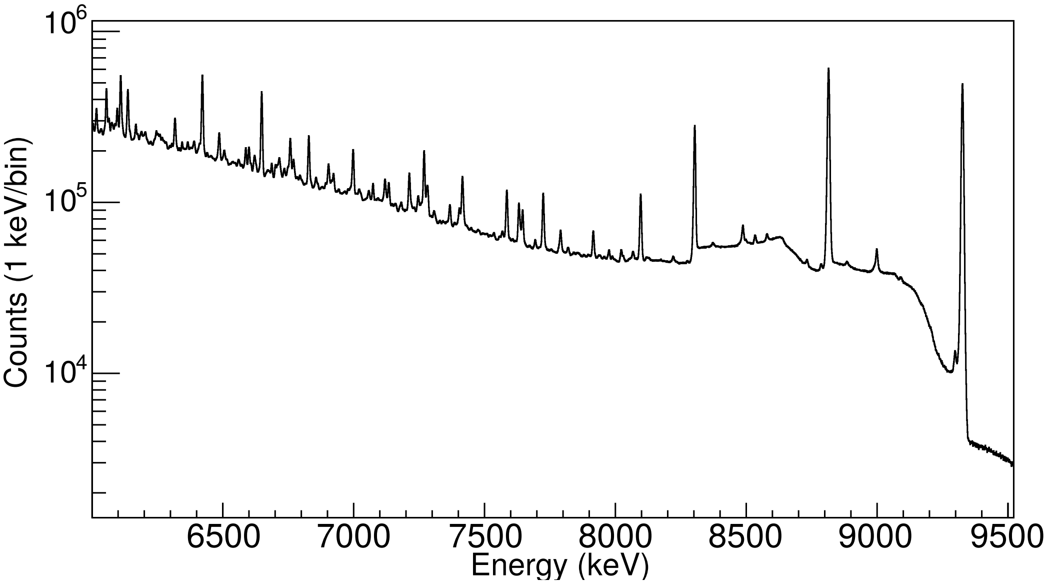

Figure 5.6: Similarly to the above Figure 5.5, the γ-ray spectrum of singles addback events for different energy regions is shown. Log scale was used to accentuate the weaker transitions.

Placing energy states to the level scheme was not a simple task due to many weakly populated states from primary γ rays. The general method was to identify a photopeak and subtract that energy from the 9326-keV separation energy. If the resultant energy corresponded to a photopeak in the spectrum, it was likely the case that this was a primary transition populating a level, or a ground state transition decaying from a level. For example, Figure 5.7 shows a gated spectrum on the 1229.7-keV transition from the first excited 2^+ level. A subtraction of 1229.7 keV from 9326 keV produces 8096.3 keV. An obvious photopeak at 8096.7 keV is observed and, with prior knowledge of the 1229.7-keV level, placed as a primary transition from the capture state. For transitions which were not primary or ground state transitions, a more exhaustive, but similar gating routine was performed using the same γ-γ coincidence matrix. Since the level scheme of ^{118}Sn has been well studied (see Reference [50] for the evaluated data), there were many transitions that could be used for starting blocks in a cascade—making for a slightly easier placement of γ rays to the level scheme.

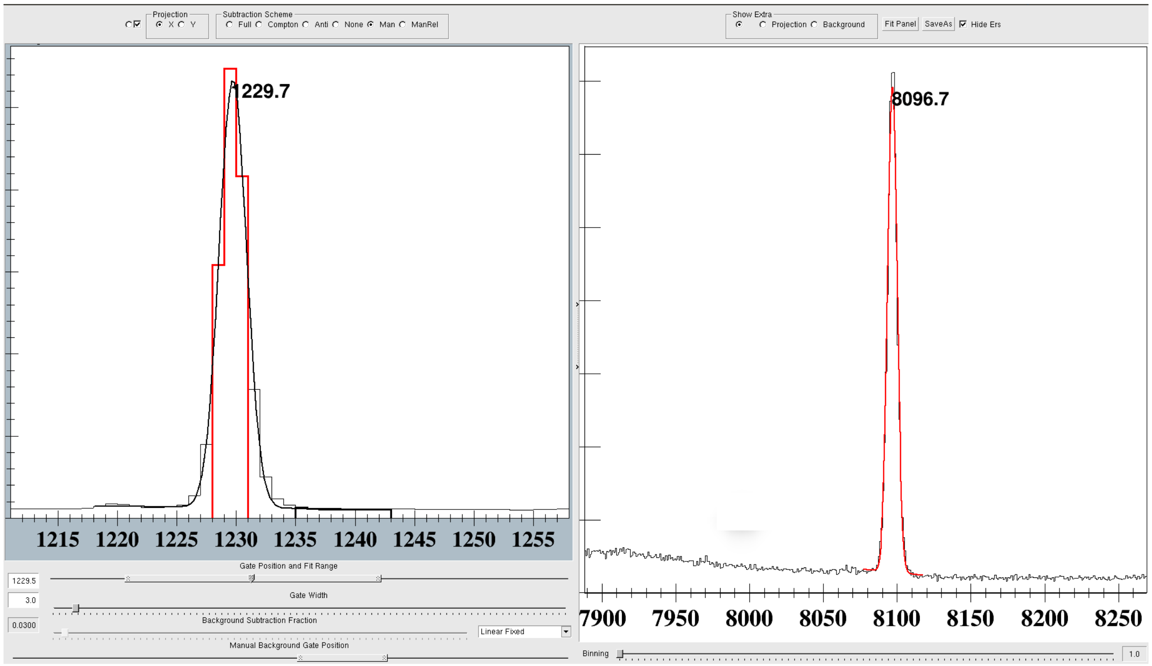

Projection: ● X ○ Y

Subtraction Scheme: ○ Full ○ Compton ○ Anti ○ None ● Man ○ ManRel

Show Extra: ● ○ Projection ○ Background

☑ Hide Ers

Gate Position and Fit Range: 1229.5

Gate Width: 3.0

Background Subtraction Fraction: 0.0300

Linear Fixed

Binning: 1.0

Figure 5.7: Example of γ-γ coincidence gating. On the left is the gate placed on 1230 keV, and on the right is the projection of all coincidence events. In this example, the projection is focused on the 8096.7-keV primary transition which directly populates the 1230-keV level from the neutron capture state. The gating tool is from the jRoot Tools [92].

5.3.1 Angular Correlations

As with GRIFFIN, the geometry of FIPPS allowed for angular correlations to be performed for cascades with significant γ-γ-coincidence statistics. Typically, the number of events in a photopeak in a gated projection needed to be greater than 100000 counts in order to yield a meaningful angular correlation. In some cases, it was possible to *fold* the statistics about the y-axis, or where $\cos(\theta) = 0$.

Table 5.2: The number of unique angles produced from the 30 FIPPS HPGe crystals when paired. Although the $\cos(\theta) = 0$ is shown, this is not used in angular correlations.

Angles (degrees)	Weights	Angles (degrees)	Weights
0	32	91.709	56
19.887	56	107.763	28
24.428	28	111.39	28
28.27	28	112.162	28
31.696	28	115.904	28
44.288	56	131.011	56
48.989	56	135.712	56
64.096	28	148.304	28
67.838	28	151.73	28
68.61	28	155.572	28
72.237	28	160.113	56
88.291	56	180	28

Table 5.3: From the experimental fits of four $J = 0 \rightarrow 2 \rightarrow 0$, where the $2 \rightarrow 0$ is the 1230-keV, groundstate transition the experimental a_2 and a_4 were extracted from the angular correlation fits and compared to the theoretical values, $A_2 = 0.357$ and $A_4 = 1.143$. By taking a ratio of the experimental fit parameters, a_2 and a_4, to the theoretical values, quality factors, q_2 and q_4, were determined as a measure of attenuation.

E_γ	a_2	a_4	q_2	q_4
528	0.333(9)	0.96(1)	0.934(24)	0.838(10)
827	0.35(1)	0.967(13)	0.97(3)	0.846(13)
1267	0.35(2)	0.98(2)	0.98(5)	0.86(2)
1700	0.28(5)	0.95(7)	0.77(15)	0.83(6)
Weighted Average	-	-	0.949(18)	0.843(7)

This is a common procedure as the symmetry is even (i.e. y = $\cos(\theta) = \cos(-\theta)$). However, this does decrease the number of angles by half, or the degrees of freedom, which means there is a higher tolerance for the fit to be inconclusive when comparing different spins.

In the present angular correlations, only the FIPPS detectors were used and not the IFIN. This was due to the IFIN-IFIN and IFIN-FIPPS detector pairs having differing angles from FIPPS-FIPPS as well as a decreased efficiency. Both of these reasons are a result of the IFIN detectors being 20 cm away from the target compared to 9 cm for the FIPPS detectors. Another reason the IFIN detectors were excluded was that the angles between crystals were incorrect. It is unclear if the positions of the crystals were documented incorrectly, or if there was another issue.

The angular correlations performed with FIPPS used the same event-mixing technique as with GRIFFIN (see Section 4.2.4) when the statistics allowed for it. Otherwise, in some cases, the number of detector pairs for each angle were used as weights to normalize the angular correlations. The 23 unique detector-pair angles and their weights are shown in Table 5.2.

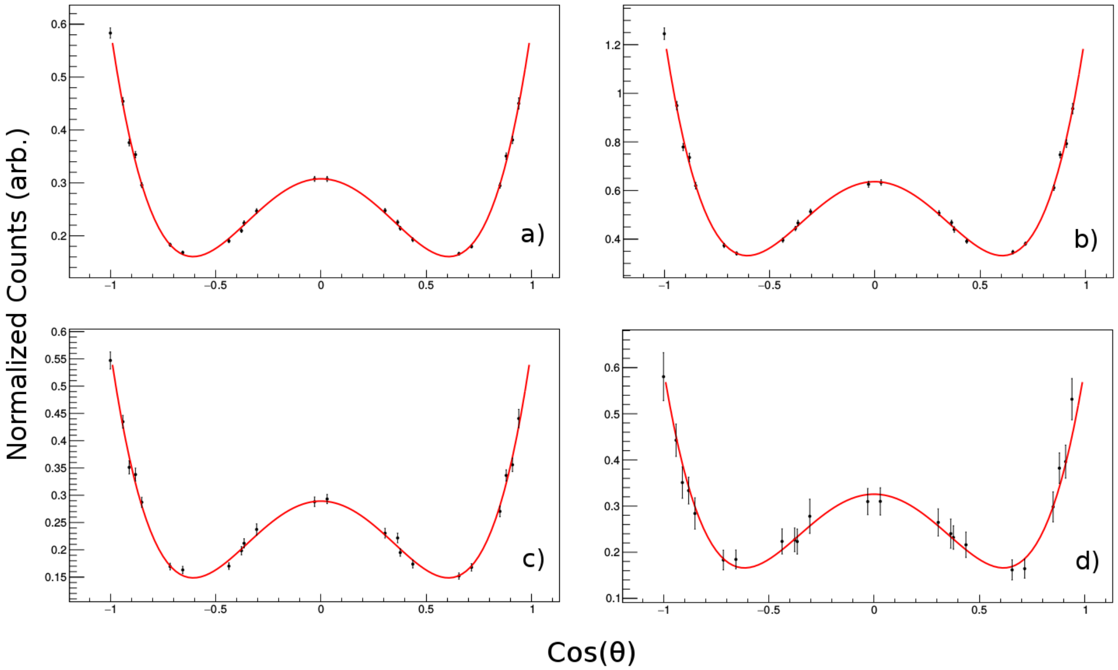

Figure 5.8: Shown are the $0 \rightarrow 2 \rightarrow 0$ angular correlations used to obtain the a_2 and a_4 fit parameters to be compared with the theoretical values. All of the transitions used populated the 1230-keV level from which the 1230-keV transition was used to gate on. The transitions used were 528 keV from the 1758-keV level (a), 827 keV from the 2057-keV level (b), 1267 keV from the 2496-keV level (c) and 1700 keV from the 2929-keV level (d) with reduced χ^2 of 1.59, 1.46, 1.26 and 0.51, respectively. The fit parameters are shown in Table 5.3.

Table 5.4: Experimentally determined mixing ratios, δ for select $J = 2 \rightarrow 1230$ keV transitions. The reduced χ^2 is given for the angular correlation fit. The values are in good agreement with the previous measured values in the β-decay experiment as well as the literature.

Transition (keV)	δ_{exp}	χ^2_ν	δ_β [61]	δ_{lit} [50]
813	-2.27(12)	0.66	-2.28(7)	-2.34(16)
1098	-8.2(12)	0.34	-14(4)	56(31)
1173	0.83(5)	0.14	0.85(3)	1.07(9)
1447	2.8(4)	1.0	-	2.46^{17}_{13}

Simulations of the attenuation factors were not performed as with the GRIFFIN angular correlations, but rather determined experimentally from four $0 \rightarrow 2 \rightarrow 0$ cascades. These cascades have pure $E2$ transitions, meaning that mixing is not possible. By fitting the angular correlations for each of the energies, the fit parameters can be compared to the theoretical values, A_2 and A_4, to determine the attenuation. The angular correlations all were in a direct cascade with the 1230-keV transition from the first excited 2^+ and shown in Figure 5.8. The transitions were 528 keV, 827 keV, 1267 keV, and 1700 keV from the $J = 0^+$ levels of 1758 keV, 2057 keV, 2497 keV, and 2930 keV, respectively. Quality factors, q_2 and q_4 were determined as a scaling factor between the measured fit parameters, a_2 and a_4, and the theoretical values A_2 and A_4. The quality factors were determined to be, $q_2 = 0.949(18)$ and $q_4 = 0.843(7)$ and shown in Table 5.3. The uncertainty on the q values obtained with the 1700-keV transition highlight the need for a large number of statistics. The total number of prompt coincidence event in the 1700-keV peak was 7.7e4 compared with 3.2e5, 9.1e5, and 1.6e6 for 1267 keV, 827 keV, and 528 keV, respectively. Although a direct comparison to the GRIFFIN array cannot be made, the values for these factors are very much inline with the simulations for GRIFFIN clovers positioned at 11 cm.

For the previously known levels without a firm spin assignment, the only angular correlation which was sufficient to definitively assign spin to was for the 2929-keV. The previous assigned spin was given as $J = 0^+, 1^+$ [50]. The cascade of 1700 keV $\rightarrow$ 1230 keV $\rightarrow$ 0 keV produced the angular correlation shown in Figure 5.9. Based on the shape and the reduced χ^2 minimization, the spin is given as $J = 0^+$.

Select transitions were measured for mixing ratios, δ, as a means to test the quality factors and compare the results to known values. All of the angular correlations used to obtain the mixing ratios were from $2 \rightarrow 2 \rightarrow 0$ cascades with the $2 \rightarrow 0$ being the 1230-keV transition. The transitions used were the 813-keV, 1098-keV, 1173-keV, and the 1447-keV from the 2042-keV, 2328-keV, 2403-keV, and the 2677-keV levels, respectively. The angular correlations are shown in Figures 5.10 to 5.13 and the results are summarized in Table 5.4.

The results of the mixing ratios were all in good agreement with the previous literature values [50, 61]. This suggests that the quality factors are a good empirical approximation for the attenuation of the γ rays and can be used to not only determine the spins of the levels of interest, but also the mixing ratios.

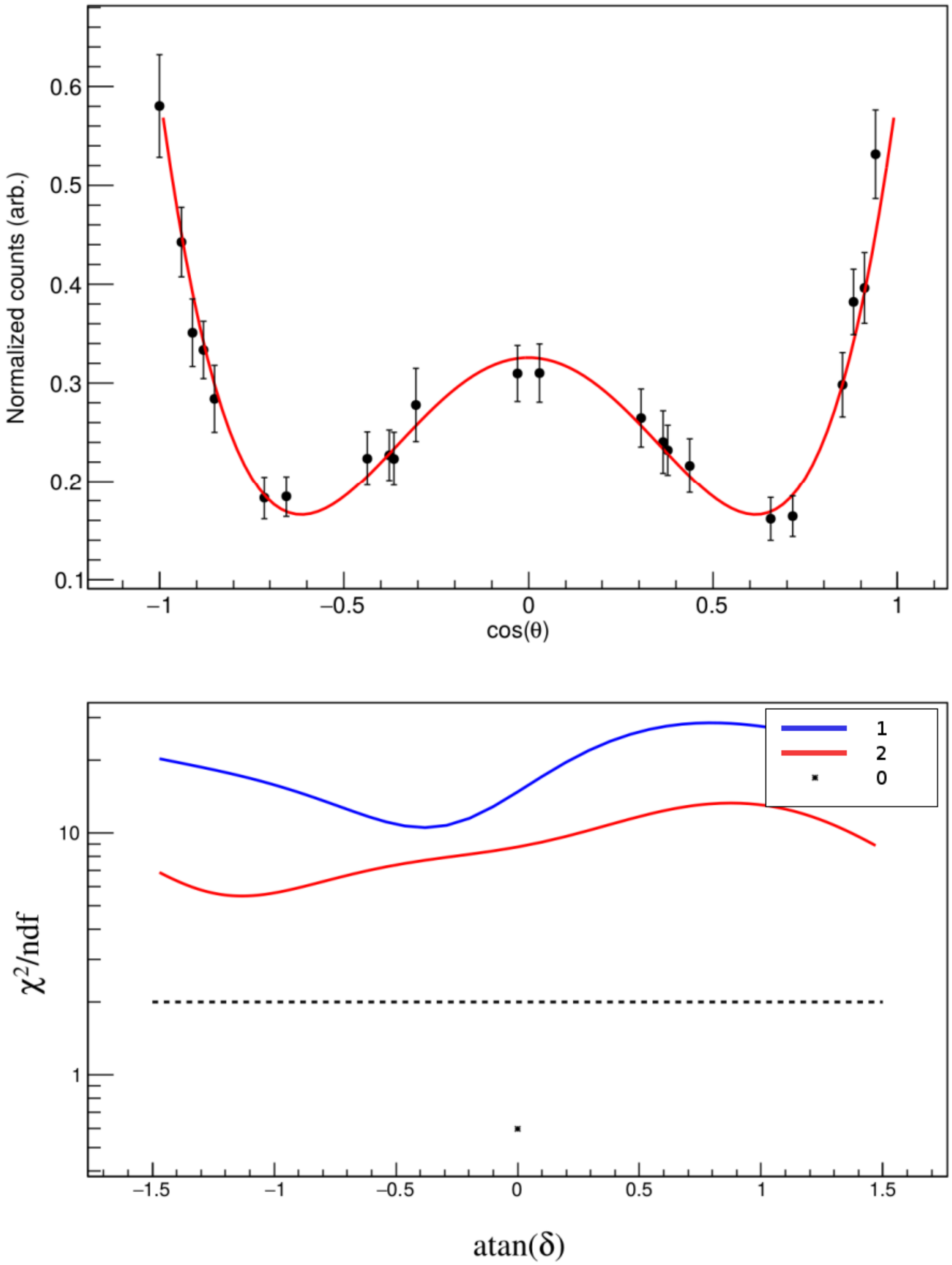

Figure 5.9: The γ-γ angular correlation (top) for the 1700-keV $\rightarrow$ 1230-keV $\rightarrow$ 0-keV cascade from which a spin to the 2929-keV level is assigned as $J = 0$. Previously, the spin was given as $J = 0^+, 1^+$ [50]. The χ^2 minimization (bottom) shows that the spin is not a 1^+. The reduced χ^2 of the angular correlation is 0.51.

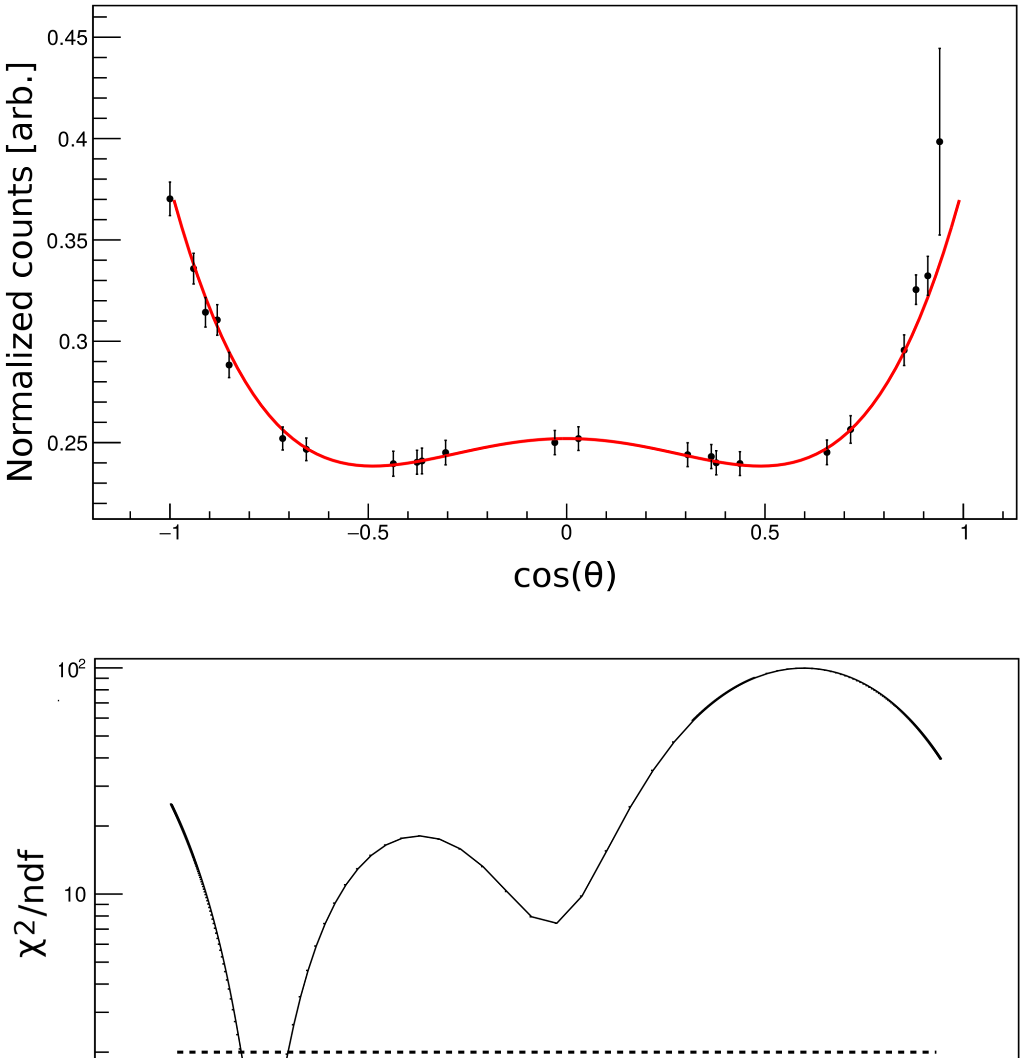

Figure 5.10: The γ-γ angular correlation (top) for the $J = 2_2^+$, 2043-keV level cascade with 813-keV $\rightarrow$ 1230-keV $\rightarrow$ 0-keV cascade from which the mixing ratio of the 813-keV transition was determined. The evaluated value is $\delta = -2.34(16)$ [50] and the measured value in the previous section for β-decay is $\delta = -2.28(7)$. The χ^2 minimization (bottom) was fit to determine the mixing ratio as $\delta = -2.27(12)$ in good agreement. The reduced χ^2 of the angular correlation is 0.66.

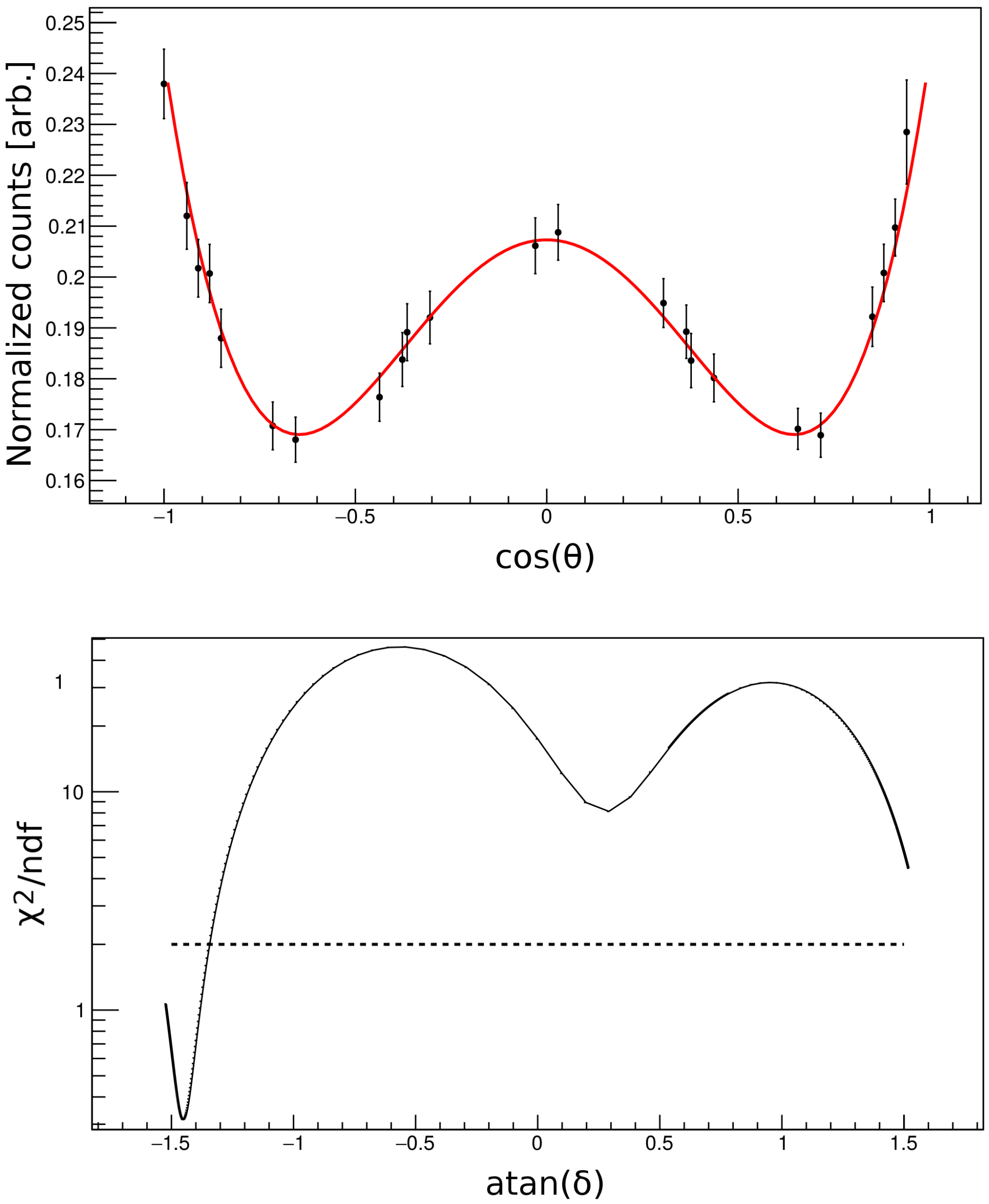

Figure 5.11: The γ-γ angular correlation (top) for the $J = 2_3^+$, 2328-keV level cascade with 1098-keV $\rightarrow$ 1230-keV $\rightarrow$ 0-keV cascade from the mixing ratio of the 1098-keV transition was determined. The evaluated value is $\delta = 56(31)$ [50] (given as $1/\delta = 0.018(10)$ and the measured value in the previous section for β-decay is $\delta = -14(4)$. The χ^2 minimization (bottom) was fit to determine the mixing ratio as $\delta = -8.2(12)$ in good agreement with the β-decay experiment. The reduced χ^2 of the angular correlation is 0.34.

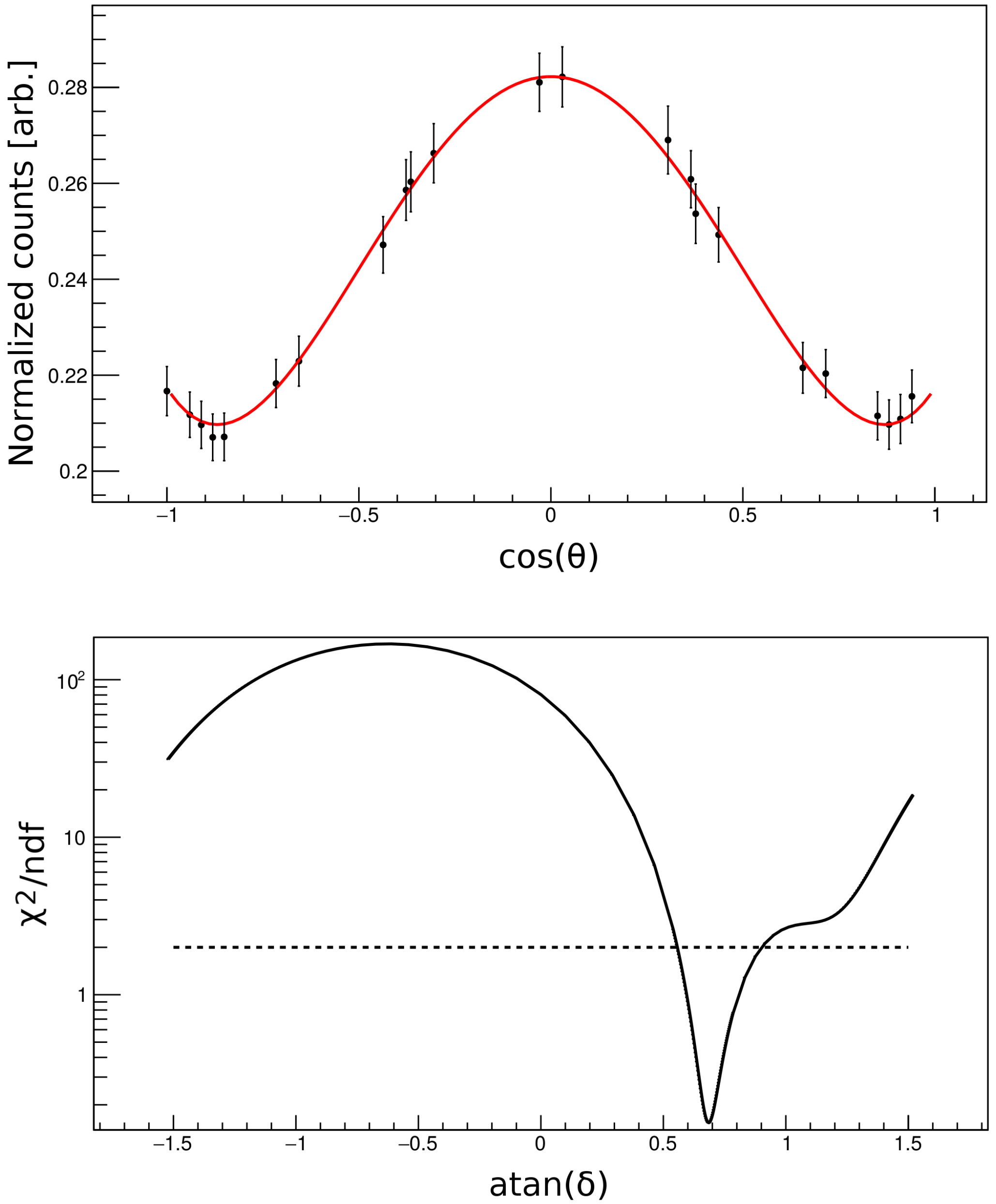

Figure 5.12: The γ-γ angular correlation (top) for the $J = 2_4^+$, 2403-keV level cascade with 1173-keV → 1230-keV → 0-keV cascade from the mixing ratio of the 1173-keV transition was determined. The evaluated value is $\delta = 1.07(9)$ [50] and the measured value in the previous section for β-decay is $\delta = 0.85(3)$. The χ^2 minimization (bottom) was fit to determine the mixing ratio as $\delta = 0.83(5)$ in good agreement with the β-decay experiment. The reduced χ^2 of the angular correlation is 0.14.

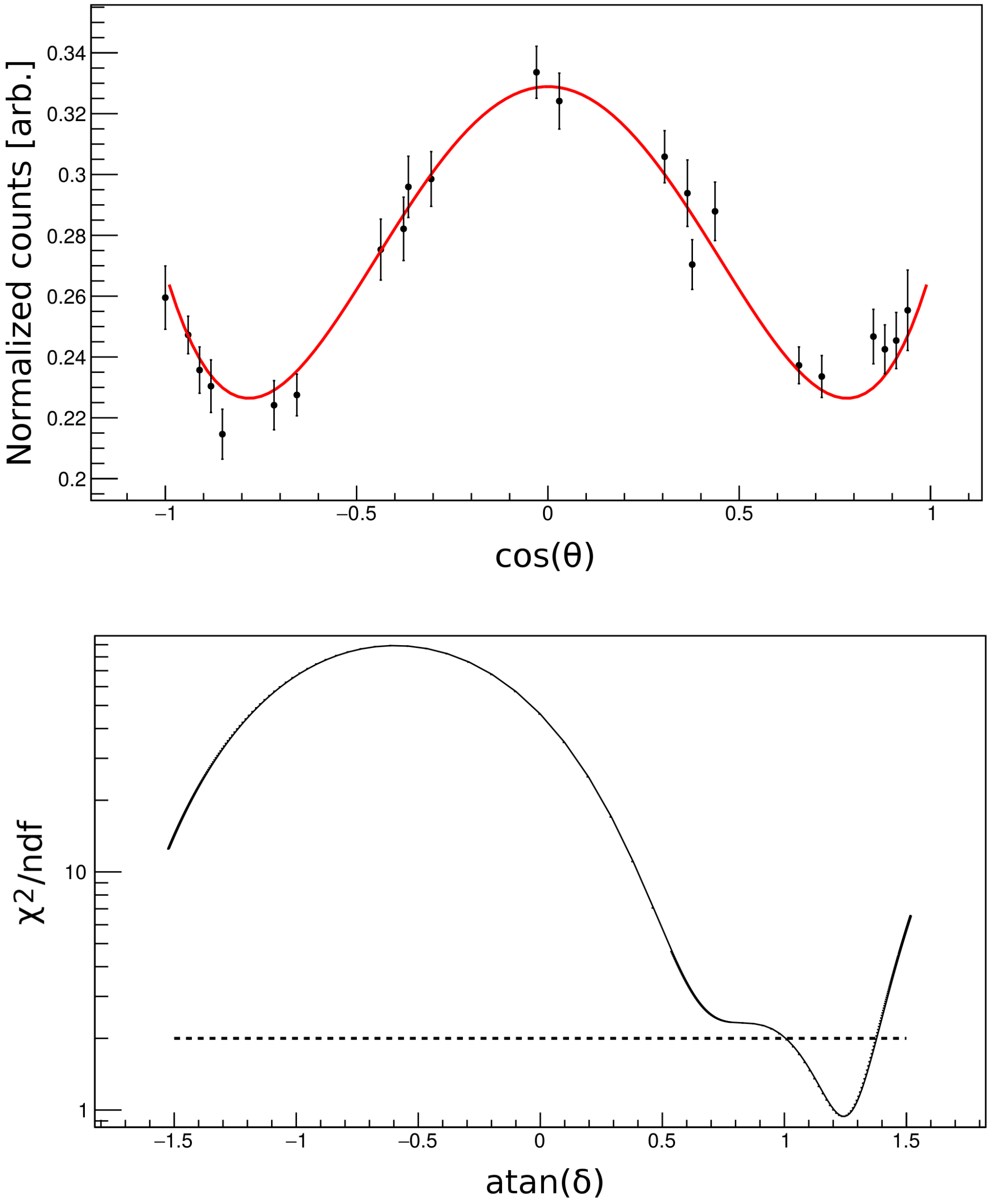

Figure 5.13: The γ-γ angular correlation (top) for the $J = 2^+_5$, 2677-keV level cascade with 1447-keV → 1230-keV → 0-keV cascade from the mixing ratio of the 1447-keV transition was determined. The evaluated value is $\delta = 2.46^{17}_{13}$ [50]. The χ^2 minimization (bottom) was fit to determine the mixing ratio as $\delta = 2.8(4)$ in good agreement with the previous measured value. The reduced χ^2 of the angular correlation is 1.0.

5.3.2 Newly Placed Levels

The 46 newly placed levels are listed in bold in Table 5.1 and were identified using γ-γ coincidences. A brief description for a selection of these levels with their proposed spin is given below. Unless stated, angular correlations were not possible to assign spin due to limited statistics.

3215.87(18) keV: Gating on the 6109.8(5)-keV primary transition produced a spectrum with three transitions to different states with $J = 2^+$. These transitions had energies of 888 keV, 1174 keV, and 1987 keV and fed the levels of 2327 keV, 2043 keV, and 1230 keV, respectively. There were no observations of a ground state transition, nor transitions to any other 0^+ states. Angular correlations were performed (shown in Figure 5.14), even though the statistics were too low to obtain event-mixing normalization. Instead, normalization was done by the number of detector pairs. Furthermore, the prompt coincidence events were folded about the y-axis to increase statistics. Based on the γ-decay selection rules and angular correlations, the spin of the 3215.87 level is assigned as a $J = 0^+$.

3352.9(2) keV: Similar to the 3215.87-keV, three transitions of 1025 keV, 1310 keV, and 2123 keV populated the $J = 2^+$ states of 2327 keV, 2043 keV, and 1230 keV, respectively. The level was identified through a common transition between these gates of 5973 keV. Angular correlations were able to identify the level as having a spin of $J = 0$ as shown in Figure 5.15. A tentative parity assignment of $\pi = +$ was given. This is based on the $E2$ transitions being more probable than $M2$.

3375.49(12): This level has many transitions decaying from it to states with spin of $J = 0^+, 1^+$, and 2^+. It is also populated by a primary transition from the capture state. Angular correlations, shown in Figure 5.16, were performed by gating on the 1098-keV transition which decays from the $J = 2^+$, 2328-keV level to the 1229-keV level with a mixing ratio, δ, of $-14(4)$ [61] and fitting the 1048-keV transition depopulating this newly observed level. A χ^2 minimization plot suggests a spin of $J = 1$ with a mixing ratio of $\delta = 0.67(10)$.

3450.4(3) keV: This level was identified from gates on the transitions of 487 keV and 962 keV which feed the $J = 4^+$ states at 2963 keV and 2280 kV, respectively. A spin of $J_i = 4^-, 5^-$ was given based on no observed primary transition, and no ground state transition. Furthermore, there are no transitions to the lower-lying 2^+ states. Since $E1$ transitions are more likely than $E2$ (see Section 1.3), this is likely why there is no observed feeding to negative parity states.

3554.1(3) keV: This level has only two transitions identified to decay from it—a 591-keV transition and a 650-keV transition which populate the 2963-keV, $J = 4^+$ state and the 2904-keV, $J = 2^+$ state, respectively. Given that there are no observed primary transitions to this level and no ground state decay, it is likely a spin of $J = (3, 4)$. The parity is not assigned here. It should be noted that there is another 961-keV transition which originates from the newly identified 3699.31(17)-keV level. However, it is believed this is a doublet based on the observed transitions in γ-γ coincidence gating.

3690.4(3): Gating on the photopeak of 452 keV from the 2774-keV, $J = 4^-$ state, as well as gating on the 449-keV photopeak from the same level, reveals a 916.5-keV transition. Reverse

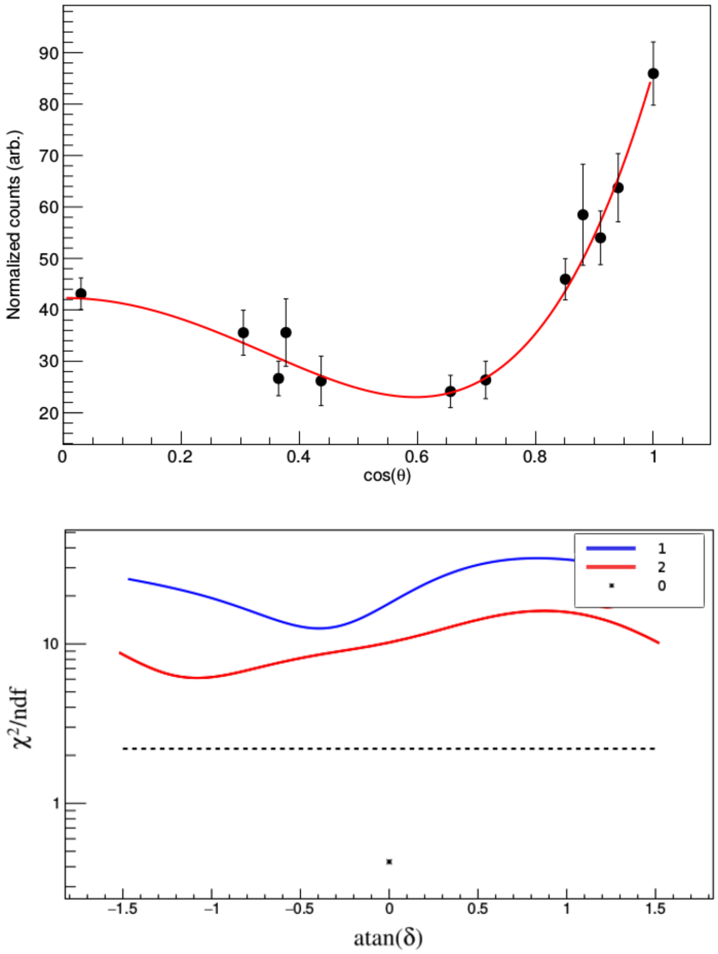

Figure 5.14: γ-γ angular correlation for the 1987-keV $\rightarrow$ 1230-keV $\rightarrow$ 0-keV, $J_i \rightarrow 2^+ \rightarrow 0^+$ cascade. The angular correlation (top) resulted in a spin assignment of $J_i = 0$ for the 3216-keV level based on the χ^2 minimization plot (bottom). The reduced χ^2 for the angular correlation fit was 0.44. The dotted line represents the 3σ limit. For a pure $E2$ transition, there can be no mixing for $J_i = 0$ and only a single point for atan(δ). The statistics were too low for event-mixed normalization and using the full number of angle pairs. Instead, the normalization was done using number of detector pairs for each angle, and the statistics were folded about the y-axis.

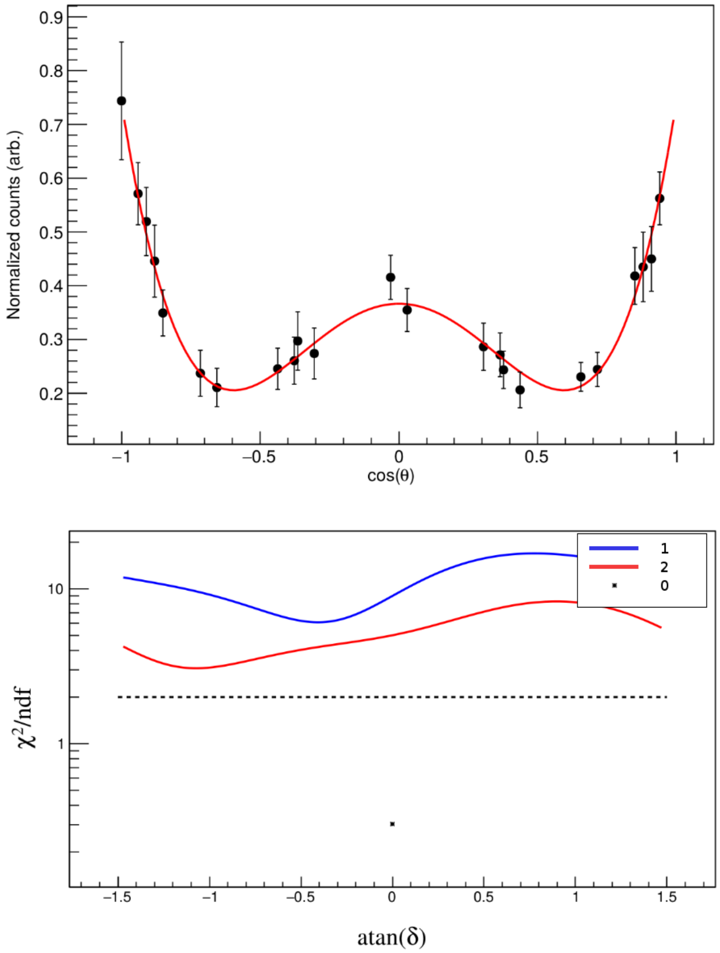

Figure 5.15: γ-γ angular correlation for the 2123-keV $\rightarrow$ 1230-keV $\rightarrow$ 0-keV, $J_i \rightarrow 2^+ \rightarrow 0^+$ cascade. The angular correlation (top) resulted in a spin assignment of $J_i = 0$ for the 3353-keV level based on the χ^2 minimization plot (bottom). The reduced χ^2 was 0.284. The dotted line represents the 3σ limit. For a pure $E2$ transition, there can be no mixing for $J_i = 0$ and only a single point for atan(δ).

gating on the 916.5-keV photopeak shows the same 452-keV and 449-keV photopeaks as well as the transitions in coincidence below them. A photopeak of 1365.6 keV is also identified when gating on the 1095-keV transition from the 2325-keV, $J = 3^-$ state. Based on the feeding to states with $J = 3^-$ and 4^-, and no observed feeding from the capture state, it is expected that the spin of this 3690.6-keV level is $J = 5^-$.

3881.91(3): This level is directly fed from the neutron capture state by a 5444-keV transition. Only one transition of 1557 keV is observed to populate the 2325-keV $J = 3^-$ level. Based on this, a tentative spin of $J = 2^-$ is assigned.

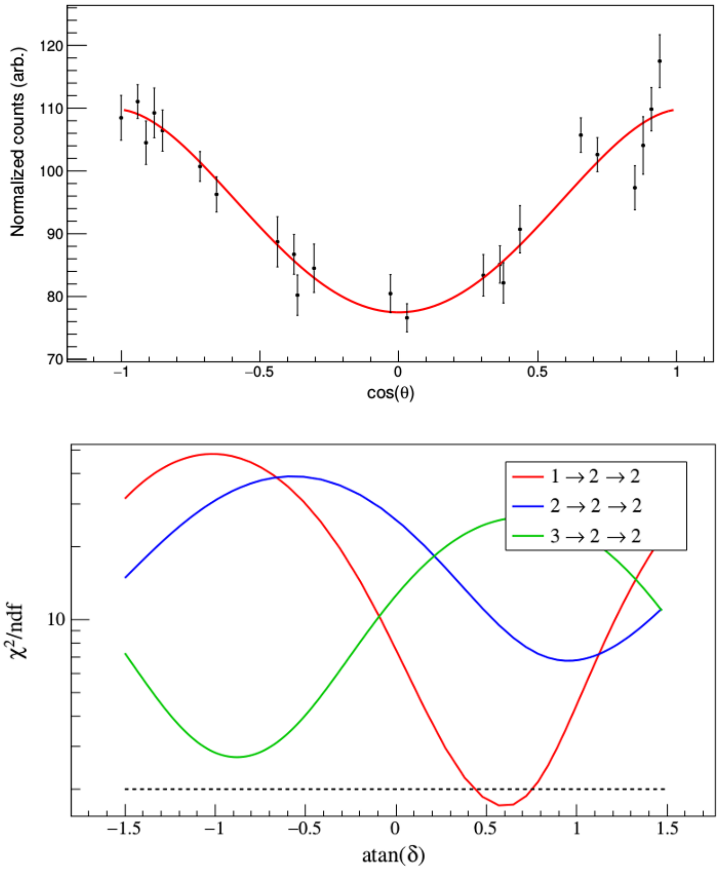

Figure 5.16: γ-γ angular correlation for the $E_{\gamma 1} = 1048$-keV and $E_{\gamma 2} = 1098$-keV transitions in the $J_1 = 2^+$, 3375-keV $\rightarrow J_2 = 2^+$, 2328-keV $\rightarrow J = 2^+$, 1230-keV cascade. The angular correlation (top) resulted in a spin assignment of $J_i = 1$ and a mixing ratio of $\delta = 0.67(10)$ for the 1048-keV transition based on the χ^2 minimization plot (bottom). The reduced χ^2 of the angular correlation was 1.67. The dotted line represents the 3σ limit.

4014.7(3): This level is directly fed from the neutron capture state by a 5311-keV transition. Only one transition of 1690 keV is observed to populate the 2325-keV $J = 3^-$ level. Based on this, a tentative spin of $J = 2^-$ is assigned.

4023.94(15), 4117.80(15): These levels have several transitions to $J = 0^+, 2^+, 4^+$ states and are both directly populated by transitions from the neutron capture state. This suggests a tentative spin assignment of 2^+ to both of these levels.

4028.37(19), 4034.41(19): These levels are both populated directly from the capture state. The 4028-keV level decays to $J = 1^+$ and 2^+ states and the 4034-keV level decays to 2^+ states. These states are both tentatively assigned as $J = 3$.

4191.57(57): This level decays to $J = 2^+, 3^-$ and 4^- states and is directly populated by the neutron capture state. Based on on this, the level is tentatively assigned a spin of $J = (2^-, 3^-)$.

4667.8(4): This level has only one observed transition decaying to the 3270-keV, $J = 1$ level. It is also directly populated by a 4658-keV from the capture state. An tentatively assigned spin of $J = (3^-)$ is given.

4769.65(15): This level is directly populated by a 4556.5-keV transition from the capture state and decays to several levels with spins of $J = 1^+, 2^+$ and 4^-. Based on no observed ground state decay, and a decay to the 4^- state(although with a branching ratio of only 9(4)%), the spin of this level is tentatively assigned as a $J = (2^-, 3^+)$.

4848.02(19): This state is directly populated from the neutron capture state by a 4477-keV transition, and decays to states with spins of $J = 1^+$ and 2^+. Based on this, a spin of $J = 2^-, 3^+$ is tentatively given.

5123.9(4): This level decays with only one observed transition to the 2738-keV, $J = 1^+$ state. It is also populated from the neutron capture state by a 4202.51-keV transition. A tentative spin of $J = 3^+$ is given.

All other newly identified states: The remaining states that are newly observed are all directly populated from the neutron capture state, and decay to the ground state and/or excited 0^+ states. Based on these observations and the γ-decay selection rules, the levels are all tentatively assigned as $J = (1, 2^+)$. Furthermore, these are the states which could belong to the PQR.

5.3.3 Pygmy Quadrupole Resonance Candidate States

To establish any energy levels which may belong to the PQR, it was necessary to identify states with $J = 2^+$. It was expected that, if the capture state is predominantly a $J = 1^+$ state, states of $J = 0, 1$ or 2 were populated by primary transitions. Based on the single particle estimates for γ decay, the most likely transitions should be electric dipole, $E1$, which would require a change in parity. Yet, many of the states with known spin and parity which were populated directly from the capture state were of positive parity. This implies $M1$ and $E2$ transitions. The ground state decay, or any decay to a 0^+ state via γ-ray emission would mean that a $J = 0$ is not possible. The majority of the states of interest could only be limited to $J = 1$ or 2. The tentative assignments are based on the γ-decay selection rules. The observation of a decay to the ground state from these levels also indicates a minimum spin of 1, and likely a maximum of 2^+. A 2^- is possible, but $M2$ transitions would compete weakly to the ground state compared to $E1$ transitions to low-lying 2^+ states.

The present experiment does not probe for pygmy resonances directly, but rather indirectly from the primary transitions. As such theoretical calculations were performed to compare the level densities which can be used to help predict the number of each type of state. Furthermore, the branching ratios were measured to identify the states with enhanced ground-state feeding. As previously mentioned, this is a possible signature of the PQR.

5.3.4 Theoretical Calculations

The level density for each spin was explored with comparisons to microscopic shell-model calculations using the full *gdsh*-valance space as well as generalized-seniority calculations, both performed by Dr. Chong Qi. The generalized-seniority scheme is a simplistic, yet powerful approach to understanding the shell structure through the nuclear pairing interaction and the number of broken pairs [93]. The generalized-seniority calculations were performed with the same Hamiltonian that used a truncated shell-model space that included up to seniority, $\nu = 8$, or equivalently four broken pairs, as outlined in Reference [94]. All states up to 8 MeV were essentially projected; however, only the lower-spin states were considered for comparisons to the present experiment as the lower spins are predominantly populated from the primary transitions. The other calculation uses a monopole optimized realistic nucleon-nucleon interaction as outline in Reference [95] as well as the full valence space of orbitals between $N = 50$ and $N = 82$ which correspond to the $g_{7/2}, d_{5/2}, s_{1/2}$ and $h_{11/2}$. In the previous theoretical study [95], only the $d_{5/2}, s_{1/2}$ and $h_{11/2}$ orbitals were employed.

The results from each of the calculations produced excited energy levels up to 6 MeV with spins up to $J = 5$ with both even and odd parities. Only $J = 0^+$, 1 and 2 are compared, shown in Figure 5.17, as these are the dominant spins observed in the experimental results and are the spins of interest for the PQR (2^+), as well as the PDR (1^-). The $J = 0^+$ states are also of interest with respect to shape coexistence. However, the present calculations assume a ^{100}Sn core, such that cross-shell excitations do not take place and the 2p-2h 0^+ bandhead will not be reproduced.

From a level density point of view, the agreement between experiment and theory is good, with the exception of the lower-lying $J = 2^+$ states around 2 MeV region. As there are many experimentally observed states with tentative spins of $J = (1, 2^+)$, these were placed to both spins in Figure 5.17 (in magenta) as a means to compare to the calculated states of the same spin. In the figure, blue levels are the positive parity states produced by the shell model calculations using the full valence space and red are the negative parity states. Green levels are the positive parity states produced with the general-seniority calculations and purple are the negative parity states.

Generally for the $J = 1$ and 2 levels, both calculations predict higher negative parity energies than positive parity energies. The only way to couple to $J = 1^-$ is with three neutron orbitals. This is because the negative parity orbital is the $h_{11/2}$ and the positive parity with highest orbital angular momentum is the $g_{7/2}$. These can couple to a minimum of 2^-. However, the $g_{7/2}$ is expected to be higher in energy (see Figure 5.18) and the 2^- states are likely to also be higher in energy. The lower observed energy of the 2^+ states is due to the mixing with the proton excitations across the shell closure which means the calculations will not produce these. Although it would be reasonable to assume that a second broken pair should amount to a 2^+ state at twice the first excited state, this is not possible with the lowest energy orbitals—all orbitals are full except the $d_{3/2}$.

Only the three lowest $J = 1$ (3270 keV and 3375 keV) states are known—2738 keV with positive parity, 3270-keV with unassigned parity, and the newly identified 3375-keV with unassigned parity. Based on the first instance of $J = 1^-$ in ^{116}Sn at 3334 keV [20], it is likely that the 3270-keV level

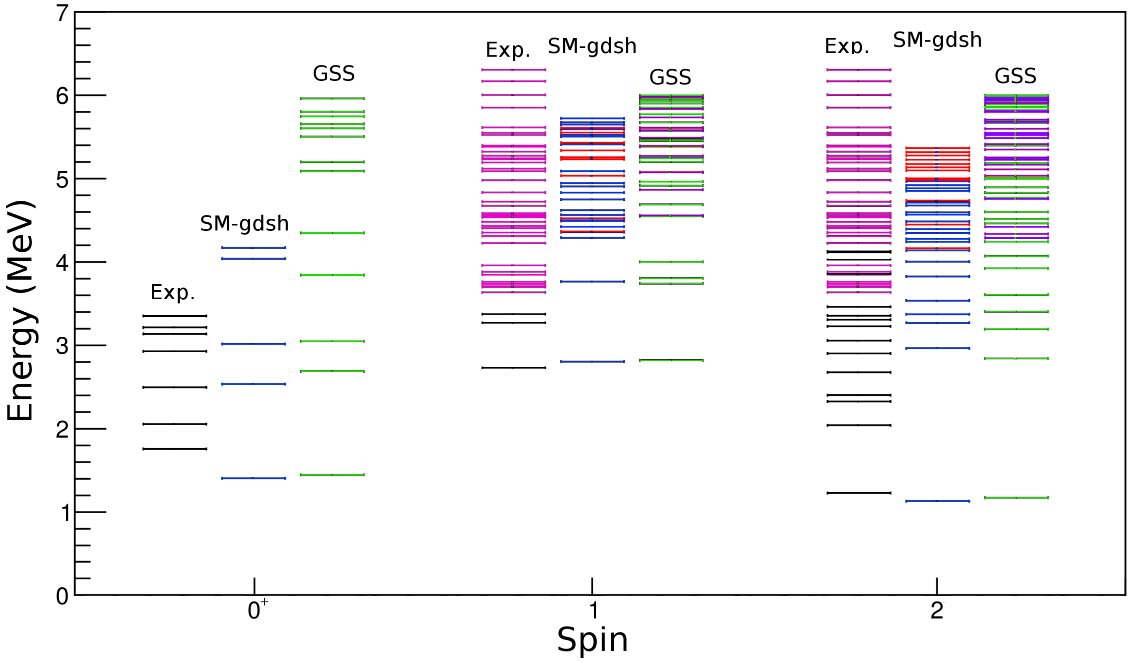

Figure 5.17: Experimentally observed states (black) for spins of $J = 0^+, 1$ and 2 compared to the large scale shell-model calculations with full *gdsh* valence space (blue and red) and the general-seniority scheme calculations (green and purple). The magenta coloured experimental levels are identical for $J = 1$ and 2 as these states could not be firmly assigned as one or the other.

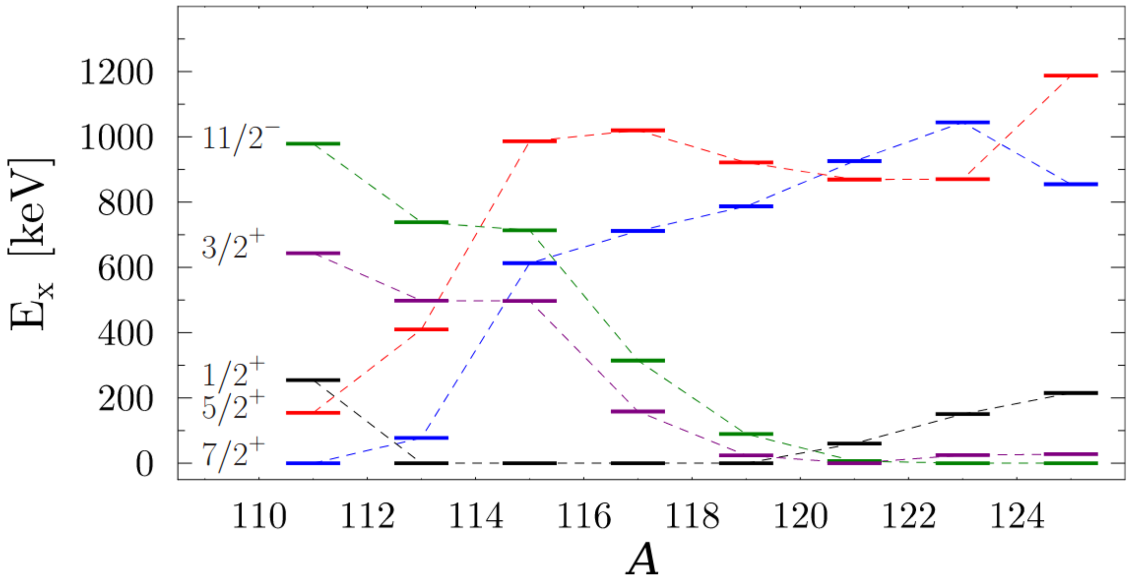

Figure 5.18: The low-lying states in odd-A Sn isotopes which are taken as the single-particle levels of the valence space—$g_{7/2}$ (blue), $d_{5/2}$ (red), $s_{1/2}$ (black), $d_{3/2}$ (purple), and $h_{11/2}$ (green). Based on this, the ground-state in ^{118}Sn is expected to have a full occupancy of the $g_{7/2}$ and $d_{5/2}$ with contributions $\mathrm{d}^4_{3/2}$ and $\mathrm{s}^2_{1/2}\mathrm{d}^{-2}_{3/2}$. This is expanded on in Table 5.5. Adapted from Reference [74] with permission.

also has negative parity. The calculations reproduce the first $J = 1^+$ reasonably well, but after that it is hard to say much on the spin assignment.

For the 0^+ states, the lower energies from the calculations are not expected for the first excited 0^+. This state is known to be related to the 2p-2h which, as mentioned, are not included in the present calculations. The shell model calculations include an average number of particles in each orbital. For the yrast states (lowest energy for each spin and parity) these are shown in Table 5.5. What this reveals is that the most likely configuration for the ground-state is in line with the single-particle states presented in Figure 5.18 with the higher-lying $d_{5/2}$ and $g_{7/2}$ states in ^{117}Sn being predominantly occupied and the lower-lying $d_{3/2}$ consisting of a pair of neutrons. The $s_{1/2}$ and $h_{11/2}$ seem to share the last remaining two neutrons.

5.3.5 Branching Ratios

The branching ratios of the γ-ray transitions have been measured, as shown in Table 5.1, and may provide insight to possible PQR states. If an enhanced branching ratio to the ground state, b_0, is truly a signature of the $J = 2^+$, PQR states, then it could be possible to assign states that may belong to this excitation mode. Of course, the spins of the states would need to be known to acknowledge this fingerprint critically.

Comparing to the branching ratios shown in Figures 5.2 and 5.3 from References [11, 12], the measured ground-state branching ratios are shown for the 3–6 MeV levels in Figure 5.19. The den-

Table 5.5: The average occupancies of each orbital, j, for the yrast states based on the shell-model calculations. The number of particles, on average, in each orbital can be calculated with the values given below multiplied by the number of particles each orbital can hold $(2j+1)$.

j	0^+	1^+	2^+	1^-	2^-
$0g_{7/2}$	0.833	0.878	0.821625	0.845	0.832
$1d_{5/2}$	0.860	0.907	0.8575	0.801	0.798
$1d_{3/2}$	0.425	0.406	0.44375	0.340	0.369
$2s_{1/2}$	0.546	0.533	0.528	0.457	0.464
$0h_{11/2}$	0.282	0.237	0.288	0.347	0.346

Table 5.6: A comparison of the $E0$ quantities measured indirectly as shown in Figure 5.20. The previously measured values are tabulated in Reference [21].

	$q_k^2(E0/E2)$	$X(E0/E2)$	$\rho^2(E0)\times 10^3$
Ref. [21]	8.4(19)	4.2(10)	> 36
This experiment	12.7(11)	6.3(6)	> 38

sity of states in the 3–5 MeV are comparable to the previous studies on the PQR for the ^{112,114,124}Sn isotopes. However, on average, the present experiment observes less ground-state feeding. The greatest branching ratios occur above 5 MeV which are above the expected PQR region. In Figure 5.2, the PQR states are between 3 and 4 MeV with nearly all being above $b_0 = 0.4$. In Figure 5.3, the majority of PQR states are between 3.5 and 4.5 MeV with most being above $b_0 = 0.5$.

5.3.6 Indirect $E0$ Measurement

In order to measure the $E0$ transition between the 2057-keV and 1758-keV 0^+ states, and indirect measurement of the 528-keV, $E2$ transition from the 1758-keV level was compared to the 827-keV, $E2$ transition from the 2057-keV level. This was done by gating on the 7269-keV primary transition as shown in Figure 5.20 and observing both of these $E2$ transitions. It was assumed any $E0$ strength from the 1758-keV to the ground state was negligible such that all of the 299-keV, $E0$ transition between 2057-keV and 1758-keV states contributes to the observed 528-keV photopeak.

The measured values are shown in Table 5.6 and are compared to the values in Reference [21]. The half-life of the 2057-keV level is known to an upper limit of 200 ps which is similar to the half-life of 163(20) ps for the 0_3^+ in the neighbouring ^{116}Sn. However, this only gives a lower limit on the $\rho^2(E0)\times 10^3$ value of > 36 [21]. The reason for the 10^3 factor is because $\rho^2(E0)$ values are typically 10^{-3} to 10^{-1}. The measured value obtained indirectly in the present experiment was determined to be > 38.

Not only is this in good agreement, it shows that $E0$ transitions, with the right circumstances, can be indirectly measured. Other $E0$ transitions were investigated through indirect measurements carried out in the same manner. However, no further observations were made.

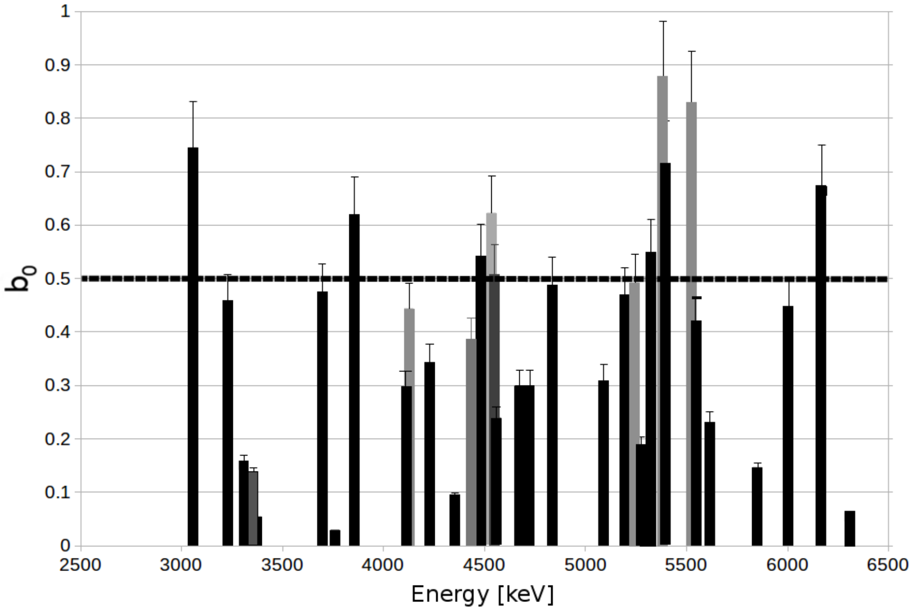

Figure 5.19: The absolute ground-state branching ratio, b_0, for the potential 2^+ states in the 3–5 MeV corresponding to the PQR energy region. Additional states beyond 6 MeV are included to highlight the large ground-state branching observed in what could also be the isoscalar PDR region ($J = 1^-$ states). The different shades of grey are used to separate states with similar energies.

5.3.7 Discussion

The neutron capture experiment proved to be successful in populating a large number of states in the 3–5-MeV region of interest that may belong to the PQR excitation mode. However, from the 60 levels placed in this energy region, only seven are assigned, or tentatively assigned as $J = 2^+$. A further 28 could possibly have $J = 2^+$, but other spins cannot be excluded. With this in mind, level density comparisons to shell-model and general seniority calculations were made, as well as comparisons to the previous PQR studies.

The two calculations produced levels up to 6 MeV with comparable level densities to the present experiment—provided the 28 states with $J = 1$ or 2 are split between the two spins. The shell-model calculations produced 29 $J = 1$ states compared to 34 for the generalized-seniority calculations and 34 $J = 2$ states similarly compared to 57. Experimentally, the total number of $J = 1$ and 2 states was 52. If 30 of these are $J = 2$, for example, it is expected, based on both sets of calculations, that the highest-lying $J = 2$ states are of negative parity. Only 5 $J = 2^-$ states below 5 MeV were produced by each of the calculations. For the shell-model calculations, all of the $J = 2^+$ states were below 5 MeV, whereas 18 of the 34 $J = 2^+$ states produced with the generalized-seniority calculations were above 5 MeV.

Similarly for the $J = 1$ states, both calculations predominantly produce positive parity for $J = 1$ below 5 MeV. With this in mind, as well as the gamma decay from these states to the ground state, it is most likely that these states are $J = (1, 2^+)$.

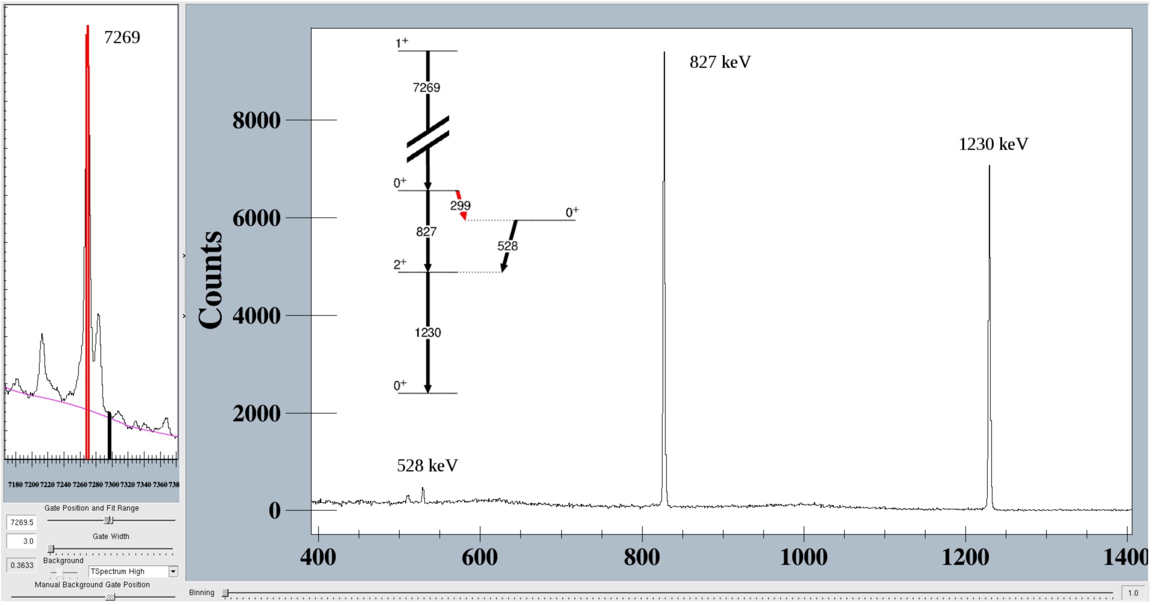

Gate Position and Fit Range 7269.5

Gate Width 3.0

Background 0.3633 TSpectrum High

Manual Background Gate Position

Binning 1.0

Figure 5.20: The projection of the γ-γ coincidence matrix is displayed with one axis on the left where the energy gate is placed, and the other axis is projected on the right. Here an obvious 827 keV and 1230 keV cascade is seen when gating on the primary transition of 7269 keV that directly feeds the 2057-keV, 0^+ level. Furthermore, a 528-keV peak is observed, indicating an unobserved $E0$ transition connecting the two excited 0^+ states (partial level scheme is inset to show the γ-ray cascades). From the branching ratio between the 827-keV and the 528-keV (which is assumed to represent the events of the missing 299-keV, $E0$ transition), the $\rho^2(E0)$ was determined (see Table 5.6).

It is difficult to say much about the PQR with the present neutron capture experiment due to these spin uncertainties. The branching ratios which were obtained do show an enhanced ground-state feeding which is suggested to be a property of PQR states. It is possible that the states above 5 MeV are $J = 1^-$ and could belong to the lower energy, isoscalar PDR rather than the PQR. Thermal neutron capture experiments, however, can populate states with very different configurations. This makes it even more difficult to determine nuclear structure beyond what is already known.

One such known structure that ^{118}Sn exhibits shape coexistence with a deformed intruder band built on a proton 2p-2h excitation across the shell closure (as expressed in the β-decay study). One of the findings in the β-decay study was a triplet at $\approx$285 keV. The separation of intensities reduced the previously reported relative branching ratio of 2.5(2) for the 284.5-keV to 1.31(17). This reduced the $B(E2)$ value from 39(7) W.u. to 21(4) W.u., suggesting less collectivity in the 2p-2h 2043-keV state.

The present experiment was in good agreement with the β-decay study. Here, the relative branching ratio for the 284.5-keV transition is 1.1(3) which compares well, albeit with higher uncertainty. This supports that the $B(E2)$ is in fact, less than what was previously given. It also supports the scenario in which the higher energy 2^+ states are mixed with the 2p-2h configuration and shares some of the $B(E2)$ strength.

Further to the topic of shape coexistence, the present experiment shows the possibility for indirect $E0$ measurements. Although some prior knowledge of the level scheme is necessary—lifetimes and spins, for example— an enhanced $E0$ can very well be indirectly measured through an $E2$ transition directly below. In this experiment, six $J = 0^+$ levels are observed via primary transitions. The 2057-keV level, from which the 299-keV $E0$ transition was indirectly measured, was populated by the 7269-keV primary transition with a 0.46(4)% branching ratio from the neutron capture state. Three other 0^+ states had similar branching ratios, but no observations of $E2$ transitions from other 0^+ states were in coincidence. This may suggest that these 0^+ states belong to a different structure than the 2p-2h configuration and are not very mixed.

Chapter 6

Conclusion

The long isotopic chain of semi-magic Sn provides an important testing ground for theoretical models used to predict how nuclear structure evolves from the neutron-deficient to the neutron-rich landscapes. With a closed shell of protons, $Z = 50$, Sn consists of 10 stable isotopes—the most of any element. Yet, many topics remain open for experimental and theoretical study. The recent studies on shape coexistence in ^{116}Sn [65] and PQR in ^{112,114,124}Sn [11, 12] led to the two present studies on ^{118}Sn.

The β-decay study was carried out at TRIUMF and utilized the GRIFFIN spectrometer. The 5^+ isomer in ^{118}In was observed to β decay directly to 17 states, and a total of 99 γ-ray transitions were placed to 23 low-lying excited states in ^{118}Sn. One level and 43 γ-ray transitions were newly observed. The primary goal was to investigate the proton 2p-2h states that give rise to shape coexistence. Previous findings on ^{116}Sn suggest a higher-lying 2.03-MeV, 0_3^+ state as the 2p-2h bandhead, rather than the 1.76-MeV, 0_2^+ state. This was based on the large $B(E2)$ value of 100(10) W.u. for the 2p-2h $2_2^+ \rightarrow 0_3^+$ compared to 44(6) W.u to the 0_2^+.

In the present β-decay experiment, no evidence for a reassignment of the 2057-keV, 0_3^+ level to the 2p-2h bandhead in ^{118}Sn was evident. In fact, the 2p-2h states with $J = 0^+, 2^+$ and 6^+ were all observed, but the 0_3^+ was not. The 0_3^+ is higher in energy than the 2p-2h, 2042-keV, 2_2^+, which would make it unlikely to be the bandhead to begin with and is likely the reason why it was not observed. A measure of mixing between 0^+ states, as well as shape evolution is through the transition probabilities for $E0$ decays, $\rho^2(E0)$. From Reference [21], the $\rho^2(E0 : 0_3^+ \rightarrow 0_2^+) > 36$ which suggests the 0_3^+ is strongly mixed with the 0_2^+. This is also the case with the $E0$ between the same states in ^{116}Sn where the $\rho^2(E0) = 86(16)$. Even if the 0_2^+ is not the bandhead in ^{116}Sn, it shares much of the same character with the 0_3^+ as evidenced by the enhanced $E0$ transition.

Another finding related to the 2p-2h band was a reduction in intensity of the 284.5-keV transition ($2_2^+ \rightarrow 0_2^+$). This transition was separated from the 285.2-keV and 286.0-keV transitions using γ-γ coincidences. The previous relative branching ratio for the 284.5-keV transition was 2.5(2) [66] and for the 285.2-keV was 5.1(6) [58]. These two transitions are in direct coincidence with each other and their intensities were likely summed together. In the present β-decay experiment, the branching ratios were determined to be 1.31(17) for the 284.5-keV transition and 2.3(8) for the 285.2-keV transition. The importance in this finding is related to the collectivity of the 2p-2h, 2_2^+ level at 2042 keV. The $B(E2)$ of the 284.5-keV was reduced from 39(7) W.u. in Reference [58] to 21(4) W.u. in the present experiment. This suggests that the 2_2^+ level is less collective than previously thought, and that there is likely a greater mixing with higher-lying 2^+ states. However, this is difficult to confirm without the necessary lifetimes of all of the states.

The ^{117}Sn(n,γ) experiment performed at the ILL utilized the FIPPS array which detected a significant number of γ-ray transitions from ^{118}Sn up to the neutron separation energy of 9326 keV. This experiment was aimed to distinguish $J = 2^+$ states in the 3–5-MeV region that corresponds to the predicted PQR states. A total of 96 levels and 423 γ-ray transitions were placed to the level scheme with 46 levels and 357 transitions being newly observed. Of these energy states, 60 are within the PQR energy region. However, the spins could only be tentatively assigned $J = (1,2^+)$ based on the γ-decay selection rules.

Angular correlations were attempted to firmly assign the spin, but the states of interest were too weakly populated. There were, however, four levels which were assigned spins based on the angular correlation measurements. The previously known 2929-keV level had a tentative spin of $J = 0^+, 1^+$. Angular correlations were able to exclude the 1^+, allowing for a firmly assigned spin of $J = 0^+$. The other three levels were the newly observed 3216-keV, 3353-keV, and 3375-keV and were assigned spins of $J = 0^+$, $J = 0^{(+)}$ and $J = 1$, respectively. Furthermore, the 1048-keV transition which decays from the 3375-keV level, has a measured mixing ratio of $\delta = 0.67(10)$.

Shell-model calculations and generalized-seniority calculations were performed to predict the expected level densities. While the number of levels calculated agreed fairly well with the present experiment, without having firmly assigned spins, it is difficult to say much in regards to the PQR. When comparing all of the $J = (1,2^+)$ levels from the experiment to the $J = 1,2$ of both calculations, there is a case for the lower energies in the 3–5-MeV region being 2^+ and the higher energies being 1^-. This is based on both calculations generally producing more positive parity states at lower energy, and more negative parity states at higher energy. With the observed ground state decay from these states, $E1$ from 1^- and $E2$ from 2^+ would be the most probable decays (compared to $M1$ and $M2$ from 1^+ and 2^-, respectively).

Enhanced ground state branching ratios are also considered to be a signature of the PQR states. The previous experimental studies which identified PQR states in ^{112,114}Sn [11] and ^{124}Sn [12] show enhanced ground state feeding of potential 2^+ states that are nearly 50% of the total branching or greater. However, some of these states are not confirmed as 2^+ in the ^{112,114}Sn study. In the present study, there are several transitions in the region of interest that have enhanced ground state feeding of nearly 50% or more of the total branching. Due to the uncertainty on the spins, it is difficult to make a strong case for these states to be of a PQR mode. If the previous assumption of the lower-lying states in this region being predominantly $J = 2^+$ and the higher-lying being $J = 1^-$, this would be promising for studying both the PQR states, as well as the lower-lying isoscalar PDR states with thermal neutron capture.

In the studies of the PQR in ^{112,114,124}Sn of References [11] and [12], hadronic inelastic scattering experiments, $(p,p'\gamma)$ and $(\alpha,\alpha'\gamma)$, respectively, probed the isoscalar component of the PQR since these reactions favour the excitation of surface modes. In the present (n,γ) experiment, all excited states can be populated by primary transitions (within the γ-decay selection rules) making it difficult to distinguish between surface modes and single particle states. It would be a good complimentary experiment to perform an (α,α') inelastic scattering reaction on a ^{118}Sn target to identify the possible PQR mode.

With both of the present experiments studying the nuclear structure of the same nucleus, comparisons between the two were also made. For instance, the 284.5-keV and 285.2-keV transitions were identified in the neutron capture experiment with comparable branching ratios to the β-decay experiment. This confirms the previously assessment of these states and establishes the lower $B(E2) = 21(4)$ W.u. value. Where the β-decay experiment failed to populate the 2057-keV, 0_3^+ states, the (n,γ) experiment populated this state with a strong primary transition which was used to establish the $E0$ transition which connects the 0_3^+ to the 0_2^+.

The $E0$ was indirectly measured by gating on the 7269-keV primary transition which populates the 2057-keV, 0_3^+ level. An $E2$ transition from the 1758-keV, 0_2^+ to the 1230-keV 2_1^+ level was observed in coincidence and was assumed to be the result of an unobserved 299-keV, $E0$ transition populating the 1758-keV level. The $\rho^2(E0) > 38$ was measured indirectly from the peak area of the 528-keV, $E2$ transition and is in good agreement with the previous reported value of $\rho^2(E0) > 36$.

The other 0^+ states which are populated from primary transitions were investigated for potential $E0$ transitions with no observations. Three of these 0^+ states are populated with similar primary transition intensities. By not observing these $E0$ transitions indirectly, this could possibly suggest that the $\rho^2(E0)$ is relatively small and the structure of the higher-lying 0^+ states are of a different configuration than the 0_2^+ and 0_3^+. While this is not necessarily a new technique for measuring $E0$ transitions, it could be an option if the level scheme allows for it. Furthermore, the relatively high γ-ray intensity of the 828-keV transition ($0_3^+ \to 2_1^+$) of 5.3(2) per one hundred 1230-keV events ($2_1^+ \to 0_1^+$) would make the ^{117}Sn(n,γ) experiment a good candidate for lifetime measurements using LaBr$_3$ detectors.

As such, a recently proposed experiment to measure the same ^{117}Sn$(n,\gamma)^{118}$Sn reaction at the ILL with FIPPS is scheduled to run in the fall of 2023. The intention of this experiment is to couple the FIPPS array with LaBr$_3$(Ce) detectors used for fast-timing measurements of nuclear levels. It is likely that the lifetimes of several low-lying 2^+ states as well as the 0_3^+ state will be established with better precision than the current values. The FIPPS array is also now coupled with BGOs for Compton suppression which will make the γ-ray analysis much easier to decipher.

Bibliography

[1] Kenneth S Krane. *Introductory nuclear physics*. Wiley, New York, NY, 1988.

[2] R F Casten. *Nuclear Structure from a Simple Perspective; 1st ed.* Oxford Univ. Press, New York, NY, 1990.

[3] Tomoaki Togashi, Yusuke Tsunoda, Takaharu Otsuka, Noritaka Shimizu, and Michio Honma. Novel shape evolution in sn isotopes from magic numbers 50 to 82. *Phys. Rev. Lett.*, 121:062501, Aug 2018.

[4] Paul E. Garrett, Magda Zielińska, and Emmanuel Clément. An experimental view on shape coexistence in nuclei. *Progress in Particle and Nuclear Physics*, 124:103931, 2022.

[5] Kris Heyde and John L. Wood. Shape coexistence in atomic nuclei. *Rev. Mod. Phys.*, 83:1467–1521, Nov 2011.

[6] A Migdal, J Levinger, and A Migdal. Nuclear photo-disintegration. *J. Phys.(USSR)*, 8:331, 1944.

[7] G. C. Baldwin and G. S. Klaiber. Photo-fission in heavy elements. *Phys. Rev.*, 71:3–10, Jan 1947.

[8] E.G. Lanza, L. Pellegri, A. Vitturi, and M.V. Andrés. Theoretical studies of pygmy resonances. *Progress in Particle and Nuclear Physics*, 129:104006, 2023.

[9] A Zilges. The pygmy dipole resonance – experimental studies of its structure and new developments. *Journal of Physics: Conference Series*, 590:012006, apr 2015.

[10] Zilges, Andreas and Savran, Deniz. The pygmy dipole resonance - past, presence, and future. *EPJ Web of Conferences*, 93:01028, 2015.

[11] N. Tsoneva, M. Spieker, H. Lenske, and A. Zilges. Fine structure of the pygmy quadrupole resonance in 112,114sn. *Nuclear Physics A*, 990:183–198, Oct 2019.

[12] Mark Spieker, N. Tsoneva, Vera Derya, Janis Endres, D. Savran, M.N. Harakeh, Sotirios Harissopulos, R.-D Herzberg, Anastasios Lagoyannis, N. Pietralla, Lucia Popescu, Marcus Scheck, Friederike Schlüter, Kerstin Sonnabend, V.I. Stoica, Heinrich Wörtche, and A. Zilges. The pygmy quadrupole resonance and neutron-skin modes in 124sn. *Physics Letters B*, 752:102, 11 2015.

[13] K. Heyde. *Basic Ideas and Concepts in Nuclear Physics: An Introductory Approach*. Institute of Physics Publishing, third edition, 2004.

[14] S.S.M. Wong. *Introductory Nuclear Physics*. Wiley, second edition, 1998.

[15] Brookhaven National Laboratory National Nuclear Data Center. Nudat (nuclear structure and decay data).

[16] Maria Goeppert Mayer. Nuclear configurations in the spin-orbit coupling model. i. empirical evidence. *Phys. Rev.*, 78:16–21, Apr 1950.

[17] G Friedlander, J W Kennedy, E S Macias, and J M Miller. Nuclear and radiochemistry, 3rd edition. 1 1981.

[18] V. F. Weisskopf. Radiative transition probabilities in nuclei. *Phys. Rev.*, 83:1073–1073, Sep 1951.

[19] B.A. Brown. Lecture notes in nuclear structure physics. `http://nuclear.fis.ucm.es/PDFN/documentos/BAB-lecture-notes-NUCLEAR-PHYSICS.pdf`, note = Accessed: 2023-06-20, November 2005.

[20] Jean Blachot. Nuclear data sheets for a = 116. *Nuclear Data Sheets*, 111(3):717–895, 2010.

[21] T. Kibédi, A.B. Garnsworthy, and J.L. Wood. Electric monopole transitions in nuclei. *Progress in Particle and Nuclear Physics*, 123:103930, 2022.

[22] Tibor Kibedi, T.W. Burrows, M. Trzhaskovskaya, Charles Nestor, and P. Davidson. Internal conversion coefficients - how good are they now? *http://dx.doi.org/10.1051/ndata:07771*, 05 2008.

[23] A. MacLean. Gamma-gamma angular correlation measurements with griffin. Master's thesis, University of Guelph, 2016.

[24] G. F. Knoll. *Radiation Detection and Measurement*. Wiley, third edition, 2000.

[25] J. Dilling, R. Krücken, and G. Ball. Isac overview. *Hyperfine Interactions*, 225(1):1–8, Jan 2014.

[26] M. Lindroos. Review of isol-type radioactive beam facilities. page 45. European Physical Society Accelerator Group, 2004.

[27] I. Bylinskii and M. K. Craddock. The triumf 500 mev cyclotron: the driver accelerator. *Hyperfine Interactions*, 225(1-3):9–16, 2014. ISAC and ARIEL: The TRIUMF Radioactive Beam Facilities and the Scientific Program.

[28] Sebastian Raeder, Henning Heggen, Jens Lassen, Friedhelm Ames, Daryl Bishop, Pierre Bricault, Peter Kunz, Anders Mjøs, and Andrea Teigelhöfer. An ion guide laser ion source for isobar-suppressed rare isotope beams. *Review of Scientific Instruments*, 85(3):033309, 2014.

[29] Pierre G. Bricault, Friedhelm Ames, Marik Dombsky, Peter Kunz, and Jens Lassen. Rare isotope beams at isac—target & ion source systems. *Hyperfine Interactions*, 225(1):25–49, Jan 2014. ISAC and ARIEL: The TRIUMF Radioactive Beam Facilities and the Scientific Program.

[30] A.B. Garnsworthy *et al.*. The griffin facility for decay-spectroscopy studies at triumf-isac. *Nuclear Instruments and Methods in Physics Research Section A: Accelerators, Spectrometers, Detectors and Associated Equipment*, 918:9 – 29, 2019.

[31] U. Rizwan, A.B. Garnsworthy, C. Andreoiu, G.C. Ball, A. Chester, T. Domingo, R. Dunlop, G. Hackman, E.T. Rand, J.K. Smith, K. Starosta, C.E. Svensson, P. Voss, and J. Williams. Characteristics of griffin high-purity germanium clover detectors. *Nuclear Instruments and Methods in Physics Research Section A: Accelerators, Spectrometers, Detectors and Associated Equipment*, 820:126 – 131, 2016.

[32] M.S.C. Winokan. Design and prototyping of a new scintillatorarray for β-tagging in griffin. Master's thesis, University of Surrey, 2019.

[33] Bildstein, V., Garrett, P.E., Ashley, S.F., Ball, G.C., Bianco, L., Bandyopadhyay, D., Bangay, J., Crider, B.P., Demand, G., Deng, G., Dillmann, I., Finlay, A., Garnsworthy, A.B., Hackman, G., Hadinia, B., Krücken, R., Leach, K.G., Martin, J-P., McEllistrem, M.T., Pearson, C.J., Peters, E.E., Prados-Estévez, F.M., Radich, A., Sarazin, F., Sumithrarachchi, C., Svensson, C.E., Vanhoy, J.R., Wong, J., and Yates, S.W. Descant and ayed neutron measurements at triumf. *EPJ Web of Conferences*, 93:07005, 2015.

[34] Bill Mills. Griffincollaboration/efficiencycalculator: Griffin online efficiency calculator, April 2020.

[35] A.B. Garnsworthy, C.J. Pearson, D. Bishop, B. Shaw, J.K. Smith, M. Bowry, V. Bildstein, G. Hackman, P.E. Garrett, Y. Linn, J.-P. Martin, W.J. Mills, and C.E. Svensson. The griffin data acquisition system. *Nuclear Instruments and Methods in Physics Research Section A: Accelerators, Spectrometers, Detectors and Associated Equipment*, 853:85 – 104, 2017.

[36] Giovanna Cicognani and Jacques Jestin. Annual report. Institut Laue-Langevin. `https://www.ill.eu/fileadmin/user_upload/ILL/1_About_ILL/Documentation/Annual_report/AR-21/Annual_report_2021.pdf`, 2021.

[37] Michelagnoli, Caterina, Blanc, Aurelien, Ruiz-Martinez, Emilio, Chebboubi, Abdelaziz, Faust, Herbert, Froidefond, Emmanuel, Kessedjian, Gregoire, Jentschel, Michael, Köster, Ulli, Mutti, Paolo, and Simpson, Gary. Fipps (fission product prompt spectrometer) and its first experimental campaign. *EPJ Web Conf.*, 193:04009, 2018.

[38] Institut laue-langevin. reactor safety faq. `https://www.ill.eu/reactor-and-safety/safety/reactor-safety-faq`. Accessed: 2022-11-28.

[39] Institut laue-langevin. fipps characteristics. `https://www.ill.eu/users/instruments/instruments-list/fipps/characteristics`. Accessed: 2022-11-28.

[40] Institut laue-langevin. the schematic view of neutron guides and instruments. `https://www.ill.eu/fileadmin/user_upload/ILL/3_Users/Instruments/PlanInstILL-2022-2023.pdf`. Accessed: 2022-11-28.

[41] Kazuki Fueda, Ryu Takami, Kenta Minomo, Kazuya Morooka, Kenji Horie, Mami Takehara, Shinya Yamasaki, Takumi Saito, Hiroyuki Shiotsu, Toshihiko Ohnuki, Gareth T.W. Law, Bernd Grambow, Rodney C. Ewing, and Satoshi Utsunomiya. Volatilization of b4c control rods in fukushima daiichi nuclear reactors during meltdown: B–li isotopic signatures in cesium-rich microparticles. *Journal of Hazardous Materials*, 428:128214, 2022.

[42] Munawar Karim and J. C. Overley. Analyzing power of the $^6\mathrm{Li}(\vec{n},^3\mathrm{H})^4\mathrm{He}$ reaction from 0.2 to 2.4 mev. *Phys. Rev. C*, 15:467–476, Feb 1977.

[43] Institut laue-langevin. fipps description. `https://www.ill.eu/users/instruments/instruments-list/fipps/description/instrument-layout`. Accessed: 2022-11-30.

[44] L. Knafla, A. Esmaylzadeh, A. Harter, J. Jolie, U. Köster, M. Ley, C. Michelagnoli, and J.-M. Régis. Development of a new gamma-gamma angular correlation analysis method using a symmetric ring of clover detectors. *Nuclear Instruments and Methods in Physics Research Section A: Accelerators, Spectrometers, Detectors and Associated Equipment*, 1042:167463, 2022.

[45] Mark Johnson. @MarkJ_Neutron. `https://twitter.com/markj_neutron/status/1103709939455930368?lang=ca`. Accessed: 2022-12-01.

[46] C. M. Petrache, J.-M. Régis, C. Andreoiu, M. Spieker, C. Michelagnoli, P. E. Garrett, A. Astier, E. Dupont, F. Garcia, S. Guo, G. Häfner, J. Jolie, F. Kandzia, V. Karayonchev, Y.-H. Kim, L. Knafla, U. Köster, B. F. Lv, N. Marginean, C. Mihai, P. Mutti, K. Ortner, C. Porzio, S. Prill, N. Saed-Samii, W. Urban, J. R. Vanhoy, K. Whitmore, J. Wisniewski, and S. W. Yates. Collectivity of the 2p-2h proton intruder band of $^{116}\mathrm{Sn}$. *Phys. Rev. C*, 99:024303, Feb 2019.

[47] Vinzenz Bildstein, Ryan Dunlop, pcbend, GRSIUser, SmithJK, James Smallcombe, Ryan Braid, gdemand, jhenderson88, bolaizol, AndrewMac1, Alex Laffoley, Jennifer Pore, Michelle Dunlop, cbray0, Daniel Yates, Kurtis, tiguser, tammyzidar, and test12345678test. Griffincollaboration/grsisort: Yappy yak, October 2019.

[48] Ryan Dunlop, Vinzenz Bildstein, pcbend, GRSIUser, SmithJK, James Smallcombe, Ryan Braid, gdemand, jhenderson88, bolaizol, AndrewMac1, Alex Laffoley, Jennifer Pore, Michelle Dunlop, cbray0, Daniel Yates, Kurtis, tiguser, tammyzidar, and test12345678test. Griffincollaboration/grsisort: Riveting rhino, October 2019.

[49] Fons Rademakers, Philippe Canal, Axel Naumann, Olivier Couet, Lorenzo Moneta, Vassil Vassilev, Danilo Piparo, Sergey Linev, Gerardo GANIS, Bertrand Bellenot, Guilherme Amadio, wverkerke, Enrico Guiraud, Pere Mato, TimurP, Matevž Tadel, wlav, Enric Tejedor, Andrei Gheata, Jakob Blomer, Stefan Roiser, marsupial, Anirudha Bose, CristinaCristescu, Raphael Isemann, Xavier Valls, Oksana Shadura, Kim Albertsson, Brian P Bockelman, and Omar Zapata. root-project/root: Patch release of v6.18 series, September 2019.

[50] K. Kitao. Nuclear data sheets update for a = 118. *Nuclear Data Sheets*, 75(1):99 – 198, 1995.

[51] Khalifeh Abusaleem and Balraj Singh. Nuclear data sheets for a = 71. *Nuclear Data Sheets*, 112(1):133–273, 2011. NUCLEAR PHYSICS AND RADIATION PHYSICS.

[52] Balraj Singh and Jun Chen. Nuclear data sheets for a=73. *Nuclear Data Sheets*, 158:1–257, 2019.

[53] Balraj Singh and Ameenah R. Farhan. Nuclear data sheets for a = 74. *Nuclear Data Sheets*, 107(7):1923–2102, 2006.

[54] D.J. Horen and M.B. Lewis. Nuclear data sheets for a = 75. *Nuclear Data Sheets*, 16(1):25–54, 1975.

[55] M. Shamsuzzoha Basunia. Nuclear data sheets for a = 28. *Nuclear Data Sheets*, 114(10):1189–1291, 2013.

[56] M.R. Bhat. Nuclear data sheets for a = 57. *Nuclear Data Sheets*, 85(3):415–536, 1998.

[57] Ryan Dunlop. *β and β-delayed neutron decay of the $N \approx 82$ nuclei $^{128-130}$Cd and ^{131}In studied with the Gamma-Ray Infrastructure for Fundamental Investigations of Nuclei (GRIFFIN)*. PhD thesis, University of Guelph, 2019.

[58] S. Raman, T. A. Walkiewicz, L. G. Multhauf, K. G. Tirsell, G. Bonsignori, and K. Allaart. Decays of ^{118}In, ^{120}In isomers to levels in ^{118}Sn, ^{120}Sn, and ^{122}Sn. *Phys. Rev. C*, 37:1203–1228, Mar 1988.

[59] J. Hattula, E. Liukkonen, and J. Kantele. Levels of ^{118}Sn populated in the decay of ^{118}In and ^{118}Sb isomers. *Z. Physik*, 231:203–215, March 1970.

[60] J. Kantele and M. Karras. Nuclear levels of even sn isotopes populated in the decay of in isomers. *Phys. Rev.*, 135:B9–B21, Jul 1964.

[61] K. Ortner, C. Andreoiu, M. Spieker, G. C. Ball, N. Bernier, H. Bidaman, V. Bildstein, M. Bowry, D. S. Cross, M. R. Dunlop, R. Dunlop, F. H. Garcia, A. B. Garnsworthy, P. E. Garrett, J. Henderson, J. Measures, B. Olaizola, J. Park, C. M. Petrache, J. L. Pore, K. Raymond, J. K. Smith, D. Southall, C. E. Svensson, M. Ticu, J. Turko, K. Whitmore, and T. Zidar. Collective 2p-2h intruder states in ^{118}Sn studied via β decay of ^{118}In using the griffin spectrometer at triumf. *Phys. Rev. C*, 102:024323, Aug 2020.

[62] H.W. Fielding, R.E. Anderson, P.D. Kunz, D.A. Lind, C.D. Zafiratos, and W.P. Alford. A study of the (3he, n) reaction on isotopes of tin. *Nuclear Physics A*, 304(2):520 – 532, 1978.

[63] J. Bron, W. H. A.Hesselink, A. Van Poelgeest, J. J. A. Zalmstra, M. J. Uitzinger, H. Verheul, K. Heyde, M. Waroquier, H. Vincx, and P. Van Isacker. Collective bands in even sn isotopes. *Nucl. Phys. A*, 318:335, 1979.

[64] P Stránský, A Frank, and R Bijker. On prolate shape predominance in nuclear deformation. *Journal of Physics: Conference Series*, 322(1):012018, oct 2011.

[65] J. L. Pore, D. S. Cross, C. Andreoiu, R. Ashley, G. C. Ball, P. C. Bender, A. S. Chester, A. Diaz Varela, G. A. Demand, R. Dunlop, A. B. Garnsworthy, P. E. Garrett, G. Hackman, B. Hadinia, B. Jigmeddorj, A. T. Laffoley, A. Liblong, R. Kanungo, B. Noakes, C. M. Petrache, M. M. Rajabali, K. Starosta, C. E. Svensson, P. J. Voss, Z. M. Wang, J. L. Wood, and S. W. Yates. Study of the β^--decay of 116m1in: A new interpretation of low-lying 0+ states in 116sn. *The European Physical Journal A*, 53(2):27, Feb 2017.

[66] I. V. Mikhailov and A. M. Demidov. Multipole mixes in γ transitions in ^{118}Sn. *Bull. Acad. Sci. USSR Phys. Ser.*, 53(5), March 1989.

[67] Wang M.and Audi G., Wapstra A.H., Kondev F.G., MacCormick M., Xu X., and Pfeiffer B. The ame2012 atomic mass evaluation. *Chinese Physics C*, 36(12):1603, dec 2012.

[68] P. Guazzoni, L. Zetta, A. Covello, A. Gargano, B. F. Bayman, T. Faestermann, G. Graw, R. Hertenberger, H.-F. Wirth, and M. Jaskola. ^{118}Sn levels studied by the ^{120}Sn(p, t) reaction: High-resolution measurements, shell model, and distorted-wave born approximation calculations. *Phys. Rev. C*, 78:064608, Dec 2008.

[69] L. C. M. do Amaral, C. V. de Barros Leite, J. M. F. Jeronymo, and A. G. de Pinho. Decay scheme of ^{118}In (4.45 min). *Z. Naturforsch.*, 24 a:1196–1202, 1969.

[70] NNDC Brookhaven National Laboratory. Logft calculator. `https://www.nndc.bnl.gov/logft/`.

[71] ANU. BrIcc Conversion Coefficient Calculator. `http://bricc.anu.edu.au/index.php`.

[72] E. Frota-PessÔa. States in 118sn from 117sn(d, p)118sn at 12 mev. *Il Nuovo Cimento A (1965-1970)*, 77(4):369–401, Oct 1983.

[73] J.K. Smith, A.D. MacLean, W. Ashfield, A. Chester, A.B. Garnsworthy, and C.E. Svensson. Gamma–gamma angular correlation analysis techniques with the griffin spectrometer. *Nuclear Instruments and Methods in Physics Research Section A: Accelerators, Spectrometers, Detectors and Associated Equipment*, 922:47 – 63, 2019.

[74] M. Spieker, P. Petkov, E. Litvinova, C. Müller-Gatermann, S. G. Pickstone, S. Prill, P. Scholz, and A. Zilges. Shape coexistence and collective low-spin states in ^{112,114}Sn studied with the $(p,p^{'}\gamma)$ doppler-shift attenuation coincidence technique. *Phys. Rev. C*, 97:054319, May 2018.

[75] A. Arima and F. Iachello. the interacting boson model. *Ann. Rev. Nucl. Part. Sci.*, 31:75–105, Sep 1981.

[76] Ka-Hae Kim, Adrian Gelberg, Takahiro Mizusaki, Takaharu Otsuka, and Peter von Brentano. Ibm-2 calculations of even-even pd nuclei. *Nuclear Physics A*, 604(2):163 – 182, 1996.

[77] S F Mughabghab. Thermal neutron capture cross sections resonance integrals and g-factors, Feb 2003.

[78] W.E. Burcham and M. Jobes. *Nuclear and Particle Physics*. Longman Group Limited, Singapore, 1995.

[79] H. MOTZ and G. BÄCKSTRÖM. Xiii - neutron capture radiation spectroscopy. In KAI SIEGBAHN, editor, *Alpha-, Beta- and Gamma-Ray Spectroscopy*, pages 769–804. Elsevier, Amsterdam, 1968.

[80] N. Tsoneva and H. Lenske. Pygmy quadrupole resonance in skin nuclei. *Physics Letters B*, 695(1-4):174–180, Jan 2011.

[81] D. Savran, T. Aumann, and A. Zilges. Experimental studies of the pygmy dipole resonance. *Progress in Particle and Nuclear Physics*, 70:210–245, 2013.

[82] M.N. Harakeh and A. Woude. *Giant Resonances: Fundamental High-frequency Modes of Nuclear Excitation*. Oxford science publications. Oxford University Press, 2001.

[83] J. S. Brzosko, E. Gierlik, A. Soltan Jr., and Z. Wilhelmi. Effect of the pigmy resonance on the calculations of the neutron capture cross section. *Canadian Journal of Physics*, 47(24):2849–2857, 1969.

[84] A. Bracco, E.G. Lanza, and A. Tamii. Isoscalar and isovector dipole excitations: Nuclear properties from low-lying states and from the isovector giant dipole resonance. *Progress in Particle and Nuclear Physics*, 106:360–433, 2019.

[85] H. Kawakami, N. Yoshikawa, K. Komura, M. Koike, and H. Yamada. Excited 0^+ states and electric monopole transitions in ^{118}Sn. *Phys. Rev. C*, 25:2013–2018, Apr 1982.

[86] A. Bäcklin, N.G. Jonsson, R. Julin, J. Kantele, M. Luontama, A. Passoja, and T. Poikolainen. 0+ states and e0 and e2 transition rates in even sn nuclei. *Nuclear Physics A*, 351(3):490–508, 1981.

[87] L.I.Govor, A.M.Demidov, and I.V.Mikhailov. Nuclear reactions ^{114,116,118,120,122,124}sn(n, n'), e=fast; measured eγ, iγ, $\gamma(\theta)$, linear polarization, doppler shift reduction. ^{114,116,118,120,124}sn deduced levels, j, π, t1/2, δ, b(γ). *Sov.J.Nucl.Phys.*, 53, 1991.

[88] Yu. E. Loginov, L. M. Smotritsky, and P. A. Sushkov. γ-spectrum from ^{117}sn(n γ)^{118}sn reaction and scheme of excited states of ^{118}sn nucleus. *Bull.Rus.Acad.Sci.Phys.*, 66:1601, 2002.

[89] S.B.Borzakov, H.Faikov-Stanczyk, Ts.Ts.Panteleev, S.A.Telezhnikov, Yu.V.Grigoriev, L.M.Smotritsky, and B.P.Konstantinov. Gamma-ray transitions of sn-118 observed in radiative capture of thermal neutrons. Number 8, page 334, 2000.

[90] E.A.Rudak, A.V.Soroka, and V.N.Tadeush. Spectra of g-rays from (n,g) reactions on tellurium and tin isotopes. page 42, 1978.

[91] V. P. Alfimenkov, S. B. Borzakov, Vo Vang Thuan, Yu. D. Mareev, L. B. Pikelner, I. M. Frank, A. S. Khrykin, and E. I. Sharapov. γ-ray spectra from the neutron resonances ^{81}br, ^{117}sn, ^{139}la violating the space parity. *Yad.Fiz.*, 39:1057, 1984.

[92] James Smallcombe. jrootanalysistools: Samuel johnson, March 2020.

[93] A.I. Morales, G. Benzoni, H. Watanabe, G. de Angelis, S. Nishimura, L. Coraggio, A. Gargano, N. Itaco, T. Otsuka, Y. Tsunoda, P. Van Isacker, F. Browne, R. Daido, P. Doornenbal, Y. Fang, G. Lorusso, Z. Patel, S. Rice, L. Sinclair, P.-A. Söderström, T. Sumikama, J.J. Valiente-Dobón, J. Wu, Z.Y. Xu, A. Yagi, R. Yokoyama, H. Baba, R. Avigo, F.L. Bello Garrote, N. Blasi, A. Bracco, A.M. Bruce, F. Camera, S. Ceruti, F.C.L. Crespi, M.-C. Delattre, Zs. Dombradi, A. Gottardo, T. Isobe, I. Kojouharov, N. Kurz, I. Kuti, S. Lalkovski, K. Matsui, B. Melon, D. Mengoni, T. Miyazaki, V. Modamio-Hoybjor, S. Momiyama, D.R. Napoli, M. Niikura, R. Orlandi, Zs. Podolyák, P.H. Regan, H. Sakurai, E. Sahin, D. Sohler, H. Schaffner, R. Taniuchi, J. Taprogge, Zs. Vajta, O. Wieland, and M. Yalcinkaya. Is seniority a partial dynamic symmetry in the first νg9/2 shell? *Physics Letters B*, 781:706–712, 2018.

[94] L. Y. Jia and Chong Qi. Generalized-seniority pattern and thermal properties in even sn isotopes. *Phys. Rev. C*, 94:044312, Oct 2016.

[95] Chong Qi and Z. X. Xu. Monopole-optimized effective interaction for tin isotopes. *Phys. Rev. C*, 86:044323, Oct 2012.

Appendix A

β decay of ^{118}In — Publication

PHYSICAL REVIEW C **102**, 024323 (2020)

Collective 2p-2h intruder states in ^{118}Sn studied via β decay of ^{118}In using the GRIFFIN spectrometer at TRIUMF

K. Ortner,[1,*] C. Andreoiu,[1] M. Spieker,[2,†] G. C. Ball,[3] N. Bernier,[3,4] H. Bidaman,[5] V. Bildstein,[5] M. Bowry,[3,‡] D. S. Cross,[1] M. R. Dunlop,[5] R. Dunlop,[5] F. H. Garcia,[1] A. B. Garnsworthy,[3] P. E. Garrett,[5] J. Henderson,[3,§] J. Measures,[3,6] B. Olaizola,[3] J. Park,[3,4,‖] C. M. Petrache,[7] J. L. Pore,[1,¶] K. Raymond,[1] J. K. Smith,[3,#] D. Southall,[3,**] C. E. Svensson,[5] M. Ticu,[1] J. Turko,[5] K. Whitmore,[1] and T. Zidar[5]

[1] *Department of Chemistry, Simon Fraser University, Burnaby, British Columbia, Canada V5A 1S6*
[2] *National Superconducting Cyclotron Laboratory, Michigan State University, 640 South Shaw Lane, East Lansing, Michigan 48824, USA*
[3] *TRIUMF, 4004 Wesbrook Mall, Vancouver, British Columbia, Canada V6T 2A3*
[4] *Department of Physics and Astronomy, University of British Columbia, Vancouver, British Columbia, Canada V6T 1Z4*
[5] *Department of Physics, University of Guelph, Guelph, Ontario, Canada N1G 2W1*
[6] *Department of Physics, University of Surrey, Guildford GU2 7XH, United Kingdom*
[7] *Université Paris-Saclay, CNRS/IN2P3, IJCLab, 91405 Orsay, France*

(Received 5 December 2019; revised 13 May 2020; accepted 22 June 2020; published 18 August 2020)

The low-lying structure of semimagic ^{118}Sn has been investigated through the β decay of ^{118}In ($T_{1/2} = 4.45$ min) to study shape coexistence via the reduced transition probabilities of states in the 2p-2h proton intruder band. This high-statistics study was carried out at TRIUMF-ISAC with the GRIFFIN spectrometer. In total, 99 transitions have been placed in the level scheme with 43 being newly observed. Three low-lying γ-ray transitions with energies near 285 keV have been resolved from which the $2^+_{\text{intr.}} \rightarrow 0^+_{\text{intr.}}$ 284.52-keV transition was determined to have half of the previous branching fraction leading to a $B(E2; 2^+_2 \rightarrow 0^+_2)$ of 21(4) W.u. compared to 39(7) W.u. from the previous measurement. Calculations using *sd* IBM-2 with mixing have also been made to compare the experimental $B(E2)$ values to the theoretical values and to make comparisons to the ^{114,116}Sn isotopes previously studied using the same theoretical model.

DOI: 10.1103/PhysRevC.102.024323

I. INTRODUCTION

The semimagic isotopes of Sn continue to be of great interest. They are benchmark nuclei for state-of-the-art shell-model calculations and offer a strong foundation to our understanding of shape evolution in the $Z = 50$ region (see, e.g., Ref. [1]). While the Sn isotopes are close to spherical in their ground state, deformed bands built on excited 0^+ states are observed throughout this isotopic chain and have been interpreted as having two-particle-two-hole, 2p-2h, character [2,3]. The presence of these deformed intruder states is considered to be an important feature in the $Z = 50$ region [3–5] and the degree of mixing between deformed and normal states needs to be further explored [3].

Enhanced cross sections of the excited 0^+ states in even-even $^{108-118}$Sn were identified in the (^{3}He, n) experiments by Fielding *et al.* [6], and it was later suggested that the observed 0^+_2 state in even-even $^{112-118}$Sn is the bandhead of an intruding rotational band due to 2p-2h proton excitations across the shell gap by Brön *et al.* [2]. In a recent β^- decay study of ^{116}In to ^{116}Sn, a newly obtained $B(E2;\, 2^+_2 \rightarrow 0^+_3)$ value suggested the 0^+_3 state as the 2p-2h bandhead instead of the 0^+_2 [7]. Furthermore, *sd* IBM-2 with mixing calculations were made to test the mixing between the intruder and normal configurations in ^{116}Sn [8] and ^{114}Sn [5]. In both cases the conclusion was that the 0^+_3 is the intruding bandhead but is strongly mixed with the 0^+_2 state.

Although the intruder band lies at lower excitation energy in ^{118}Sn—the $2^+_{\text{intr.}}$ state is 14 keV below the 0^+_3 level—obtaining accurate $B(E2)$ values can indicate the degree of collectivity of the intruder band and the amount of mixing between deformed and normal states [9].

Many studies have been performed on ^{118}Sn providing a comprehensive level scheme which includes the 2p-2h intruder band built on the excited 0^+_2 state at 1758 keV [10]. Two studies, β decay of ^{118}In [11] and $(n, n'\gamma)$ [12], contributed most of the low-lying observables to the ^{118}Sn level scheme.

---

[*] kortner@sfu.ca

[†] Present address: Department of Physics, Florida State University, Tallahassee, Florida 32306, USA.

[‡] Present address: School of Computing, Engineering and Physical Sciences, University of the West of Scotland, Paisley PA1 2BE, United Kingdom.

[§] Present address: Lawrence Livermore National Laboratory, Livermore, California 94550, USA.

[‖] Present address: Department of Physics, Lund University, 22100 Lund, Sweden.

[¶] Present address: Lawrence Berkeley National Laboratory, Berkeley, California 94720, USA.

[#] Present Address: Department of Physics, Pierce College, Puyallup, Washington 98374, USA.

[**] Present address: Department of Physics, University of Chicago, Chicago, IL 60637, USA.

One notable discrepancy between these studies, which needs clarification, is related to the $I_\gamma(2_3^+ \to 2_2^+)$ for 285.3 keV and the $I_\gamma(2_2^+ \to 0_2^+)$ for 284.6 keV [11,12]. In each of these experiments, both the 2_2^+ intruder state and the 2_3^+ state were populated. However, in the $(n, n'\gamma)$ study, only the 284.6-keV transition was observed [12], while the ^{118}In β-decay study only observed the 285.3-keV transition [11]. It is likely that the intensities of these transitions have been grouped together in the ENSDF [10] and as a result, the adopted $B(E2;\, 2_2^+ \to 0_2^+)$ of 39(7) W.u. is too large. Since the characterization of the collectivity in the normal and intruder configurations is important, the present work sought to resolve this issue in ^{118}Sn.

A high-statistics experiment to investigate the decay properties of the proton 2p-2h band in ^{118}Sn using the β decay of ^{118}In and the high-resolution GRIFFIN spectrometer located at TRIUMF-ISAC [13] has been performed. New results, which include updated $B(E2)$ values, and a discussion of the new observations are presented. Furthermore, *sd* IBM-2 calculations with mixing have been performed to further elucidate the character of the states of interest.

II. EXPERIMENT

Measurements of the β decay of ^{118}In were performed at the TRIUMF Isotope Separator and ACcelerator (ISAC) facility which houses the Gamma Ray Infrastructure For Fundamental Investigations of Nuclei (GRIFFIN) [13]. GRIFFIN is a high-efficiency γ-ray spectrometer consisting of 16 high-purity germanium (HPGe) clover detectors [14] which was coupled to the ancillary SCintillating Electron Positron Tagging ARray (SCEPTAR), comprised of 20 plastic scintillators for tagging β particles [13] and was fixed within a 20 mm Delrin shield. The detector signals were read out and processed by the GRIFFIN data acquisition system [15].

A radioactive beam of ^{118}In was mass separated from the reaction products of a 9.8 μA, 480 MeV proton beam impinged onto a UC$_x$ target. A high-purity beam was obtained using the Ion-Guide Laser Ion Source (IG-LIS) to suppress isobaric contaminants. The beam was transported and implanted into mylar tape at the center of the GRIFFIN chamber. The isotope ^{118}In decays via the 1^+ ground state with $T_{1/2} = 5$ s [16], a 5^+ isomeric state with $T_{1/2} = 4.45$ min [17] and an 8^- isomeric state with $T_{1/2} = 8.5$ s [18]. The tape was cycled after 5 min of implant and five minutes of decay to obtain statistics which favored observation of the 5^+ isomeric state, which populates the states of interest in ^{118}Sn. Analysis was performed on data after 25 s of decay, reducing the contributions from the 1^+ and 8^- by five and three half-lives, respectively. Furthermore, nearly 99% of the 8^- state decays internally to the 5^+ state through a 138.5 keV γ ray, and 95% of the 1^+ state β-decays to the 0^+ ground state in ^{118}Sn. The tape was moved out of the chamber and into a lead box after each decay cycle to start a new implant cycle. The total run time was approximately 80 min during which 2×10^9 γ-singles events and 1×10^9 γ-γ coincidence events were recorded. Since the isotope of interest was sufficiently free of isobaric contaminants and the implant rate was quite high, SCEPTAR was not used to generate β-γ coincident spectra.

The relative efficiency of the 16 HPGe clovers in addback mode [13] was determined using standard sources of ^{56}Co, ^{60}Co, ^{133}Ba, and ^{152}Eu. Addback is a technique in which coincident γ-ray energies between adjacent crystals in a single clover detector are summed. Compton scattered γ-ray events are recovered increasing the peak-to-total ratio, and ultimately increasing the total photopeak efficiency. For this analysis, the addback mode was applied to determine the peak intensities. The peak centroids and areas were obtained using maximum-likelihood fitting of a modified Gaussian with parameters for skewedness, linear or quadratic background and step sizes. Corrections to the γ-ray intensities due to summing were determined using a matrix of γ-γ coincidences between detector pairs separated by 180° as described in Ref. [13].

Energy calibrations were made using a linear fit between two strong photopeaks and then nonlinearity corrections were made using many of the well-known photopeaks in ^{118}Sn. A systematic uncertainty of 0.2 keV was determined on the γ-ray energies based on the nonlinearity residuals applied to the calibration sources. Cross-talk corrections were made using Compton events in the γ-γ coincidence matrix from the ^{60}Co source as outlined in section 4.1.1 in Ref. [13]. The uncertainty on γ-ray intensities is based on the uncertainty in peak areas, background estimations, relative efficiencies, and summing corrections.

For weak transitions, γ-γ coincidence matrices were used to obtain their energies and intensities. This used a method of gating on a stronger γ-ray transition directly below the weak γ ray in the same cascade [19,20]. To correct for summing in gated coincidence spectra, coincidence matrices of detector pairs separated by 180° were constructed from energy gates corresponding to the same gates used in the γ-γ coincidence matrices. The γ-γ coincidences between any two of the 64 GRIFFIN crystals were also used to obtain γ-γ angular correlations to determine the multipole mixing ratios δ (see Sec. III C).

To calculate the $\log(ft)$ values, the β feeding to individual levels needs to be determined. This was done through an intensity balance of γ intensity depopulating a level minus γ intensity populating the same level. To obtain absolute β feeding of each level, the total ground-state feeding was used to normalize the relative β feeding.

The $B(E2)$ values for transitions with known lifetime measurements, mixing ratios δ (from [10] or our measured values as described in Sec. III C), or for transitions which are assumed pure $E2$, were calculated using our measured γ-ray branching ratios BR$_\gamma$. All BR$_\gamma$ used in these calculations, and in the $\log ft$ calculations took into account internal conversion. The internal conversion coefficients were applied to γ-ray intensities for energies below 600 keV and the coefficients were taken from [10] when possible, or calculated using BrIcc [21].

III. RESULTS

A. Level scheme

In this β-decay study of the 5^+ isomer of ^{118}In, 99 γ rays have been assigned to 23 low-lying excited states in ^{118}Sn. Of

TABLE I. Levels in ^{118}Sn populated by the β^- decay of the 5^+ isomer of ^{118}In ($E_x = 60$ keV, $T_{1/2} = 4.45$ min). The relative intensity of the observed transitions, I_γ, are compared to the previous β^- decay study [11], and the branching ratios, BR_γ, and $B(E2)$ values are compared to the ENSDF [10].

E_{level} [keV]	$T_{1/2}$ (ps) Ref. [10]	$J_i^\pi \rightarrow J_f^\pi$	E_γ [keV]	$I_{\gamma,\mathrm{rel}}$	$BR_{\gamma,\mathrm{rel}}$	$B(E2)$ [W.u.]	$I_{\gamma,\mathrm{rel}}$ Ref. [11]	$BR_{\gamma,\mathrm{rel}}$ Ref. [10]	$B(E2)$ [W.u.] [10]
1229.50(10)	0.49(2)	$2_1^+ \rightarrow 0_1^+$	1229.57(20)	100	100	12.1(5)	100	100	12.1(5)
1758.24(14)	21(3)	$0_2^+ \rightarrow 2_1^+$	528.70(20)	0.129(4)	100	19(3)		100	19(3)
2042.62(10)	2.9(4)	$2_2^+ \rightarrow 0_2^+$	284.52(20)	0.051(7)	1.31(17)	21(4)		2.5(2)	39(7)
		$2_2^+ \rightarrow 2_1^+$	813.11(21)	3.91(9)	100.0(23)	7.2(10)	3.88(12)	100.0(24)	6.9(1)
		$2_2^+ \rightarrow 0_1^+$	2042.70(22)	3.27(10)	83.6(26)	0.072(10)	3.63(8)	92.2(25)	0.075(11)
2280.21(11)	0.76(13)	$4_1^+ \rightarrow 2_2^+$	237.80(22)	0.050(4)	0.058(5)	16(3)	0.04(2)	0.05(2)	14(7)
		$4_1^+ \rightarrow 2_1^+$	1050.54(20)	85(2)	100.0(26)	17(3)	84.4(26)	100(3)	17(3)
2324.29(21)	$0.19^{+0.04}_{-0.03}$	$3_1^- \rightarrow 2_1^+$	1094.98(63)	1.46(7)	100(5)		1.5(5)	100(4)	
		$3_1^- \rightarrow 0_1^+$	2323.9(3)	0.0148(13)	1.02(9)			1.1(1)	
2327.73(12)	>0.2	$2_3^+ \rightarrow 2_2^+$	285.26(22)	0.038(14)	2.3(8)		0.081(10)	5.1(6)	
		$2_3^+ \rightarrow 0_2^+$	569.39(20)	0.041(2)	2.40(14)	< 26			
		$2_3^+ \rightarrow 2_1^+$	1098.2(6)	1.70(7)	100(4)	< 42	1.6(3)	100(19)	< 20
		$2_3^+ \rightarrow 0_1^+$	2327.7(6)	0.326(13)	19.1(8)	< 0.19	0.374(12)	23.4(8)	
2403.05(11)	$0.18^{+0.08}_{-0.04}$	$2_4^+ \rightarrow 2_2^+$	360.67(22)	0.0121(18)	0.91(13)			1.8(2)	
		$2_4^+ \rightarrow 0_2^+$	644.73(20)	0.0190(8)	1.44(6)	12(5)			
		$2_4^+ \rightarrow 2_1^+$	1173.44(22)	1.32(3)	100.0(26)	17(7)	1.43(5)	100(3)	22(10)
		$2_4^+ \rightarrow 0_1^+$	2403.05(22)	0.0029(3)	0.222(20)	0.0025(11)			
2488.59(11)	>0.55	$4_2^+ \rightarrow 4_1^+$	208.46(21)	3.96(8)	60.3(12)		2.71(8)	52(7)	
		$4_2^+ \rightarrow 2_2^+$	445.90(21)	6.56(14)	100.0(22)		5.76(17)	100(3)	
		$4_2^+ \rightarrow 2_1^+$	1259.11(22)	3.87(10)	59.2(16)	< 2.5	3.99(12)	67(3)	< 2.8
2677.10(11)	>0.28	$2_5^+ \rightarrow 2_1^+$	1447.51(21)	0.035(3)	87(6)	< 3.9	0.047(5)	86(4)	< 3.7
		$2_5^+ \rightarrow 0_1^+$	2677.18(20)	0.0405(25)	100(6)	< 0.25	0.039(5)	100(4)	<0.23
2733.53(11)	$0.5^{+0.6}_{-0.2}$	$4_3^+ \rightarrow 4_1^+$	452.7(3)	0.098(11)	6.2(7)	100^{+70}_{-50}			
		$4_3^+ \rightarrow 2_2^+$	690.89(21)	0.0199(18)	1.26(12)	$2.5^{+1.6}_{-1.4}$			
		$4_3^+ \rightarrow 2_1^+$	1504.0(3)	1.58(4)	100(3)	$4.0^{+2.6}_{-2.2}$	1.65(5)	100	4(6)
2878.4(3)		$(5^-) \rightarrow 4_2^+$[a]	598.2(3)	0.067(6)	100		0.069(11)	100(3)	
2903.53(12)	$0.077^{+0.020}_{-0.013}$	$2_6^+ \rightarrow 2_1^+$	1673.76(28)	0.0216(17)	67(7)	0.9(3)		37(2)	2.2(6)
		$2_6^+ \rightarrow 0_1^+$	2903.46(21)	0.0324(24)	100(7)	0.7(2)	0.028(9)[b]	100(4)	0.8(2)
2963.04(12)		$4_4^+ \rightarrow 4_3^+$	229.6(4)	1.06(5)	1.80(8)		0.783(24)	1.38(4)	
		$4_4^+ \rightarrow 2_5^+$	286.02(20)	0.0371(17)	0.063(3)				
		$4_4^+ \rightarrow 4_2^+$	474.5(3)	3.10(7)	5.26(16)		3.00(10)	5.30(18)	
		$4_4^+ \rightarrow 2_4^+$	560.04(20)	1.161(26)	1.97(4)		0.99(4)	1.75(7)	
		$4_4^+ \rightarrow 2_3^+$	635.2(3)	1.73(4)	2.94(7)		1.77(6)	3.13(11)	
		$4_4^+ \rightarrow 3_1^-$	638.4(3)	1.60(4)	2.72(6)		1.37(4)	2.42(7)	
		$4_4^+ \rightarrow 4_1^+$	682.94(20)	59.0(13)	100.0(23)		56.6(17)	100(3)	
		$4_4^+ \rightarrow 2_2^+$	920.4(3)	0.476(12)	0.807(20)		0.506(21)	0.89(4)	
		$4_4^+ \rightarrow 2_1^+$	1733.56(22)	0.446(13)	0.76(5)				
2999.12(18)		$6_1^+ \rightarrow 4_2^+$	510.88(21)	0.094(8)	100(8)		0.13(2)	100(17)	
		$6_1^+ \rightarrow 4_1^+$	718.57(21)	0.090(7)	96(7)		0.076(13)	60(3)	
3056.88(14)		$2_7^+ \rightarrow 0_1^+$	3056.90(22)	0.0108(11)	100	0.5(2)		100(4)	0.5(2)
3374.10(11)		$4_5^+ \rightarrow 4_4^+$	411.16(22)	0.045(5)	8.2(9)		0.037(7)	4.6(9)	
		$4_5^+ \rightarrow 2_6^+$	470.66(22)	0.00084(6)	0.154(10)				
		$4_5^+ \rightarrow 4_3^+$	640.50(21)	0.0222(11)	4.05(20)				
		$4_5^+ \rightarrow 2_5^+$	696.87(22)	0.0067(12)	1.23(23)				
		$4_5^+ \rightarrow 4_2^+$	885.43(20)	0.259(7)	47.3(12)		0.264(20)	33(3)	
		$4_5^+ \rightarrow 2_4^+$	971.0(3)	0.139(6)	25.4(10)		0.35(6)	44(8)	
		$4_5^+ \rightarrow 2_3^+$	1046.31(21)	0.070(7)	12.8(13)				
		$4_5^+ \rightarrow 4_1^+$	1094.10(20)	0.548(23)	100(4)		0.805(20)	100(3)	
		$4_5^+ \rightarrow 2_2^+$	1331.3(3)	0.0127(18)	2.3(3)				
		$4_5^+ \rightarrow 2_1^+$	2144.64(21)	0.108(11)	19.7(20)		0.121(5)	15.0(6)	

TABLE I. (*Continued.*)

E_{level} [keV]	$T_{1/2}$ (ps) Ref. [10]	$J_i^\pi \rightarrow J_f^\pi$	E_γ [keV]	$I_{\gamma,\text{rel}}$	$BR_{\gamma,\text{rel}}$	$B(E2)$ [W.u.]	$I_{\gamma,\text{rel}}$ Ref. [11]	$BR_{\gamma,\text{rel}}$ Ref. [10]	$B(E2)$ [W.u.] [10]
3397.46(13)		$4_6^+ \rightarrow 4_3^+$	663.92(20)	0.0338(16)	43.0(20)				
		$4_6^+ \rightarrow 4_2^+$	908.72(20)	0.079(4)	100(5)				
		$4_6^+ \rightarrow 2_4^+$	994.18(22)	0.0166(11)	21.1(14)				
		$4_6^+ \rightarrow 2_3^+$	1070.06(23)	0.035(3)	45(4)				
		$4_6^+ \rightarrow 4_1^+$	1117.3(3)	0.043(4)	54(5)				
		$4_6^+ \rightarrow 2_1^+$	2168.3(4)	0.008(3)	10(4)				
3460.21(11)		$4_7^+ \rightarrow 2_7^+$	403.41(22)	0.0047(4)	1.20(10)				
		$4_7^+ \rightarrow 2_6^+$	556.54(21)	0.0064(4)	1.64(11)				
		$4_7^+ \rightarrow 4_3^+$	726.62(21)	0.019(1)	4.93(27)				
		$4_7^+ \rightarrow 2_5^+$	783.10(22)	0.024(4)	6.0(11)				
		$4_7^+ \rightarrow 4_2^+$	971.6(6)	0.39(3)	100(8)		0.32(7)	96(21)	
		$4_7^+ \rightarrow 2_4^+$	1057.15(22)	0.0148(10)	3.79(26)				
		$4_7^+ \rightarrow 2_3^+$	1132.42(20)	0.090(3)	23.1(8)		0.099(9)	30(3)	
		$4_7^+ \rightarrow 4_1^+$	1180.21(20)	0.159(9)	40.7(23)		0.163(10)	49(3)	
		$4_7^+ \rightarrow 2_2^+$	1417.57(21)	0.0240(15)	6.1(4)		0.027(5)	8(2)	
		$4_7^+ \rightarrow 2_1^+$	2230.7(9)	0.280(11)	71.4(28)		0.333(11)	100(3)	
3592.15(11)		$4_8^+ \rightarrow 2_7^+$	535.21(22)	0.0036(3)	1.37(11)				
		$4_8^+ \rightarrow 4_3^+$	858.52(21)	0.108(4)	41.2(16)		0.117(20)	42(7)	
		$4_8^+ \rightarrow 2_5^+$	915.20(22)	0.0034(6)	1.30(26)				
		$4_8^+ \rightarrow 4_2^+$	1103.37(21)	0.083(7)	31.5(27)				
		$4_8^+ \rightarrow 2_3^+$	1189.25(22)	0.0140(8)	5.31(29)				
		$4_8^+ \rightarrow 2_3^+$	1264.34(20)	0.051(6)	19.4(24)				
		$4_8^+ \rightarrow 4_1^+$	1312.1(6)	0.181(6)	68.7(23)		0.187(9)	67(3)	
		$4_8^+ \rightarrow 2_2^+$	1549.52(20)	0.264(8)	100.0(29)		0.281(12)	100(4)	
		$4_8^+ \rightarrow 2_1^+$	2362.79(21)	0.064(3)	24.1(12)		0.068(4)	24(1)	
3704.34(11)		$4_9^+ \rightarrow 2_6^+$	800.76(20)	0.0168(9)	12.3(7)				
		$4_9^+ \rightarrow 4_3^+$	970.80(21)	0.110(5)	81(3)				
		$4_9^+ \rightarrow 2_5^+$	1027.16(22)	0.0043(8)	3.2(6)				
		$4_9^+ \rightarrow 4_2^+$	1215.71(21)	0.030(3)	22.4(23)				
		$4_9^+ \rightarrow 2_4^+$	1301.37(20)	0.0411(18)	30.3(14)		0.056(6)	37(4)	
		$4_9^+ \rightarrow 2_3^+$	1376.65(20)	0.0265(24)	19.5(18)		0.038(5)	25(3)	
		$4_9^+ \rightarrow 4_1^+$	1424.1(3)	0.019(4)	27(6)		0.021(5)	14(3)	
		$4_9^+ \rightarrow 2_2^+$	1661.57(21)	0.0292(24)	21.5(18)		0.041(6)	27(4)	
		$4_9^+ \rightarrow 2_1^+$	2475.06(20)	0.136(7)	100(5)		0.150(7)	100(5)	
3753.74(14)		$4_{10}^+ \rightarrow 4_3^+$	1020.14(20)	0.070(3)	39.0(17)				
		$4_{10}^+ \rightarrow 4_2^+$	1265.14(20)	0.064(6)	36(3)		0.138(9)	78(5)	
		$4_{10}^+ \rightarrow 4_1^+$	1473.55(21)	0.179(6)	100(3)		0.177(8)	100(5)	
		$4_{10}^+ \rightarrow 2_2^+$	1711.16(22)	0.0178(16)	9.9(9)				
		$4_{10}^+ \rightarrow 2_1^+$	2524.3(3)	0.0061(11)	3.4(6)				
3816.19(15)		$4_{11}^+ \rightarrow 2_6^+$	912.6(3)	0.00150(18)	1.72(21)				
		$4_{11}^+ \rightarrow 4_3^+$	1082.8(3)	0.0063(6)	7.2(7)				
		$4_{11}^+ \rightarrow 4_2^+$	1327.66(22)	0.0190(22)	21.8(26)				
		$4_{11}^+ \rightarrow 4_1^+$	1536.1(4)	0.0069(12)	7.9(14)				
		$4_{11}^+ \rightarrow 2_1^+$	2586.57(21)	0.087(5)	100(6)		0.096(6)	100	
3838.33(16)		$4_{12}^+ \rightarrow 2_6^+$	934.7(3)	0.00085(15)	1.06(20)				
		$4_{12}^+ \rightarrow 4_3^+$	1104.5(3)	0.0030(12)	3.8(15)				
		$4_{12}^+ \rightarrow 4_2^+$	1350.2(4)	0.0081(16)	10.2(21)				
		$4_{12}^+ \rightarrow 4_1^+$	1558.0(3)	0.0144(24)	18(3)				
		$4_{12}^+ \rightarrow 2_1^+$	2608.96(21)	0.080(4)	100(5)		0.086(6)	100	

[a] Listed as (4, 5, 6^+) in [10] but suggested to be 5^- in Ref. [12,23]. A 5^- assignment also fits with the logft value in Table II.

[b] Observed by Raman *et al.* but not placed in level scheme.

these transitions, 43 were newly observed, including six which depopulate a newly placed level at 3398 keV. Table I shows all γ rays observed in this experiment from an initial level of spin and parity J_i^π to a final level of spin and parity J_f^π, and their corresponding intensities, branching ratios, and $B(E2)$ transition strengths, and compares them to the ENSDF [10].

Of the 51 γ rays placed by Raman *et al.* [11], 49 were observed with relative intensities for most of the strong transitions in reasonably good agreement. However, there are several transitions where the γ-ray intensities and/or branching ratios differ by more than 2 σ. Some of these can be easily explained from the fact we used γ-γ coincidence matrices, while Raman states they did not.

A 1265.14-keV transition from the 3753-keV level was observed by Raman in a singles spectra with an intensity of 0.138(9). We observe the 1265.14-keV transition and a newly observed 1264.34-keV transition from the 3592-keV level with intensities of 0.064(6) and 0.051(6), respectively. It is suspected that these were not resolved as two distinct transitions and the intensity placed by Raman is the sum of their intensities.

Raman identified the transition of 971.0 keV from the 3374-keV level and assigned an intensity of 0.35(6) based on an intensity balance of the 2403-keV level which the 971.0-keV transition populates. The remaining intensity of 0.32(7) was assigned to the 971.6-keV transition from the 3460-keV level. We observed more intensity feeding into the 2403-keV level, indicating that the 971.0-keV transition should have less intensity from what Raman observed. Furthermore, a third transition of 970.8 keV was resolved with an intensity of 0.110(5) from the 3704-keV level. Our summed intensity of 971.0-keV, 971.6-keV, and 970.8-keV transitions is in agreement with the summed intensities Raman observed, although we determined an intensity of only 0.139(6) for the 971.0-keV transition compared to 0.35(6).

Another discrepancy is the intensity given to the 1094.10-keV transition from the 3374-keV level. We observe, from γ-γ coincidence, an intensity of 0.548(23) compared to 0.805(20). It is unclear how Raman was able to separate this from the 1094.98-keV transition depopulating the 2327-keV level without γ-γ coincidence.

One interesting difference is between our $B(E2)$ value of <42 W.u. for the 1098.2-keV transition depopulating the 2327-keV level compared to $B(E2)$ value of <20 W.u. listed in the ENSDF [10]. It is unclear how the value of <20 W.u. was established given our measured absolute BR_γ for the 1098.2-keV transition is nearly the same as listed in the ENSDF [10].

We did not observe the 756-keV and the 1116-keV transitions assigned by Raman to the decay of a new level in ^{118}Sn at 3159 keV. However, a 1117.3-keV transition was observed and originates from a newly observed 3398-keV level as shown in Fig. 1. All of the γ rays which depopulate this level were observed through γ-γ coincidences and a spin of $J^\pi = 4^+$ was assigned to this level based on the log ft value of 6.72 (shown in Table II) and on the observation of 994.18-keV, 1070.06-keV, and 2168.3-keV transitions which feed into the 2_4^+, 2_3^+, and 2_1^+ levels, respectively.

New transitions of 2524.3 keV and 1711.2 keV were observed and assigned to the decay of the 3754-keV level to the 1230-keV 2_1^+ and 2043-keV 2_2^+ levels, respectively. This suggests a spin assignment of 4^+ for the 3754-keV level which was previously given a $J = 4$, 5, or 6 with no parity [11]. The 4^+ assignment is also reasonable given the log ft value of 5.874(14), as shown in Table II, which is consistent with an allowed transition of $\Delta J = 1$ and no change in parity.

TABLE II. β-feeding intensity was measured to calculate log ft values [24]. Conversion electron coefficients were taken into account and were calculated using BrIcc [21]. The 2^+ levels with nonzero β intensities are discussed in Sec. III.

$5^+ \rightarrow J^\pi$	Energy [keV]	I_{β^-}%	log ft	I_{β^-}%	log ft
		This work		Ref. [10]	
4^+	2280.21	19.7(24)	5.92(6)	22(3)	5.83(6)
4^+	2488.59	10.24(20)	6.033(18)	8.5(4)	6.058(23)
4^+	2733.53	0.17(6)	7.58(16)	0.67(7)	6.90(4)
(5^-)	2878.4	0.065(6)	7.9(5)	0.066(11)	7.78(8)
2^+	2903.53	0.027(3)	10.08(6)	–	–
4^+	2963.04	66.2(8)	4.752(8)	62(3)	4.712(24)
6^+	2999.12	0.178(10)	7.28(4)	0.198(24)	7.17(6)
2^+	3056.88	0.0021(11)	10.84(22)	–	–
4^+	3159.28	–	–	0.104(18)	7.25(8)
4^+	3374.10	1.17(3)	5.98(3)	1.51(8)	5.78(3)
4^+	3397.46	0.207(8)	6.70(3)	–	–
4^+	3460.21	0.98(3)	5.93(3)	0.90(8)	5.87(5)
4^+	3592.15	0.733(14)	5.83(4)	0.63(4)	5.79(4)
4^+	3704.34	0.398(10)	5.89(4)	0.294(16)	5.89(3)
4^+	3753.74	0.325(9)	5.88(4)	0.302(15)	5.77(3)
4^+	3816.19	0.117(6)	6.19(6)	0.092(7)	6.14(4)
4^+	3838.33	0.102(5)	6.19(5)	0.083(7)	6.13(5)

Spin assignments of 4^+ were also made for the 3816.19-keV and 3838.33-keV levels based on observed transitions to 2^+ states and on the log ft values in Table II. The previous assignment of $J = 1^+$, 2^+, or 3^+ to the 3816.19-keV level would indicate at least a second forbidden transition which is not in line with the log ft value obtained. Similarly, the 3838.33-keV level was previously assigned a $J = 4$ with no definite parity. This should be a 4^+ based on the log ft value.

A 1734-keV transition from the 2963-keV level had been observed previously by Hattula *et al.* [22] and do Amaral *et al.* [17], but no evidence for this transition was reported by Raman *et al.* [11]. A significant amount of summing of the 683-keV transition with the 1051-keV transition gives rise to uncertainty for a 1734-keV transition which can be understood from Fig. 1. However, summing corrections were performed for the 1734-keV photopeak and its relative intensity was determined to be 0.446(13), in agreement with the earlier reports [17,22].

Nonzero β-feeding intensity is observed to the 2^+ 2904-keV and 3057-keV levels corresponding to unique second forbidden transitions (see Table II). The log ft values are 10.08(6) and 10.84(22), respectively, which are lower than expected. Higher than expected β intensity is likely due to unobserved transitions. For instance, it is possible that there is a 59.5-keV transition connecting the 4^+ 2963-keV level to the 2904-keV level. However, this transition, if present, was not observed due to the low efficiency for γ ray detection at this energy and the high probability for internal conversion.

B. 285 keV triplet

A triplet of 284.5-keV, 285.3-keV, and 286.0-keV transitions was resolved using γ-γ coincidences and gating on tran-

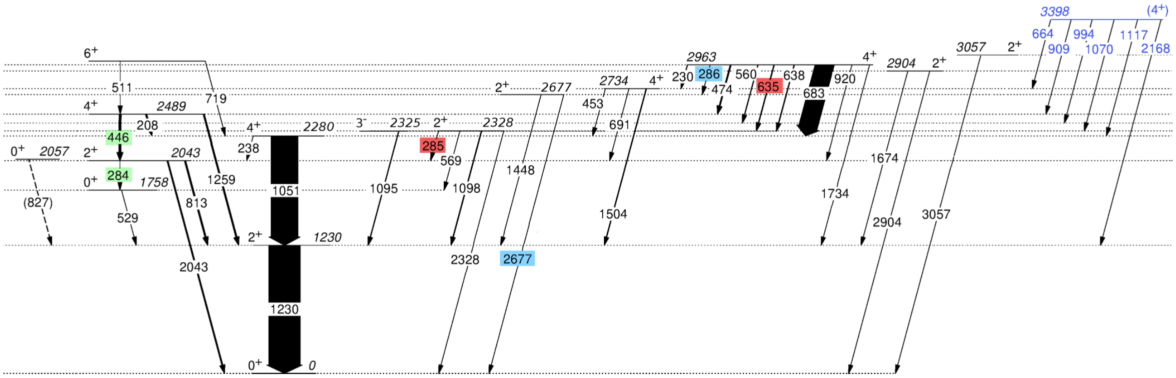

FIG. 1. Partial level scheme of ^{118}Sn populated in the β decay of the 5^+ isomer of ^{118}In. The widths of the arrows represent the relative intensities of the γ rays. Included, but not observed, is the 0_3^+ level at 2057 keV The 3398-keV level (blue) is newly placed based on five newly observed transitions depopulating it.

sitions in their respective cascades as shown in Fig. 1. In the study by Raman *et al.* [11], γ-γ coincidences were not made and the 285.2 keV γ ray which they observed was placed to the 2_3^+, 2328-keV level. In another study by Mikhailov *et al.* [12], γ-γ coincidences were measured and a 284.66-keV transition was placed to the 2_2^+, 2043-keV level. They did not observe the 285.2-keV transition, despite populating the 2_3^+, 2328-keV level. We observed 284.5-keV and 285.3-keV γ rays directly in coincidence with each other making them difficult to separate. The 284.5-keV transition was determined by gating from above on 446 keV and the relative branching ratio of 284.5 keV was determined, from the same gate, to be 1.33(6) compared to the previously adopted 2.5(2) [10]. This reduces the $B(E2; 2_2^+ \rightarrow 0_2^+)$ from 39(7) W.u. to 21(4) W.u., indicating a less collective transition than the previous value suggests.

The Compton edge of the 446-keV full-energy peak, occurring at ≈284 keV, made it difficult to isolate the 285.3-keV transition when gating from below on 2043 keV and on 813 keV. A gate was instead placed from above on 635 keV to isolate the 285.3-keV transition. The small contribution from the 284.4 keV transition in coincidence with 285.3 keV was taken into account. It was assumed there was no β feeding to the 2_2^+ and 2_3^+, based on the β-decay selection rules, such that the relative intensities could be determined from gating from above. The relative intensity of 285.3 keV was determined to be 0.038(14), half of the previous value of 0.081(10) [11].

The newly observed 286.0 keV γ-ray transition from the 2963.141 keV level is in a separate cascade and was far easier to decouple from the other two. A gate was placed below on the 2677.18 keV transition to isolate the 286.0 keV transition. Figure 2 shows an overlap of all three transitions and the subtle shifts of the peak centroids.

C. γ-γ angular correlations

The geometry of GRIFFIN allows γ-γ angular correlations to be performed, using 51 correlation angles between detector pairs. The statistics for γ-γ angular correlations were not sufficient to assign spins to the levels with no definite spin assignment.

Angular correlations for cascades with sufficient statistics were made to obtain δ values. Table III summarizes the χ^2 of the angular correlation fit and the δ which was determined through χ^2 minimization. The form of the angular correlation fit is

$$W(\theta) = A_{00}[1 + a_2 P_2(\cos\theta) + a_4 P_4(\cos\theta)], \qquad (1)$$

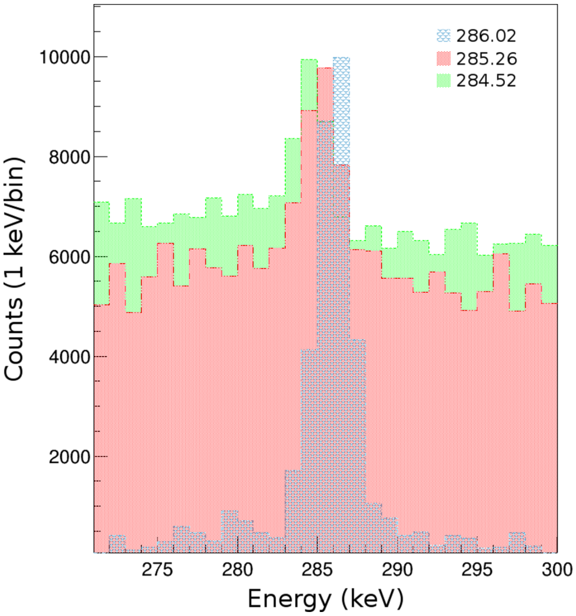

FIG. 2. Overlap of the transitions making up the 285-keV triplet. The individual spectra have been scaled to better show the energy differences. The corresponding coincidental transitions gated on to observe these energy shifts can be seen in Fig. 1 (represented by color).

TABLE III. The angular correlations made in this study are summarized by the transition gated on, $E_{\gamma 1}$, and the corresponding transition, $E_{\gamma 2}$, used to make the angular correlation [e.g., Fig. 3(a)].

$E_{\gamma 1}$ [keV]	$E_{\gamma 2}$ [keV]	$J_2 \rightarrow J_1 \rightarrow J_0$	χ^2_ν	δ	δ [10]
1230	813	$2^+_2 \rightarrow 2^+_1 \rightarrow 0^+_1$	1.39	−2.28(7)	−2.34(16)
	1098	$2^+_3 \rightarrow 2^+_1 \rightarrow 0^+_1$	0.86	−14(4)	56(31)[a]
	1173	$2^+_4 \rightarrow 2^+_1 \rightarrow 0^+_1$	1.21	0.85(3)	1.07(9)
1050	208	$4^+_2 \rightarrow 4^+_1 \rightarrow 2^+_1$	1.36	−0.19(4)	−0.17(4)
	683	$4^+_4 \rightarrow 4^+_1 \rightarrow 2^+_1$	1.15	0.224(3)	0.09(5)

[a] Listed as $1/\delta = 0.018(10)$ [10].

where a_2 and a_4 are coefficients which depend on the γ-ray multipolarities and their mixing ratios, θ is the angle between the successive γ rays in a cascade, and $P_i(\cos\theta)$ are Legendre polynomials.

Due to the finite size of the GRIFFIN detectors, the a_2 and a_4 coefficients are attenuated and energy-dependent attenuation factors need to be applied when fitting the angular correlations with Eq. (1). Attenuation factors which have previously been determined in Method 4 of Ref. [25] were applied to these coefficients. However, these attenuation factors were obtained with a setup which did not include the Delrin shield. Therefore, simulations have been performed for several energy pairs with the inclusion of the Delrin shield. It was determined that the attenuation factors differentiated by at most 1% which is within the uncertainty of our angular

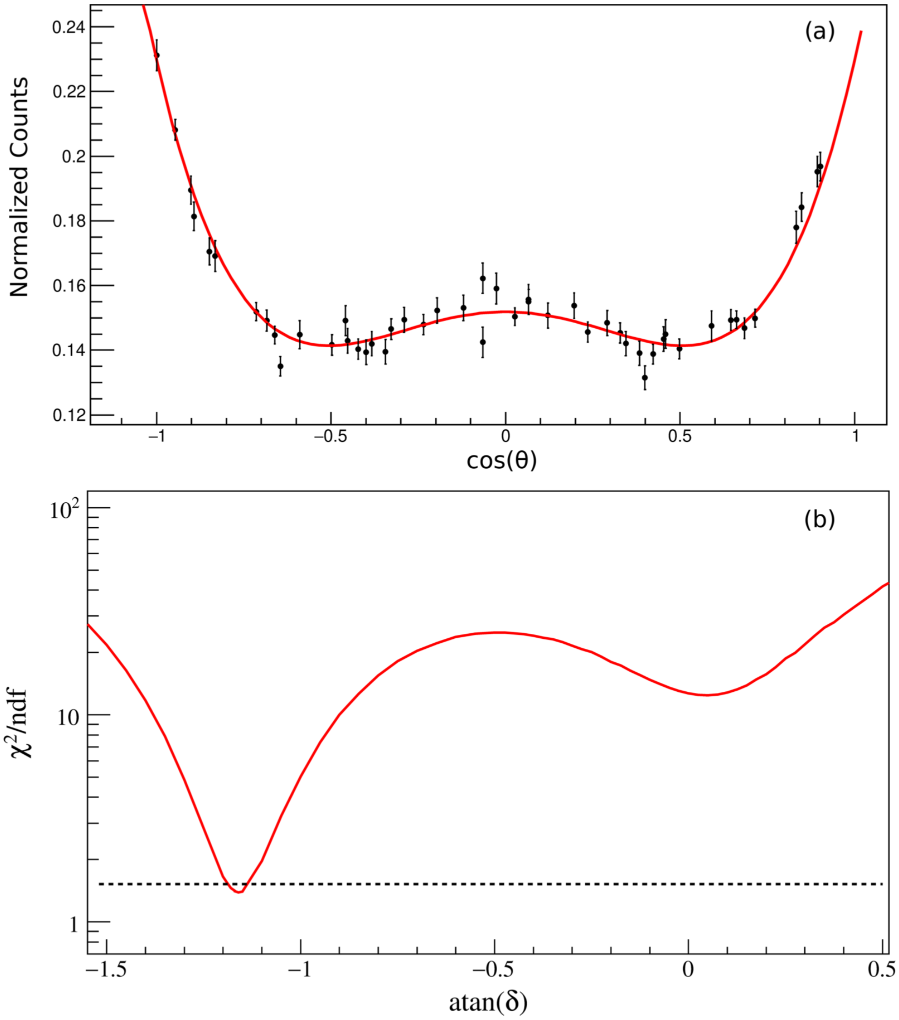

FIG. 3. Angular correlation (a) of the $2^+_2 \rightarrow 2^+_1 \rightarrow 0^+_1$ (813 keV–1230 keV coincidence) and its corresponding χ^2 minimization plot (b) to determine the mixing ratio. In (b), the dashed line represents the 3σ limit to identify the mixing ratio for a given spin assignment. In this case, the $2^+_2 \rightarrow 2^+_1$ has a $\delta = -2.28(7)$ which agrees with the literature value of $-2.34(16)$.

correlation fits. An example of the angular correlation for the $2_2^+ \rightarrow 2_1^+ \rightarrow 0_1^+$ cascade is shown with the corresponding χ^2 minimization in Fig. 3.

The largest discrepancy which could impact future calculations, such as $B(E2)$ values, is the mixing ratio obtained for the 683-keV transition. The newly measured value of 0.224(3) would increase the $B(E2)$ by nearly a factor of six from the previous value of 0.09(5). In addition, the sign of the δ of the 1098–1230-keV transition differs from the one previously reported [10].

IV. *sd* IBM-2 CALCULATIONS WITH MIXING

As in previous studies on the mixing between the normal and intruder configuration in ^{114}Sn [5] and ^{116}Sn [8], an *sd* IBM-2 calculation with mixing was performed using the computer code NPBOS [26]. Following the adopted approach for ^{114,116}Sn [5,8], the intruder states in ^{118}Sn are described using the corresponding Pd isotone, ^{114}Pd, and the parameters determined in Ref. [27]. The c_4^{ρ} parameter of the residual nucleon-nucleon interaction in the Hamiltonian was slightly adjusted from 0.10 [27] to 0.05 to bring the intruder 4_2^+ state closer in energy to the normal 4_1^+ state. The *sd* IBM-2 Hamiltonian H has been described in detail in Refs. [27,28] and the mixing Hamiltonian H_{mix} in, e.g., Ref [29]. For completeness, they are presented here:

$$H = \varepsilon_\pi n_{d_\pi} + \varepsilon_\nu n_{d_\nu} + \kappa Q_\pi \cdot Q_\nu + M_{\pi\nu} + V_{\pi\pi} + V_{\nu\nu}, \qquad (2)$$

where

$$Q_\rho = (d^\dagger \times s + s^\dagger \times \tilde{d})^{(2)}_\rho + \chi_\rho (d^\dagger \times \tilde{d})^{(2)}_\rho, \qquad (3)$$

is the *sd* IBM-2 quadrupole operator for $\rho =$ protons π and neutrons ν,

$$\begin{aligned} M_{\pi\nu} = {} & \frac{1}{2}\xi_2[(s_\nu^\dagger \times d_\pi^\dagger - d_\nu^\dagger \times s_\pi^\dagger)^{(2)} \\ & \times \ (s_\nu \times \tilde{d}_\pi - \tilde{d}_\nu \times s_\pi)^{(2)}]^{(0)} \\ & + \sum_{k=1,3} \xi_k[(d_\nu^\dagger \times d_\pi^\dagger)^{(k)}(\tilde{d}_\pi \times \tilde{d}_\nu)^{(k)}]^{(0)} \end{aligned} \qquad (4)$$

is the Majorana operator, and the residual nucleon-nucleon interaction is given by

$$\begin{aligned} V_{\rho\rho} = {} & \sum_{L=0,2,4} \frac{1}{2} c_L^\rho [(d_\rho^\dagger \times d_\rho^\dagger)^{(L)}(\tilde{d}_\rho \times \tilde{d}_\rho)^{(L)}]^{(0)} \\ & + \frac{1}{2} v_0^\rho \{[(d_\rho^\dagger d_\rho^\dagger)^{(0)}(s_\rho s_\rho)^{(0)}]^{(0)} + \text{H.c.}\} \\ & + \sqrt{\frac{5}{2}} v_2^\rho \{[(d_\rho^\dagger d_\rho^\dagger)^{(2)}(\tilde{d}_\rho s_\rho)^{(2)}]^{(0)} + \text{H.c.}\} \\ & + \kappa_{\rho\rho} \big(Q_\rho Q_\rho\big)^{(0)}. \end{aligned} \qquad (5)$$

To reduce the number of parameters, Kim *et al.* chose $c_L^\pi = c_L^\nu = c_L$ and $\kappa_{\rho\rho} = v_0^\rho = v_2^\rho = 0$ for the Pd isotopes [27]. For the normal states in ^{118}Sn, we found the following parameters: $e_\nu = 1.26\,\text{MeV}$, $\kappa_{\nu\nu} = -0.0002\,\text{MeV}$, $\chi_\nu = -0.005\,\text{MeV}$, $c_0^\nu = -0.45\,\text{MeV}$, $c_2^\nu = 0\,\text{MeV}$, and $c_4^\nu = -0.11\,\text{MeV}$. All other parameters were set to 0. This parameter choice is, in fact, similar to the one used for ^{114,116}Sn [5,8]. The normal and intruder states were calculated separately and were then admixed using the mixing Hamiltonian H_{mix} with $\alpha = 0.25$ and $\beta = 0$:

$$H_{\text{mix}} = \alpha(s_\pi^\dagger s_\pi^\dagger + s_\pi s_\pi)^{(0)} + \beta(d_\pi^\dagger d_\pi^\dagger + \tilde{d}_\pi \tilde{d}_\pi)^{(0)}. \qquad (6)$$

The energy gap Δ between the two configurations was set to 2.45 MeV, which is the same value as the one previously reported for ^{116}Sn [8].

After mixing, $E2$ transitions between the excited states were calculated using the $T(E2)$ operator following the consistent-Q formalism:

$$T(E2) = e_0(e_{\pi_0} Q_\pi + e_{\nu_0} Q_\nu) + e_2(e_{\pi_2} Q_\pi + e_{\nu_2} Q_\nu). \qquad (7)$$

These parameters were used to obtain the results discussed in the following section: $e_0 = 1$, $e_{\nu_0} = 0.07\,eb^2$, $e_{\pi_0} = 0\,eb^2$, $e_2 = 1.43$, $e_{\nu_2} = 0.10\,eb^2$, and $e_{\pi_2} = 0.042\,eb^2$.

V. DISCUSSION OF THE RESULTS

Recent, detailed experimental studies by Garrett *et al.* [30] showed that, in addition to the often discussed proton 2p-2h structure, multiple structures with proton multiparticle-multihole character coexist at comparably low excitation energies in ^{110,112}Cd ($Z = 48$). The experimental results were supported by beyond-mean-field (BMF) calculations, which predicted 2p-2h character for both deformed band structures built on the 0_2^+ and 0_3^+ states in ^{112}Cd ($N = 64$). In the previous IBM studies [5,8], it was assumed that the intruder band structure in ^{114,116}Sn ($N = 64, 66$) was caused by proton 2p-2h excitations across the $Z = 50$ shell closure and that it should resemble the yrast structure of the 0p-4h Pd isotopes. As pointed out by Garrett *et al.*, their results also suggest that the ground-state structure of Pd nuclei is more complex than the simple, spherical π(4h) configuration [30]. This cannot be accounted for in conventional *sd* IBM-2 calculations with mixing. However, as pointed out by Kim *et al.* [27], the more neutron-rich Pd isotopes ($N \geqslant 64$) are clearly nonvibrational nuclei and closer to the γ-soft, O(6), limit of the IBM. It is worth noting that the recent measurement of the lifetimes of the yrast 4^+ and 6^+ states in ^{114}Pd [31] are consistent with a rigid triaxial structure.

The experimental $B(E2; 2^+ \rightarrow 0^+)$ reduced transition strengths for the yrast 2^+ to the ground state in Pd ["π(4h)"] and Xe ["π(4p)"] as well as from the intruder $2^+_{\text{intr.}}$ to the 0_2^+ state in Sn are compared in Fig. 4. In terms of absolute magnitude, the experimental $B(E2; 2^+_{\text{intr.}} \rightarrow 0_2^+)$ strength is indeed more comparable to the strength in the Pd isotopes than the one in the Xe isotopes. It is likely the half-life for the yrast 2^+ state in ^{112}Pd is too long [31]; a shorter value would yield a smoother trend as observed in the Xe isotopes. The decay of the $2^+_{\text{intr.}}$ to the 0_3^+ state has only been observed in ^{116}Sn. From this observation, the 0_3^+ was assigned as the bandhead of the intruder structure in ^{116}Sn [7]. Previous IBM studies supported this interpretation [8] and pointed at a possibly similar scenario in ^{114}Sn [5]. The 0_2^+ and 0_3^+ are, however, strongly mixed. This is also why they share the $B(E2; 0_i^+ \rightarrow 2_1^+)$ transition strength in the IBM. Otherwise, the intruder state would show no collective transition strength to the 2_1^+ state. Unlike for the $2^+_{\text{intr.}}$ and the second excited 2^+ state of the

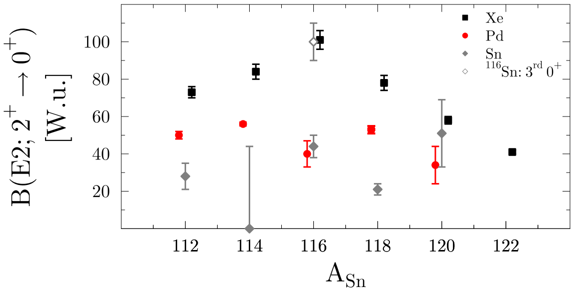

FIG. 4. $B(E2;2^+ \rightarrow 0^+)$ reduced transition strength between yrast states in Pd (red circles) and Xe (black squares), and between the $2^+_{\text{intr.}}$ and 0^+_i states in Sn [$i = 2$ (filled diamonds)]. The $B(E2)$ values for all Xe and Pd isotopes are from [34] except ^{114}Pd which is from [31]. The values for ^{112}Sn and ^{114}Sn (upper limit) are from [5], ^{116}Sn from [7], and ^{120}Sn from data in the ENSDF [35]. The $B(E2;2^+_{\text{intr.}} \rightarrow 0^+_3)$ value (open diamond) is currently only known in ^{116}Sn [7,8].

normal configuration, the $\Delta L = 0$ and $\nu = \tau$ selection rules do not forbid mixing between the states [32,33]. In ^{116}Sn, the $B(E2;2^+_{\text{intr.}} \rightarrow 0^+_3) = 100(8)$ W.u. matches the one observed in the yrast structure of ^{120}Xe (see Fig. 4). The experimentally observed $B(E2;4^+_i \rightarrow 2^+_{\text{intr.}})$ strengths in ^{116}Sn are, however, significantly lower than the strength predicted by the IBM and are only comparable to the yrast value in ^{120}Xe when summed. At the same time, the summed $B(E2;2^+_{\text{intr.}} \rightarrow 0^+_i)$ value ($i = 2, 3$) would significantly exceed the expectations. As pointed out in the previous studies [5,8], strong mixing between the two configurations is observed and much more data are needed to draw more definite conclusions. Since the $B(E2)$ transition strength is shared between mixed states (compare Fig. 5), if only part of the transition strength is observed experimentally, clear structure assignments can be challenging.

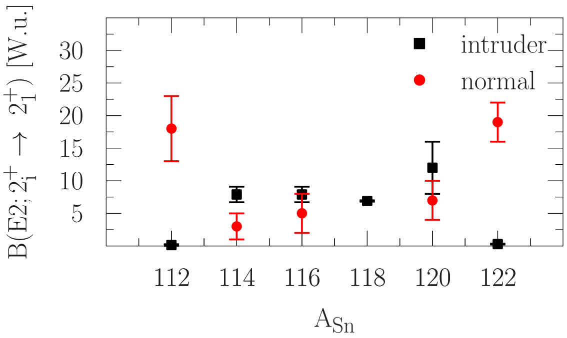

FIG. 5. $B(E2;2^+_i \rightarrow 2^+_1)$ reduced transition strength in the even-A Sn isotopes [5,7,35,36] to illustrate how strength originally attributed to the normal structure gets fragmented between the low-lying 2^+ states once the $2^+_{\text{intr.}}$ drops below the $2^+_{\text{norm.}}$ in ^{114}Sn. In ^{122}Sn, the intruder structure moves up energetically and the strength becomes concentrated in one state again.

TABLE IV. *sd* IBM-2 calculations with mixing for low-lying excited states in ^{118}Sn compared to experimental data. The lifetimes were taken from the ENSDF [10] as were mixing ratios δ for any transition which we were not able to obtain a δ value for. States predicted to originate from the intruder structure are marked with #, states from the normal configuration with †. Note, however, that most of the states are strongly mixed and often contain comparable amplitudes of the normal and intruder configuration in their wave function.

$J^\pi_i \rightarrow J^\pi_f$	E_x [keV]	$E_{x,\text{IBM}}$ [keV]	$B(E2)$ [W.u.]	$B(E2)_{\text{IBM}}$ [W.u.]
$2^+_1 \rightarrow 0^+_1$	1230	1231†	12.1(5)	10
$0^+_2 \rightarrow 2^+_1$	1758	1714$^\#$	19(3)	16
$2^+_2 \rightarrow 0^+_1$	2043	2098$^\#$	0.072(10)	0.008
$\rightarrow 2^+_1$			7.2(10)	0.13
$\rightarrow 0^+_2$			21(4)	35
$0^+_3 \rightarrow 2^+_1$	2057	2099†		10
$\rightarrow 2^+_2$				11
$4^+_1 \rightarrow 2^+_1$	2280	2270†	17(3)	19
$\rightarrow 2^+_2$			16(3)	18
$2^+_3 \rightarrow 0^+_1$	2328	2256$^\#$	< 0.19	0.00010
$\rightarrow 2^+_1$			< 42	16
$\rightarrow 0^+_2$			< 26	0.5
$\rightarrow 2^+_2$			< 762	29
$2^+_4 \rightarrow 0^+_1$	2403	2728†	0.0025(11)	0.0002
$\rightarrow 2^+_1$			17(7)	4
$\rightarrow 0^+_2$			12(5)	0.05
$\rightarrow 2^+_2$			< 81	26
$\rightarrow 2^+_3$				0.6
$4^+_2 \rightarrow 2^+_1$	2489	2702$^\#$	< 2.5	1.2
$\rightarrow 2^+_2$			< 764	39
$\rightarrow 4^+_1$			< 673	0.3
$4^+_3 \rightarrow 2^+_1$	2733	2903$^\#$	4^{+5}_{-4}	0.014
$\rightarrow 2^+_2$			3(3)	0.09
$\rightarrow 4^+_1$			100^{+120}_{-100}	19
$\rightarrow 2^+_3$				28
$\rightarrow 4^+_2$				12
$6^+_1 \rightarrow 4^+_1$	3000	3034$^\#$		42
$\rightarrow 4^+_2$				20

This work adds ^{118}Sn to the study and discusses possible mixing between the normal and intruder configurations based on a comparison of the new experimental data and IBM calculations, which were introduced above. In Sn, the intruder structure is energetically lowest in ^{116,118}Sn (compare [8]). No microscopic calculations as for ^{110,112}Cd are presently available. Large-scale Monte Carlo shell model (MCSM) calculations did, however, highlight the importance of proton excitations in Sn to understand the evolution of the $B(E2;2^+_1 \rightarrow 0^+_1)$ transition probabilities and showed that a second-order phase transition appears to take place from a moderately deformed to a spherical ground state for the more neutron-rich Sn isotopes when passing ^{116}Sn [1]. The results of the *sd* IBM-2 calculations with mixing and the comparison to the corresponding experimental data are presented in Table IV. The parameters are given in Sec. IV.

Despite a few discrepancies, whose origin was already discussed for ^{116}Sn [8] and attributed to the selection rules of the O(5) symmetry present in the U(5) and O(6) group chains of the IBM [32,33], the agreement between the IBM results and the data is good both for the energies and transition probabilities (see Table IV). In contrast to ^{116}Sn, only one excited 0^+ state is found below the 2^+ state of the lowest-lying intruder structure. A significant decrease of the $B(E2; 2^+_{\text{intr.}} \rightarrow 0^+_2)$ strength by about a factor of 2 as compared to ^{116}Sn is also observed. To account for this experimental observation, the effective proton charge has been set to $e_{\pi_2} = 0.042\, eb^2$ ($e_{\pi_2} = 0.161\, eb^2$ in ^{116}Sn and $0.105\, eb^2$ in ^{114}Sn). All other parameters in the $E2$ operator [compare Eq. (7)] are the same as in the studies of ^{114,116}Sn [5,8]. It should be noted that e_{π_2} was drastically changed in ^{116}Sn to obtain two very collective $B(E2; 2^+_{\text{intr.}} \rightarrow 0^+_{2,3})$ values [8]. It remains to be seen if a similar effect will be observed in ^{114}Sn. Based on all presently available experimental data in ^{118}Sn, a scenario, where due to mixing the $2^+_{\text{intr.}}$ would drop below the $0^+_{\text{intr.}}$, is not favored. With support from the IBM calculation the 0^+_2 state is identified as the bandhead of the intruder structure in ^{118}Sn and, in doing so, can also account for the collective $B(E2; 0^+_2 \rightarrow 2^+_1)$ (see Table IV) generated due to mixing between the normal and intruder 0^+ states. Furthermore, the evolution of the excitation energy of the intruder bands in stable Sn isotopes reveals a global minimum for the lowest 2^+ intruder state in ^{118}Sn. Compared to ^{116}Sn, lower excitation energies for the 4^+ and 6^+ intruder states are also observed [10]. To further characterize the intruder structure and mixing with the normal configuration in ^{118}Sn, lifetime measurements for the 0^+_3, 2^+_3, 4^+_2, and 6^+_1 states are crucial. Additionally, precise measurements of branching ratios and of multipole mixing ratios δ in coincidence experiments are needed. The revised and smaller $E2$ branching ratio for the 6^+_1 state of 5.8(8) is now closer to the IBM result of 2.1 but still significantly larger.

VI. CONCLUSION

The study of the β decay of ^{118}In to low-lying excited states in ^{118}Sn was performed using the GRIFFIN spectrometer at the TRIUMF-ISAC facility. We were able to identify 99 γ-ray transitions from 23 levels, of which 43 transitions and one level are newly observed. Using GRIFFIN's full array of 16 HPGe clover detectors allowed us to resolve three transitions near 285 keV which led to the reduction of the intensities previously assigned to 284.5 keV and 285.3 keV by half. This ultimately reduced the $B(E2; 2^+_{\text{intr.}} \rightarrow 0^+_{\text{intr.}})$ value from 39(7) W.u. to 21(4) W.u.. Less collectivity in the $2^+_{\text{intr.}}$ state is not entirely supported by the present calculations, although it is possible that the $B(E2)$ strength is fragmented between the $2^+_{\text{intr.}}$ and $2^+_{3,4}$ states.

The experimental results were in reasonably good agreement with the predictions of *sd* IBM-2 calculations with mixing, similar to previous comparisons for ^{114,116}Sn. The 0^+_3 state in ^{114,116}Sn had previously been suggested to be the bandhead of the π 2p-2h intruder band. However, this is not the case in ^{118}Sn. Despite strong mixing with the 0^+_3 state, the 0^+_2 is still considered the bandhead and is supported by the IBM. Given the strong configuration mixing of many of the other states, it is difficult to conclusively assign structure. In future campaigns, lifetime measurements of excited states in even-even stable Sn isotopes would provide a better understanding of configuration mixing and the evolution of the structure of these nuclei.

ACKNOWLEDGMENTS

The infrastructure of GRIFFIN has been funded through contributions from the Canada Foundation for Innovation, TRIUMF, University of Guelph, British Columbia Knowledge Development Fund, and the Ontario Ministry of Research and Innovation. TRIUMF receives funding through a contribution agreement through the National Research Council Canada. This work was supported by the Natural Sciences and Engineering Research Council of Canada. M.S. acknowledges support by the National Science Foundation under Contract No. PHY-1565546 (NSCL).

---

[1] T. Togashi, Y. Tsunoda, T. Otsuka, N. Shimizu, and M. Honma, Phys. Rev. Lett. **121**, 062501 (2018).

[2] J. Bron, W. H. A.Hesselink, A. V. Poelgeest, J. J. A. Zalmstra, M. J. Uitzinger, H. Verheul, K. Heyde, M. Waroquier, H. Vincx, and P. V. Isacker, Nucl. Phys. A **318**, 335 (1979).

[3] K. Heyde and J. L. Wood, Rev. Mod. Phys. **83**, 1467 (2011).

[4] P. E. Garrett, J. Phys. G: Nucl. Part. Phys. **43**, 084002 (2016).

[5] M. Spieker, P. Petkov, E. Litvinova, C. Müller-Gatermann, S. G. Pickstone, S. Prill, P. Scholz, and A. Zilges, Phys. Rev. C **97**, 054319 (2018).

[6] H. Fielding, R. Anderson, P. Kunz, D. Lind, C. Zafiratos, and W. Alford, Nucl. Phys. A **304**, 520 (1978).

[7] J. L. Pore, D. S. Cross, C. Andreoiu, R. Ashley, G. C. Ball, P. C. Bender, A. S. Chester, A. Diaz Varela, G. A. Demand, R. Dunlop, A. B. Garnsworthy, P. E. Garrett, G. Hackman, B. Hadinia, B. Jigmeddorj, A. T. Laffoley, A. Liblong, R. Kanungo, B. Noakes, C. M. Petrache, M. M. Rajabali, K. Starosta, C. E. Svensson, P. J. Voss, Z. M. Wang, J. L. Wood, and S. W. Yates, Eur. Phys. J. A **53**, 27 (2017).

[8] C. M. Petrache, J.-M. Régis, C. Andreoiu, M. Spieker, C. Michelagnoli, P. E. Garrett, A. Astier, E. Dupont, F. Garcia, S. Guo, G. Häfner, J. Jolie, F. Kandzia, V. Karayonchev, Y.-H. Kim, L. Knafla, U. Köster, B. F. Lv, N. Marginean, C. Mihai, P. Mutti, K. Ortner, C. Porzio, S. Prill, N. Saed-Samii, W. Urban, J. R. Vanhoy, K. Whitmore, J. Wisniewski, and S. W. Yates, Phys. Rev. C **99**, 024303 (2019).

[9] A. Bohr and B. R. Mottelson, *Nuclear Structure* (World Scientific, Singapore, 1998).

[10] K. Kitao, Nucl. Data Sheets **75**, 99 (1995).

[11] S. Raman, T. A. Walkiewicz, L. G. Multhauf, K. G. Tirsell, G. Bonsignori, and K. Allaart, Phys. Rev. C **37**, 1203 (1988).

[12] I. V. Mikhailov and A. M. Demidov, Bull. Acad. Sci. USSR Phys. Ser. **53**, 69 (1989).

[13] A. Garnsworthy *et al.*, Nucl. Instrum. Methods Phys. Res. A **918**, 9 (2019).

[14] U. Rizwan, A. Garnsworthy, C. Andreoiu, G. Ball, A. Chester, T. Domingo, R. Dunlop, G. Hackman, E. Rand, J. Smith, K.

Starosta, C. Svensson, P. Voss, and J. Williams, Nucl. Instrum. Methods Phys. Res. A **820**, 126 (2016).

[15] A. Garnsworthy, C. Pearson, D. Bishop, B. Shaw, J. Smith, M. Bowry, V. Bildstein, G. Hackman, P. Garrett, Y. Linn, J.-P. Martin, W. Mills, and C. Svensson, Nucl. Instrum. Methods Phys. Res. A **853**, 85 (2017).

[16] J. Kantele and M. Karras, Phys. Rev. **135**, B9 (1964).

[17] L. C. M. do Amaral, C. V. de Barros Leite, J. M. F. Jeronymo, and A. G. de Pinho, Z. Naturforsch. **24**, 1196 (1969).

[18] J. Hattula, E. Liukkonen, and J. Kantele, Nucl. Phys. A **125**, 477 (1969).

[19] W. D. Kulp, J. L. Wood, J. M. Allmond, J. Eimer, D. Furse, K. S. Krane, J. Loats, P. Schmelzenbach, C. J. Stapels, R.-M. Larimer, E. B. Norman, and A. Piechaczek, Phys. Rev. C **76**, 034319 (2007).

[20] A. H. Wapstra, in *Alpha-, Beta- and Gamma-Ray Spectroscopy*, Vol. 1, edited by K. Siegbahn (North-Holland, Amsterdam, 1965), p. 539.

[21] ANU, BrIcc Conversion Coefficient Calculator, http://bricc.anu.edu.au/index.php.

[22] J. Hattula, E. Liukkonen, and J. Kantele, Z. Phys. **231**, 203 (1970).

[23] P. Guazzoni, L. Zetta, A. Covello, A. Gargano, B. F. Bayman, T. Faestermann, G. Graw, R. Hertenberger, H.-F. Wirth, and M. Jaskola, Phys. Rev. C **78**, 064608 (2008).

[24] NDC Brookhaven National Laboratory, Logft calculator, https://www.nndc.bnl.gov/logft/.

[25] J. Smith, A. MacLean, W. Ashfield, A. Chester, A. Garnsworthy, and C. Svensson, Nucl. Instrum. Methods Phys. Res. A **922**, 47 (2019).

[26] T. Otsuka and N. Yoshida, Program NPBOS, JAERI-M 85 report (Japan Atomic Energy Research Institute, 1985).

[27] K.-H. Kim, A. Gelberg, T. Mizusaki, T. Otsuka, and P. von Brentano, Nucl. Phys. A **604**, 163 (1996).

[28] G. Puddu, S. Scholten, and T. Otsuka, Nucl. Phys. A **348**, 109 (1980).

[29] M. Délèze, S. Drissi, J. Kern, P. Tercier, J. Vorlet, J. Rikovska, T. Otsuka, S. Judge, and A. Williams, Nucl. Phys. A **551**, 269 (1993).

[30] P. E. Garrett, T. R. Rodríguez, A. D. Varela, K. L. Green, J. Bangay, A. Finlay, R. A. E. Austin, G. C. Ball, D. S. Bandyopadhyay, V. Bildstein, S. Colosimo, D. S. Cross, G. A. Demand, P. Finlay, A. B. Garnsworthy, G. F. Grinyer, G. Hackman, B. Jigmeddorj, J. Jolie, W. D. Kulp, K. G. Leach, A. C. Morton, J. N. Orce, C. J. Pearson, A. A. Phillips, A. J. Radich, E. T. Rand, M. A. Schumaker, C. E. Svensson, C. Sumithrarachchi, S. Triambak, N. Warr, J. Wong, J. L. Wood, and S. W. Yates, Phys. Rev. Lett. **123**, 142502 (2019).

[31] E. R. Gamba, A. M. Bruce, S. Lalkovski, M. Rudigier, S. Bottoni, M. P. Carpenter, S. Zhu, J. T. Anderson, A. D. Ayangeakaa, T. A. Berry, I. Burrows, M. C. Gallardo, R. J. Carroll, P. Copp, D. M. Cullen, T. Daniel, G. F. Martínez, J. P. Greene, L. A. Gurgi, D. J. Hartley, R. Ilieva, S. Ilieva, F. G. Kondev, T. Kröll, G. J. Lane, T. Lauritsen, I. Lazarus, G. Lotay, C. R. Niţă, Z. Podolyák, V. Pucknell, M. Reed, P. H. Regan, J. Rohrer, J. Sethi, D. Seweryniak, C. M. Shand, J. Simpson, M. Smoleń, E. A. Stefanova, V. Vedia, and O. Yordanov, Phys. Rev. C **100**, 044309 (2019).

[32] J. Jolie and H. Lehmann, Phys. Lett. B **342**, 1 (1995).

[33] H. Lehmann and J. Jolie, Nucl. Phys. A **588**, 623 (1995).

[34] S. Raman, C. Nestor, and P. Tikkanen, At. Data Nucl. Data Tables **78**, 1 (2001).

[35] K. Kitao, Y. Tendow, and A. Hashizume, Nucl. Data Sheets **96**, 241 (2002).

[36] T. Tamura, Nucl. Data Sheets **108**, 455 (2007).